Department of Exploration Geophysics

Application of Vertical Seismic Profiling for the characterisation of hard rock

Andrew John Greenwood

This thesis is presented for the Degree of

Doctor of Philosophy

of

Curtin University

February 2013

Declaration

To the best of my knowledge and belief this thesis contains no material previously published by any other person except where due acknowledgment has been made.

This thesis contains no material which has been accepted for the award of any other degree or diploma in any university.

Signature: ………………………………………….

Date: ………………………...

Abstract

Seismic imaging in hard rock environments is gaining wider acceptance as a mineral exploration technique and as a mine-planning tool. However, the seismic images generated from hard rock targets are complex due to high rock velocities, low contrasts in elastic rock properties, fractionated geology, complicated steep dipping structures and mineralogical alterations. In order to comprehend the complexity and utilise seismic images for structural mapping and rock characterisation, it is essential to correlate these images to known geology. An ideal tool for this purpose is Vertical Seismic Profiling or VSP. The VSP method can provide not only a means to correlate seismic images to geology but also to study the properties of the transmitted seismic field as it is modified by different rock formations, the origin of the reflected events and the corresponding reflector geometry. However, the VSP technique is rarely used in hard rock environments because of the cost and operational issues related to using clamping geophones in exploration boreholes, which are 96 mm or less in diameter. Consequently the main objective of this research is to produce an efficient VSP methodology that can be readily deployed for mineral exploration.

An alternative to the clamping geophone is the hydrophone. Hydrophones are suspended in, and acoustically coupled to the borehole wall through, the borehole fluid. Borehole acoustic modes known as "tube-waves" are generated by seismic body waves passing the water column and are guided in the borehole due to the high acoustic impedance contrast between the rock and fluid. Tube-waves are 1-2 orders in magnitude higher in amplitude than seismic signal and mask reflected energy in hydrophone VSP profiles. As such the use of borehole hydrophone arrays to date has been restricted to direct body wave measurements only. I have effectively mitigated tube-waves in hydrophone VSP surveys with specific acquisition methodologies and refined signal processing techniques. The success of wavefield separation of tube-waves from hydrophone data depends critically upon; having high signal to noise ratio, well sampled data, pre-conditioning of the field data and processing in the field record (FFID) domain. Improvements in data quality through the use of high viscosity drilling fluids and baffle systems have been tested and developed. The

increased signal to noise ratio and suppression of tube-wave energy through these technologies greatly enhances the performance of hydrophone VSP imaging.

Non-standard wavefield separation techniques successfully removed strong coherent tube-wave noise. The additional wavefield separation steps required to remove high amplitude tube-waves does degrade the overall result with some fidelity and coherency being lost. However, a direct comparison of hydrophone and borehole clamping geophone VSP surveys has been conducted in the Kambalda nickel district and the two methodologies produced comparable results. The difference was that the hydrophone data were collected in a fraction of the time compared to clamping geophone equipment with significantly less risk of equipment loss and with reduced cost.

The results of these field experiments and the data processing methodology used, demonstrate the potential of hydrophone VSP surveys in the small diameter boreholes typical of hard rock exploration. Thus, these results show that hydrophone VSP is a viable, cost effective and efficient solution that should be employed more routinely in hard rock environments in order to enhance the value of the surface seismic datasets being acquired.

Acknowledgements

Table of contents

Table of figures

List of tables

List of common abbreviations and definitions used

+TT   Addition of FB time to convert to TWT or from -TT to FRT

-TT   Subtraction of FB time which flattens the First breaks to 0 ms or a defined time datum. Usually applied before 2D median filtering of P_d.

+ve   positive

-ve   negative

3C   Three component geophone

AGC   Automatic gain control

AI   Acoustic impedance

CDP   Common depth point

Down dip   geological down dip direction, usually below a deviated borehole in the negative offset direction.

FB   First breaks

FI   Felsic intermediate

FRT   Field record time.

FWS   Full Waveform Sonic

H_1 Horizontal component in the radial direction

H_2 Horizontal component in the transverse direction

MB   Mafic basalt

OVSP   Offset VSP

P_d Down-going P-wave

P_u Up-going P-wave

P_D Wavefield separated down-going P-wave profile

P_U Wavefield separated up-going P-wave profile

S_d Down-going S-wave

S_u Up-going S-wave

S_D Wavefield separated down-going S-wave profile

S_U Wavefield separated up-going S-wave profile

SG   Specific gravity

SNR   Signal to noise ratio

T_d Down-going tube-wave

T_u	Up-going tube-wave
TWT	Two way time
UM	Ultramafic
Up dip	geologically up dip, typically above a deviated borehole
V_p	P-wave velocity
V_s	S-wave velocity
V_t	Tube-wave velocity
VSP	Vertical Seismic profile
W	Hydrophone
W_{dt}	Hydrophone data after tube-wave separation
W_D	Hydrophone down-going profile
W_U	Hydrophone up-going profile
WVSP	Walk away VSP
X	Horizontal geophone component
Y	Horizontal geophone component
Z	Vertical geophone component
ZVSP	Zero offset VSP

1 Introduction

1.1 Prelude

Western Australia is minerals rich with over A$50b worth of mineral resource projects either committed or under construction (Prospect, 2011). These are shown in Figure 1. Many of these base metal, gold and nickel projects are located in the Yilgarn Craton, Australia's premier mineral province. It draws more than half of Australia's minerals exploration expenditure, possesses approximately 40% of Australia's known gold reserves and 90% of Australia nickel reserves (McKay, 2010).

The fundamental geology of Western Australia and the location of the Yilgarn Craton are shown in Figure 2. The Yilgarn Craton is Archaean in age and has been accreted from former continental crust and volcanic arcs 2670-2650 Ma ago (Myers, 1993). The accretion is chronicled by voluminous tholeiitic basalt, extensive komatiite volcanism and widespread granite and granodiorite intrusions which comprise over 70% of the craton (Swager, 1997). Accretion occurred in several phases separated by pauses in subduction with renewed activity occurring episodically. During these episodes, emplacement of the majority of the gold mineralisation occurred as well as regional metamorphism and deformation (Surhone et al., 2010). The Yilgarn Craton is geologically dived into granite-gneiss metamorphic and granite-greenstone terranes. The granite-gneiss metamorphic terrane is subdivided into the South-western Province and Western Gneiss Belt. The granite-greenstone terrane is subdivided into the North-East Goldfields, the Southern Cross and the greenschist metamorphic Murchison Provinces. The greenstone belts and granites range in age from approximately 3.1-2.9 Ga, to 2.75-2.65 Ga. (Myers and Hickman, 1990).
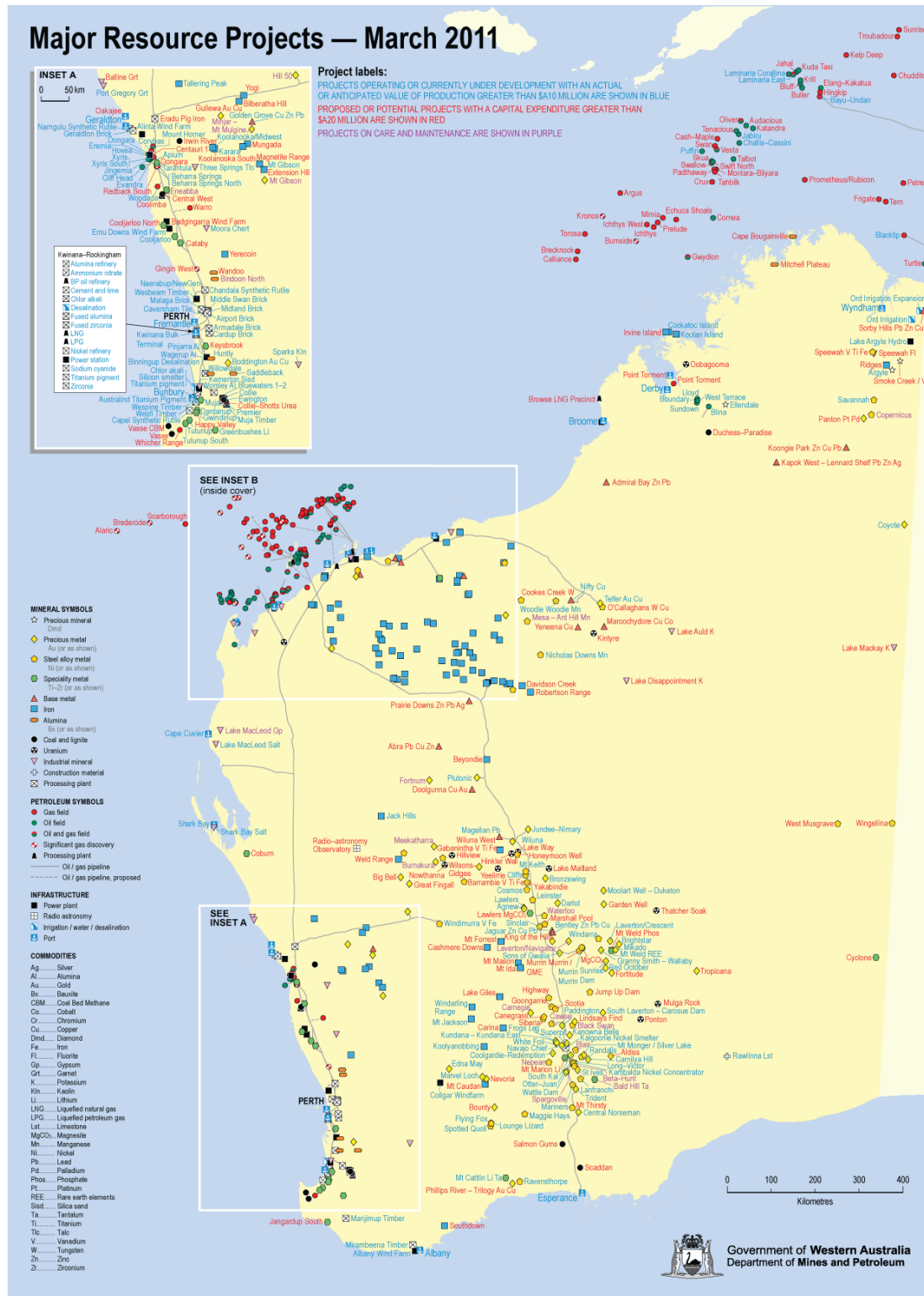
Figure 1-1. Major resource map of Western Australia at March 2011 (Prospect, 2011).

Charting of economic ore deposits within the Yilgarn has traditionally relied on outcrop mapping, grid drilling and geophysical potential field techniques such as magnetic, electromagnetic (EM) and gravity methods. However these methods are only reliable to about 500 m depth as their resolving power decreases with depth (Eaton et al., 2003). In addition, geophysical anomalies are often masked by a thick conductive overburden within the Yilgarn Craton. As such, the major shallow economic resources have now been found. Exploration needs to focus on extending current reserves and discovery of deeper targets to replace the current deposits being mined (Debicki, 1996).
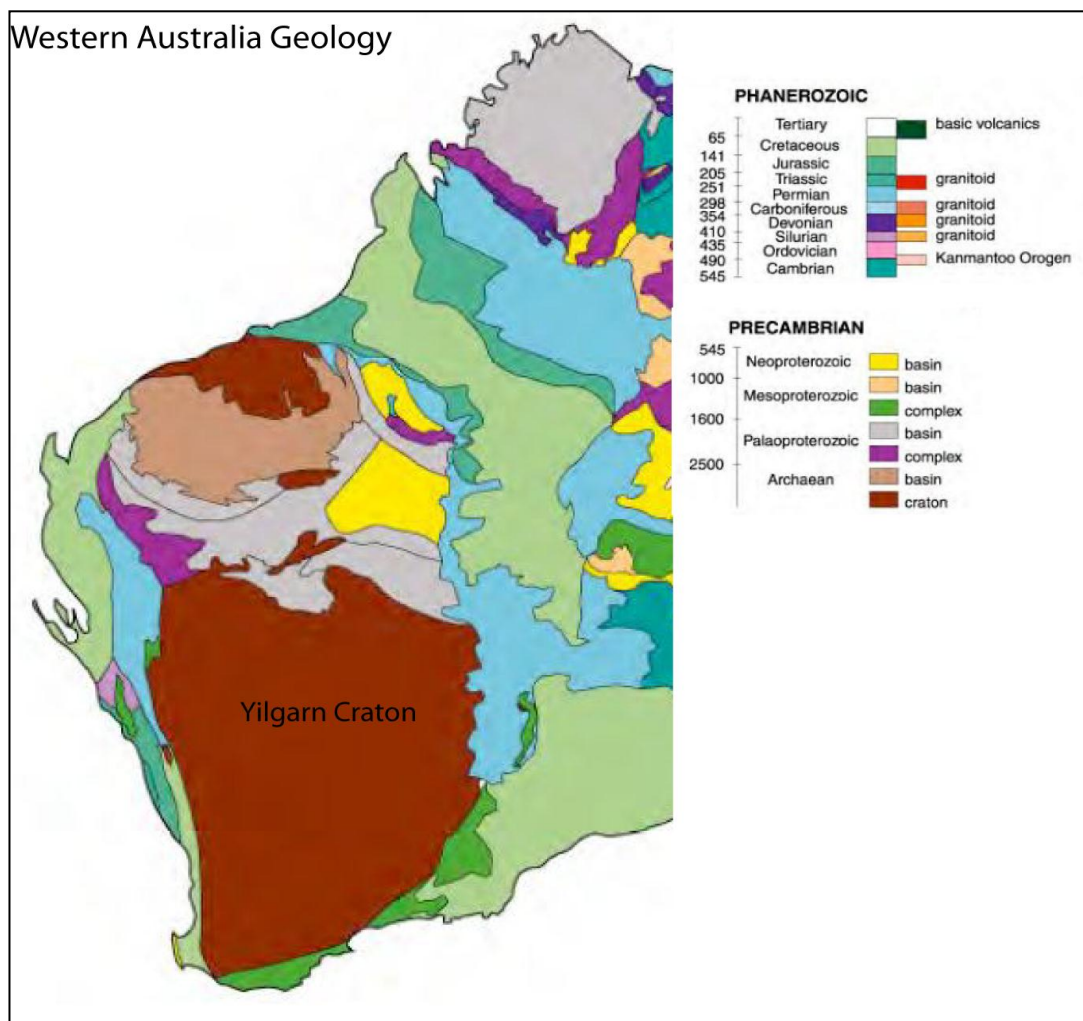
Figure 1-2. Basic geological of Western Australia. Modified from D'Addario (1986).

In brown-fields where operating mines already exist, projected mine extension and mine development make extensive use of Down-Hole EM (DHEM) acquired from

surface and underground boreholes[1]. From these data, conductive plates can be modelled which represent potential sulphide bodies (Duncan et al., 1998; Elders and Wellington, 1998; Stolz, 2003). These plates however have non unique solutions for their thickness and lateral extent. As such, this technique gives limited information on structure and reserves. Recent developments in Borehole Radar are helping to better delineate targets and subsequently help mine planning (Turner et al., 2000; Osman et al., 2003) but cannot "see" more than 30 m - 50 m from the borehole.

In contrast to potential field methods, seismic methods are considered a high resolution exploration tool since the loss of resolution is monotonic with depth (Urosevic et al., 2005). Seismic resolution is dependent on seismic wavelength which in turn depends on the acoustic velocity of the rock and frequency of the seismic source. These factors are relative to the rock type, its elastic parameters and the seismic wavelet generated, but tend not to vary significantly in hard rock environments such as the Yilgarn.

Seismic techniques are the standard tool in petroleum exploration and also common in coal exploration. Adaption of seismic techniques to mineral exploration however has been slow because of the geological complexity encountered, small range in elastic properties, and in the case of the Yilgarn, a thick highly heterogeneous regolith cover that is typically present. In addition to the "fractal-like" geology, reactivated, altered and highly fractured zones cause significant scattering of seismic energy. All of these factors combine to produce complex seismic responses and highly variable reflection patterns.

1.2 Early applications of hard rock seismic

In western countries, in the 1970's and 1980's, many tests of high-resolution seismic imaging methods in hard rock environments had been conducted. Studies included seismic imaging of shallow sedimentary hosted mineral deposits (Wright, 1981) and high-resolution seismic images from faulted and fractured environments to

---

[1] In mineral exploration it is common practice to use the term borehole as opposed to petroleum exploration where it common place to use the term drill hole. Borehole will be used to refer to all mineral and drill hole for petroleum instances.

characterise nuclear waste sites in the Canadian Shield (Green and Mair, 1983). Pretorius et al. (1989) demonstrated the usefulness of an integrated seismic and petrophysical approach to image key geologic structures for mineral exploration in the Witwatersrand Basin, South Africa. Following this, petrophysical lab measurements of common sulphides and crystalline rocks have been carried out by (Salisbury et al., 1996). This has confirmed high impedance contrasts and reflectivity from massive sulphide ore bodies giving rise to the application of seismic methods for exploration of such deposits (Zhou and Greenhalgh, 1997; Day-Lewis et al., 2005). These results inspired the application of seismic methods for mineral exploration worldwide and in Australia.

In Australia during the 1990's, Geoscience Australia (GA) collected provincial scale seismic traverses throughout the Eastern Goldfields (Drummond et al., 2000) and in 1999 the Australian National Seismic Imaging Resource (ANSIR) acquired several regional seismic transects in the vicinity of existing gold mines in the Yilgarn Craton. These transects were targeted at deep crystalline structures and yielded impressive images showing continuity and structural complexity at depth. However due to the acquisition parameters and processing procedures used these images did not provide useful information shallower than 2 km. In 2002 reprocessing of an ANSIR transect which crossed the Wallaby gold mine 20 km east of Laverton, Western Australia. Reprocessing focused on targeting shallow structures (200 to 500 m) by reducing the maximum shot receiver offset used in processing, muting Normal Move Out stretch and resolving shallow static issues with refraction static analysis. The reprocessing produced coherent structures from 200 m down to the deepest structures (Urosevic, et al., 2005). Subsequently reprocessing of a transect which crossed Sunrise Dam gold mine (55 km south of Laverton) was requested by Barrick Gold (formerly Placer Dome Asia Pacific). Again structural features were imaged and correlated to years of drilling and geological information. These hard rock seismic successes brought about the M363 project. This project was initiated in 2004 by Curtin University of Technology department of Exploration Geophysics and was supported by the State Government research institute, Minerals and Energy Research Institute of Western Australia (MERIWA) and sponsored by four gold mining companies. This was an experimental program with 150 line kilometres of reflection seismic data crossing six gold mines in the Yilgarn Craton (Urosevic and Evans,

2007). This project finally broke the dogma of reflection seismic not producing relevant information for mineral exploration in Australian hard rock environments. A few mining companies have welcomed the success and conducted larger scale 2D and 3D seismic surveys in the Kambalda and Agnew – Wiluna regions of the Yilgarn. The complexity of hard rock terranes is in general such that the conventional seismic acquisition, processing and interpretational approaches still requires adaption and development for these environments. Steeply dipping structures are difficult to image with surface seismic methods as reflections often are not reflected towards the surface. Further advances require an understanding of the origins of recorded seismic reflection events and characterising this in terms of underground geology.

Through the use and analysis of transmitted and reflected wavefields in boreholes, the origin of seismic events can be determined (Gulati, 1998). This is of great importance for the interpretation of complex seismic images. Therefore it is essential to incorporate the use of borehole seismology and geological information into the imaging and interpretation processes of mineral seismic exploration (Urosevic and Evans, 2007). Appropriately, seismic targets and "borehole ties" are now being drilled. These borehole ties should but do not always include the use of petrophysical studies, Full Waveform Sonic (FWS) and density wire-line logging, seismic velocity check-shot surveys and Pulse-Transmission (PT) tests on core samples.

1.3 Vertical Seismic Profiling

Borehole seismic methods place either the receiver or source down-hole and occasionally both. In general, where a surface source and borehole receivers are employed, the term Vertical Seismic Profiling (VSP) is used. When surface receivers and a borehole source are used, the term Reverse VSP is used. This terminology and use of "VSP" is adhered to in this thesis unless specifically stated.

A major advantage of VSP over surface seismic is in having the receiver in bedrock. This eliminates many of the noise sources typically associated with surface seismic such as wind, air waves, surface waves, electrical interference, poor geophone

coupling and irregular near surface layers. In general seismic wavefields travel only once through formations that are above the receiver (wavefields may travel through these upper layers if they have been reflected up to the surface and back down, these events are known as multiples and usually occur when there are high contrasting boundaries near the surface which reflect more energy than they transmit). This reduces the damaging effects of lossy layers, results in higher signal to noise ratios and higher resolution of seismic responses.

Events recorded in a VSP survey can be directly related to the rock units and contacts. With receivers in the borehole at specified distances and placed at stratigraphic boundaries, both incident and reflected wavefields can be measured. This enables accurate measurements of formation velocities, frequencies, seismic attenuation and reflectivity of units intersected by the borehole allowing characterisation of units seismically. Furthermore we can understand the origin of reflection events with direct correlation to core logs and wire-line data. It is of particular interest to study various seismic attributes that could help characterise such rock units in a remote sense. This has not been attempted in hard rocks in Australia.

1.4 VSP – A brief history

The first documented borehole seismic application was patented by Fessenden (1917). His patent describes how an ore body can be detected with acoustic sources and receivers between two boreholes. Following on from this Barton (1929) proposed possible uses of seismic measurements from boreholes to map structures. McCollum and LaRue (1931) went further to describe the utilization of existing wells for seismic work and proposed a method to determine geologic structure using surface sources and receivers in a single well. These early observations laid the foundation for VSP and Cross Well Profiling (CWP). However the possibilities of VSP for exploration were largely ignored for many years and studies were for the most part restricted to velocity determination from analysis of first arrival travel times (Dix, 1939) and the development of the velocity "check-shot" method (Dix, 1945).

In the 1950's the use of closely spaced down-hole receivers (< 200 ft) and analysis of the signal after the first arrivals identified reflected (up-going) wavefields and a way to determine multiple arrivals from VSP (Jolly, 1953; Levin and Lynn, 1958). Techniques to separate the up- and down-going wavefields were then developed and the up-going events used for calibration of surface seismic (Balch et al., 1982). These separation techniques formed the primary processing requirements for VSP imaging.

Extensive research was conducted in the 1960's and 70's by Russian geophysicist Gal'perin at the Institute of Physics of the Earth, Academy of Sciences, USSR (IPE AS USSR). His monograph was first published in 1971 and translated to English in 1974 (Gal'perin, 1974). Gal'perin studied seismic wavefield propagation in real media using 3-component (3C) clamping geophones, allowing all seismic wave modes to be studied. In the Gal'perin implementation, 3C geophones are set at 66.7 degrees to each other. This has its advantages in recording but has been reduced to a nowadays standard of 3 orthogonally set geophone elements which, measure particle motion in the x, y and z planes, allowing analysis and separation of the different wavefields and modes observed in a borehole. Gal'perin validated his work with physics and established VSP as our in-field seismic laboratory.

During the 1980's commercial VSP work was primarily conducted in petroleum exploration with Zero-offset VSP (ZVSP) check shot surveys being performed. Processing was commonly reduced to single component analysis of the vertical component for slowness calculations, time to depth conversions and producing corridor stacks for calibration of 2D seismic sections (Hardage, 2000). VSP was, and still is considered expensive due to the deployment time of clamping geophone shuttles, due to the limited number of geophone shuttles able to be deployed simultaneously and associated drill rig stand by cost (Chopra and Hardage, 2010). Scientific studies conducted during this time made advances in measurements of absorption and dispersion (Ganley and Kanasewich, 1980), porosity estimation (Stone, 1983), measurements of seismic attenuation (Kan et al., 1983; Spencer et al., 1983), different wavefield separation techniques (Suprajitno and Greenhalgh, 1985; Moon et al., 1986; Freire and Ulrych, 1988), imaging away from the well with offset VSP (Gaiser et al., 1983; Monash et al., 1984), and VSP migration (Dillon, 1988). Hardage (2000) offers an excellent review of early western VSP research.

In the 1990's commercial work focused on 3C VSP and imaging away from the well using offset (OVSP) and Walk-away VSP (WVSP) geometries. Processing used all three components to separate the P and S wavefields and an interpretative approach to wavefield separation was developed for check shot and image processing (Hinds et al., 1996).

With the improvement in development of downhole engineering and electronics, shuttles have become smaller, a necessary development to shift the natural frequency of the tool away from the seismic frequency band of interest (Hardage, 2000). Downhole telemetry advancements have seen a higher numbers of receiver modules being deployed, some now measuring up to 100 or more depth intervals, decreasing the survey / rig time. With this progression, VSP work has extended to 3D and multi azimuth surveys (Krohn et al., 1995).

The 2000's have seen a focus on development of 3D VSP, increasing lateral imaging away from the well (Muller et al., 2010), measuring anisotropy, porosity and recovering seismic attributes. Campbell et al. (2005) showed that ZVSP can return, as standard: well tie correlation, direct measurements of seismic Q, geometric divergence, identification of interbed multiples, 2D phase analysis and 3D match filter design for surface seismic data, and calculation of acoustic impedance from Bayesian inversion.

With all the advantages VSP has to offer it is still a rarity in petroleum exploration to undertake 3D 3C VSP and virtually non-existent in hard rock environments.

1.5 Borehole seismology in hard rocks

Only a few hard rock exploration VSP surveys have been documented in western literature. The Bell Allard Ore body in Mattagami, Quebec is probably the most widely acknowledged study. Here a 2D surface line located a 1 km deep anomaly believed to originate from massive sulphides (Calvert and Li, 1999). Due to the possibility of out-of-plane reflections from complex dipping structures, VSP was

employed to confirm the existence of the ore body (Adam et al., 2000). Two VSP's were conducted; one in the borehole that intersected a massive sulphide deposit recorded strong P and converted S waves. The other VSP conducted in a borehole 200 m to the northeast of the deposit imaged a basalt/rhyolite contact.

In New Brunswick Canada 3C-VSP was trialled at the Half-mile Lake massive sulphide deposit (Bellefleur et al., 2004) to test the viability of VSP for imaging a known ore body. Multi offset and multi azimuth VSP successfully located a deep sulphide lens connected to the ore body but was unable to image its shape accurately.

Very exciting results on the imaging of internal fractures in Precambrian crystalline rocks were presented by Juhlin et al. (1991). They used both surface seismic and Vertical Seismic Profiling (VSP) to verify the ability of the seismic method to map internal composition and fractures of crystalline rock in Sweden. The results were verified by correlation with wireline logs and borehole core analysis. Similarly multi-azimuth VSP has been used to characterise crystalline rocks and fracture zones for deep nuclear waste disposal site identification in Finland (Cosma and Heikkinen, 1996).

1.6 Hydrophones as an alternative borehole receiver

Hard rock boreholes are typically drilled with HQ - 96 mm, NQ - 76 mm and BQ - 61 mm diameter drill bits. These are small in diameter compared to petroleum holes for which most down-hole technology has been developed and there are few "slim-line" borehole seismic tools available. Slim-line tools are costly and each 3C shuttle weighs between 6 to 15 kg. Deployment of multiple shuttles becomes logistically expensive and the financial risk can outweigh the cost of a mineral exploration borehole. As such shuttles are typically restricted to strings of 8 or less and more commonly only one or two. The limitation of only a few shuttles requires multiple moves in the borehole to acquire full borehole coverage (aperture) which is time expensive and requires repeat shooting at the surface. It is also virtually impossible to separate wavefields with deployment of a small number of shuttles (less than 8).

Wavelet repeatability of multiple shots at a single source point then becomes a major factor in data quality and not always achievable.

An alternative to conventional VSP tools is the hydrophone. Hydrophones are highly sensitive broadband pressure sensors. They are slim-line (< 50 mm), lightweight, rapidly deployable and do not require clamping. Strings of 24 to 48 receivers can be manufactured for the same cost as a single slim-line 3C shuttle and can cover 10's to 100's of meters of borehole aperture per shot.

Hydrophones require the borehole to be fluid filled. Fluids do not support shear waves, however it has been shown that S-wave energy can be transformed into a pressure wave within the borehole by radial deformation of the borehole wall, which creates a pressure wave in the fluid (White, 1953). Thus it is possible to collect both P- and S wavefields in fluid filled boreholes with hydrophone receivers.

Hydrophones have been tested for the purpose of borehole surveying. Results to date however have been limited to velocity and borehole tomography applications due to strong coherent noise known as tube-waves masking events after the direct arrivals (Marzetta et al., 1988; Milligan et al., 1997; Greenhalgh and Bierbaum, 2000; Gulati et al., 2001). Cao and Greenhalgh (1995) successfully used a 24 channel hydrophone string in a cross-well survey to delineate ore lodes tomographically in Western Australia but failed to succeed with reflection VSP imaging.

Milligan, et al. (1997) trialled suppressing tube-waves with closed cell foam baffles. This was successful in suppressing the tube-wave; however at depth the cells collapse under pressure reducing the suppression. Gulati, et al. (2001) also noted that tube-wave effects were much reduced at large shot offsets in his experiment and determined that it is likely possible to seismically image with hydrophones under certain circumstance. However this has never been tested at depths greater than 100 m or in an Australian hard rock environment.

1.7 Objectives and challenges

The primary objectives of this research are; to determine the applicability of borehole seismic methods to characterise seismically hard rocks of mineral importance found in the Yilgarn Craton, advance the current knowledge and understanding of the seismic signatures of hard rocks in Western Australia and improve imaging of mineral hosting structures with the application of VSP methodologies. Finally these objectives are to be achieved with methodologies that are inexpensive and efficient and as such can be accepted and adopted by mining industry for exploration of mineral deposits.

Complex geological targets and specific practices implemented by the mineral exploration industry have made these objectives challenging. To achieve these objectives further developments of acquisition techniques, signal processing and analysis were needed. For example hard rock exploration boreholes are typically drilled at high angles to orthogonally intersect prospective mineral targets. VSP in angled boreholes results in receivers having some lateral extent. When combined with walk-away and offset sources this configuration increases the spatial trace density of VSP, theoretically promoting seismic imaging around the borehole if the geology is not overly complex as unfortunately is often the case. Paramount to successful imaging requires migration of reflection events to a common image plane. Kirchhoff migration has been tested for this purpose.

A fundamental part of the study was to establish the viability of hydrophones as an alternative to 3C shuttles. A 24 channel hydrophone string was acquired for this purpose. New acquisition methodology and hardware had to be developed to overcome specific issues associated with borehole hydrophone acquisition for imaging proposes. Understanding and combating tube-waves both in acquisition and processing was of crucial importance to this study.

This research is intended as proof of concept of VSP as an exploration tool in Australian hard rock terranes, a way to look forward, expanding the effective radius of boreholes with the benefit of having direct correlation back to the drill core information.

1.8 Outline of thesis

The thesis is organised in the following way:

Chapter 2. This chapter introduces the principles of borehole seismic measurements and VSP imaging with respect to dipping targets at typical mining depths. I highlight the ambiguity in determining the origin of reflection events and approaches to be tested in subsequent chapters.

Chapter 3. Investigates the viability of borehole reflection seismology in hard rock environments. Numerical models of complex geological environments found within the Yilgarn Craton are presented. Synthetic seismic records are produced from these models using current mineral exploration drilling and proposed walk away VSP geometries. Kirchhoff depth migration imaging approach is tested in these complex models. The major limitations of the technique, field surveying parameters and data processing strategies are discussed.

A seismic pre-feasibility study acquired with a single 3C geophone borehole tool and short 2D surface line at Ranger Uranium mine Northern Territory is also presented here. This study incorporates the use of Petrophysical data (Pulse transmission, FWS, Density and gamma) to evaluate and characterise seismic responses of the hosting structure and lithologies.

Chapter 4. Specific acquisition issues that arise from suspension of hydrophones within the fluid and the non-compliance of hard rock boreholes are analysed and discussed. Methodologies to address these challenges that were developed through the course of my research are presented in this chapter.

Two specific and challenging issues are the suppression and separation of cable- and tube-waves from data at the acquisition phase. Development of experimental hydrophone baffle hardware which creates self-destructive interference of tube-waves has been presented here.

Chapter 5. To validate a borehole hydrophone array as a seismic imaging tool a comparison of borehole hydrophone array and 3C clamping geophone VSP surveys has been made and is presented in this chapter. Both data sets were acquired within the same borehole using the same acquisition geometry. The survey was conducted in North Kambalda and resides within the largest hard rock 3D seismic survey collected in Australia.

Chapter 6. The first hard rock hydrophone VSP imaging surveys conducted in Australia are presented in this chapter. Emphasis is made on tying VSP back to geologic and petrophysical data and characterising the seismic responses.

Results from the Kambalda Hydrophone / 3C geophone survey are analysed as well as offset VSP. These are tied into the Kambalda 3D surface seismic. Also presented in this chapter is a geologically poorly constrained green field exploration study in the Agnew-Wiluna region of Western Australia. Here I demonstrate the potential of imaging away from the well with VSP to delineate the structural architecture.

Chapter 7. Discusses the findings and presents conclusions drawn from this research with respect to the original objectives. The potential and limitations of VSP in hard rock environments of the Yilgarn are discussed. Particular reference is made to the development of a hydrophone array as a borehole seismic tool.

2 Principles of Vertical Seismic Profiling

2.1 Introduction

Many narratives cover the aspects of Vertical Seismic Profiling, One of the most accessible primers is Vertical Seismic Profiling: Principles (Hardage, 2000). Seismic wave propagation with particular reference to seismic modes found within the borehole environment, including tube-wave propagation is well covered by the collected works of White (2000) while VSP processing principles and strategies are covered by Hinds et al (1996).

In this chapter I present basic principles of: acoustic properties and seismic characterisation of mineralisation; seismic reflection and transmission; construction of VSP in time and space; the identification of down- and up-going wavefields; manipulation of VSP time for processing; construction of the VSP image point and the non-uniqueness of VSP data collected with typical mineral exploration borehole geometries.

VSP is widely accepted as having a surface source and down-hole receivers, however, reciprocity of seismic transmission allows the positions of receivers and source to be exchanged. This is typically termed reverse VSP or RVSP. In this document VSP will refer to surface sources and down-hole receivers unless specifically stated.

2.2 Reflectivity of Hard Rocks

Many factors influence the strength of seismic reflections at lithological boundaries; however, the most important is the contrast of acoustic impedance between lithological units. Acoustic Impedance Z is defined as the product of density and the compressional wave velocity of the unit.

$$Z_i = \rho_i V_i \qquad \textbf{Equation 2-1}$$

where ρ_i is the density and V_i is the P-wave velocity of the unit i. The ratio of reflected to incident energy is known as the reflection coefficient R and for pressure measurements is defined at normal incidence by:

$$R = \frac{\rho_2 V_2 - \rho_1 V_1}{\rho_2 V_2 + \rho_1 V_1} = \frac{Z_2 - Z_1}{Z_2 + Z_1} \qquad \textbf{Equation 2-2}$$

For elastic media, the S-wave impedance and reflectivity can also be calculated by substituting P-wave velocity with the S-wave velocity.

For a reflection event to be detected above background noise, the accepted minimum reflection coefficient required is 0.06 (Yilmaz, 2001). This equates to an acoustic impedance contrast $(Z_2 – Z_1)$ of 2.5 kg /m^{2}s in a hard rock environment (Salisbury, et al., 1996) and is equivalent to the difference between mafic and felsic rocks (Figure 2-2). These rock units are common in environments of mineral deposition and are often the target of exploration, as mineralisation commonly occurs along this interface.

The Nafe-Drake curve (Nafe and Drake, 1963) is shown in Figure 2-1a. This curve relates density and P-wave velocity for common rock units and follows the assumption that velocity increases with density. Initially developed from petroleum and marine sedimentary studies, this has been expanded to include volcanic, intrusive, and metamorphic rocks such as, Felsic, Mafic and Ultramafic rocks. Sulfides however, do not plot along the Nafe-Drake curve (Figure 2-1b), they display higher densities and a wider range of velocities because of differences in bonding and mean atomic weight (Birch, 1961). As such, ore minerals have much higher impedances than common felsic and mafic host rocks and make strong reflectors. As sulfides are commonly disseminated within the host rock, all mineralised rock units have a unique characteristic V_P and density relationship.
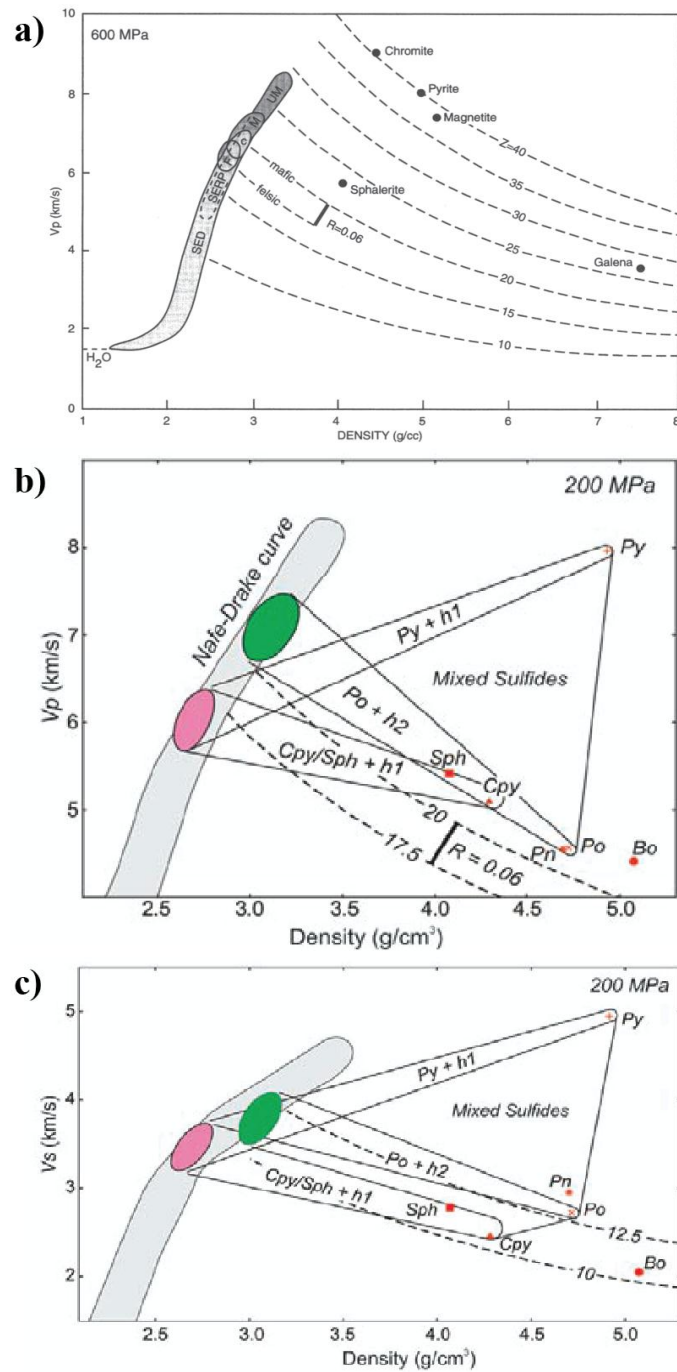
Eaton 2003

Figure 2-1. Panel a) relationship of P-wave velocity and density with common rocks and constant acoustic impedance lines shown. Panel b) and c) relationship of P- and S-wave velocity with Density with respect to common sulphides. The minimum reflection coefficient of *R = 0.06* is shown in all plots (Salisbury et al, 1996 and 2000).

17

2.3 Reflection and transmission of Seismic waves

At normal incidence, an incident P- or S-wave will only generate reflected and transmitted P- or S-wave respectively. For non-normal incidence, reflectivity is more complicated; an incident P-wave generates reflected P- and S-waves, as well as transmitted P- and S-waves. This is graphically shown in Figure 2-2 for a simple two layer case.

The amplitudes of the reflected and transmitted waves depend on the angle of incidence and the material properties (Castagna, 1993). Angles of the incident, reflected and transmitted waves are related by Snell's law:

$$p = \frac{\sin \theta_1}{V_{p1}} = \frac{\sin \theta_2}{V_{p2}} = \frac{\sin \varphi_1}{V_{s1}} = \frac{\sin \varphi_2}{V_{s2}} \qquad \textbf{Equation 2-3}$$

where p is the ray parameter, θ and φ are the angles of P- and S-wave propagation and subscripts 1 and 2 indicate material properties or angles of propagation in layers 1 and 2 respectively. The angle dependence of reflection and transmission coefficients of plane waves at a surface is given by Zoeppritz's equations Zoeppritz and Geiger (1919). The solutions of these are complicated and have been simplified by many authors (Bortfeld, 1961; Aki and Richards, 1980; Shuey, 1985) by making assumptions of boundary conditions. Much research is devoted to the use of the Zoeppritz equations in Amplitude with Offset (AVO) analysis. While this is not of primary interest to this study, accurate determination of transmitted and reflected V_p and V_s wavefields attained through VSP and FWS surveys is integral to part of this study.
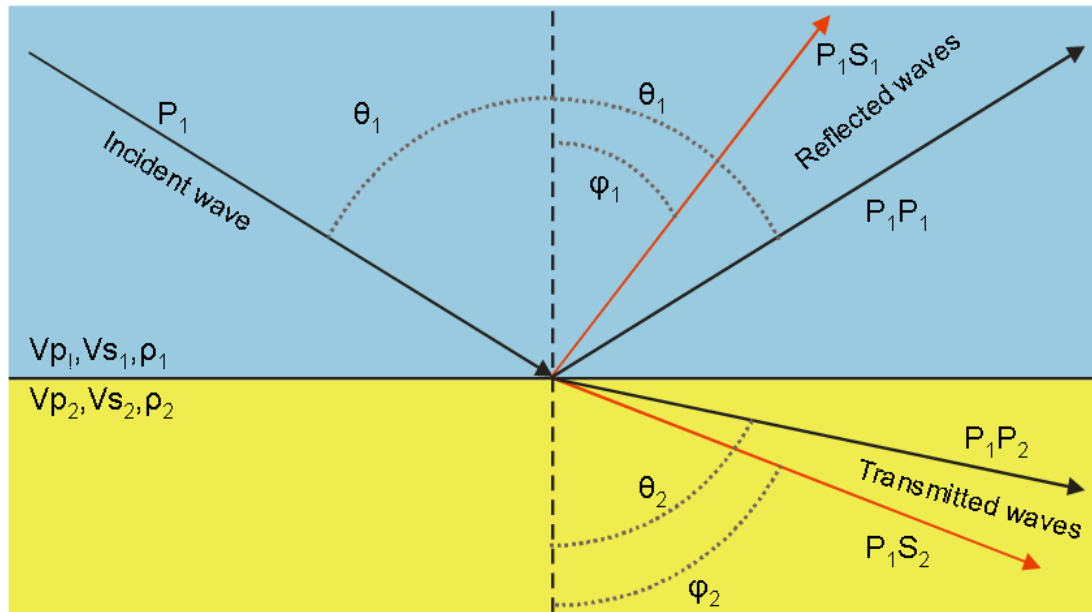
Figure 2-2. A P-wave incident at an interface resulting in both P- and S-wave reflections and transmissions. Conversion of P- (black) to shear-wave (red) occurs at the reflection boundary. Reflected and transmitted waves, both primary and converted obey Snell's Law (Equation 2-3). From Harrison (2009), after Yilmaz (2001).

2.4 Resolution of the Seismic method

Delineation of ore bodies with seismic methods is dependent on the vertical and horizontal resolution of the method. Vertical resolution is determined by the dominant frequency of the seismic wavelet and the thickness of the target. The minimum thickness (t_{min}) detectable in noise-free conditions is commonly estimated from the quarter-wavelength criterion (Widess, 1973);

$$t_{min} = \frac{V}{4f} \qquad \textbf{Equation 2-4}$$

where, V is the seismic velocity and f is the dominant frequency of the wavelet.

Horizontal resolution is typically defined by the width of the Fresnel zone (Equation 2-5), but modelling studies have shown that the minimum diameter of one wavelength is required to avoid attenuation of reflection amplitudes (Berryhill, 1977). Thus the lateral resolution for a continuous reflector and a point source are

$$d_f > \sqrt{\frac{2zV}{f}}$$

Equation 2-5

$$d_{pt} = \frac{V}{f}$$

Equation 2-6

where d_f is the width of the Fresnel zone, z is the depth of the reflector/target and d_{pt} is the diameter of a point source reflector. From these two equations, assuming a dominant frequency of 100 Hz, target depth of 1 km and an average formation velocity of 6 km/s, it should be possible to image an ore body 15 m thick and either, 60 m in diameter (point source) or 350 m in extent as a reflector (Salisbury, et al., 1996).

2.5 Elastic Parameters

Determination of the compressional (P-wave) and shear-wave (S-wave) velocities and knowledge of the formation density (ρ) allows calculation of the V_P/V_S ratio and the rocks elastic parameters. Elastic parameters are important to engineers and geophysicists as to define how the rock responds to seismic body waves. Knowledge of these also allows full seismic characterisation. The relationship between each of the elastic parameters, V_P, V_S and density are summarised in Table 2-1.

Table 2-1. Elastic constant equations.

Elastic Constant	Units	Equation
Poisson Ratio (σ)	-	$\sigma = 0.5 - \dfrac{0.5}{(V_P/V_S)^2 - 1}$
Bulk Modulus (κ)	GPa	$\kappa = \rho\left(V_P^2 - \dfrac{4}{3}V_S^2\right)$
Compressibility (β)	GPa^{-1}	$\beta = \left(\rho V_P^2 - \dfrac{4}{3}\rho V_S^2\right)^{-1}$
Shear Modulus (μ)	GPa	$\mu = \rho V_S^2$
Young's Modulus (E)	GPa	$E = \rho V_S^2 \dfrac{\left(3V_P^2 - 4V_S^2\right)}{\left(V_P^2 - V_S^2\right)}$
Seismic Parameter (ϕ)	(km/s)^2	$\phi = V_P^2 - \dfrac{4}{3}V_S^2$
Lame's constant (λ)	GPa	$\lambda = \rho\left(V_P^2 - 2V_S^2\right)$

After Birch 1961, ρ = density in gm/cm^3, V_p = compressional wave velocity in km/s, V_s = shear wave velocity in km/s.

2.6 Hard Rock Characterisation

Important messages can be taken from the previous sections with respect to characterisation of hard rock environments. The wide range of seismic velocities of sulfides infers that each mineral deposit, depending on its mineral composition, will have a unique seismic character and elastic response. Direct detection of an ore body is dependent on its size and depth, and these dimensions are of the same size as the illuminating dominant seismic wavelength. Thus the geological complexity of metamorphic terranes will in general impede seismic detection and characterisation of the host rocks.

2.7 Down-going and up-going wavefields in VSP

One of the principal differences of VSP with respect to surface seismic is that the surface seismic method can only record waves which are reflected or refracted back to the surface, or direct waves which travel along the air and surface interface. Whereas, in VSP we can record transmitted (down-going) wavefields as they propagate past the borehole as well as reflected (up-going) wavefields. Ideally in a homogenous, horizontally layered earth, with a vertical borehole, a shot point at the borehole collar (zero-offset – ZVSP) will produce a down-going wavefield which propagates normal to the surface and coincides with the borehole track; the first energy (First Break – FB) arriving at the borehole receiver is the down-going Primary compressional wave (P-wave). In this ideal ZVSP instance, the FB arrival time is linear with respect to depth, across all borehole receivers that reside within a common "elastic" layer. When our seismic traces are displayed in depth and time, the slope of the FB arrival times represents the velocity of the layer and in effect, represents the borehole in the space - time (x, y, t) domain.

The FB travel times of ZVSP are used to calculate the average (total travel time form source to receiver) or interval (travel time between receivers) P-wave velocity structure of the earth. A 1D velocity model can then be created to convert surface seismic from time to depth and is used in seismic imaging processes.

Any horizontal horizon that intersects our ideal vertical borehole and has sufficient acoustic impedance will reflect the down-going P-wave. The reflected up-going wave must travel normal to the reflecting horizon, which again propagates along our borehole track, through the same media as its down-going predecessor. Thus the up-going P-wave must have an equal but opposite slope to the FB. These principles of down-going and up-going propagation for a ZVSP in a vertical borehole and horizontal reflectors are shown in Figure 2-3.

It should be noted here that seismic reflections can only be recorded by receivers positioned above the reflecting horizons. The depth of reflection events can be determined directly from the receiver depth at which the reflected wavefield intersects the borehole path; similarly layers and depths at which multiples are produced can be determined directly from VSP profiles as shown in Figure 2-4. Any up-going event which does not intersect the borehole path is either a multiple or an off-hole event.
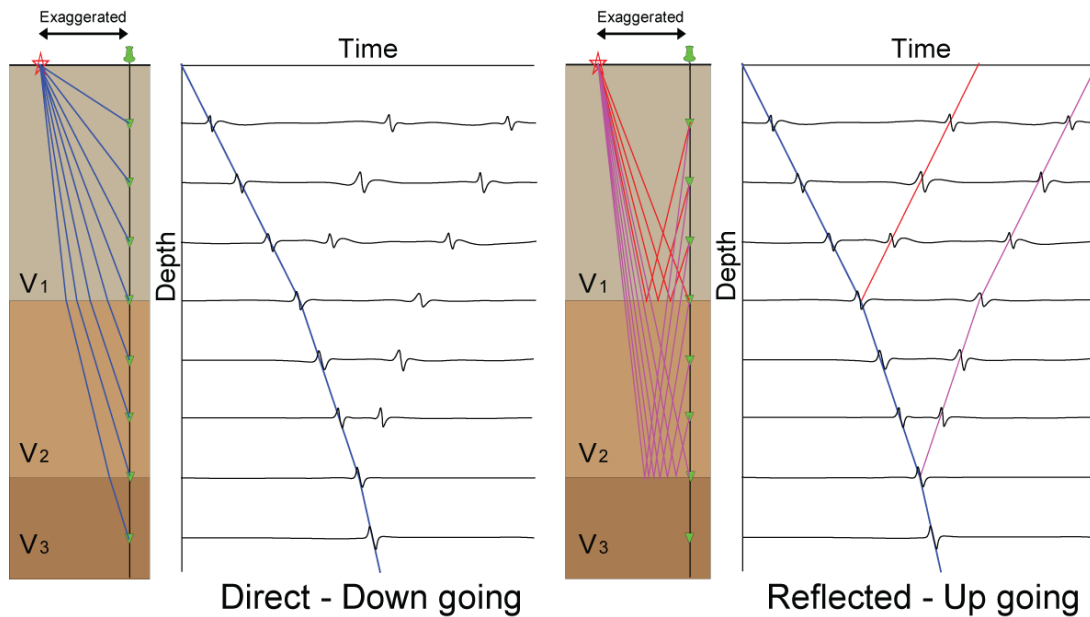
Figure 2-3. Principle of recording down-going and up-going wavefields in a VSP experiment.
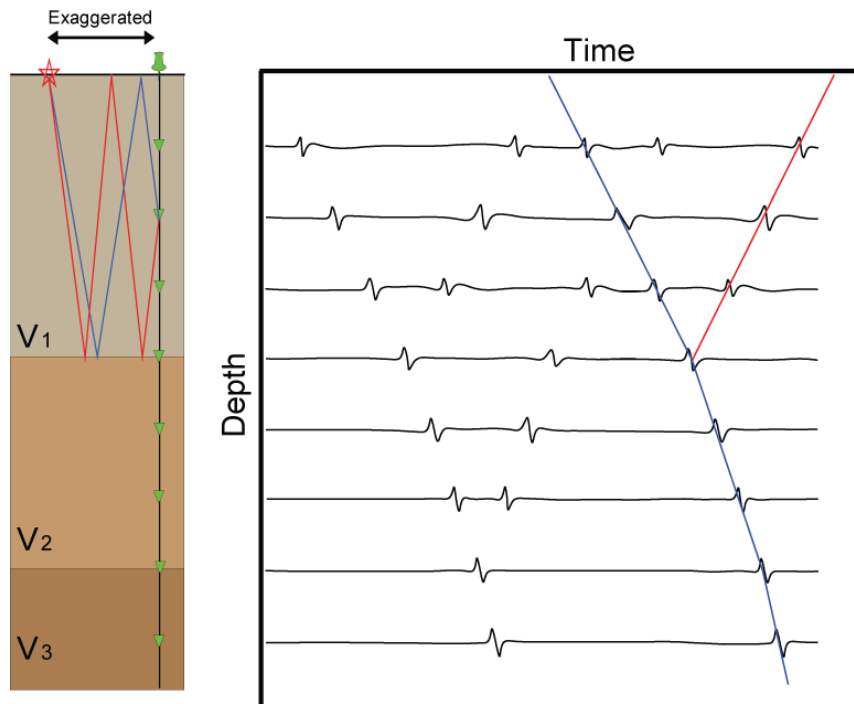
Figure 2-4. Schematic of multiple identification in a ZVSP profile.

2.8 VSP profiles

Traditionally VSP profiles are displayed with horizontal traces where time increases to the right and trace depth increases positively down as depicted in Figures 2-3 and 2-4. More commonly, processing packages display VSP data in the same way as surface seismic data. This is as it is collected in the field in Field Record Time (FRT), with trace offset along the horizontal axis and time increasing down as shown below in the upper right panel of Figure 2-5.

Signal that arrives after the FB that is not a down-going wave (e.g. S – wave or coherent noise such as cable and tube waves) is either noise or signal which has been reflected from below the receiver or out of plane bodies. The time after the FB, is in essence, the listening time within a record. This listening time is recording Two Way Travel (TWT) time as opposed to direct arrivals which have travelled only one way to the receiver. To convert VSP profiles to a common TWT time base, requires the addition of the direct arrival times (+TT) to the individual traces. This corrects for all receivers as if they were surface geophones and flattens reflected signal in our ideal borehole, to horizontal events in the +TT profile. This addition of FB travel time and horizon flattening is depicted in Figure 2-5. The +TT profile can then be compared

directly with surface seismic time profiles. In the case of offset VSP, reflections are hyperbolic and a Normal Move-Out (NMO) correction needs to be applied to flatten horizontal reflectors correctly.
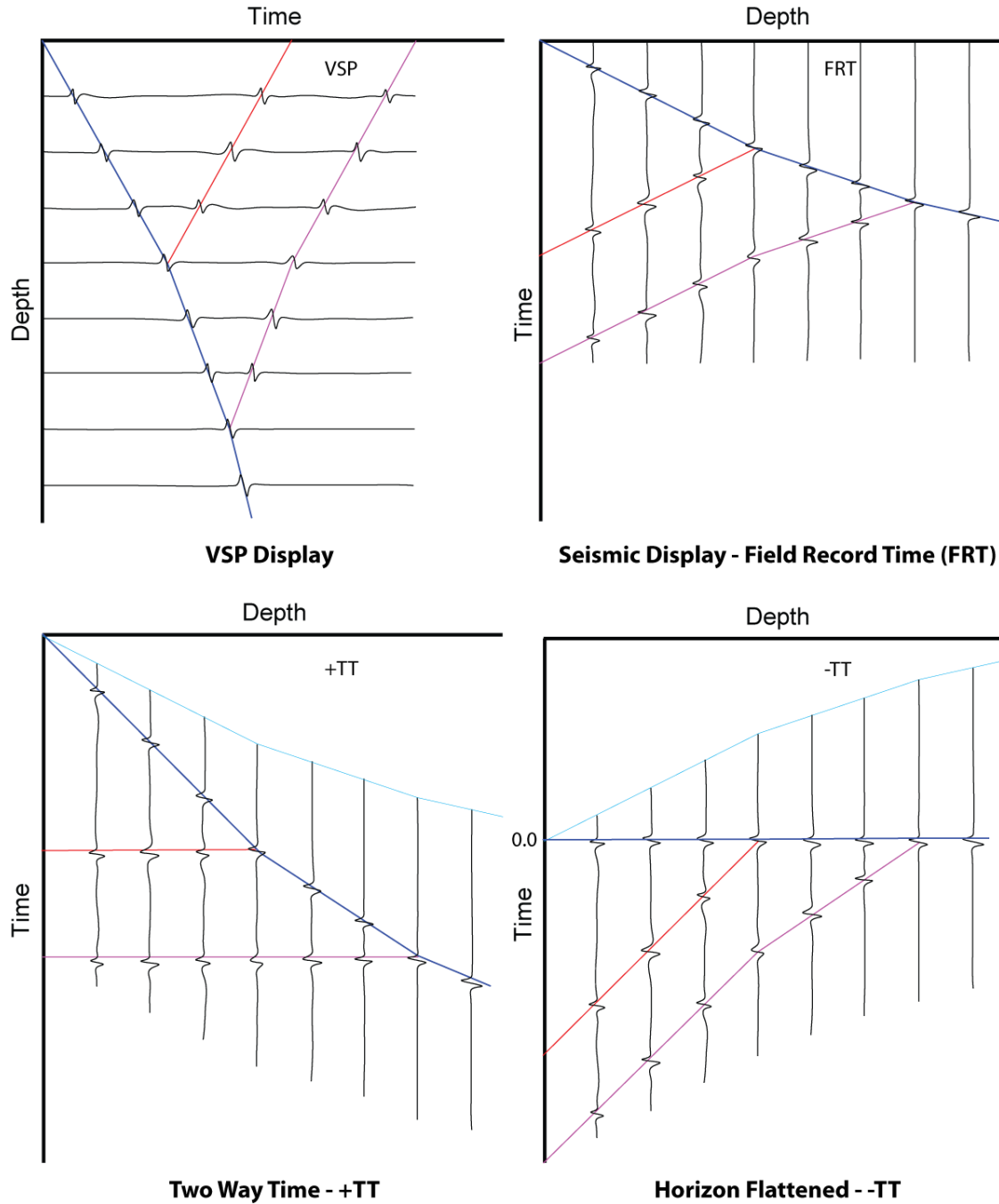
Figure 2-5. Differences in VSP display and Seismic display of Field Record Time (FRT) and the principles of horizon flattening by adding FB times and converting to Two Way Time (+TT) or subtracting primary FB times (–TT).

A similar approach of subtracting the FB times can be used to flatten first breaks to 0.0 ms or a predefined datum. This is also depicted in Figure 2-5. Flattening of horizons to the +TT and –TT domains are a useful tool in the VSP processors tool box for identifying up- or down-going wavefields, wavefield separation and / or enhancement of horizons by 2D filters (Discussed in Chapter 5). Further explanation of VSP principles, travel time, +TT and –TT can be found in Hinds, et al. (1996).

This technique of flattening can be extended to separate out wavefields travelling at different velocities. For example if strong shear waves are recorded, the first arriving S-wave could be picked and the pick times used to separate, enhance or remove this wavefield.

2.9 Origin of the reflection point

The principle of mapping a reflection point from a subsurface horizon is the same in VSP as in the surface seismic reflection method and borrows many principles from optics. Given a source point and a regular planar reflecting horizon, a line normal to the reflector can be traced from the source to the reflector and an imaginary source (source image) plotted equidistant away from reflector on the opposing side; an image ray can then be traced from the source image to the receiver. The reflection point is the point where the image ray intersects the reflector horizon. Propagation and reflection rays can then be traced from the source to the reflection point and from the reflection point to the receiver. This is graphically explained in Figure 2-6.
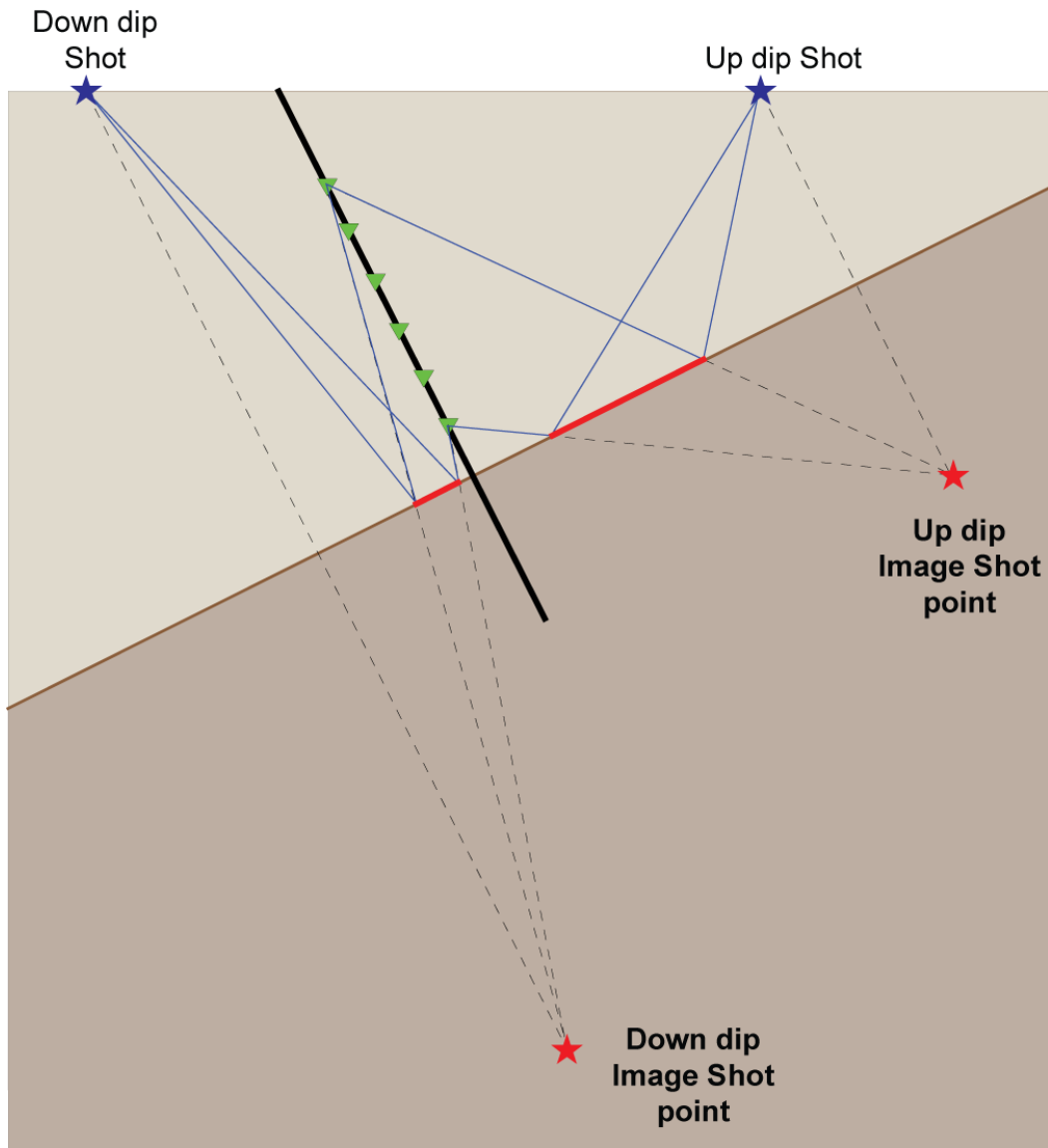
Figure 2-6. Construction of the VSP image point in dipping environment and realisation of the imaging aperture.

Typically in mineral exploration, the lithology is dipping and boreholes are drilled at angles to intersect the lithology at near normal incidence. This is primarily to map the true thickness of stratigraphic layers but also assists borehole stability and reduces the load (weight of drill rods) on drilling equipment. The effect of dipping lithology is to move the reflection image point geologically up-dip in a seismic section. It can be visualised from Figure 2-6 that if the dip were to be increased, the source image would move in the up dip direction thus moving the reflection point up-dip.

For steeply dipping strata and structures (> 45 degrees) such as those commonly found in mineral exploration, it is not possible within a single VSP profile to determine the origin of a reflector uniquely (without some prior knowledge), as reflections can originate from either side of the borehole. In fact reflections can originate from 360 degrees around the borehole unlike surface seismic where reflections can only occur in the half space below the receiver surface. The paradox of the origins of reflections within a VSP profile is illustrated in Figure 2-7 where, given the same VSP shot and receiver geometry, a geologic dip of 45 degrees gives a very similar reflection response (shape and angle) as that of an opposite -75 degree geologic dip. Reflection travel-times originating from planes that do not intersect the borehole will not intersect the direct arrivals and will arrive latter in time. The direction of the incoming energy can also be determined by analysing a 3C receiver.

Determination of the image point origin may be aided by using multiple source locations (walk away or multiple offset VSP) and by constructing a depth image by the process of migration. Migration is commonly referred to as imaging and is discussed in the next section.

An interesting point to note here from Figure 2-7 is that a borehole drilled vertically into steeply dipping strata results in no imaging on the down-dip side of the borehole regardless of which side of the hole the shot point is on. In contrast a borehole that is designed to intersect the strata orthogonally as shown in Figure 2-6 results in some down-dip imaging given there are shot points on the down-dip side.

A simple MATLAB (mathematical computational software) code was written to produce the examples in Figure 2-7. This code was extended to incorporate the use of dipping borehole (or if required any 2D borehole track) and can be found in Appendix I. This code has been used in subsequent chapters to illuminate difficulties and limitations of VSP imaging in complex dipping environments.
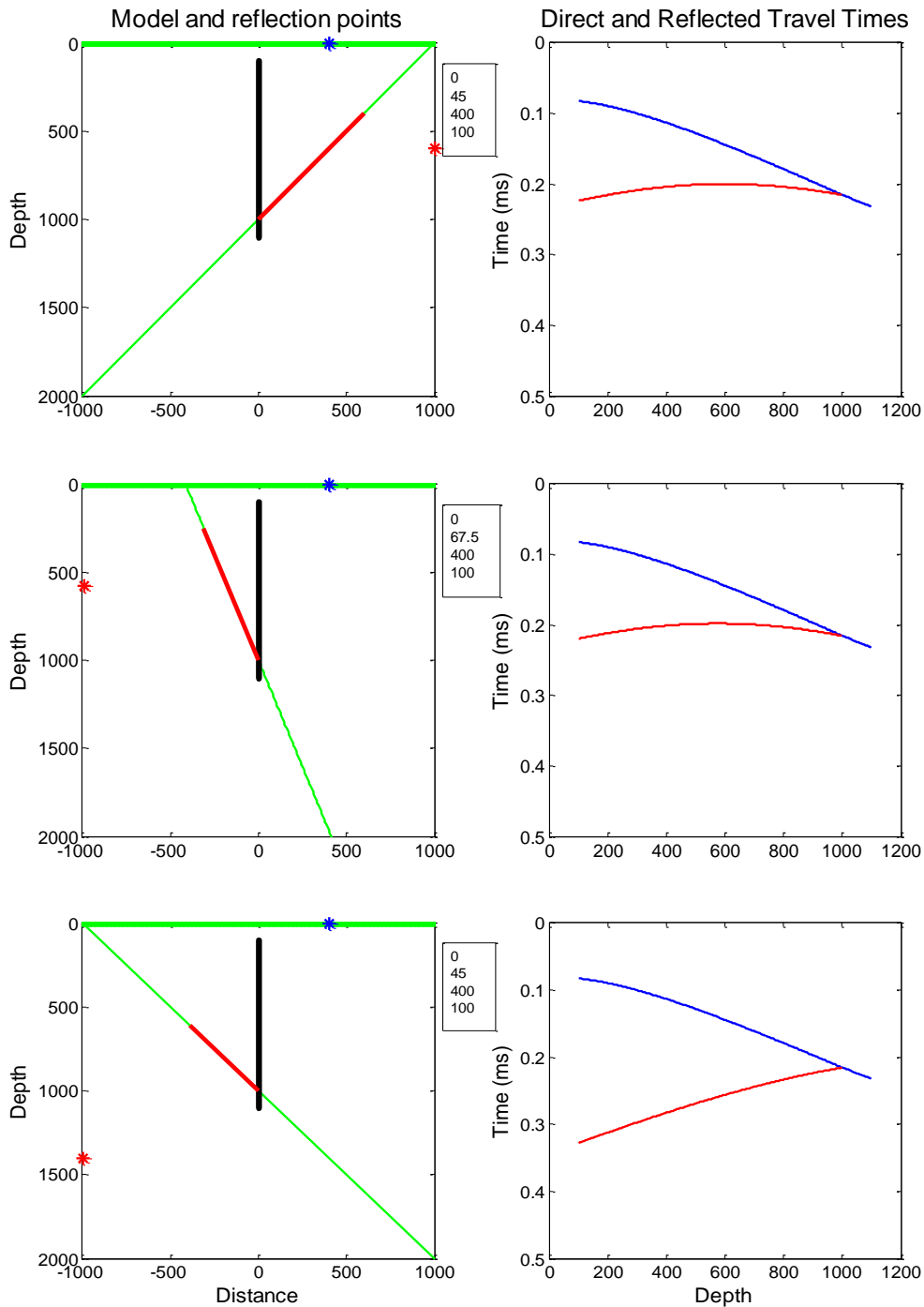
Shot (blue asterix) 400 m offset from VSP recievers (black line), The corresponding image point (red asterix) and reflection surface (red line) is shown. Direct ray (blue) and refeltor travel time time curves are shown in the right panels.

Figure 2-7. Synthetic results of different dipping structures showing the similarity and difficulty in establishing dip and origin of reflectors in a VSP profile. The same receiver-shot geometry and velocity parameters were used for the three dip angles of 45, -67.5 and -45 degrees. (MATLAB code Appendix I).

2.10 Construction of the VSP image

Mapping of offset VSP data from the time-depth domain, in which it was recorded, to the offset-depth domain, in which it can be interpreted, is performed through either VSP-CDP transformation or pre-stack migration. As demonstrated in the previous sections and Figures 2-6 and 2-7, reflections can occur from positions intermediate to the source and receiver location. Wyatt and Wyatt (1981) recognised this and described a procedure "VSP-CDP stack" to convert time-depth offset-VSP data to an offset-depth image similar to depth migrated surface seismic sections. Following this, Dillon and Thompson (1984) published a comprehensive study of the ways in which multiple VSP acquisition geometries (offset, walk-away and deviated well) could be used to illuminate the sub surface structure using the VSP-CDP approach. The VSP-CDP transform in essence, calculates velocity from VSP direct arrivals, then determines the origin (depth and offset) of events arriving after the first arrivals from the velocity and geometry of the source and receiver. This is graphically illustrated in Figure 2-8. The VSP-CDP method is a single-channel process and events on a trace are mapped without regard to events on adjacent traces. Also the layering is assumed horizontal. As such only reflections from horizontal and near-horizontal interfaces are correctly handled and migration imaging of more complex structures is needed. However, VSP-CDP mapping is simple, computationally quick, and robust in the presence of noise (Van Schaack and Costa, 1996), thus a very useful tool in VSP image processing.

Variable velocities and dipping horizons cause seismic elements to be recorded at surface receiver positions that are laterally shifted with respect to their subsurface positions (Robein, 2010). This is shown in Figure 2-9 for a dipping reflector. In such environments, seismic elements need to be moved using depth migration, which employs lateral and depth variations in the velocity model to achieve correct positioning of seismic elements (Telford et al., 1990). Migration is an inversion operation involving the rearrangement of seismic information elements so that reflections and diffractions are plotted at their true locations. The inversion process transforms the seismic data, recorded as a function of arrival time, into a scaled version of the true subsurface geometry of the geologic features that produced the seismic reflection event. i.e. the subsurface image is created at the coincident time of

incident and reflected wavefields which is commonly known as Claerbout's imaging principle (Claerbout, 1971) which is the basis of all migration and inversion image reconstruction schemes.
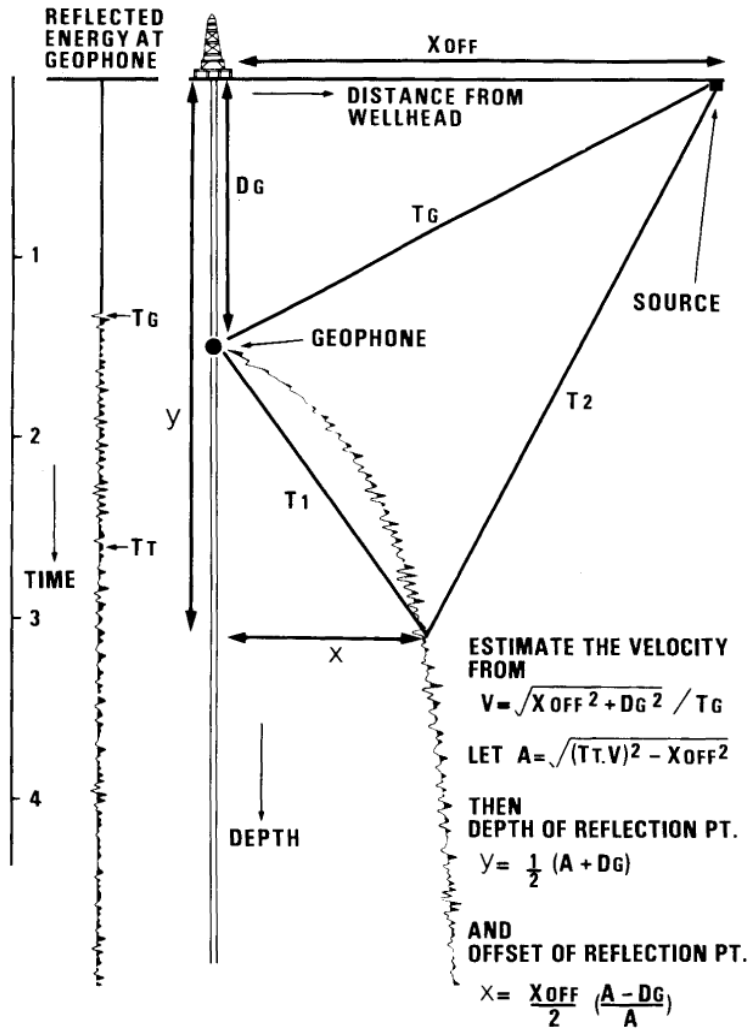
Figure 2-8. Construction of the VSP-CDP transform from offset-VSP data (Dillon, 1984).

INPUT SITUATION:
distance
depth
dip of reflector
receiver location
normal rays
reflector

RECORDED TIME SECTION:
time
time dip
reflector on the time section
actual reflector
The reflector is misplaced horizontally and vertically. It is longer than the actual reflector and dips less steeply.

TIME/DEPTH SECTION AFTER MIGRATION:
distance
time/depth
reflector now has correct dip
migrated reflector
Reflector now correctly positioned

Figure 2-9. Principle of misplaced reflections in time sections and the correct positioning through migration (Bancroft, 2007).

The imaging process depends on a specific earth model (velocity model) used for focusing and positioning the seismic elements. Focusing is the collapsing of diffractions, maximizing amplitude and reproducing the seismic wavelet character. Positioning is the correct locating of diffraction origins and the sharpening of event terminations such as faults, unconformities, wedges and volcanic intrusive events.

There is extensive research and continual developments in algorithms for seismic modelling and model based depth imaging by industry and academic institutes. References for more information on migration are; Claerbout (1970), Schneider (1978), Gardner (1985), Bording and Lines (1997), Fagin (1998) and Bancroft (2007).

The most common algorithm used for VSP imaging is based on the Kirchhoff integral (Schneider, 1978) and is presented by Dillon (1988) as;

$$U(r,t) = \frac{-1}{2\pi} \int dS_0 \; \frac{\partial}{\partial n} \left[\frac{U\left(r_0, t + \frac{R}{C}\right)}{R} \right]$$

Equation 2-7

where $R = |r - r_0|$, $U(r,t)$ is the wavefield to be calculated at some point r, $U(r_0, t)$ is the wavefield measured over the surface S_0, and n is the normal to the elemental surface area dS_0 at r_0, C is the velocity and, hence, R/C is the propagation time from r to r_0. The above integral expresses Schneider's equation (4) as a reverse time extrapolation, with the directional derivative as found in Figure 2-10 from Dillon (1988)(Schneider, 1978).
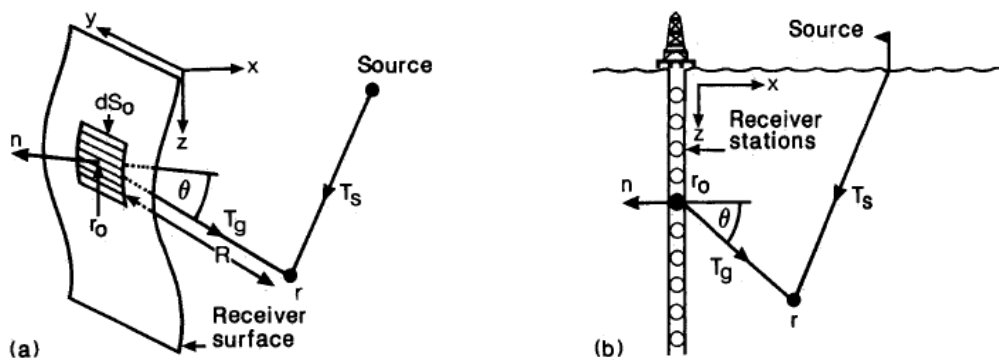
Figure 2-10. Wavefield extrapolation and imaging. (a) Geometry for wavefield measured on a near-planar vertical surface. (b) Geometry for wavefield measured at a vertical well (Dillon, 1988).

In its simplest and most practical form, Kirchhoff migration can be performed in the following way: for a chosen scatterer or depth sample (image space or geology),

compute the travel time for each source-receiver pair using a given velocity model, Extract the sample value (amplitude) for a given time from the time section (seismic traces), apply amplitude correction (obliquity and spherical divergence), then accumulate (for image gather) the results in the image space for a chosen depth. The summation process is limited by the aperture angle which is determined by the maximum dip angle expected in the area, while the weights are chosen according to the incidence angle. The Kirchhoff integral can handle almost any configuration of source-receiver geometry, irregular spacing and dip up to 90º (Dillon, 1988).

An important point to note here is that in Dillon (1988), a synthetic zero-offset VSP, with a 45 degree deviated well produced a superior migrated image compared to a vertical well with a single large offset shot. A vertical incidence survey with multiple shots and multiple receiver positions in the same 45º deviated well produced the best depth migrated image. As mineral exploration employs deviated boreholes (typically 30 degrees from vertical) seismically imaging below the borehole with VSP will be possible due to the lateral aperture (horizontal offset) of the receivers.

2.11 Hydrophones, pressure, geophones and particle velocity

A major component of this study is the establishment of hydrophone array methodology for borehole seismic reflection studies. Borehole clamping geophones are the "gold standard" for VSP studies. As such, it is necessary to understand and define the relationship between hydrophones, which measure a pressure scalar field, and geophones, which measure particle velocity, a vector field.

It can be shown from first principles using Newton's and Hooke's laws, that, geophones measure particle velocity and hydrophones measure pressure fields as represented by equations 2-8 and 2-9 respectively

$$\frac{\partial v}{\partial t} = -\frac{1}{\rho}\frac{\partial P}{\partial z}$$ **Equation 2-8**

$$\frac{\partial P}{\partial t} = -M\frac{\partial \psi}{\partial t \partial z} = -M\frac{\partial v}{\partial z}$$ **Equation 2-9**

where P – pressure, ρ – density, v – velocity, t – time, ψ – displacement and M – elastic modulus. Through differentiation and substitution it can then be shown that

$$\frac{\partial^2 v}{\partial t^2} = \frac{M}{\rho}\frac{\partial^2 v}{\partial z^2}$$ **Equation 2-10**

$$\frac{\partial^2 P}{\partial t^2} = \frac{M}{\rho}\frac{\partial^2 P}{\partial z^2}$$ **Equation 2-11**

These equations are of the same form and can be solved using the general solution to the one-dimensional wave equation (d'Alembert's solution) and by substituting $c^2 = M/\psi$ where c is the velocity and M and ψ are held constant to obtain expressions for displacement U and pressure P

$$U = f\left(t - \frac{z}{c}\right) + g\left(t + \frac{z}{c}\right) \quad \text{and} \quad P = \rho c f\left(t - \frac{z}{c}\right) - \rho c g\left(t + \frac{z}{c}\right)$$

where $d = f\left(t - \frac{z}{c}\right)$ is the down-going wavefields and $u = g\left(t + \frac{z}{c}\right)$ are the up-going wavefields

or $\qquad\qquad U = f + g$ **Equation 2-12**

$$\frac{P}{\rho c} = f - g$$

Equation 2-13

Now $\frac{P}{\rho c}$ and U have the same units. So the difference between pressure and particle velocity is the sign. However, they are two independent variables; $U = U_{(z,t)}$ and $P = P_{(z,t)}$. Equation 2-12 is the general solution when M and ρ are held constant i.e. when $c = $ constant.

The relationship between pressure and velocity fields can be conceptually visualised using an example of simple harmonic motion. When the amplitude of a vibrating body is greatest, its velocity is zero, that is to say that it has reached its outer limit of displacement and is momentarily motionless before returning in the opposite direction. If the velocity is zero, so is the pressure it exerts on the medium around it.

Thus, velocity and therefore pressure, is greatest mid-way between the maximum displacements of the vibrating body (Truax, 2001). In addition, particles in air are free to move more than particles in water. The opposite is true with pressure. In water, it takes more pressure to move particles, so particle velocity and pressure are always opposite and when the pressure is large, the particle velocity is low (Urosevic, 2000).

The full derivation of the above pressure and particle velocity relationship is provided in Appendix II. In addition transmission and reflection at a boundary needs to be considered.

2.12 Polarity of hydrophones and geophones

To characterise reflection events within our data we must first define the polarity convention for multi-component and hydrophone data. The multi-component polarity convention suggested by Brown et al. (2002) has been used in this document. This is based on the Society of Exploration Geophysicist (SEG) standard for impulse signal polarity and extended to 4C data (hydrophone and 3C geophone – W, X, Y, Z).

The SEG standard states for an impulse-signal at zero offset and vertical sensor where the positive direction is defined as being down (i.e. direction of increasing depth), a signal voltage initially going in the negative direction shall be produced by;

- Upward motion of a seismic motion sensor, and

- Pressure increase detected by a pressure-sensitive hydrophone.

This negative signal voltage applied to the input of a recording system shall produce a;

- Negative output,

- Wavelet minimum or trough on a seismogram.

For surface geophones planted with their spike down, this standard, results in a negative onset from refracted first arrivals and reflections created by an increase in

acoustic impedance (positive reflection coefficient). Conversely a downward motion gives a positive output from a vertical geophone. However, the standard orientation of a vertical borehole geophone is opposite to that of a surface geophone i.e. geophone spike up. As such, this results in a negative first break from a direct down-going wave in a vertical borehole geophone.

Consistent with the SEG polarity convention, hydrophone responses are treated in the same way as data from a vertical geophone such that up-going P-waves with compressional first motion, reflected from positive reflectors, register with a negative first break. Since hydrophones record pressure, the foregoing requires that all compressions register as negative breaks and dilatations give a positive output from the hydrophone. Thus, in hydrophone VSP surveys, a direct down-going P-wave with compressional first motion results in a negative onset.

Extending the polarity convention to borehole geophone horizontal axes X and Y, we use the "right hand rule" such that Z points up (thumb), the X component points in the radial or in-line direction of the source (index finger) and the Y component is transverse or cross-line direction, which is mutually orthogonal to Z and X (90^0 counter clockwise to X). This is illustrated in Figure 2-11. Accordingly, a direct arrival from a source which is offset from the collar will result in a negative onset in the X component geophone and motion 90° anti-clockwise to the X direction (i.e., the negative cross-line or Y direction) gives a negative output from the transverse or cross-line geophone. Theoretically for a purely vertical source, no energy would be recorded in either of the horizontal components, however, in practice, heterogeneity and anisotropy can generate energy on both shear components.
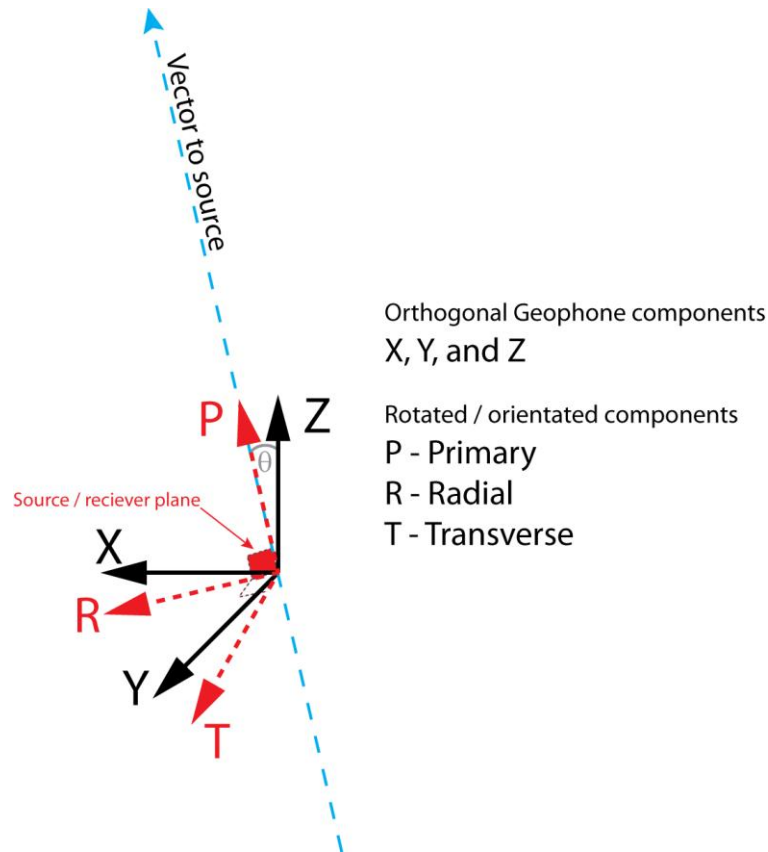
Figure 2-11. 3 component borehole geophone orientation used in this thesis and correction from Z, X and why to the primary, radial and transverse (P, R and T) orientations which maximises P-wave energy to the source receiver plane.

2.13 Summary

The principles described in this chapter form a large part of the understanding required to comprehend VSP and the work presented in the following chapters. A basic knowledge of general seismic techniques and principles by the reader is assumed.

VSP CDP mapping and Kirchhoff migration are utilised in Chapters 3, 5 and 6 to highlight imaging difficulties, limitations and possibilities in hard rock conditions. Chapters 4 and 5 require understanding the differences between a hydrophone and a geophone receiver and being able to recognize the different wavefields in VSP profiles (FRT, +TT, -TT, up-going and down-going separated profiles).

3 Feasibility of VSP in mineral exploration.

3.1 Introduction

To test the viability of borehole seismic imaging in typical hard rock exploration environments I have conducted a number of modelling experiments. These models are aimed at demonstrating the potential of recording and producing high resolution seismic images from deviated boreholes in complex hard rock environments.

The process of constructing an earth model and simulating elastic wave propagation is known as forward modelling. The result of forward modelling is a synthetic seismogram which represents the predicted seismic output of the earth model or "filter". Forward modelling can be classified into three main categories; integral-equation, ray-tracing and direct methods. Integral methods are based on Huygens' Principle (1690) which states **"*Wavefields originating from a flame can be considered the superposition of waves due to point sources located in the flame.*"** or in other words, every point on a wave front may be regarded as the source of a subsequent wave. The wavefields can be expressed mathematically as the integration or summation over volumetric wavefield densities. This method is also known as diffraction modelling.

In the ray-tracing approach, each ray emanating from a source point is computed piecewise by segments of constant travel time. Ray propagation is determined by the ray parameter (p) velocity (v) and the emergence phase angle (i) by

$$p = \frac{\sin i}{v_i}$$ **Equation 3-1**

If the velocity or elastic parameters change at the end of the segment, Snell's law is applied and the ray parameter calculated. This process is repeated for all time segments until the desired propagation time is reached.

In direct methods, the time and space derivatives of the wave equation are discretised from a continuous function to a discrete function (Bording and Lines, 1997). Direct method codes use finite difference (FD) or finite element (FE) algorithms to solve the wave equation. Often direct methods are termed full waveform modelling

techniques as the solution implicitly gives the full wavefield. For this study, full waveform modelling was conducted using TesseralCS-2D modelling package. The pressure-velocity formulations for acoustic and elastic modelling utilised by TESSERAL can be found in Appendix III. Detailed descriptions of full waveform modelling can be found in Virieux (1986) and Juhlin (1995). Many articles and books covering all aspects of forward modelling can be found e.g. Aki and Richards (1980), Bording and Lines (1997), Fagin (1998), Anderson and Cardimona (2002) and Carcione et al. (2002).

Synthetic seismograms or "synthetics" are often generated before and after field acquisition to determine if a particular geological target will generate a seismic signature. They can aide survey planning in complex environments by evaluating acquisition geometries and assist in the development of processing flows by identifying propagation of the different wavefields. For forward modelling to be useful the model must represent an authentic geologic situation, be populated with geologically representative elastic parameters (velocities and density), and implement realistic acquisition geometries (source and receiver locations/offsets) and source parameters (frequency, wavelet shape) in order to generate accurate seismic signatures. Three complex earth models have been chosen for this study. The first two models depict real geology found in the Yilgarn Craton, the Sunrise Dam gold deposit and the Spotted Quoll nickel deposit. The third model has been taken from the Ranger uranium deposit in the Northern Territory where a seismic feasibility study was conducted and presented within this chapter.

3.2 Model 1 - Sunrise Dam - Cleo gold deposit

The Sunrise Dam operation is approximately 55 km to the south of Laverton, 220 km NNE of Kalgoorlie, and 770 km NE of Perth, in the Eastern Goldfields province of the Yilgarn Craton. Between 1999 and 2006, several deep seismic reflection imaging surveys were collected in the Yilgarn Craton by ANSIR. One transect, crossed part of the Sunrise Dam gold mine. Reprocessing of the data revealed structural features that were imaged at the mine scale and correlated to years of drilling and geological

information (Urosevic and Evans, 2007), demonstrating the potential of seismic imaging in the area.

The Sunrise - Cleo gold deposit has an estimated combined 8 Moz Au in resources and past production (Brown et al., 2002). Mineralisation occurs in three major sites of deposition (Haren and Williams, 2000):

1. Shear hosted mineralisation - characterised by wide alteration assemblages and dispersed 'low grade' mineralisation haloes;
2. Pod mineralisation – characterised by high grade discrete quartz carbonate veins in narrow alteration selvedge's;
3. Banded iron formation (BIF) hosted mineralisation in anticlinal fold closures adjacent to thrust faults.

The synthetic geologic model constructed for Sunrise Dam– Cleo gold deposit has been adapted from geological cross-section of Brown, et al. (2002), which are displayed in Figure 3-1, and a cross section through the open pit. The model composed is shown as Figure 3-2. It has an overburden (regolith) layer of variable depth, volcaniclastic host rock, shallow to steep dipping mineralised shear zones, mafic intrusions, inter-bedded dolerite and BIF. Shear and pod mineralisation zones are shown to be on the scale of 20 to 50 m thick.

To simulate a VSP typical of mineral exploration, the receiver borehole was angled at approximately 60 degrees (30 degrees from vertical) and aimed to orthogonally intersect the common dip of the geology and shear zone.

Figure 3-1. Geological models of the Sunrise – Cleo gold deposit (Brown, et al., 2002). Top panel - conceptual model, Panel A - section 69,610 m and Panel B - section 69,600 m.
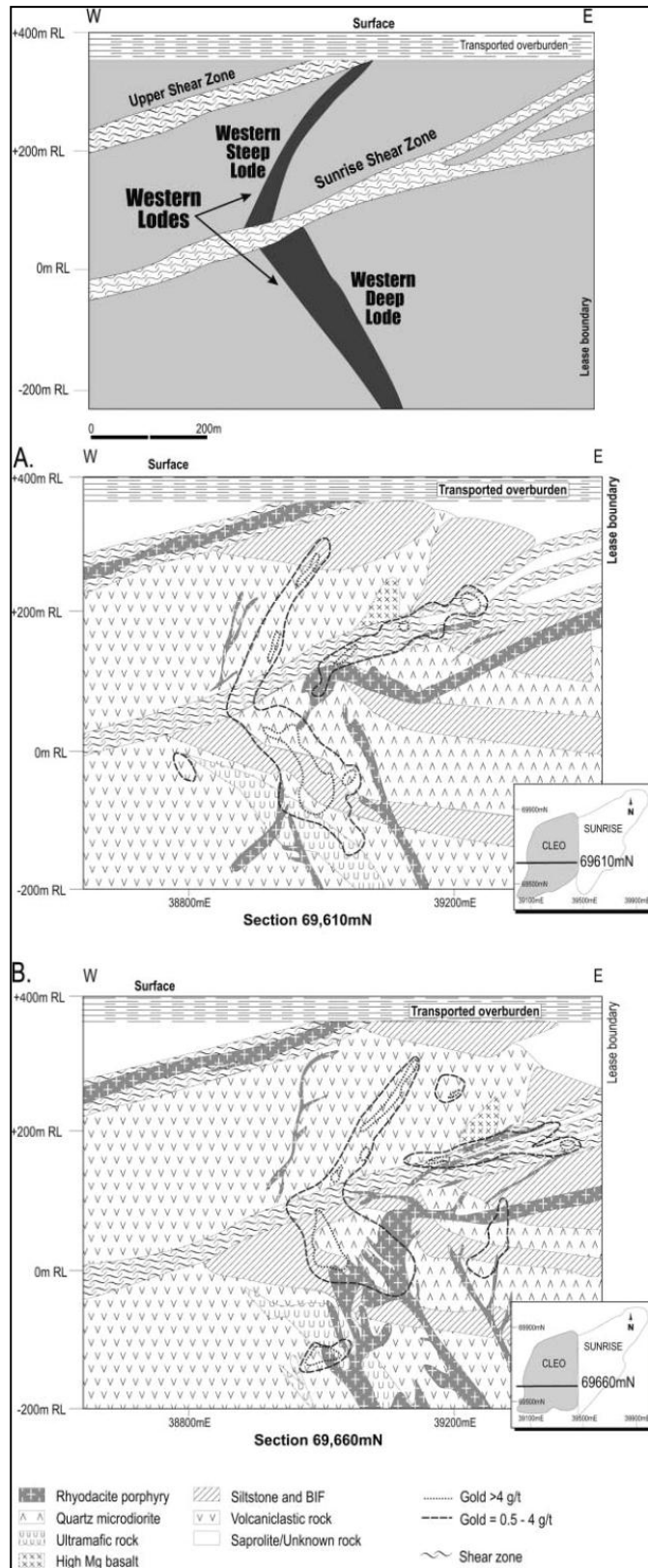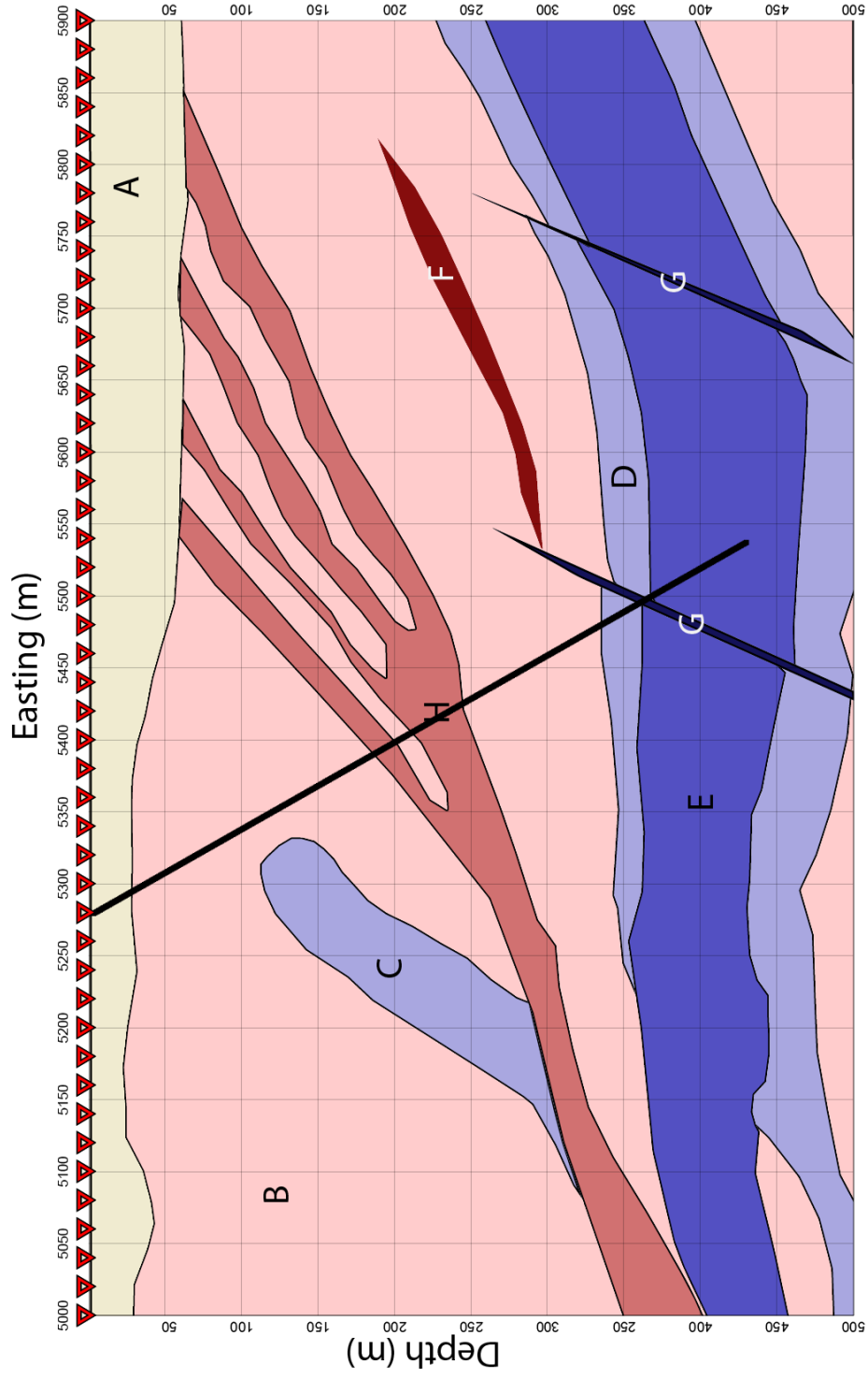
Figure 3-2. Geologic model used to generate synthetic seismograms. Seismic velocities, source receiver geometry and acquisition parameters are in Tables 3-1 and 3-2. The model consists of shallow to steeply dipping shear and intrusive structures overlain by a variable depth slow velocity layer.

3.2.1 Model parameterisation

The borehole was populated with 500 receivers at 1 m intervals. Dense sampling within the borehole was used for the initial study so wavefields could be correctly identified and separated. Dense population of receivers is at no extra cost to run time as the FD modelling scheme computation time is based on the total number of cells in the grid rather than acquisition geometry.

A total of 46 source locations (red triangles) spaced 20 m along the surface were used. The synthetic data set utilised Ricker wavelets of 40 Hz, typical to surface seismic frequency obtainable with the Curtin university 800 kg weight drop hammer, and 80 Hz. An 80 Hz dominant frequency was assumed as a first approximation for expected VSP frequency based on the fact that the seismic pulse is subject to only one way travel through the destructive overburden. According to the ¼ wavelength criterion (Section 2-4), at 80 Hz input frequency and a P-wave velocity range of 5000 to 6500 m/s, targets of 15 to 20 m minimum thickness can be resolved. Similarly at 40 Hz the minimum detectable target thickness is 30 to 40 m. Direct detection of gold assemblages by geophysical methods is at best rare and normally not possible due to the disseminated and low percentage of gold to host rock (ppm). Thus geophysical techniques target associated mineralisation, such as pyrite and pyrotite, and structures such as shear zones. The frequency of seismic wavelets chosen here reflects the detectability limits of the shear zones found at Sunrise Dam. Acoustic full-wave form modelling used a sampling rate of 0.5 ms and record length of 250 ms.

Seismic exploration in Western Australia is in its juvenile stages and there is a limited library of hard rock seismic velocities. Thus, it was difficult to populate the model with known rock velocities and densities. P-wave velocities (V_P) assigned to the model (
Table 3-1) were estimated from RMS stacking velocities used in the reprocessing of the Anglo Gold Ashanti regional seismic line (1999), which, passed over part of the Sunrise Dam deposit (Urosevic and Evans, 2007). S-wave (V_S) velocities and density (ρ) values were auto assigned to the model based on expected V_P/V_S ratios for similar type rocks or in some cases selected from the TesseralCS-2D parameter menu. The parameter menu has a library of minimum, average and maximum elastic

parameters for common sedimentary, metamorphic and igneous rock types. The modelling parameters used are detailed in Table 3-1. Note the short record length required for modelling due to very fast velocities and shallow (500 m) targets.

Table 3-1. Velocity density table for Sunrise Dam geology model

	Rock Unit / Structure	Vp (m/s)	Vs (m/s)*	Density (kg/m²)
A	Regolith	2200	1200	2000
B	Volcaniclastic	5500	2950	2800
C	Mafic Intrusion	6200	2800	3500
D	Banded Iron Formation	6200	3550	2750
E	Dolerite	6400	3650	2900
F	Felsic Porphyry	6700	4000	3100
G	Fault	5800	3050	2650
H	Shear Zone	5000	3100	2600

Table 3-2. Modelling parameters

Parameter	value
Sources	46 at 20 m spacing
Receivers	501 at 1 m from 0 to 500 m borehole depth
Wavelet	Ricker 40 Hz and 80 Hz
Sample rate	0.5 ms
Record length	250 ms
Grid size	Automatically calculated by TESSERAL.

3.2.2 Synthetic results

Modelling with a variable low velocity regolith layer present proved difficult. It required refinement of the computational grid and the solution was prone to numerical dispersion. In general, the regolith zone is known to be highly variable, diffusive and cause excessive reverberation in seismic data acquired across the Yilgarn Craton. However, to simplify numerical tests, 40 and 80 Hz synthetics were run with a reduced contrast in the regolith layer using a velocity of 5000 m/s was used to replace the regolith layer. Thus a total of 4 synthetic data sets were generated; 2 at 40Hz and 2 at 80Hz.

A total of 46 shot records were produced for each synthetic run. The data were spatially down sampled to 5 m receiver stations to simulate proposed field parameters. Thus each record has a total of 101 channels spanning 5 to 500 m borehole depth.

Every 10th record of the 80 Hz synthetic shot records with the regolith layer present is displayed in Figure 3-3. Due to the reverberation of the regolith layer it was decided to remove traces from receivers above the regolith interface, potentially negating the need to include regolith in model construction. This is a reasonable thing to do in general, as we are not interested in information within the regolith and predominately the reverberation energy is constrained to these traces. That said, when we compare shots 31 and 41 of Figures 3-3a and 3-4a, we can see that there are strong amplitude down-going events seen in 3-3a and not in 3-4a caused by this trapped energy propagating down. The remaining traces show multiple down-going and up-going wavefields. The amplitude of the direct arrivals is variable from record to record. This is due to the receiver (virtual geophone) being polarised in the vertical direction and energy arriving from different azimuths with offset. Also at the largest up-dip offsets, the direct arrivals arrive earlier in the deeper receivers, as these geophones are geometrically closer to the shot points due to the borehole deviation.

3.2.3 Wavefield separation

Wavefield separation was relatively straight forward as no noise was added to the data and S-wave energy is not present in acoustic modelling. The basic processing flow consisted of;

- Spatial down sampling of data from 1 to 5 m separated traces
- Resample traces from 0.25 to 0.1 ms.
- First break picking
- Horizon flattening to −TT, 2D spatial filtering - removal of down-going wavefield, un-flatten (+TT) and band-pass (10-20-100-200)
- *f-k* down-going quadrant reject filter and band-pass (10-20-100-200)
- Deconvolution and band-pass filter
- Top mute (at the base of the first arrivals) to remove filter artefacts.

Within the up-going wavefield separated profiles (Figure 3-3b and 3-4b), reflection events occur at 395 (a), 135 (b) and 240 (c) m and can be correlated back to the dolerite, the upper and lower shear interfaces respectively. Encouragingly the reflection events have different apparent dips at different offsets. The total wavefield obtained is complex enough to resemble real field records and hence presents a challenge for imaging.
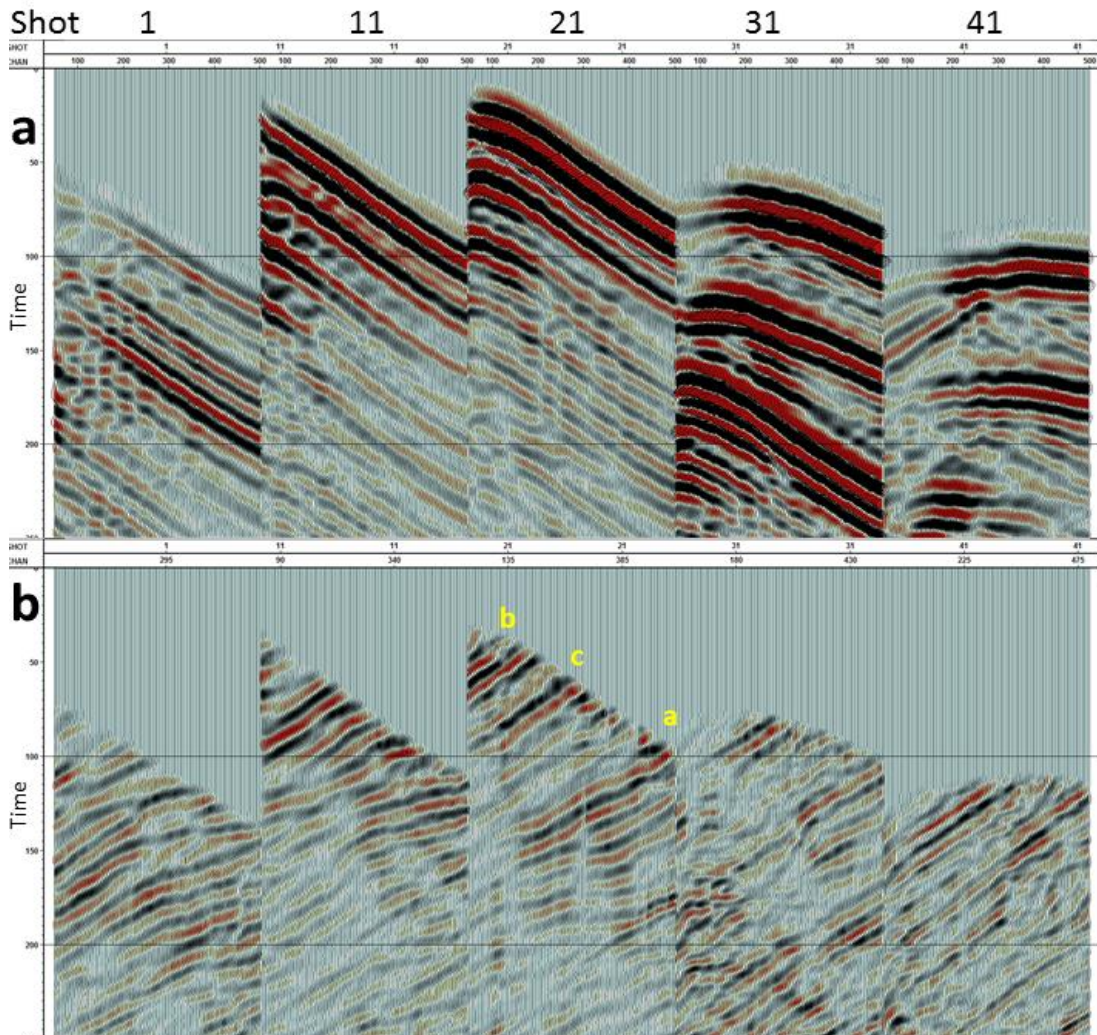
Figure 3-3. Sunrise Dam 80 Hz acoustic modelling with 5 m receiver stations from 50 to 500 m depth. a) Raw synthetics shot records b) up-going wavefield after wavefield separation processing. A low velocity regolith layer is present. Every 10th shot shown.
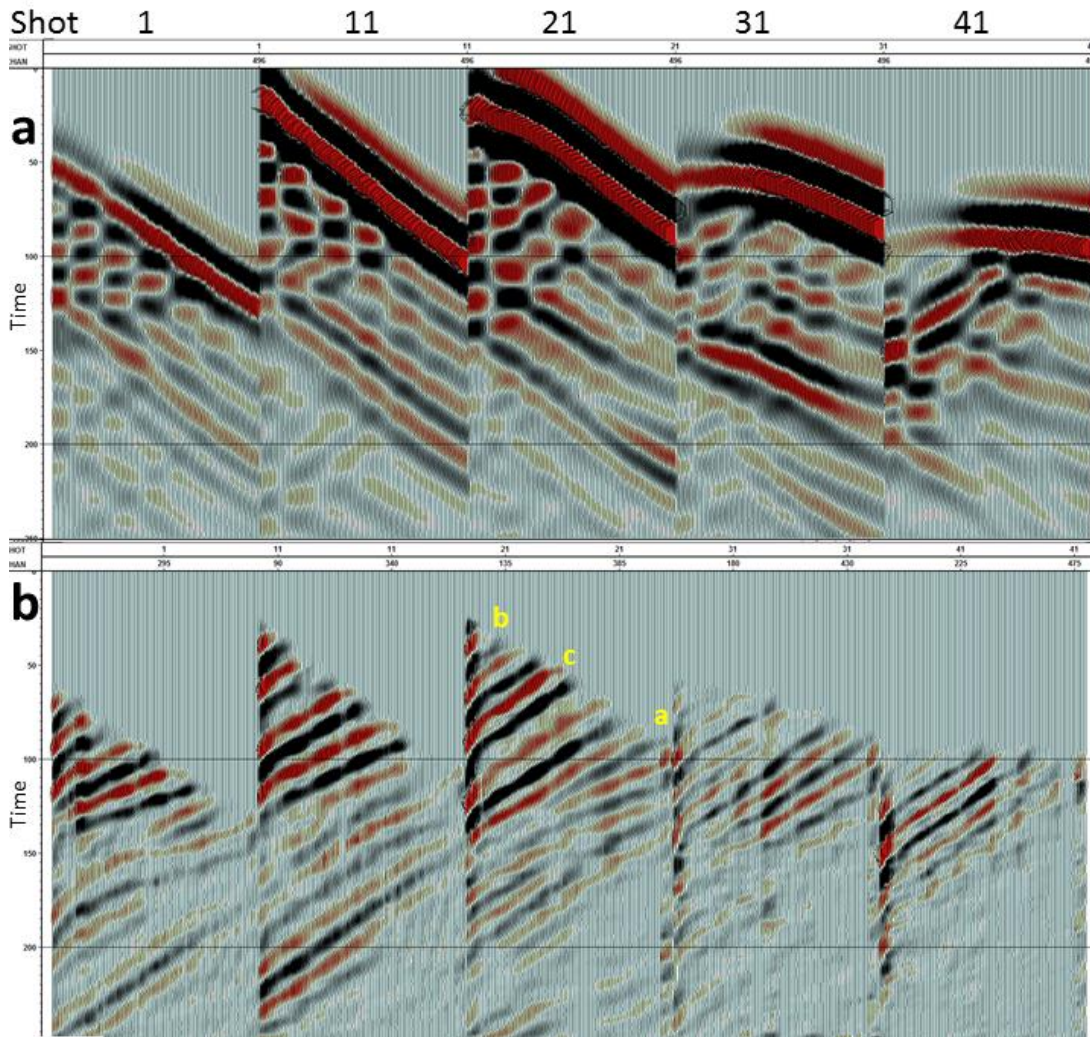
Figure 3-4. Sunrise Dam 40 Hz acoustic modelling with 5 m receiver stations from 50 to 500 m depth. a) Raw synthetic shot records b) up-going wavefield after wavefield separation processing. The regolith layer has been removed from the model by velocity replacement. Every 10th shot shown.

3.2.4 Migrated synthetic section

A general VSP imaging routine using the Kirchhoff integral was proposed by Dillon (1988) which performs pre-stack depth migration. After wavefield separation, VSP Kirchhoff migration was performed to create a 500 m depth migrated image. The migration used a vertical velocity profile defined from the model velocities and geological depths. This approach does not take lateral velocity changes into account.
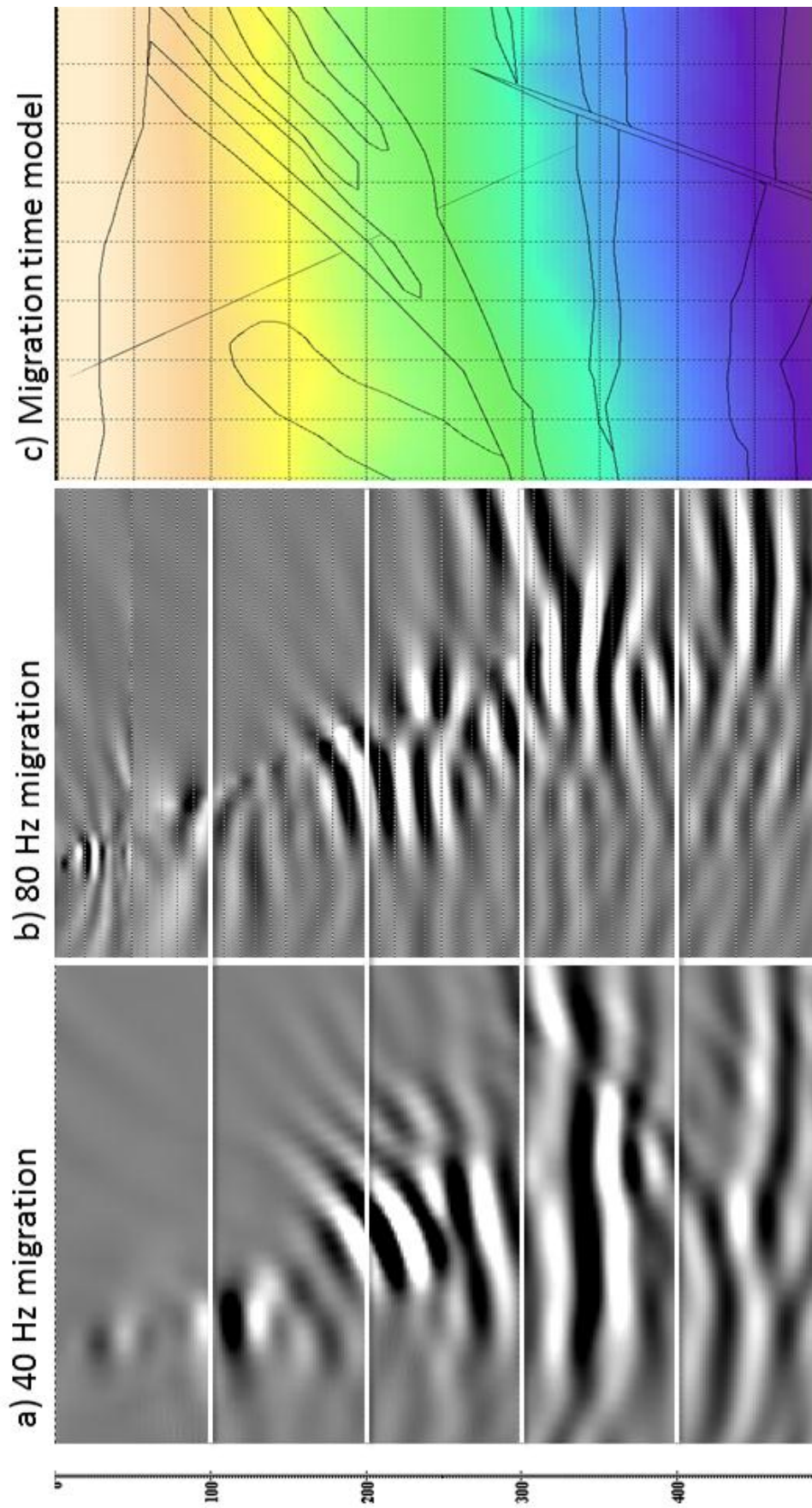
Figure 3-5. Migrated VSP sections a) 40 Hz dominant frequency with simplified geology (regolith layer / host rock velocity substitution). b) 80 Hz dominant frequency, low velocity regolith present and c) the time section used to create the migration models.

Synthetic data generated with 40 and 80 Hz source wavelets, respectively with and without the regolith layer present, are displayed in Figure 3-5 and 3-6. In general the two sections compare well, excluding the obvious difference of frequency content. Reflection events occur at the base of the regolith (50 m). Here there is a sharp boundary effect in the 80 Hz data due to the large velocity contrast used in the 1-D velocity model at 100 m top of the mafic intrusion has been defined there is better apparent continuity in the 40 Hz, however, there is better depth separation in the 80 Hz data particularly in the shear zone (150 to 275 m); Due to the effects of the regolith layer and slightly different processing required to remove these effects, there are discrepancies between the sections further away from the borehole and the horizontal reflections at 340 m and 430 m are less defined below the borehole in the 80 Hz data.
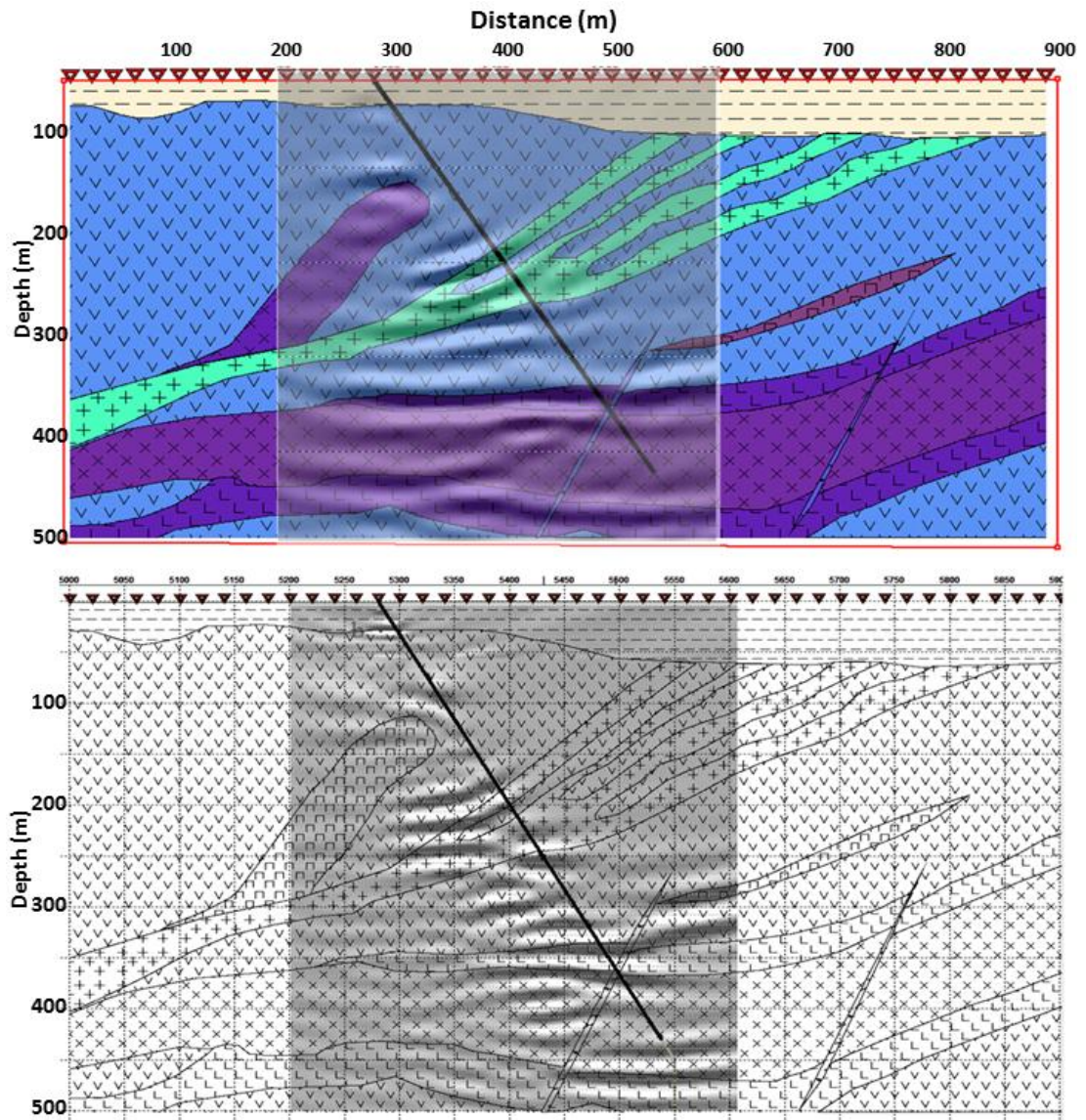
Figure 3-6. Migrated VSP sections superimposed on top of the synthetic model. Upper panel is the 40 Hz regolith negated with a replacement velocity of 5300 m/s and the bottom panel 80 Hz with a high contrast regolith present.

3.2.5 Comparison with regional seismic transect

A direct comparison between the ANSIR region scale seismic transect collected in 1999 (Section 1-2) which went through Sunrise Dam is not possible as the synthetic section through the open pit and transect are not coincidental, however, general observations can be made. The ANSIR transect was recorded with a sparse shot-receiver configuration. Receiver separation was 40 m, shot separation was 80 m (three 60000 lb Vibrator trucks), 240 active channels with a split spread geometry

51

provided maximum offsets of 4.8 km and a nominal fold of 60 for the geometry and given rock velocities. Reprocessing of the transect was conducted by Curtin University in 2005. The application of Normal Move-out (NMO) correction of far offsets resulted in the severe stretch of shallow reflected wavefields and needed to be eliminated from the data. This was performed by reducing the maximum receiver shot offset used in stacking and muting of stretched wavefields. As such, shallow targets had to be stacked with a much lower fold of 16 or less. Because of this, the expectation from the re-processing in terms of image improvement at shallow depths was low. However, the application of refraction statics to correct for the effects of the low velocity regolith overburden, greatly enhanced the results and the reprocessed brute stack showed very good image quality from approximately 200 m depth to the deepest crystalline structures (Urosevic and Evans, 2007). This is shown in Figure 3-7 along with the short section which crosses near the Sunrise Dam open pit.

Two immediate observations between the VSP synthetics and the 2002 reprocessing results can be made. The first is that the frequency content is much lower in the surface seismic and has not resolved 50 m thick structures. This is to be expected as the source sweep was designed to target deep crustal scale structures, the synthetics are noise free and do not include the destructive scattering effects that occur in the regolith overburden which the surface seismic wavefields have to pass through twice. The second observation is that the surface seismic has captured the main structural architecture of the Sunrise Dam open pit, whereas, the VSP has only captured the structural elements around and below the borehole. This is due to the fact that surface seismic utilises redundancy of data and large aperture offsets to generate good subsurface images, whereas, VSP has limited receiver aperture which restricts its lateral imaging potential. However, the VSP shows much finer detail and at 80 Hz is able to resolve the boundaries between the BIF and UM contacts.
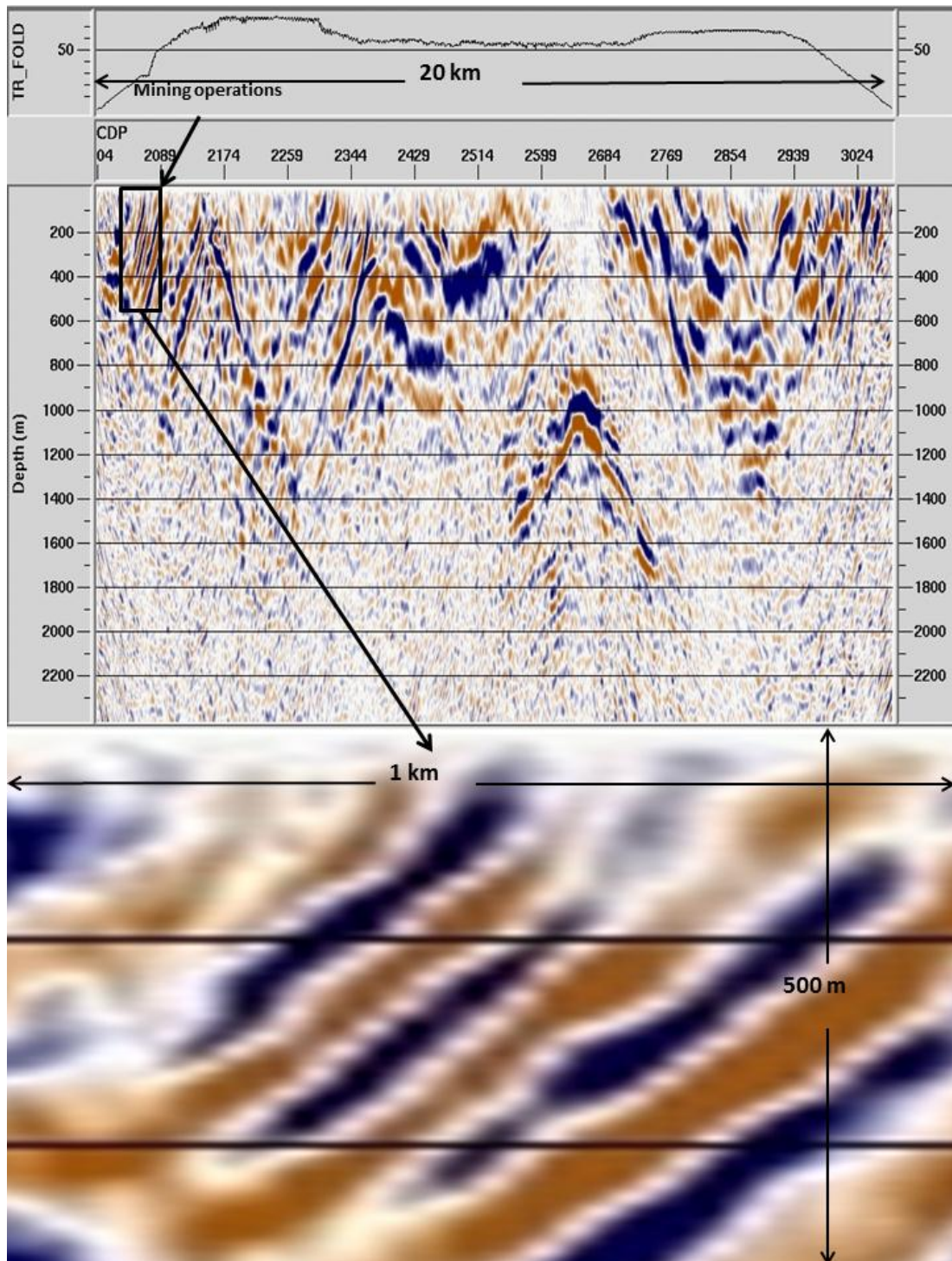
Figure 3-7. 2002 reprocessing results of the regional seismic transect collected by Geoscience Australia which transects Sunrise Dam gold mine near the open pit operations. The bottom panel is an enlargement of the transect closest to the open pit where the synthetic VSP was generated.

Comparing the VSP and surface seismic results it could be concluded that a VSP image, while higher in resolution, would be difficult to interpret without surface

seismic data and prior knowledge of the geology. When the two methods are used in conjunction most of the geological complexities could be resolved and tied back to the borehole. Wavelet frequency in the ANSIR surface seismic is not sufficient to resolve structures at the mining scale but are capable of detecting structure. High resolution VSP must use seismic wavelets greater than 80 Hz if possible.

3.3 Model 2 – Spotted Quoll nickel deposit

The second synthetic model constructed is from Spotted Quoll Nickel deposit in the Southern Cross − Forrestania Greenstone Belt of the Yilgarn Craton. Nickel is the second most common mineral mined within Western Australia. Massive sulphides bearing nickel mineralisation are often found in continuous lenses at the base of flows within the Yilgarn and worthy of a synthetic study.

At Spotted Quoll the mine is interested in determining the downward extension of the known ore reserve and the ability of seismic methods to image its extent. Nickel mineralization is confined to the lowermost komatiite unit on the western limb of the Forrestania syncline as a series of high grade massive sulphide lenses with 5 to 9 per cent Ni. These lenses are within a zone that is around 400 m in strike length, plunging at 40 to 80°E to depths in excess of 1300 m below the surface. The western ultramafic belt comprises a well layered, strongly foliated succession of intercalated ultramafic flow units, chert, basalt and meta-sediment, all overlying a thick sequence of schist (Porter and McKay, 1981). The interpretive cross section used to develop the model is shown as **Error! Reference source not found.**.

3.3.1 Model parameters – Spotted Quoll

From the cross-section of **Error! Reference source not found.**, I derived the most likely distribution of elastic parameters. The corresponding model constructed is shown in Figure 3-9. To evaluate the response and the imaging possibilities a densely sampled data set was generated. Two boreholes approximately 400 m apart were populated with receiver stations every 5 m. These are representative of boreholes WBD110 and WBD109. A total of 75 shot stations were located along the surface at 20 m stations crossing the left borehole at station 29 and the right borehole at station

54

46. Seismic velocities and densities shown in Table 3-3 were inferred from Salisbury et al. (2000), and Dobrin and Savit (1960).

Massive sulphides are typically of the order of 1 to 10 m in thick in the Yilgarn. Resolving such thin bodies with seismic methods requires the use of frequencies in the range of 150 to over 1000 Hz considering an average P-wave velocity of 6000 m/s and there are diminishing returns in increasing the frequency past about 400 Hz (resolution of 3.75 m thick sulphide lens) under such conditions. Producing seismic wavelets with such high frequency content is not achievable with current surface sources. A more achievable but still somewhat hopeful wavelet frequency of 250 Hz was used in the model which can resolve lenses as thin as 6 m was used in the synthetics.

Table 3-3. Velocity, density and model parameters for Spotted Quoll model

	Rock Unit	Vp (m/s)	Vs (m/s)*	Density (kg/m^2)
A	Granite	5900	3570	2720
B	Basalt	6400	3200	2800
C	Ultramafic (Gabbro)	6450	3420	2850
D	Schist (Sediment)	4300	2150	2350
E	Black Shale	3400	2000	2360
F	Laminated BIF (Ultramafic)	5160	2580	2620
G	Massive Sulphides	6200	3400	2970
250 Hz	Ricker wavelet			
75	Shots at 20 m station separation			
WBD110	450 receivers 35 to 485 m depth			
WBD109	585 receivers 65 to 650 m depth			

Figure 3-8. Cross Section (6403500 mN) at Spotted Quoll showing extent of current Mineral Resource and location of deeper drill holes (Western Areas, 2008).
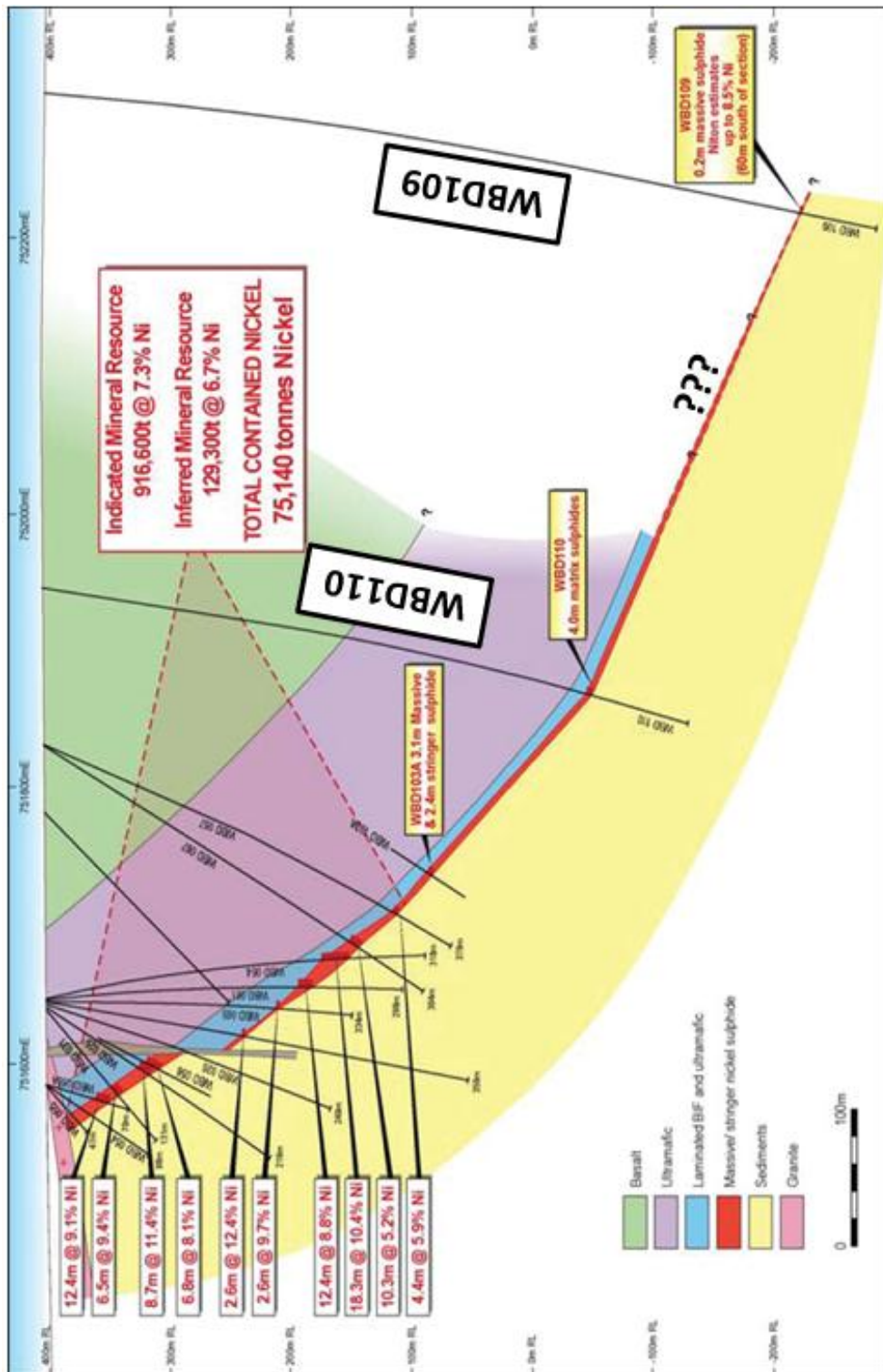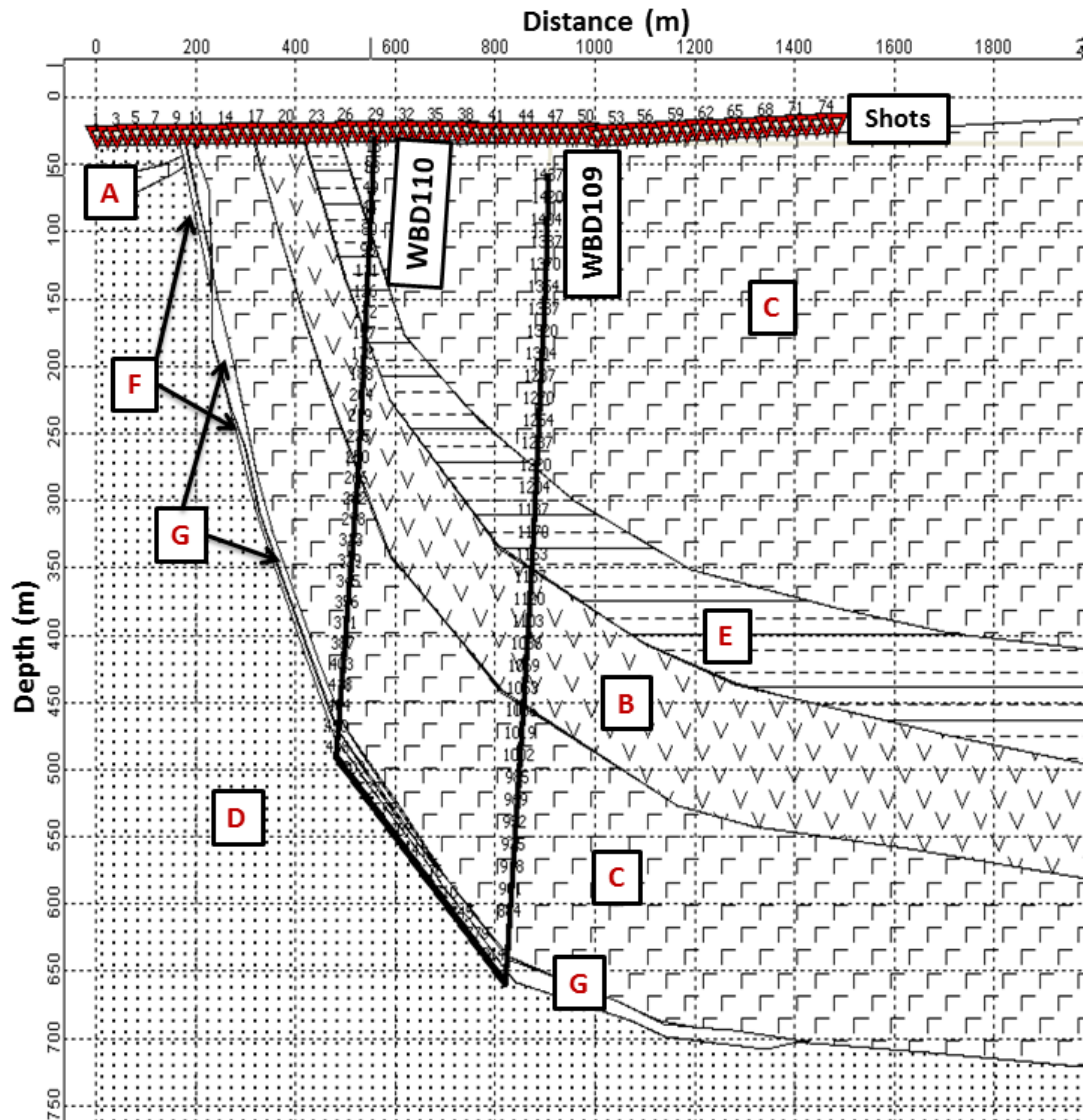
Figure 3-9. Synthetic geologic model for Spotted Quoll. respective Vp, Vs and densities used are shown in the Table 3-3. Boreholes WBD110 and WBD109 are shown with receiver stations at 5m intervals. Shot stations at 20m separations are shown across the surface.

3.3.2 Synthetic results

An analysis of shot records for WBD110 in Figure 3-10 reveals that reflection energy is minimal up-dip of the zero-offset position (shot 29). The highly dipping lithology and subsequent geometry of sources and receivers denotes that refracted energy is dominant within the up-dip shot records before 26. Once the shot and receivers are within the same geological unit (>26) then direct arrivals prevail. Within the records, there are 3 clear reflectors at 105, 170 and 450 m corresponding to the top and

bottom of the shale and at the base of lowest ultramafic unit. A noticeable change in slope of the first arrivals is due to propagation through the slow shale. It was decided to trial image processing using only the down-dip (sources 29 to 75) shot records.
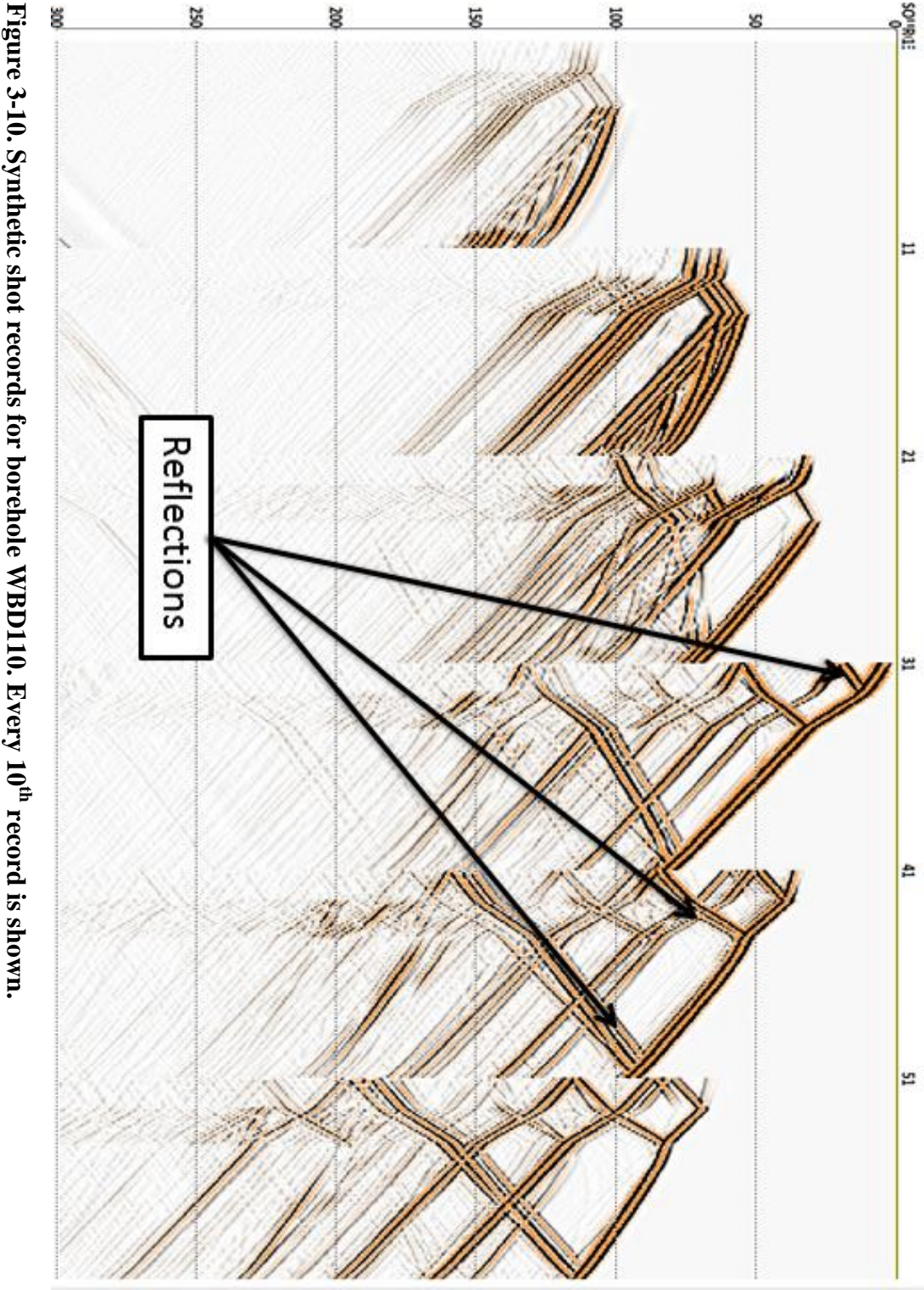
Figure 3-10. Synthetic shot records for borehole WBD110. Every 10th record is shown.

Each borehole was processed separately. Again since the synthetic data is noise free and only compressional energy is present, data processing was minimal. Receiver stations at 5 m and 10 m spacing were analysed. At 5 m receiver stations data density was sufficient to avoid aliasing, as confirmed after *f-k* domain analysis. Consequently, an *f-k* polygon reject filter was used to separate the up-going and down-going wavefields prior to migration. The resulting up-going wavefields are shown in Figure 3-11.
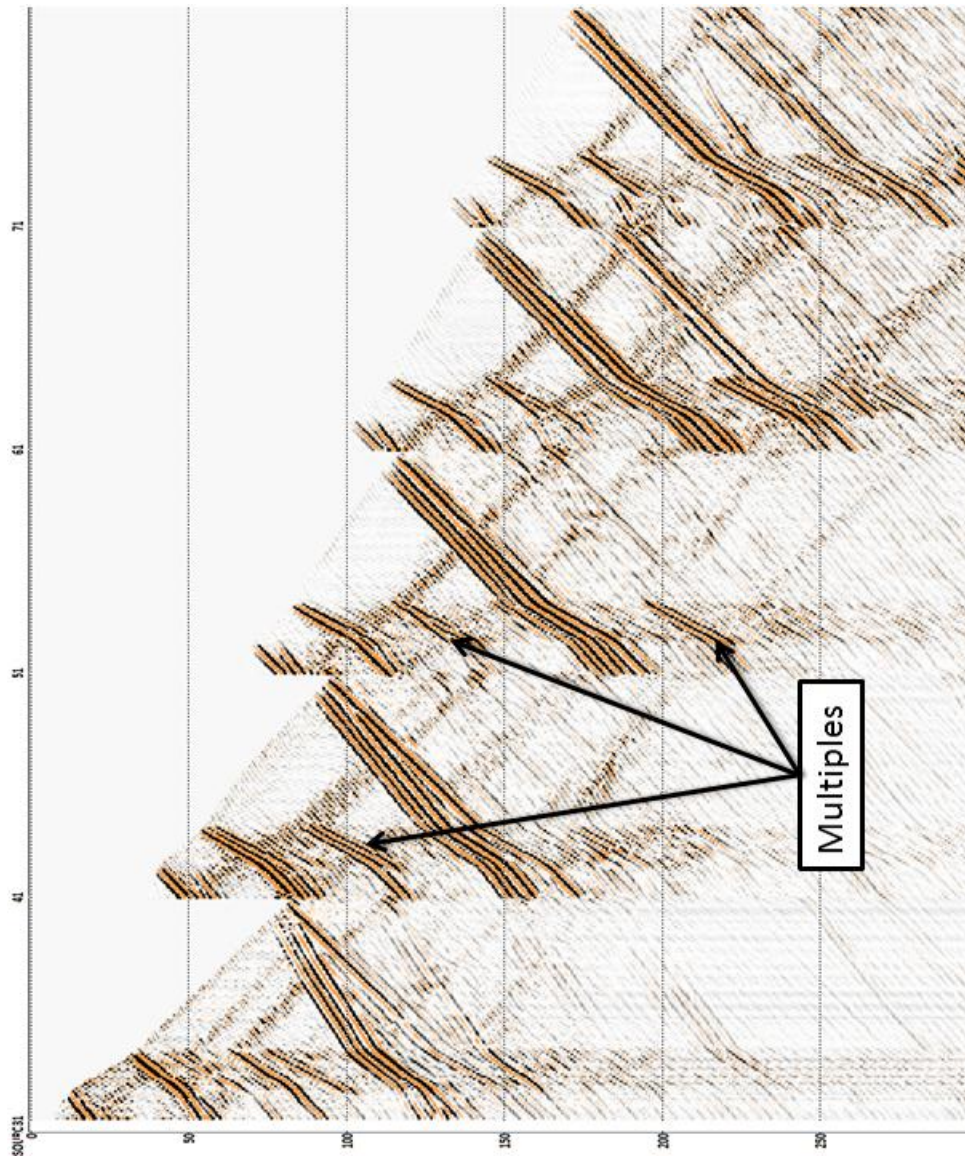
Figure 3-11. Up-going wavefield separated synthetic shot records for WBD110. Every 10th record from shots 31 to 71 is shown.

The three reflectors identified in the raw synthetic records have clearly been isolated in the wavefield separation processing. Also visible in traces Figure 3-11 are the multiples caused by strong impedance contrast of the shale at 105 and 170 m depth.

3.3.3 Velocity modelling

Hard rock seismic processing often uses constant velocity analysis and depth migration velocities close to 6000 m/s (Urosevic and Evans, 2007). This is a valid approach where there is little contrast in velocities and highly irregular and dipping structures. Constant velocity migration (CVM) panels from 5800 to 6300 m/s in 100 m/s increments were produced and are presented in Figure 3-12.
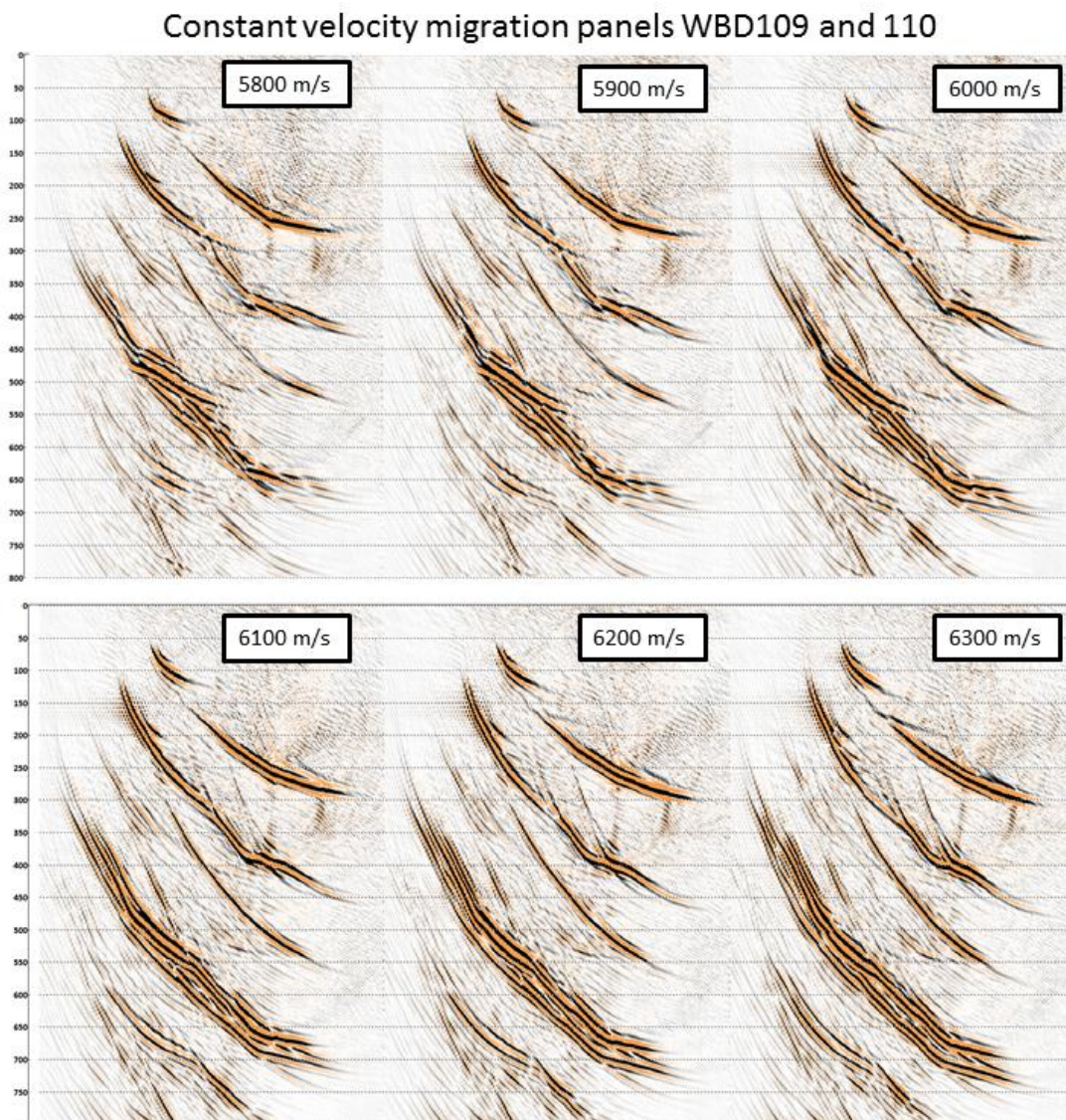
Figure 3-12. Constant velocity migration panels for sources 29 to 75. Velocity ranges from 5800 (top left) to 6300 m/s (bottom right) at 100 m/s per panel.

Inspection of the CVM panels show that at velocities below 6100 m/s the reflectors are being imaged as separate diffraction events centred on the borehole tracks. This is particularly evident in the upper horizons and gives the deepest horizon a broken appearance. At velocities above this the lowest reflections between boreholes start to align and the lowest horizon becomes more continuous. At 6300 m/s the target horizon is well defined with a continuous event traceable between the two borehole tracks.

3.3.4 Migrated synthetic section

Figure 3-13 shows the final migrated section constructed from both boreholes using a constant velocity model of 6.3 km/s and migration aperture of 1000 m. In theory diffractions extend to finite distance in time. However, in practice the useable amplitude is found within a much smaller window and the migration aperture should be large enough to encompass the largest lateral movement envisaged from the highest velocity and steepest dip (Yilmaz, 2001).

The 6.3 km/s constant velocity model depth images the target schist contact well, mapping the reflection onto the geology and the continuous reflection between the borehole, which can be attributed to the massive sulphides, thickens and thins, and has relief. The upper and lower black shale contacts however, have not been mapped to their correct depth. This can be ascribed to the low velocity of this unit (3400 m/s compared to 6300 m/s) and highlights the need for an accurate velocity model to map all contacts. That said, using an average velocity model to map a horizon at a known depth has worked well.

These VSP imaging results are encouraging for mapping UM contacts commonly associated with VHMS deposit styles in the Yilgarn Craton. If we inspect the image around each borehole separately it is evident that imaging aperture is limited on the down-dip side of the borehole. Again extending the shooting traverse would be beneficial as well as having surface seismic data to help structural analysis.

In summary, the seismic responds well to massive ore bodies, often producing high amplitude anomalies over them. This, possibly, paves a way for direct targeting of

volcaniclastic hosted Massive Sulphide (VHMS) deposits in the Yilgarn, from seismic data. The seismic response of the massive ore is however not straightforward. Seismic does not necessarily respond to the ore grade. It could be pyrite or pyrotite content for example. Hence it is of interest to examine several different geological cases and settings to understand if "common" seismic properties over these deposits could be derived.
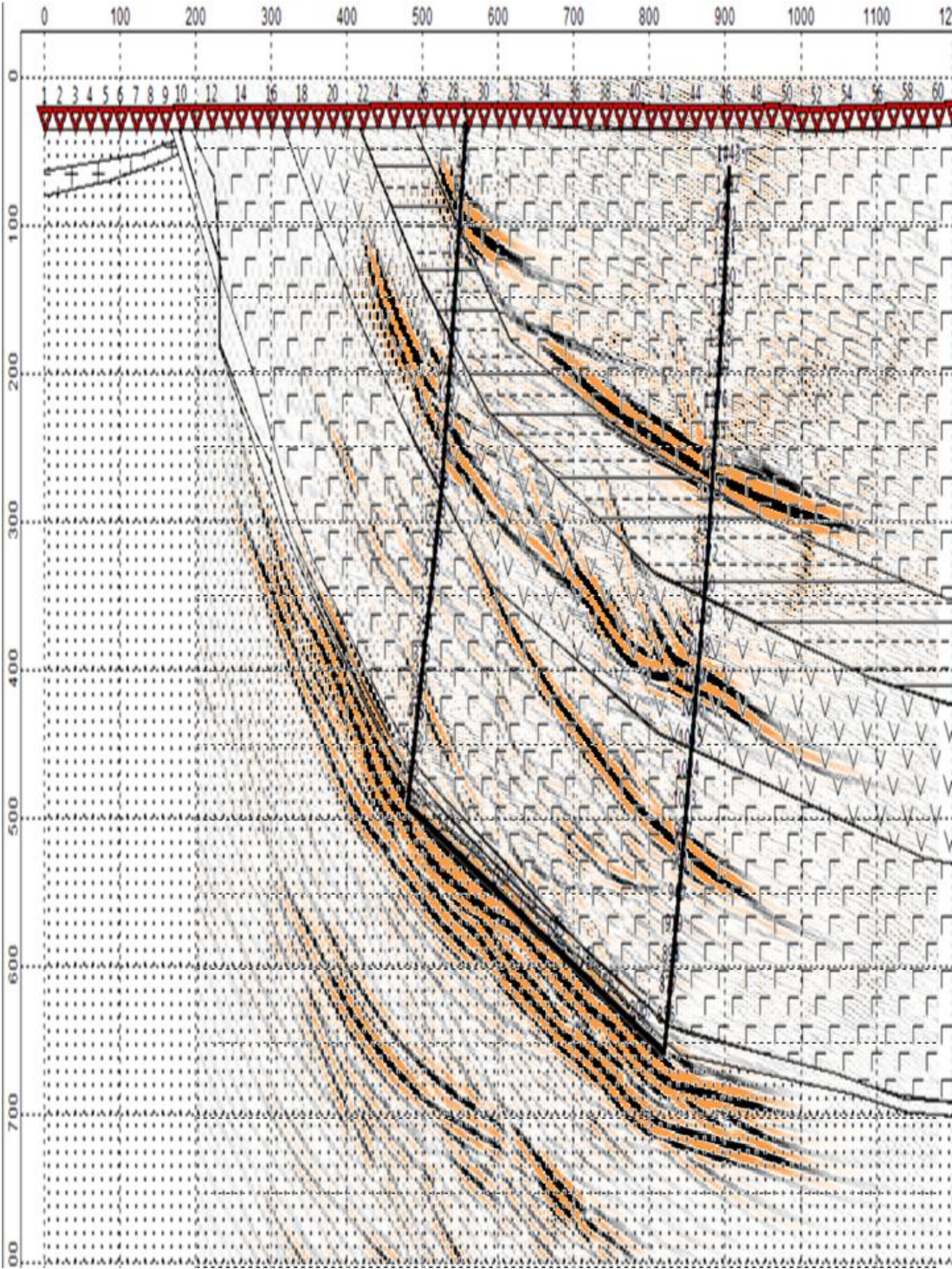
Figure 3-13. VSP Kirchhoff migration of WBD110 and WBD109 using a constant velocity model of 6.3 km/s. The target horizon is well defined with strong reflectivity between both boreholes.

3.4 Model 3 – Ranger Uranium deposit

In May 2008 a high resolution 2D seismic and VSP trial were conducted at Energy Resources Australia (ERA) Ranger uranium mine. The trials were part of a feasibility study and preplanning for a large high resolution 3D seismic survey east of the present pit operations. The location of the 2D and borehole seismic trials are shown in Figure 3-14. In advance of the trials Full Waveform Sonic (FWS) and density data were collected and synthetic modelling conducted.

Current mining at Ranger is restricted to the No.3 ore body that contains a strata-bound mineralised lens in schist and gneiss of the Cahill Formation (~2100Ma). Chlorite-quartz-muscovite schist is the main host rock and uraninite is the main ore mineral. The uraninite is present as fine disseminations in bedding-parallel breccia zones. Generalised dip of the strata is approximately 30 degrees to the east with high angle thrust and relaxation faults present. Intense chlorite alteration is a feature of the thrust occupying ore zones (Eupene et al., 1975; Hein, 2002). The dominant structures and structural complexity can be seen clearly within Ranger 3 pit and are illustrated in the photographs of Figure 3-15.

Extensive exploration drilling has been conducted east (down-dip) from the open pit. During a pre survey meeting with geologists a cross-section was sketched based on geological borehole sections. A model was created based on this sketch and is shown as Figure 3-16. The 2D and VSP surveys were planned to coincide with the modelled section and boreholes BH818 and BH714 (Figure 3-14). The collar of BH714 had been damaged after modelling and prior to the seismic trials, so the surface and VSP trials were carried out in BH711 and the accompanying W-E line.
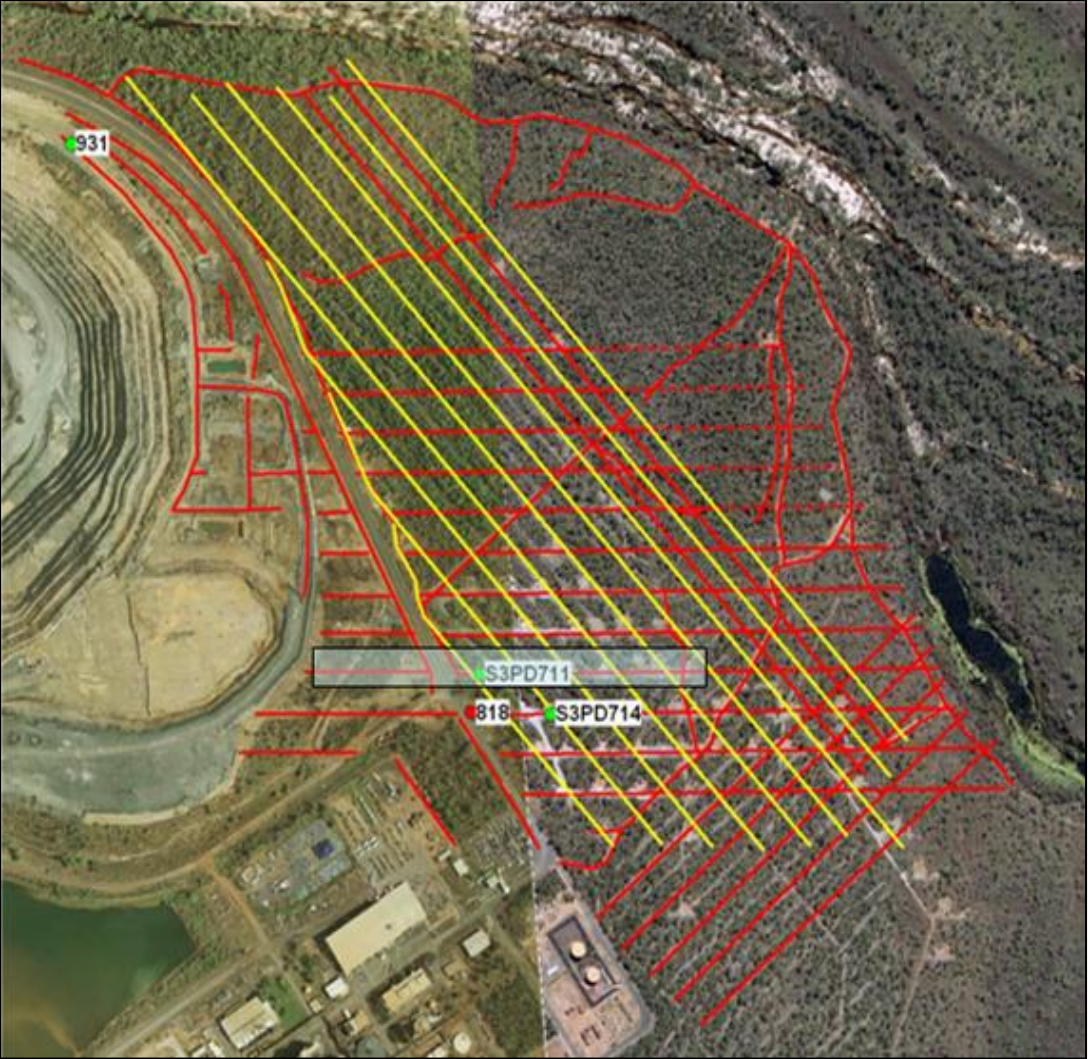
Figure 3-14. Location of borehole BH711 and the 2D (grey rectangle centered on BH711) and proposed 3D seismic surveys. Yellow and red lines are proposed 3D survey receiver and source lines respectively.
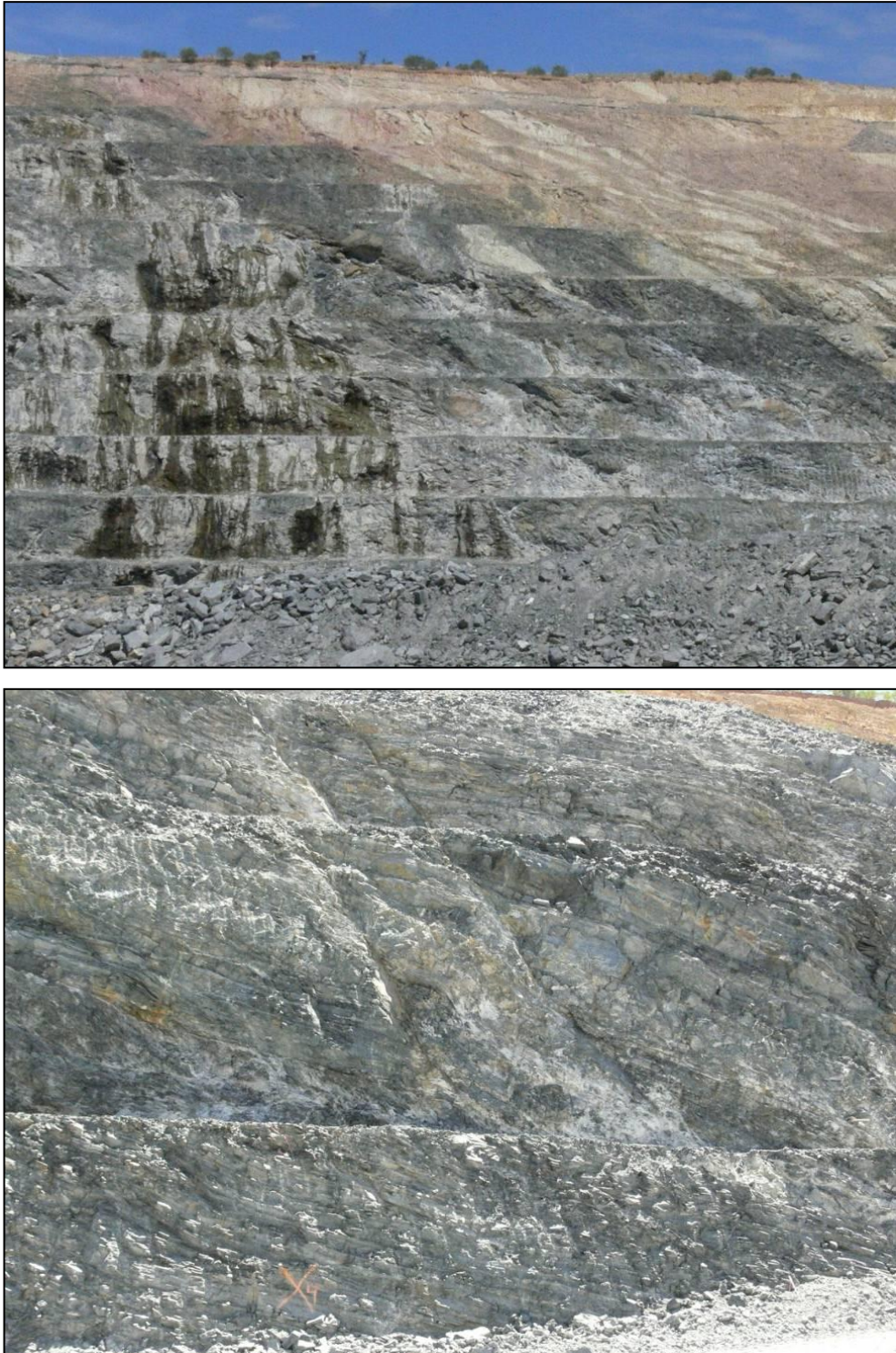
Figure 3-15. Photographs of Ranger 3 pit. For scale, each bench is approximately 10 m high. Photo A shows the dominant 30° easterly dip of the Ranger deposit. Photo B demonstrates the structural complexity, high angle thrust and relaxation faults and scale of features.

3.4.1 Model parameters

The model constructed is shown as Figure 3-16. This is based on cross-section sketches through BH818 and BH714. The model has a basic sequence of regolith, muscovite schist, chloritic schist, and carbonate overlying a gneiss basement. A shear zone separates the schist/carbonate contact. Thin layers of amphibole and chert separate the muscovite and chloritic schist's. High angle shears cross cut the schist and carbonate layers and extends down to the basement gneiss.

Full Waveform Sonic data had been acquired in the BH711 so it was possible to estimate seismic velocities directly. The FWS log of BH711 has been projected from its location some 40 m north and overlaid on the model. The unit velocities used for the model are shown in Table 3-4.

Table 3-4. ERA Ranger model velocities

	Rock Unit / Structure	Vp (m/s)	Vs (m/s)*	Density (kg/m^2)
A	Regolith	3300	1905	2245
B	Muscovite	5400	3145	2650
C	Chloritic Schist	5333	3100	2550
D	Carbonate	6200	3600	2680
E	Gneiss	5800	3050	2600
F	Amphibolites	4600	2665	2500
G	Chert	4700	2720	2455
H	Shear	5500	3205	2575
I	Porphyry	6200	3600	2850

An 80 Hz Ricker wavelet was used for elastic modelling. This wavelet was used as it representative of the 5kJ weight drop sourced used in the seismic feasibility trials conducted at Ranger. The feasibility trials are discussed later in the chapter. An 80 Hz wavelet is capable of resolving continuous planner targets as thin as 15 to 20 m in this chloritic schist environment. Sources and receivers were spaced at 20 and 5 m, respectively. Receivers spanned from 50 to 720 m borehole depth. Target depth is the 350 to 400 m shear zone in the chloritic schist.
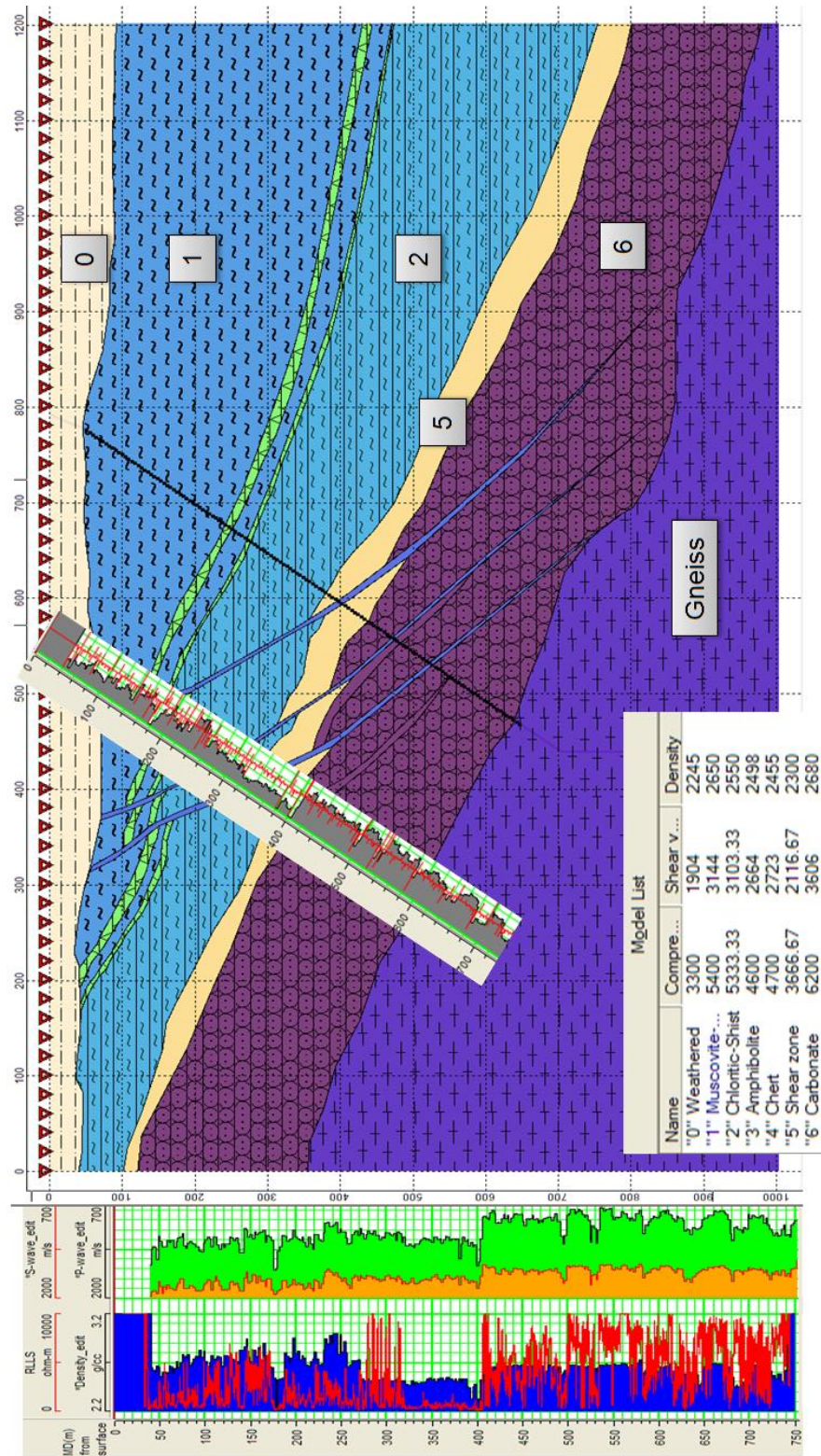
Figure 3-16. Figure 3-17. Ranger 3 geological model though BH818 and BH714. The model has 61 sources at 20 m stations along the surface and borehole BH714 is populated with receivers at 5 m stations from 100 to 700 m borehole depth. FWS and density data for BH711 is plotted to the left of the section and the impedance and P-wave logs plotted in the approximate location of BH711 parallel to this section.

3.4.2 **Synthetic results**

Elastic modelling was conducted for the 61 shot positions and the results are shown in Figure 3-18. The addition of S-wavefields in elastic modelling (as opposed to acoustic modelling) complicates the synthetic records. Both down and up-going S wavefields are present in the synthetic records. They are of higher amplitude and lower frequency than the P waves and are discernible by their shallower slopes (lower velocity) in the shot records. Their presence masks many of the potential reflected P events and complicates wavefield identification. This is particularly significant at large up-dip offsets.

There is a noticeable deviation in the direct or down-going wave signature at 460 m where the receivers transition from the schist through the shear zone and into the carbonates. Reflections are most prevalent from this horizon with mode conversions (P_d to S_d and S_u) also occurring.

Each wavefield needs to be correctly identify within the records and removed in turn, a process termed interpretive processing (Hinds, et al., 1996). Wavefield removal required multiple processing steps: FB picking, P_d removal (2D median filter), S_d removal (FK filter), S_u removal (FK filter) and deconvolution. The intermediate and final processing steps are illustrated in Figure 3-18b and c.

P-S mode converted energy is prolific throughout all records and is best observed after P_d removal (Figure 3-18b). It unveils itself in the form of Chevron patterns of up and down-going waves of identical velocity (4450 m/s). These chevrons reoccur within the gathers and illuminate the time/depths at which multiples occur in the data set. It is also noted that similar 4450 m/s events are evident in the farthest up-dip records at shallow depth where the reflection angle is likely past critical.
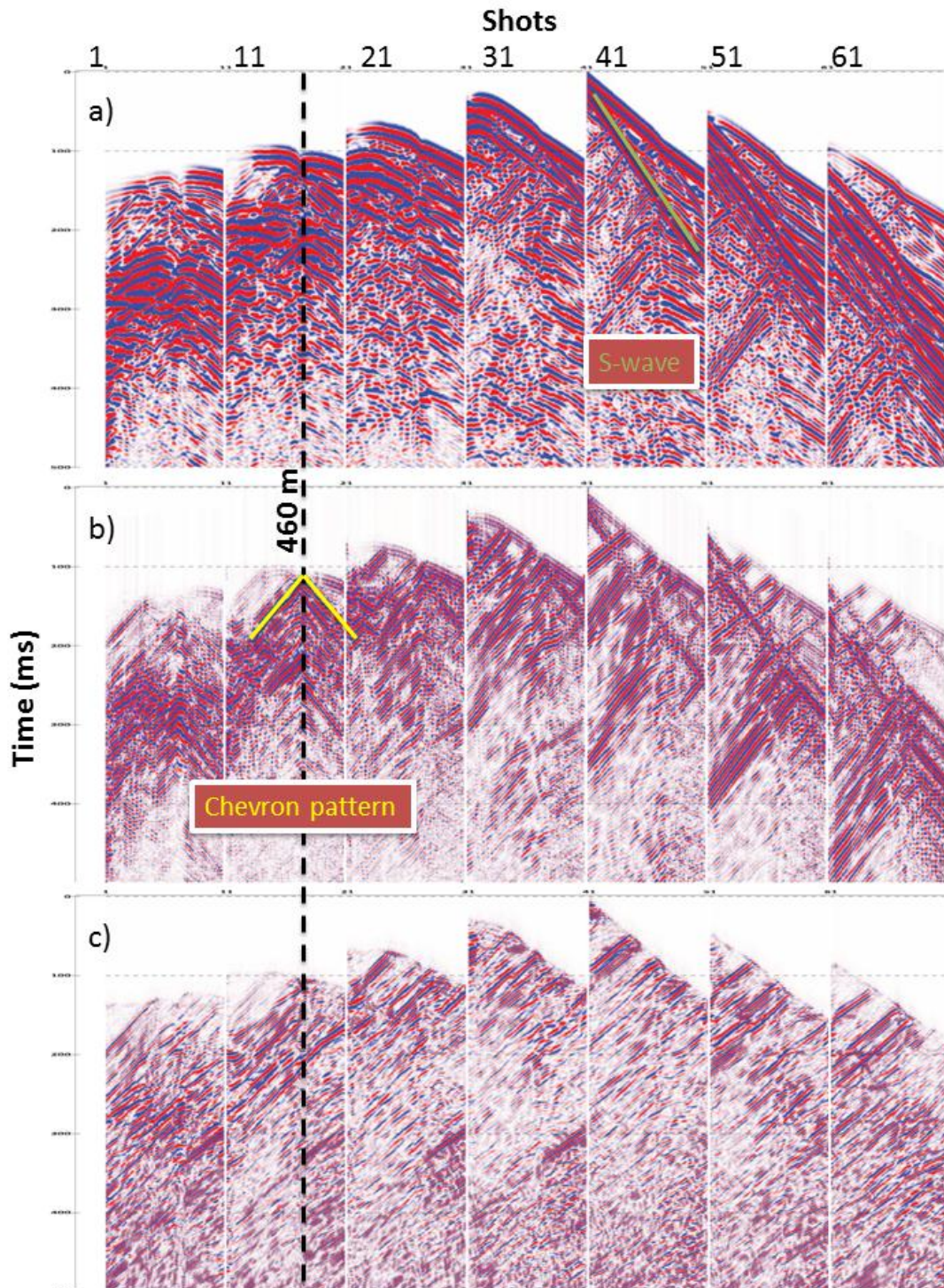
Figure 3-18. Synthetic shot records for Ranger 3 model. Every 10th record from 1-61 is shown, P_d, P_u, S_d, and S_u modes are present in the records. a) Raw records b) P_d wavefield removed c) P_d, S_d, and S_u modes removed.

A useful tool in FD modelling is the ability to take snap shots of the wave propagation at time intervals during computation. Inspecting several snap shots in succession can reveal the origin and propagation of the wavefield within the record. Snap shots were used to analyse the up-dip records for what seemed to be converted S-wave reflections noted in the previous paragraph. A snap shot of record 5 at 100 ms is shown as Figure 3-19. After analysing the wavefield propagation it was determined that the up-dip direction mode conversion is caused by interaction of the P-wave along the interfaces (amphibole and chert layers) exciting a refracted wave as indicated by the arrow in Figure 3-19.

Complete up-going wavefield separation is shown in Figure 3-18c. There are primary (P), converted (S) and multiple up-going wavefields present here. Converted events are discernible by their differences in apparent velocities and overlap primary events. In practice the H_1 and H_2 components of a 3C geophone would be utilized to assist in the identification and removal of the non-vertical (s-wave) wavefields.

Also to be noted here is the difference between apparent velocity and true velocity. Velocity is dependent upon the reference frame from which it is measured. If the reference frame (receiver string) is in line with the direction of wavefield propagation then the true, but dip-dependent velocity, is measured. If the reference frame is at an angle to propagation then the measured velocity is an "*apparent velocity*". i.e. if *V* is the true velocity and the receiver string at angle θ to propagation, then the apparent velocity $V_a = V / \sin \theta$ (Sheriff, 2002). The importance of this is that apparent velocity is always faster than the true velocity.
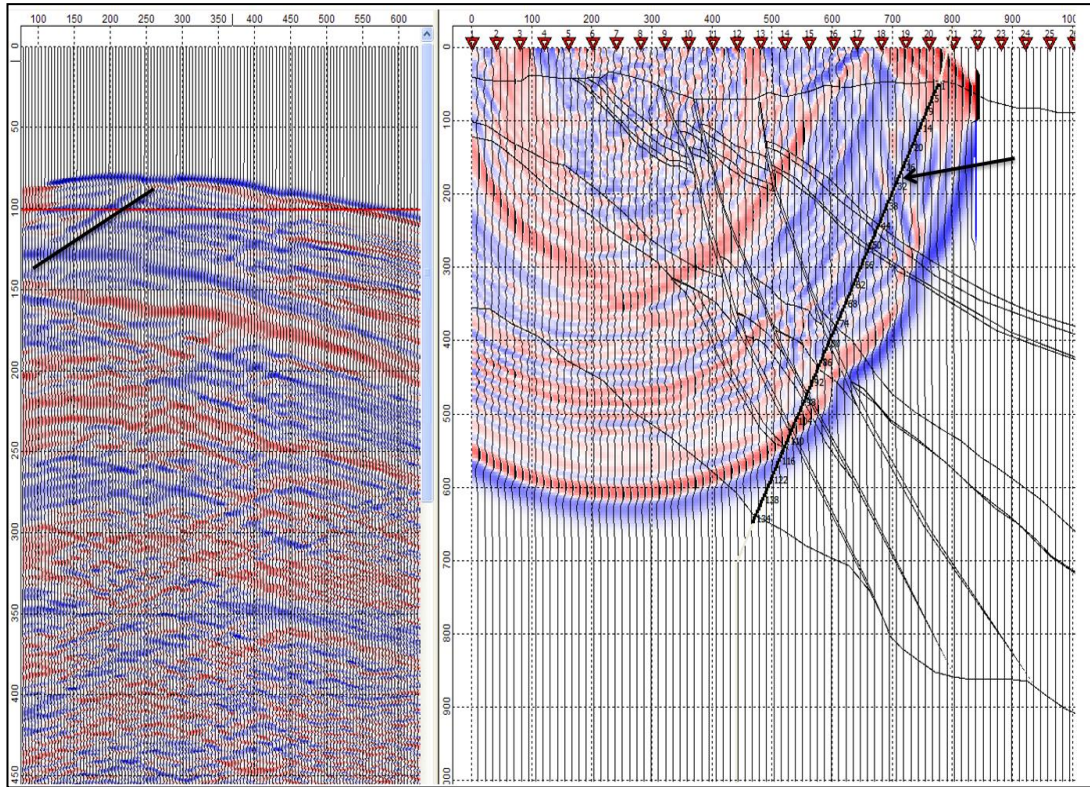
Figure 3-19. Ranger 3, Elastic modelling wavefield propagation snap shot at 100 ms for source 5 (Right panel). Left panel is the full synthetic shot gather. The up-going wavefield underlined in the shot record is caused by the converted wave indicated by the arrow in the wave propagation snap shot.

3.4.3 Migrated synthetic section

Due to the complexity of the remaining up-going wavefields, the presence of converted waves and a known dominant 30° dip, different migration were trialled. Trials included constant velocity, variable velocity (velocity model derived from ZVSP FB pick), migration aperture and preferential slope tests. After several runs from 5 to 50° of aperture and 30° preferred slope the final migration settings were an aperture of 30° and preferred slope 0°, 2 m sample interval and 5 m lateral increment. The two best migration panels from CVS and variable velocity models for the above trials are shown as Figure 3-20, V_p= 5350 m/s (main host velocity above target).

Both migrations performed poorly down-dip in the deep part of the section. The variable velocity model has generally performed better especially at the 200 and 400

m horizons below the borehole. These two horizons are not continuous down-dip but still easily traceable.

The high angle features crossing the borehole have not been imaged well. It often appears as if these features are mirrored on the opposite side of the borehole plane.

The carbonate gneiss interface has not been imaged and there are artefacts from multiples below the borehole. The migration smiles especially on the down-dip side of the borehole. The constant velocity migration suffers from artefacts about the borehole path with migration "smiles" often emanating at the borehole.
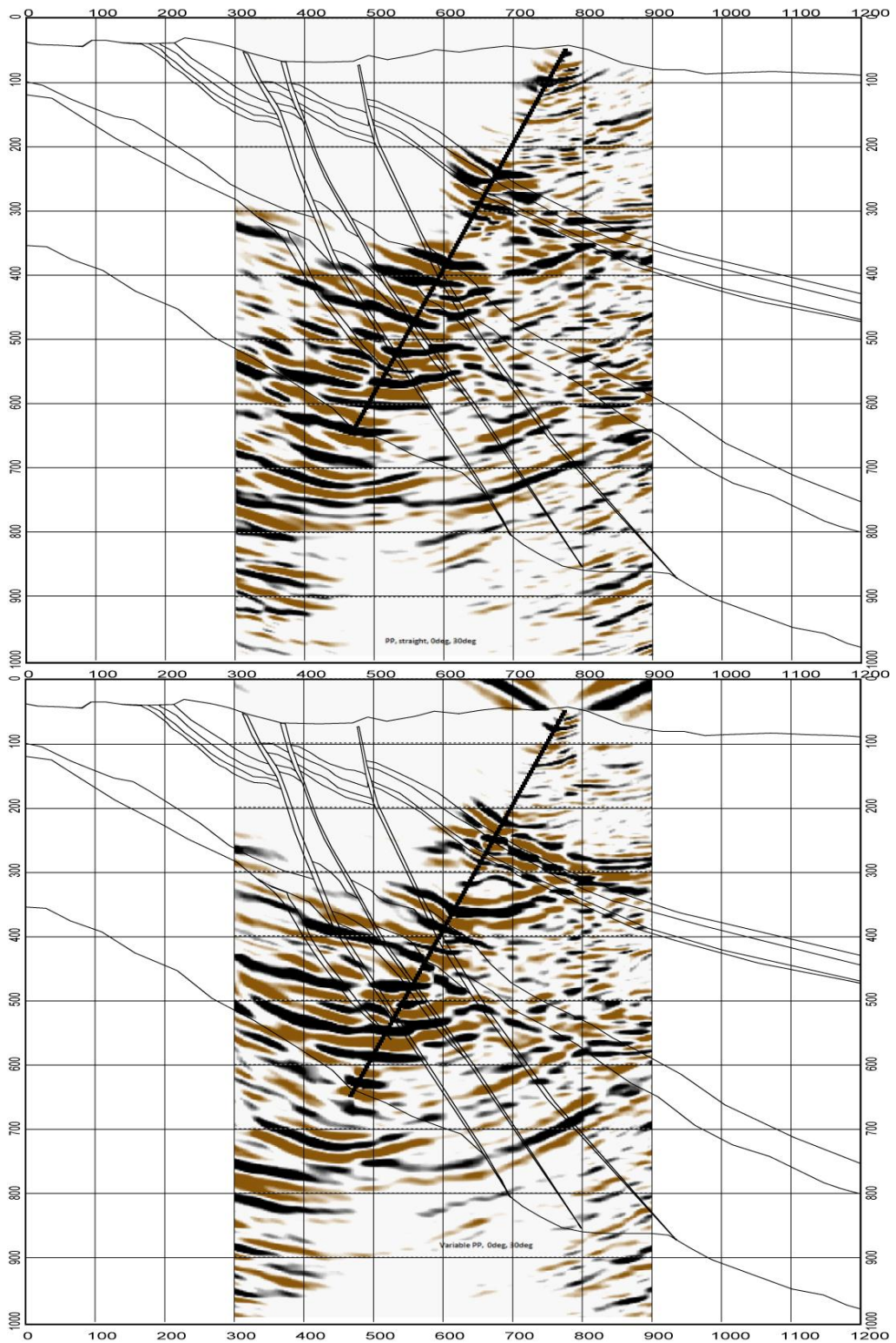
Figure 3-20. Kirchhoff depth migration of Ranger 3 synthetics. Upper panel has been migrated with a constant velocity of 5350m/s and the lower panel has been migrated with a variable velocity model derived from FB.

3.5 Ranger Feasibility field trials

The primary aims of the Ranger trials were to establish the viability of surface seismic prior to committal to a 3D surface seismic survey and determine the seismic source required for Ranger ground conditions. These aims were to be evaluated primarily from the 2D survey results and analysis of FWS and density logging. As some open boreholes were available it was opportune to collect VSP for little extra cost.

The VSP surveys consisted of:

1) Zero offset

2) Walk-over survey where source offset and receiver depth were increased proportionally such that the source/receiver offset was zero i.e. a true vertical travel path was attained.

3) 3 x receiver gathers. Where the probe was stationary at 68, 150 and 230 m borehole depth, whilst the source traversed the 2D line (3 times)

These are summarised graphically below in Figure 3-20 ray path diagram. The trials took 2 days to complete. The 2D and a walk-over VSP were conducted simultaneously on the first day and the ZVSP and WVSP surveys were conducted on the second day.
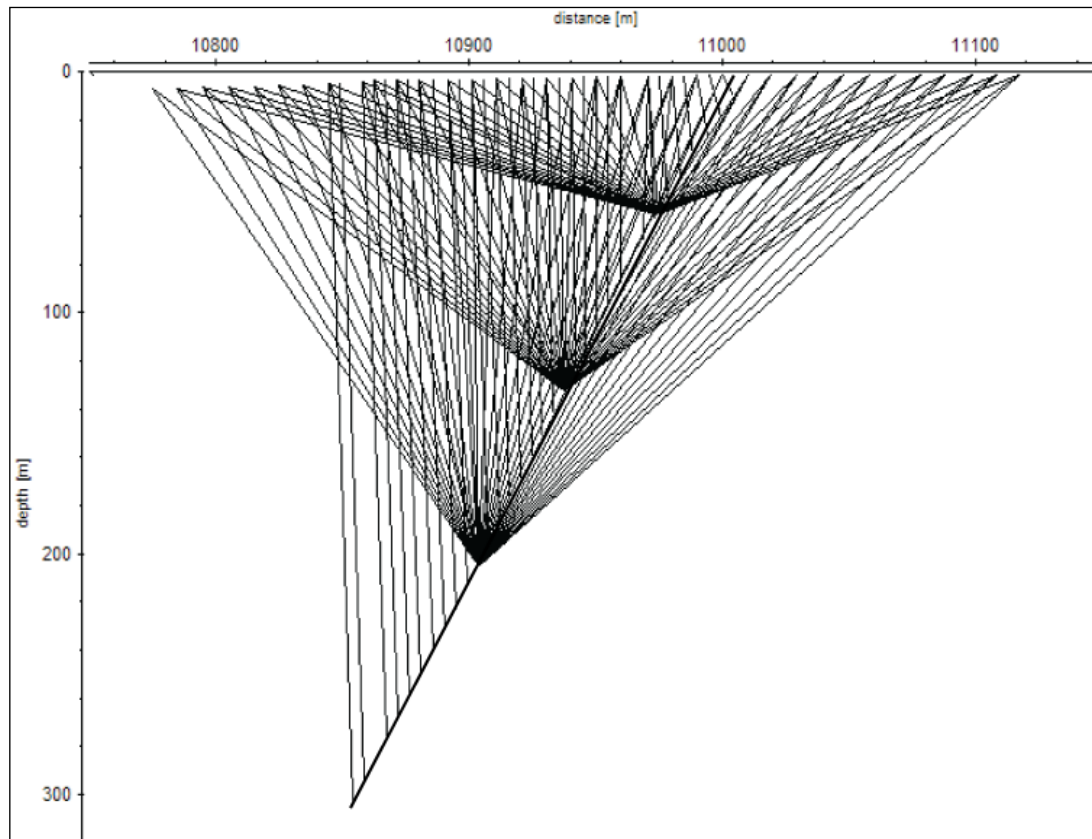
Figure 3-21. Ray path diagram of VSP surveys conducted at Ranger.

3.5.1 Field trial: Shallow 3C borehole geophone VSP

VSP data were acquired with a Geostuff BHG3 3C clamping geophone probe. The BHG3 was designed as an engineering investigation tool typically for depths up to 150 m. It has a maximum rated survey depth of 350 m, can rotate H1 and H2 components down the hole to a pre-defined magnetic orientation and requires 72 V at surface to power the clamping motor. The surveys required multiple repeat shots to attain common source positions for the numerous receiver levels in the borehole. A 5 kJ drop hammer hydraulically controlled and mounted on a skid steer (Bobcat) was used as the source. The 500 kg weight free falls 1 m onto a force spreading plate.

Data from the walk-over survey was redundant due to O-ring failure part way through the survey and all channels lost. This data set was collected coincidentally with the surface 2D and time restrictions prevented repetition of the walk-over. On day two, after collection of the ZVSP, O-ring failure occurred on the second probe during the WVSP and a horizontal channel lost.

Raw ZVSP data after horizontal component rotation is presented below as Figure 3-22. Rotation was conducted using hodogram analysis as opposed to using the mechanical orientation provided in the probe. This was to maintain a single constant coupling of the components inside the probe during the survey.
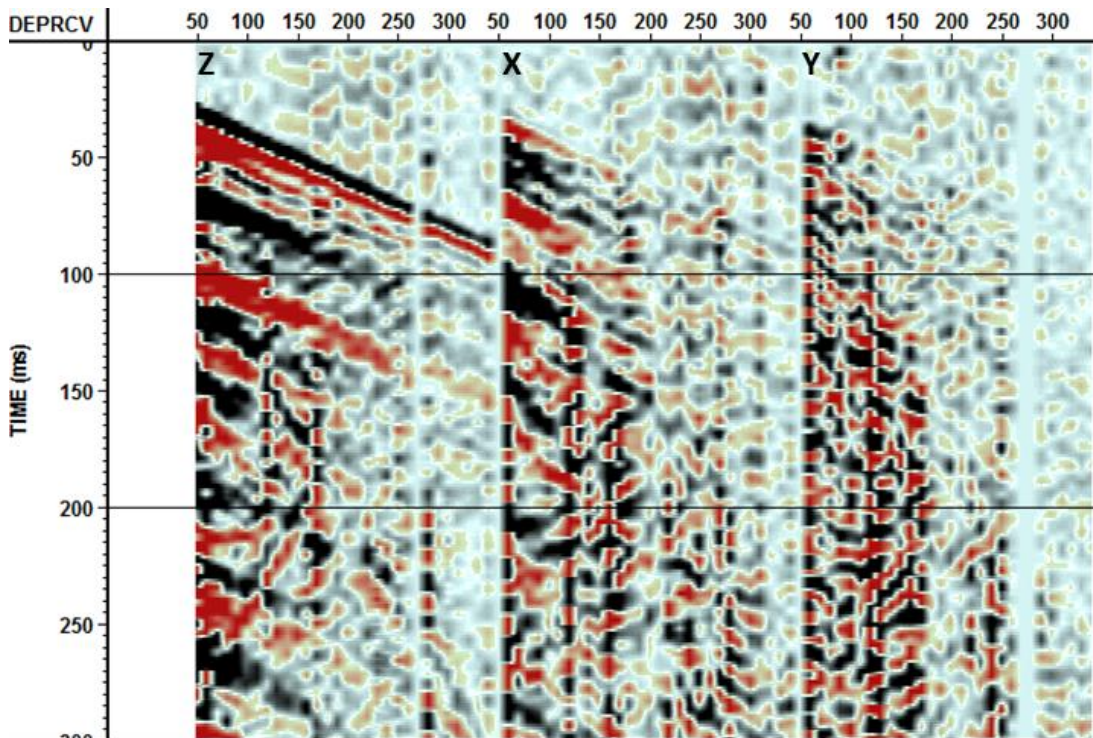
Figure 3-22. Raw ZVSP data for BH711. Receiver aperture of 50 to 330 m at 10 m stations. Noisy traces at 270 m have been edited out. DEPRCV is the borehole depth of the receiver

The raw data is of average quality with clear FB's in the vertical component but high background noise. The probe did not couple with the borehole at 270 m (23rd station) due to a washout in the borehole. Poor coupling is also evident in the X and Y components at stations 120 and 170 m borehole depth where high amplitude tool modes predominate. The most prominent features in the ZVSP data are; primary down-going multiples in the vertical (Z) component; reflected P is evident within the first 100 ms after first arrivals; principal down-going tube wave which is reflected at 160 m and multiples occurring after this; principal shear is weak but evident in the Y component and a shear reflection can be seen between 150 to 250 m depth and 110 ms.

The vertical component of the ZVSP is shown in Figure 3-23 after down-going wavefield removal. Several processing attempts were required to attain a clean looking up-going wavefield and much effort went into preconditioning the data before median filtering. Down-going removal required;

- Spherical spreading amplitude corrections (trace weighting)
- Spiking deconvolution and bandpass filter
- 2D median filtering of the down-going P-wave and bandpass filter
- FX deconvolution
- 2D median filtering enhancement of the up-going P-wave and bandpass filter
- Spectral shaping

The final up-going ZVSP P-wavefield has multiple reflection events between 50 and 200 m and on just below the bottom receiver at approximately 400 m.
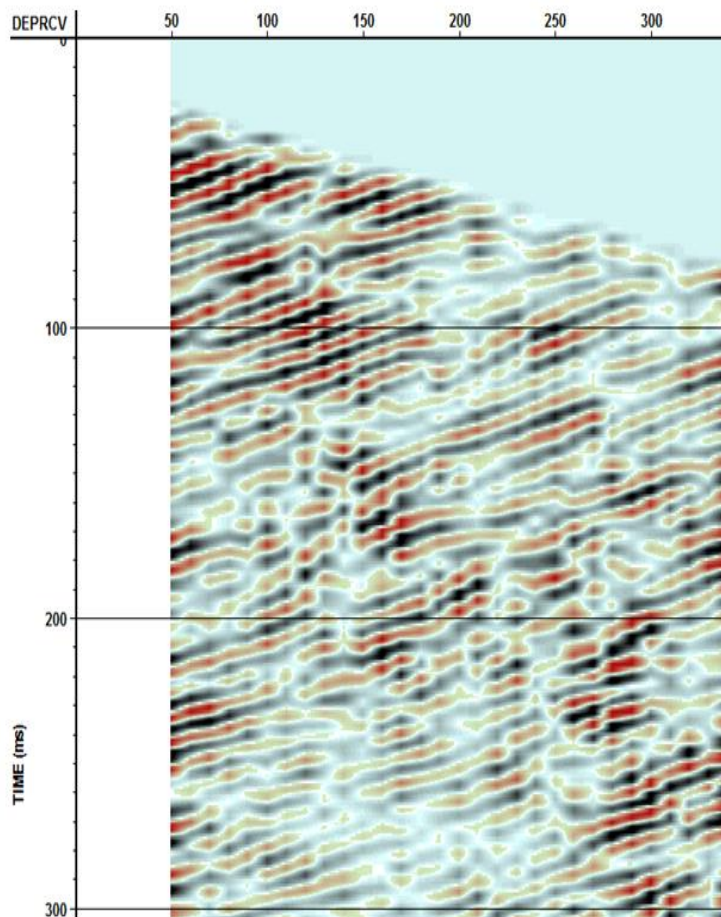
Figure 3-23. ZVSP data after removal of down-going modes.

3.5.2 1D Velocity Model

First Breaks were picked on the peak of the down-going P component and then shifted by 4 ms to the onset. A 1-D inversion of FB times and receiver depths was then used to generate a velocity profile along the borehole. This is shown as Figure 3-23. The inversion simply solves the velocity from time and depth in successive layers from surface for each depth/time pair. The model can be adjusted in terms of selected/picked layers. For evaluation of the FB time picking each depth/time pair was modelled. The average velocity from 50 to 340 m is 5240 m/s and is in good agreement with the interval velocities of the inversion. However the interval velocity model is somewhat erratic. This can be expected as measurement and time picking errors are significant. At an average velocity of 5200 m/s the travel time between 10 m spaced receivers is 1.9 ms. With data collected at 0.25 ms sampling rate, this equates to a 7% time error ($\pm$ 0.125 ms equivalent to $\pm$ 360 m/s). The data were re-sampled to 0.1 ms and FB's picked to reduce this error however the above error estimation assumes there is no error in receiver separation distances, trigger timing or ground compaction at the source location from repeat "shooting" decreasing the near surface travel time. Calculating interval velocities over larger receiver distances smooth's the model and it is common to use some other geological or geophysical data to constrain the model such that it is representative of lithology changes. One such possibility is shown in Figure 3-25 where velocity derived from inversion is compared with FWS and ultra-sonic Pulse-Transmission (PT) measurements.
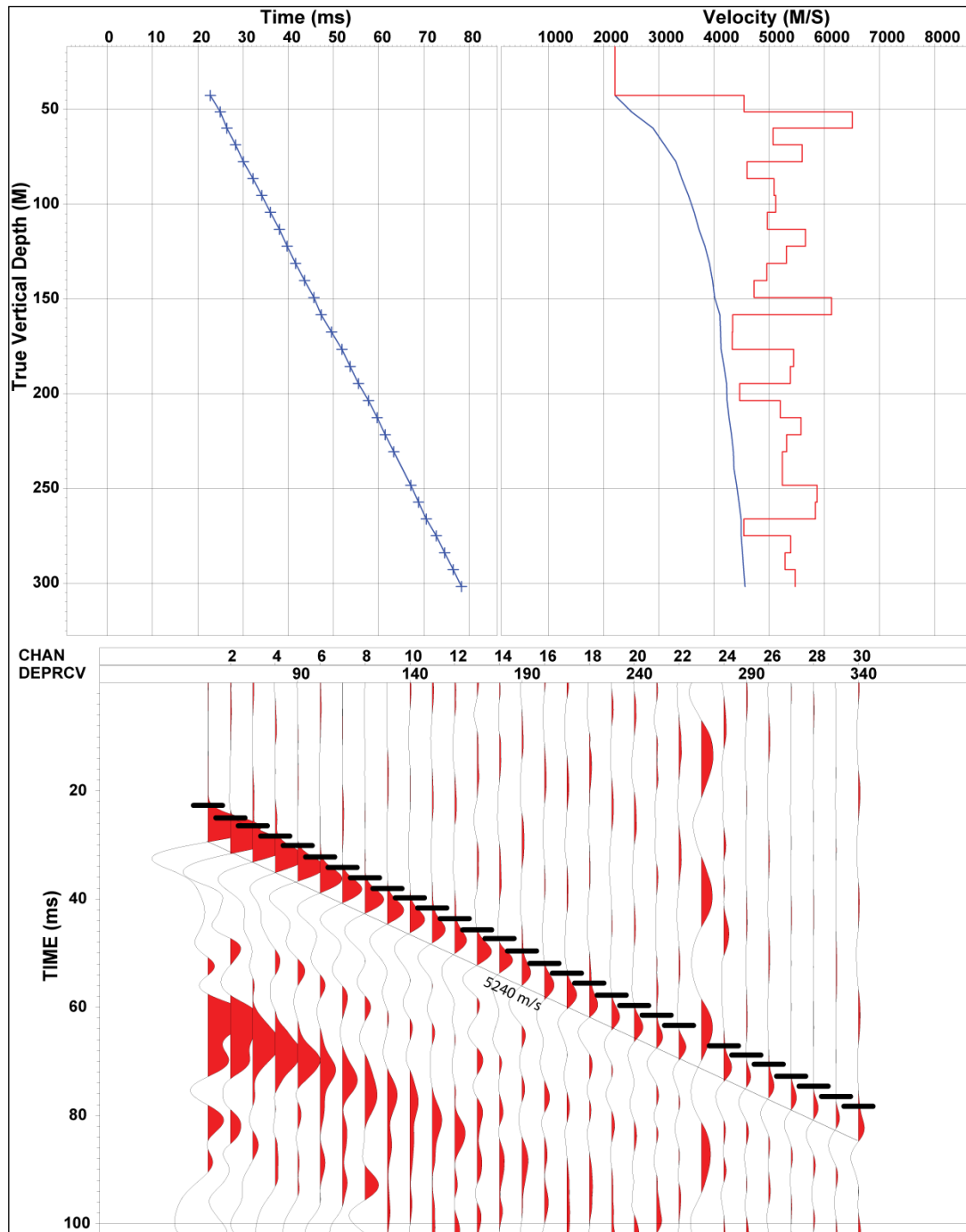
Figure 3-24. Zero offset velocity analysis of first breaks. Picks were made on the peak and shifted to the onset as shown in the bottom panel. The top panel shows pick times (left) and the corresponding interval (red) and average velocity (blue) plotted against TV depth to the right.

3.5.3 Pulse transmission Tests

Ultra sonic Pulse-Transmission (PT) tests were conducted on 23 rock samples from BH711. The PT tests were conducted with S-wave transducers and a signal generator set at 1.0 MHz. The resulting waveform was recorded and analysed on a 2 Ghz digital oscilloscope. In addition the length (or width) of the tested section, the samples weight in air and the samples weight in water were measured. All these parameters allow Vp, Vs, Specific Gravity (SG) and Acoustic Impedance (AI) to be calculated.
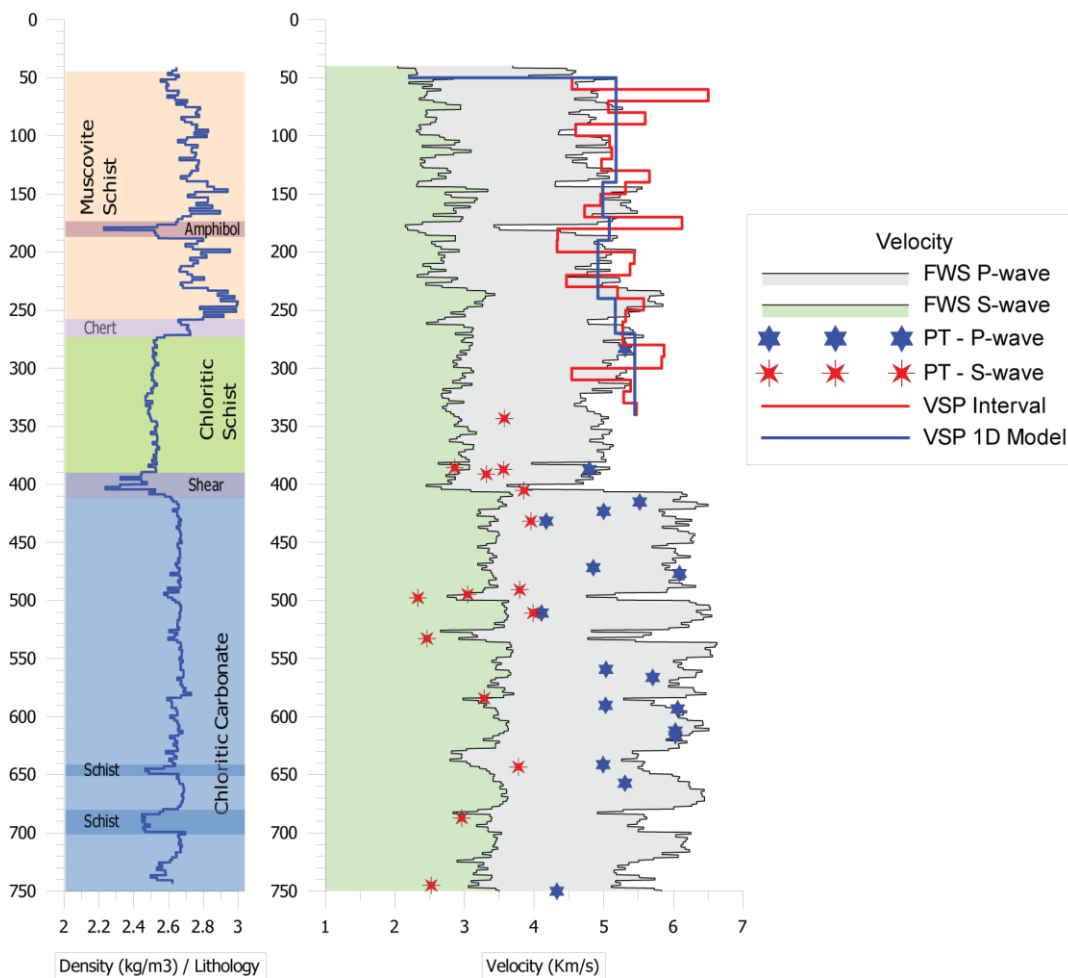
Figure 3-25. Seismic velocity in BH711 determined from FWS, VSP and ultra-sonic Pulse Transmission measurements. Also shown to the left is the basic geology and density profile.

The S-wave transducers generate a polarised wavelet such that P arrivals are positive and S arrivals negative in polarity. The determination of P and S arrivals was

complicated by foliation and soft fractures within the samples. These multiple structures created different wave modes (reflected and refracted) causing destructive interference, complicating the determination of the S arrival. P arrivals were often weak and occasionally reversed in polarity due to core structure complexity. As such there is some ambiguity in the measurements and 6 measurements were discarded from the data set. The resulting velocities typically fell within 10-15% of the FWS data. There are some large variations from this but cannot be excluded as the measurements are taken over such a small volume of rock (5 to 10 cm) compared to the FWS which samples over 2 to 3 m and the VSP at 10 plus m. These large variations may also occur as the rock has been removed from its original stress field.

3.5.4 FWS Synthetic

Acoustic Impedance (AI) is the product of velocity and density and it is used to determine the reflectivity or Reflectivity Coefficient (RC) of seismic waves at acoustic boundaries. The reflectivity for normal incidence is defined as,

$$RC = \frac{AI_2 - AI_1}{AI_2 + AI_1},$$

where the subscripts denote the successive layers with depth.

When the reflectivity is expressed as a function of time and convolved with a wavelet which represents the seismic input, the resulting time series $f(t)$ is a synthetic seismic trace that approximates the seismic response of the earth,

$$f(t) = w(t) * r(t) + n(t)$$

where $w(t)$ – input wavelet, $r(t)$ – reflectivity function and $n(t)$ – noise.

The synthetic trace is used to access the potential of seismic to image certain targets, it can be correlated to 2D or 3D surface seismic sections along the borehole path and used to evaluate potential multiples in surface seismic data, as the synthetic is free of multiples.

A synthetic trace was produced for BH711 using the FWS and wire-line density data. The raw data was blocked into to 2m layers and the reflectivity function calculated before convolution. A 120 Hz Ricker wavelet was used as the seismic impulse. This

had a 110 degree phase shift typical of surface impact source. The input; FWS, density, computed RC and blocky model data is shown in Figure 3-25 as well as the synthetic input wavelet and resulting synthetic trace.

The resulting synthetic trace has been duplicated twice for visual impact and shows several good reflection events which correspond to velocity and density boundaries. The reflection events at 170 m and 400 m where density has a sudden increase are particularly strong with a reflectivity ratio above 0.1. Where we go from a higher to lower density at 230 m the reflection, although good, it is not as strong.

An earlier attempt at wavefield separation is shown in TWT in Figure 3-25 along with the synthetic trace. Wavefield separation after component rotation used the following procedures;

- Flatten and enhance down-going P with 2D median to create down-P wavelet
- Deconvolution using the down-p wavelet
- Down-going P removed with a 2D median filter
- Removal of down S--wave with an *f-k* polygon reject filter
- +FB time to convert to TWT (Figure 3-23).

After all processing steps a gentle band-pass (10-25-150-200) filter was applied to remove any processing spikes. The final TWT profile is displayed in Figure 3-25. Reflections are clearly evident in the ZVSP TWT profile with three different dips present. The two reflections originating at approximately 400m depth are likely a P-P (blue up dipping) and P-S (red down dipping) reflections. The ZVSP data correlates well to the wire-line logs with several reflections events, two particularly strong at 270 m and 400 m (also seen in Figure 3-23).
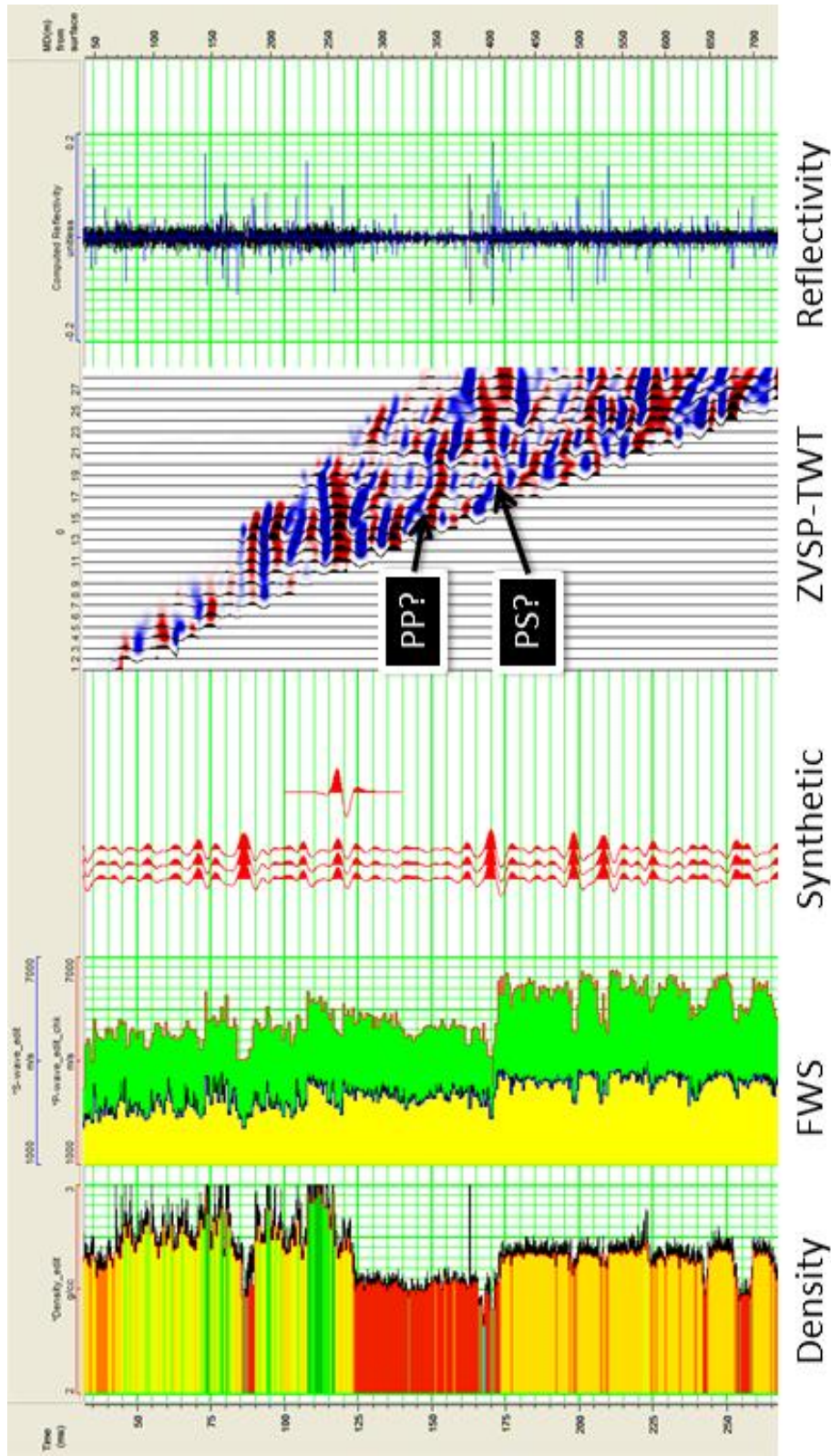
Figure 3-26. Zero-offset vertical component processed shot record. The data has had the down-going wavefield removed and converted to two-way time (TWT) and bottom mute applied. Shown from the right is; Density, P and S-wave (FWS), 120 Hz synthetic trace and input wavelet, P_u TWT 3C VSP and computed reflectivity.

Normally the TWT record would have a bottom mute applied. The mute would form a limited corridor (100 to 200 ms) from the first arrivals such that only reflected primary waves are present and any multiples removed. The remaining profile would then be stacked to create a single trace in TWT representative of the primary reflections along the borehole track. This in turn is used to depth calibrate FWS synthetics and seismic reflection sections and identify any multiples that may be present. As there are multiple dipping reflections in the processed TWT profile, it was decided not to form a corridor stack, as these dipping events would not stack to their point of origin in the hole. As such, a more qualitative approach to identifying reflection events is needed or insertion of a migrated VSP image onto the well track.

3.5.5 2D high resolution surface seismic

The 2D surface section was collected using 30 x 28 Hz geophones at 10 m spacing and 61 sources at and between every geophone resulting in a seismic fold of 30. The source was a 5 kJ weight drop hammer.

Processing steeps for the 2D section were;

- Input
- Geometry
- FB picking, kill/reverse traces
- Refraction statics
- Surface wave removal (ProMax module)
- Surgical Mute Air wave
- Spiking Deconvolution
- AGC
- Spectral shaping
- NMO
- Stack
- FX decon
- Trace math transform and 3 trace mix for display
- Time to Depth conversion

Time to depth conversion used the velocity derived from the ZVSP with deviated well track geometry. The resulting section is displayed below in Figure 3-27 and has been superimposed on the ERA model cross section in its relative position to the

original planned section. The sections are 50 m separated. Thus there are some discrepancies expected.

The 2D section compares well with expected geology. Reflections events from the amphibole and carbonate/shear horizons are clear and the dip is in agreement with known structure.
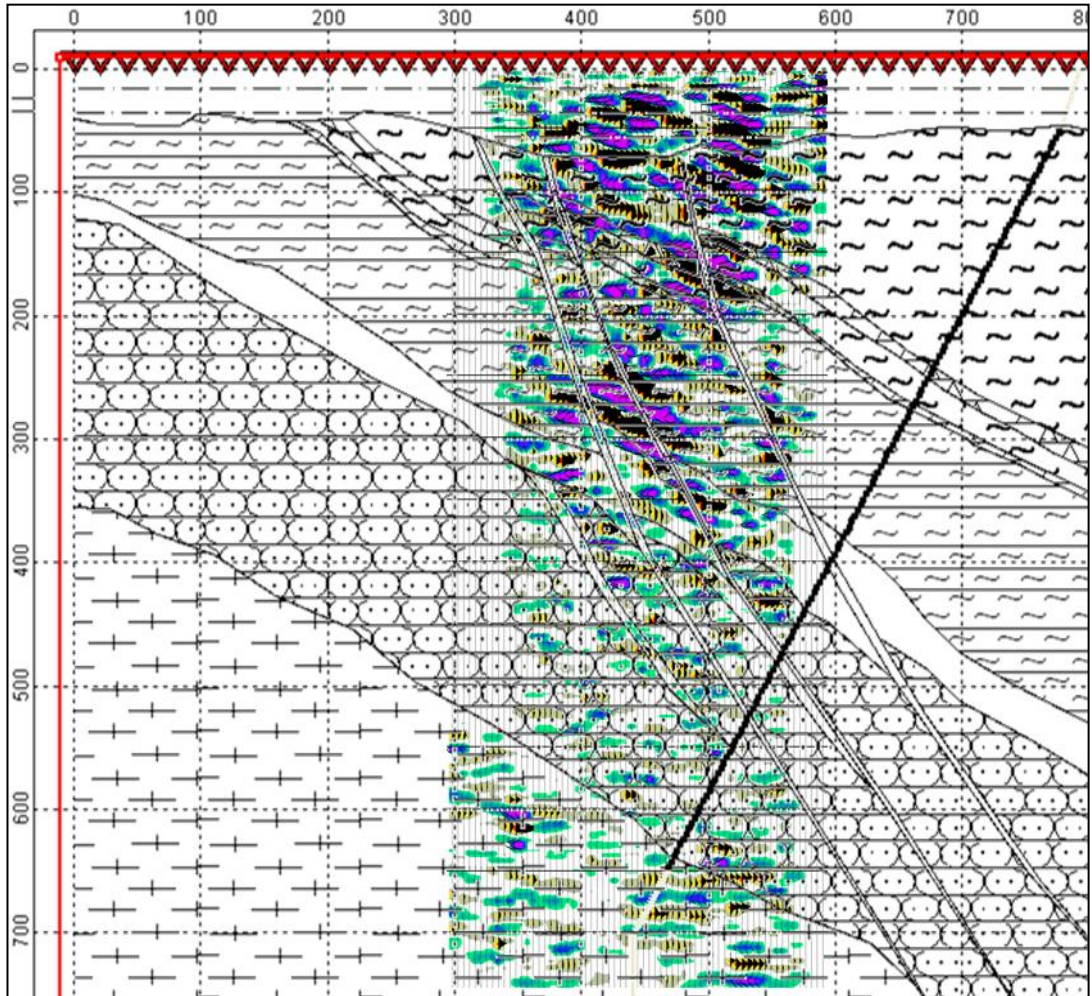
Figure 3-27. High resolution 2D section superimposed on the geologic model of Ranger 3. The section profile is 50 m off line to the north (into the page). Processing and time to depth conversion was completed using the results from BH711 ZVSP.

3.6 Conclusions

Complex geological models of gold, nickel and uranium deposits in the Yilgarn Craton and the Northern Territory have been created. Full waveform synthetic modelling of borehole reflection seismology in these environments has been tested. Synthetic modelling used borehole geometries typical of mineral exploration and has shown that it is possible to produce seismic reflection images in complex hard rock environments from angled boreholes.

Migrated images suffer from lack of aperture in the down-dip direction. Thus, large offsets and higher shot density is required on the down-dip side of the borehole to compensate for this. This is dip dependent and may never be realistically achieved if dips are such that reflections are reflected away from the borehole receivers or the offset is so large that the source energy is too weak. Also at large offsets wavefield identification is complex and correct separation of wavefields for imaging is difficult.

Up-dip and down-dip shots need to be carefully examined at each stage of processing to determine the limits at which reflection energy is no longer being added to the stack. In the up-dip direction this is reached quickly (approximately the lateral extent of the receivers in the up-dip direction). In the down dip direction it is harder to create a "rule of thumb" and modelling of each individual geologic setting is required before acquisition.

Mode converted energy is difficult to handle properly as it manifests at apparent velocities and dips that are difficult to separate from primary events. Interpretive processing is an integral part of wavefield identification and separation. Equally as important is the necessity to trial different migration velocity models. Due to the steep dips of lithological units the velocity field varies laterally and it is necessary to determine a velocity model for each hole separately.

Initial field studies conclude that, acoustic impedance contrasts are sufficient to create strong reflection events in a complex geologic environment of schist and carbonates and a combined analysis of surface and VSP images is beneficial in all cases.

4 Borehole hydrophone acquisition

4.1 Introduction

Mineral exploration, engineering and environmental monitoring boreholes are usually small in diameter (<100 mm) and relatively shallow (100 m to 1000 m) in comparison to petroleum wells for which, in the most part, VSP technology has been developed. As such, there are few lightweight, multiple-receiver, slim-line VSP tools available for mineral exploration. The acquisition efficiency of VSP is dependent on the number of geophone shuttles deployed, receiver spacing, receiver group moves required to scan the borehole and the time required for relocating and clamping shuttles. As such VSP is generally considered a costly technique, whether the drill hole is completely populated with receivers, as is now commonly done in petroleum exploration, which requires heavy surface support equipment and the fiscal value of multiple tools outweighs the cost of a mineral exploration borehole, or alternatively when a single shuttle is deployed and moved multiple times to attain the required receiver coverage, which, requires multiple shooting at each shot station and is time consuming. Consequently VSP in small diameter boreholes is at best infrequent.

An alternative seismic receiver is the hydrophone. Hydrophones are highly sensitive broadband pressure sensors. They are slim-line (<50 mm), lightweight, rapidly deployable and if deployed in a borehole do not require clamping to the wall. Hydrophone strings of 24 to 48 receivers can be manufactured for the same cost as a single slim-line 3C shuttle. Thus hydrophones are an attractive borehole seismic alternative for mineral, environmental and engineering geophysicists.

Hydrophones passively couple to the formation through the fluid column. Passive coupling and suspension within the water column leads to specific acquisition issues of cable and tube-wave noise. Tube-waves are at least 1 to 2 orders of magnitude higher in amplitude than the seismic signal we wish to measure (Cheng and Töksoz, 1982). They are generated when seismic body waves cross the borehole and they swamp seismic signals that arrive at later times in our seismic profiles, masking any potential seismic reflections. Borehole hydrophones have been used to measure

seismic direct arrivals and generate velocity profiles but have never been used as a borehole reflection imaging tool.

With the use of a 24 channel hydrophone string, over several surveys in predominately mineral exploration boreholes, I have investigated the suppression of these noise sources and the viability of hydrophones as a reflection seismic borehole receiver. Trials included hydrophone baffling, isolation / suspension of the borehole string, effects of drilling fluid viscosity and receiver acquisition parameters.

4.2 Elastic wave measurements with hydrophones and geophones

Geophones measure particle velocity, whereas, hydrophones measure pressure variations. Particle velocity and pressure are connected through the wave equation (Appendix III). Therefore, both instruments measure wavefield propagation. Both sensors produce an electric signal, geophones produce signal proportional to their particle velocity and hydrophones produce signal proportional to pressure differentials.

Geophones are a mechanical device made of a magnetic mass suspended within a coil on a spring. Movement of the coil relative to the magnetic mass induces a current in the coil through magnetic induction. The amount of allowable movement and ease of movement can be manufactured and tuned for specific peak frequencies by adjusting the stiffness of the spring and electrical dampening. However, the inherent physical limitation of materials and machining, band-limits geophone frequency ranges, typically from a few Hz to a few kHz.

Hydrophones are predominately based on piezoelectric transducers which use non conducting crystal dielectrics (e.g. quartz). Under the application of mechanical pressure the crystals become polarized and positive and negative charges become separated producing a measureable voltage. The amplitude of the generated voltage is a function of piezoelectric thickness and the applied pressure. So long as the

dielectric remains intact they are extremely sensitive and broad band (a few Hz to 100's of kHz).

Geophones are polarized and can only measure displacement in the axial orientation of the geophone. Since particle velocity is directional 3 geophone components (3C geophone) oriented orthogonally are required to measure the full wavefield. In contrast hydrophones are omni-directional and only one sensor is required to collect the total wavefield. Thus, different source geometries may be required when deploying different receiver types. For example, if one is interested in measuring shear wave splitting or anisotropy with hydrophones it would be necessary to deploy polarized shear sources at the surface, as opposed to using an omni-directional source and recording with a 3C geophone. For such measurements, despite the polarization reciprocity of sources and receivers, it is more practical to use geophones.

Shear-waves cannot propagate in water, however, it is still possible to measure S-waves with a hydrophone array. At the solid-fluid boundary, particle motion is converted into a pressure field. "*If a short length of cylinder undergoes a change in average radius, a change in volume results. This volume change should set up pressure waves*" (White, 1953). This also illustrates the fact that for any borehole hydrophone survey, the borehole needs to be fluid filled.

4.3 Borehole noise sources

The most preferred condition for a VSP survey is a stable uncased borehole with rigid geophone coupling to the formation (Hardage, 2000). The worst scenario is with multiple un-bonded casing, hydrophone receivers and a vibrator source which "rattles" the casing setting up multiple tube-wave events. An example of this is shown as Figure 4-1. This example is offered in the hope that the mistakes made here will not be repeated by others.
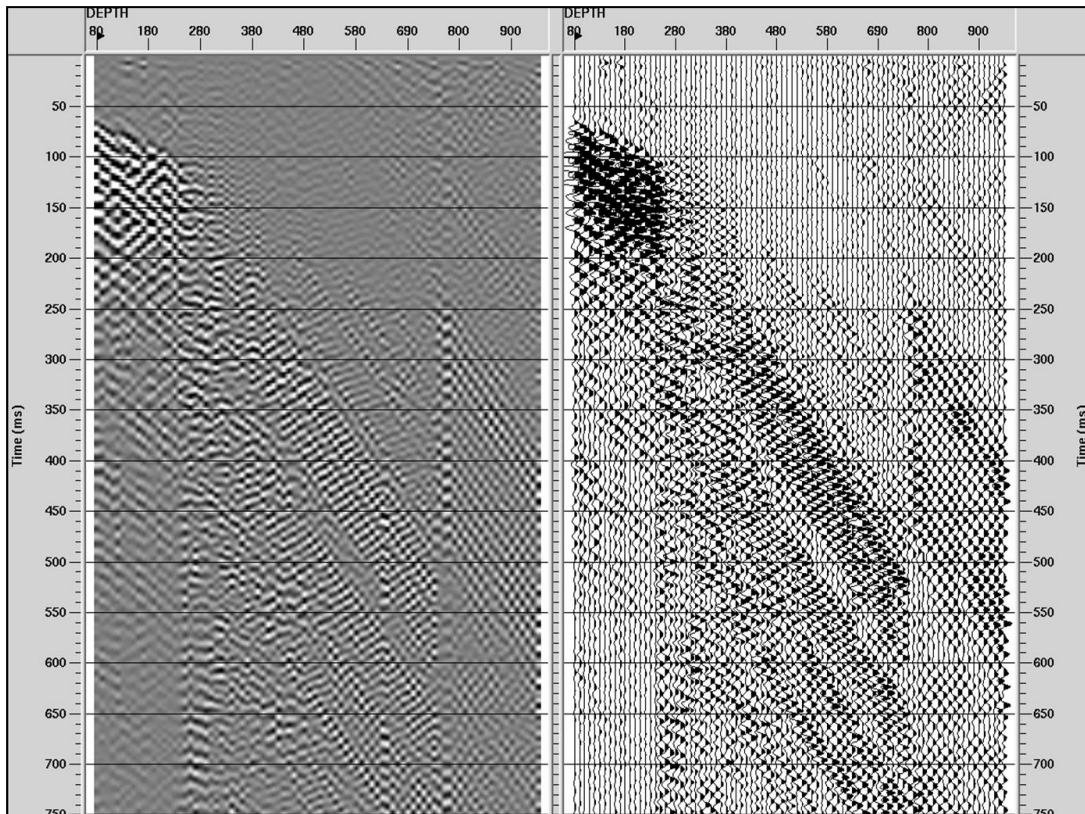
Figure 4-1. Greyscale and wiggle-trace displays of ZVSP hydrophone data in a multiple cased borehole. A 24 channel hydrophone string with hydrophone elements at 10 m separation and a 30,000 lb Enviro-vibe source was used for acquisition. Drill rods are to the end of hole, larger casing goes to a depth of 720 m and a pre-collar down to a depth of 240 m. Excessive tube-wave noise contaminates the entire shot gather, which, has been exacerbated by the vibrating source exciting drill rod resonance.

Noise sources encountered in VSP surveys are predominately related to seismic coupling and the borehole environment, the condition of the borehole, casing and acoustic modes within the fluid column (tube-waves). Other noises can be cultural, cable and tool specific modes. Geophones coupled correctly to the borehole wall will eliminate cable and tube-wave noise (Gal'perin, 1974) as a result the primary sources of noise for clamping geophones are borehole and casing conditions. More specifically;

- *Geophone coupling* – washouts, fractures and soft spots in uncased boreholes (and damaged casing in cased boreholes) inhibit the tool from coupling to the borehole. This changes the basic character of the first breaks and tool

vibration which generates strong resonant noise occurring after the direct arrivals.

- *Un-bonded / poorly bonded casing* – A medium must exist between the formation and casing which reliably transmits seismic signal. The best medium is cement (Van Sandt and Levin, 1963). Differences in bonding condition cause amplitude and wavelet shape changes in the seismic record. In the case of washouts behind the casing, tube-waves can be present adding resonance and other wavefields.

- *Multiple casing* – this is typically found at the top of boreholes and is typically un-bonded. Data exhibit a high amplitude resonant behaviour for the entire record and the data is polarized in the vertical direction by drill pipe resonance.

Full explanations and examples of VSP noise sources can be found in Gal'perin 1982, Hardage (2000) and Van Sandt (1963). The specific issues of hydrophone coupling, cable-waves and tube-waves will be discussed in the following sections.

4.4 Cable-waves

Cable-waves are vibrations transmitted along the recording cable to the tool like a guitar string transmits vibrations to the bridge of a guitar. Sources of the vibrations can include wind, generator and mobile plant noises, or seismic modes transferred to the rigid structure holding the sheave wheel. Thus, they can appear at any time within the record. The propagation velocity of cable-waves depends on the cable construction, tension and dampening caused by interaction with the borehole walls and drilling fluids. Cable-wave velocities for multi-strand armoured cable, typical "wire-line" cable for geophysical logging and geophone VSP tools, have been reported at 2500 to 3500 m/s (Dix, 1945; Gal'perin, 1974). The Curtin University 24 channel hydrophone array uses a multi-conductor kevlar reinforced polyurethane cable. Cable-waves measured with this string are approximately 2010 m/s (Figure 4-3). This is very similar to the velocity of direct arrivals in sandy sedimentary environments around Perth (~2100 m/s) where several hydro-geophysical VSP studies (Rajeswaran, 2008; Alfuhaid, 2009; Almalki et al., 2011) have been

conducted. As such, hydrophone cable-waves need to be eliminated in these environments as they will overlap and destructively interfere with any down-going wavefields in hydro-geophysical VSP surveys. In hard rock environments the cable-wave is much slower than our down-going seismic wavefields (>3000 m/s) so it can be separated more readily, however, the wave train will overlap with the persistent tube-wave, making registration and separation of the tube-wave more difficult.

4.4.1 Suppression of cable modes through cable suspension

In early hard rock experiments with the 24 channel hydrophone string, cable noise was observed. In general it was low frequency and was removed with a 20 Hz low cut filter. To minimise the occurrence of cable-waves, field procedure included stuffing the collar full of high density foam to act as a cable vibration damper, tying-off the sheave wheel to the tripod so it could not swing and placing small sand bags over the cable between the sheave and winch to eliminate cable swing. Further to this cable suspension was trialled.

Hydrophone cable suspension experiments were conducted in August 2008 immediately prior to a planned ZVSP and WVSP survey. The survey was conducted at Water Corporation borehole M345, Gnangara Road, Perth. A Seistronix EX6 distributed seismic system and an 800 kg weight droop hammer source were used for the acquisition. The source was located 8 m from the collar and the string lowered to 200 m depth such that the 24 channels occupied 200 to 430 m at 10 m stations. Initial suspension experiments used a jelly rubber to suspend the sheave wheel from the tripod. Careful observation during "shooting" noted that there was significant ground roll energy transfer into the tripod due to the close proximity of the source. This energy transfer resulted in a low frequency oscillation of the string although damped by the jelly rubber mount. It was decided that complete isolation from the tripod was required.

Complete isolation from the string was accomplished by creating a foam sandwich with high density acoustic foam and slotted plywood squares. The cable was clamped with wooden blocks and lowered onto the sandwich such that the cable was completely slack above this. This is illustrated below in Figure 4-2. Records with and

without cable suspension were recorded. These are shown as Figure 4-3. The results have been displayed at the same gain setting to allow direct comparison.

Figure 4-2. Isolation of the hydrophone string from the sheave wheel by clamping the string and suspending it upon a plywood / foam sandwich. The sandwich board would normally rest directly on the borehole collar.

Isolating the hydrophone cable from the sheave wheel and tripod by suspension significantly reduced cable noise and improved SNR. Direct arrivals at 100 ms are equivalent in both records. Coherent tube- and S-wave events have been unmasked by suppression of the cable-waves. The close proximity of the source, 8 m from the collar, has helped in illuminating the amount of energy which is transferred through the tripod onto the cable. Low amplitude down-going events are visible in the non-

isolated record prior to the first breaks. These events are produced when the weight drop is released and 8000 N ground pressure is released. This has been eliminated in the isolated field record.
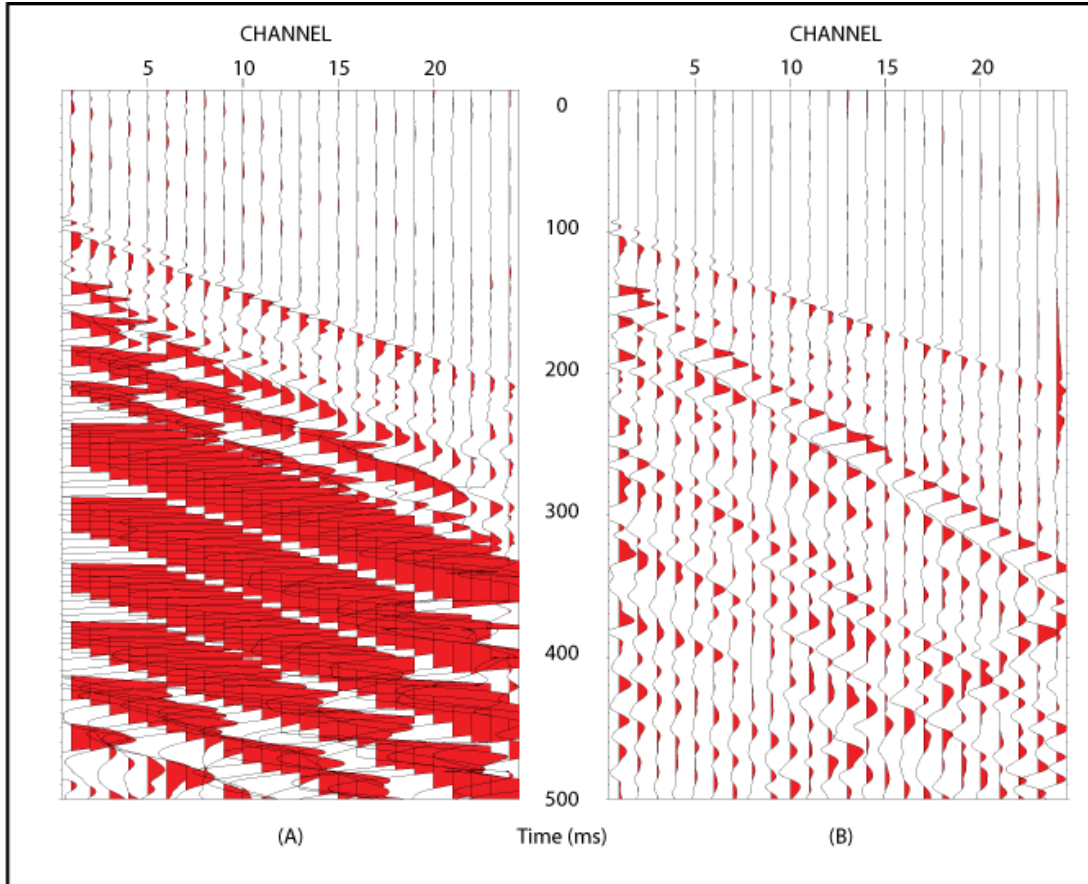
Figure 4-3. Field records of cable isolation trials. Panel A) is prior to suspension / isolation of the string and panel B) is after suspension. An 800 kg weight drop hammer source 8 m from the collar caused the very strong cable-waves transferred through the tripod and sheave wheel. Data collected in Perth 2008.

4.5 Tube-waves

Tubes waves are a coherent wave, which, travels along the borehole / fluid interface. They propagate by displacing particles within the borehole fluid and particles (in compliant rocks) in a small annulus around the borehole. Particle motion is, prograde elliptical, it is pure rectilinear in the middle of the borehole, the axial component is

discontinuous at the borehole boundary and the radial axis is continuous at the borehole boundary (Hardage, 2000). This is illustrated below in Figure 4.4.
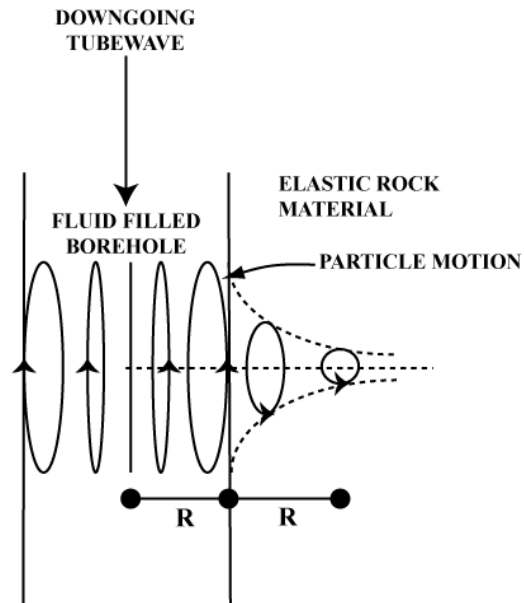
Figure 4-4. Particle motion within a borehole. Modified from (Hardage, 2000).

Cheng and Töksoz studied the particle displacement of tube-waves and the interaction of particles at the borehole wall. They compared compressional and shear propagation in competent and unconsolidated formations. They concluded that for hard formations, tube-waves are excitable at all frequencies, the major axis of motion is axial, the axial component of motion is much larger than the radial component and the axial component is larger within the fluid column by a factor of 20 at 400 Hz and a factor of 100 at 75 Hz. This is shown below in Figure 4-5 (Cheng and Töksoz, 1982).
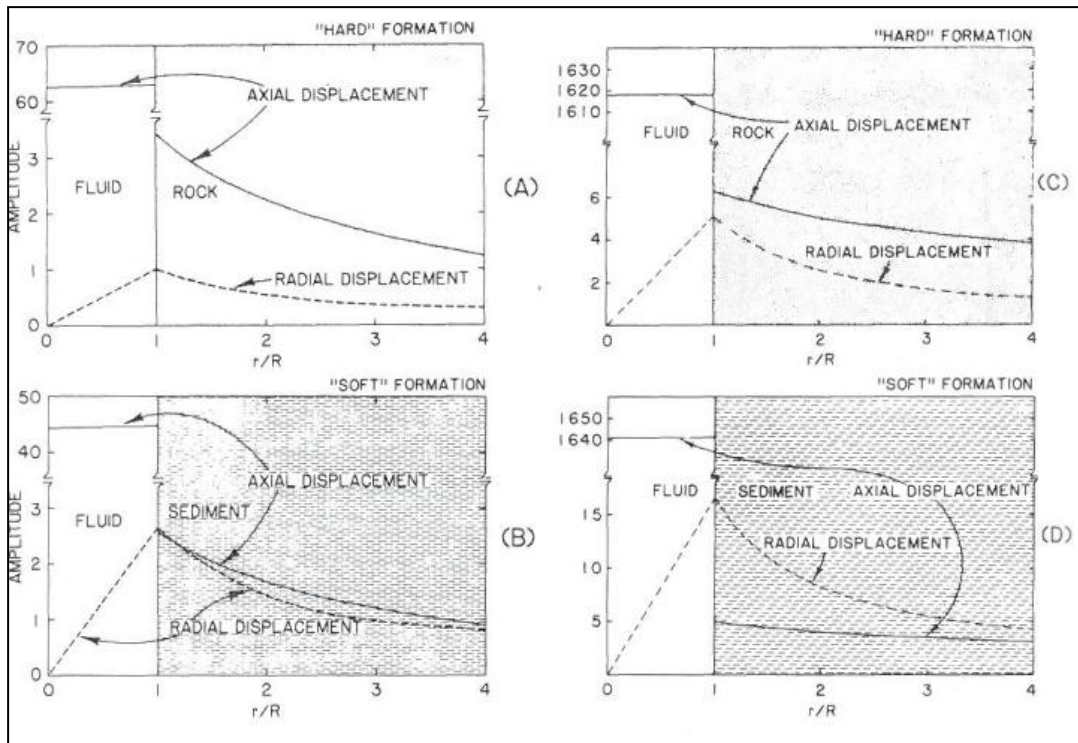
Figure 4-5. Axial and radial particle displacements created by VSP tube-waves for boreholes penetrating a hard formation and a soft sediment. R is the borehole radius. Only one frequency is analysed in each plot. These are a) 409 Hz, b) 427 Hz, c) 82 Hz and d) 74 Hz. From Cheng and Töksoz (1982).

Tube-waves are generated as seismic body waves pass the borehole and interact with impedances contrasts in the borehole environment, such as, Rayleigh waves (ground roll) crossing the top of the water column. They are the most prominent form of noise in a VSP survey as they are repeatable for every shot (Hardage, 1981). Impedance contrast can be from changes in borehole diameter, such as, washouts, casing termination and changes in drill bit size, or they can be from lithological changes in the shear modulus and porosity of the rock. Another source of tube-waves is at fractures where an incident compressional wave compresses the fracture and induces or "squirts" water into the borehole.
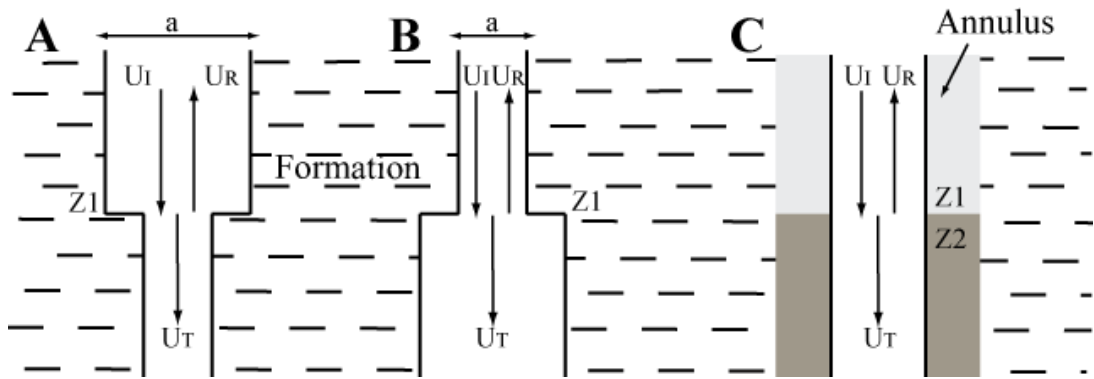
Figure 4-6. Examples of borehole impedance changes that cause tube-waves. A and B are due to changes in borehole diameter and C is due to the change in the shear modulus of the borehole. Modified from Hardage (2000).

4.5.1 Tube-wave identification

Much of the shot records in a hard rock VSP are heavily contaminated with tube-wave noise. Tube-waves are always coherent linear noise even in deviated boreholes. Linearity is due to the tube-wave and receivers coexisting along the borehole path. Linearity also infers constant velocity. In hard rock, tube-wave velocity may change by only a few per cent (Section 4.5.2). This can be more in sedimentary environments where there are larger changes in shear modulus and porosity.

By tracing each tube-wave event back to either the surface or direct arrival in the record we can determine its origin. The most common tube-wave types are, the primary down-going Rayleigh generated (down-going), casing converted (down-going), direct arrival bottom reflected (up-going) and induced from impedance contrasts in the borehole annulus (up- and down-going). These are displayed on a hard rock VSP profile in Figure 4-7. Induced tube-waves are the most damaging. They propagate up and down within the record and mask much of the record. Their occurrence is unpredictable prior to surveying unless information such as FWS, density, calliper and televiewer data is available.
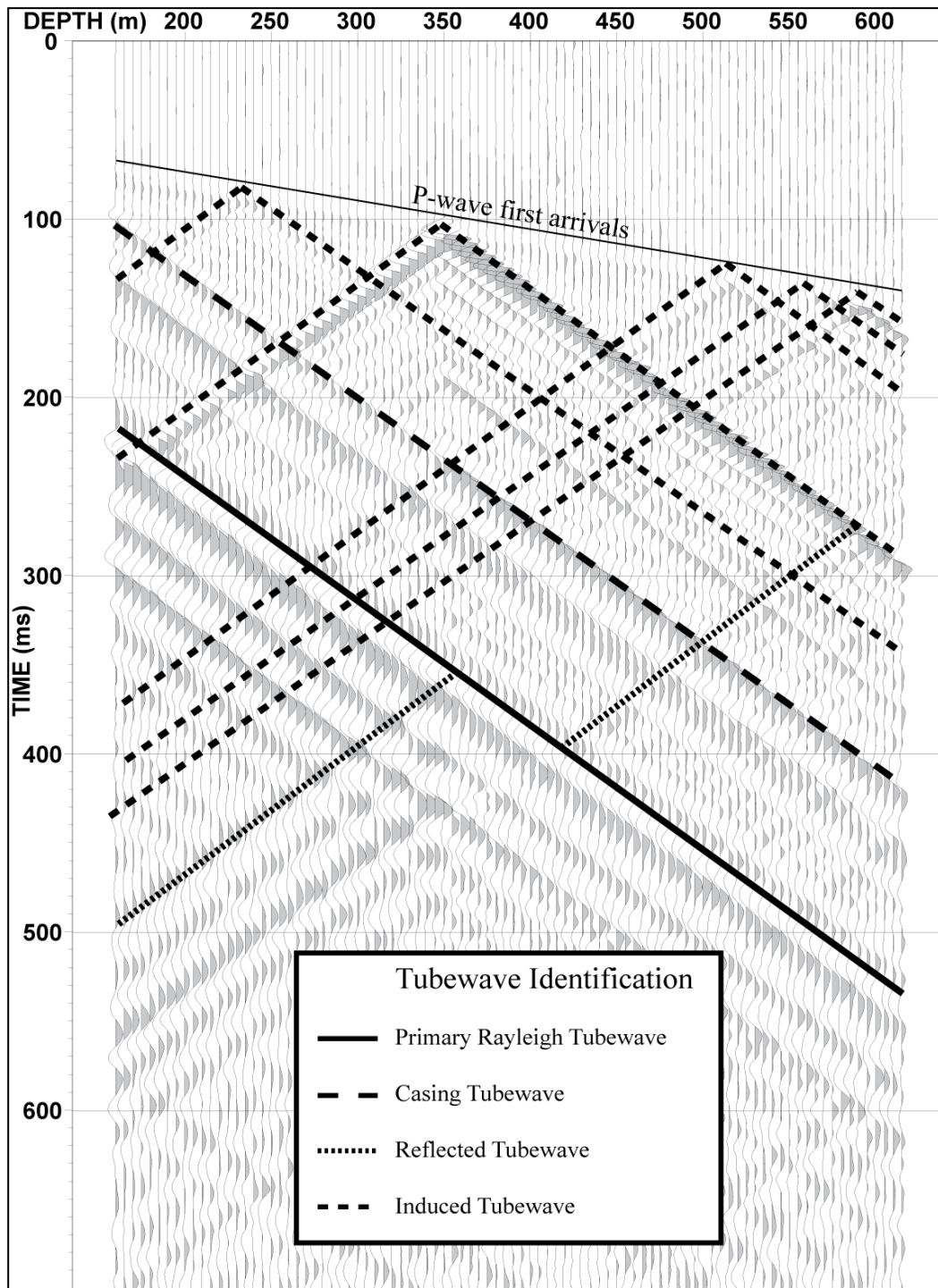
Figure 4-7. Identification of tube-waves in a hard rock borehole. Induced tube-waves from large acoustic impedances within the borehole wall cause up- and down-going tube-waves and occurs in multiple locations along the borehole. Data collected in Leinster 2009.

As illustrated by Figures 4-1, 4-3 and 4-7 achieving suppression and or removal of tube-waves in hard rock borehole hydrophone VSP acquisition would be enormously

beneficial. Unfortunately the frequencies of tube-waves overlap that of the seismic signals (50 to 160 Hz) and the amplitudes are an order greater than seismic direct arrivals and many orders of magnitude larger than reflection events. Moreover, a typical VSP geometry assumes 10 m receiver spacing or greater, at which distance tube-waves are severely aliased and cannot be effectively attenuated or removed by any known mathematical operation. Hence reducing tube-wave noise at the acquisition stage may be more effective.

4.5.2 Velocity of tube-waves

Several derivations for the calculation of tube-wave velocities exist (Biot, 1952; White, 1953; Norris, 1990; Tang, 2003). Most are variations of Biot (1952). The representation from White (1965) is shown below,

Tube-wave velocity V_{to} in an open borehole;

$$V_{to} = V_f \left[\sqrt{\frac{\mu}{(\mu + K_f)}} \right] \qquad \textbf{Equation 4-1}$$

And tube-wave velocity V_{tc} in a cased borehole;

$$V_{tc} = V_f \left[\frac{1}{\sqrt{1 + \frac{K_f D}{Ed}}} \right] \qquad \textbf{Equation 4-2}$$

Where; V_f = Fluid velocity   (1.47 km/s for pure water
                                                        (Hallenburg, 1984))

   μ = Shear modulus of rock   (approximately 33 GPa
                                                        (Schmitt et al., 2003))

   K_f = Bulk modulus of fluid   (2.2 GPa for water)

   ρ_f = Fluid density   (1000 kg/m^2 for water)

   D = Diameter of the borehole (typically 76 or 100 mm)

   E = Young's modulus of casing   (200 GPa Wikipedia)

   d = Thickness of casing   (6-7 mm measured)

Two important observations can be made here;

- Tube-wave velocity can never be faster than the fluid velocity as the product of the bracketed parts can never be greater than 1.

- In hard rock environments, the shear modulus is large compared to the incompressibility of the fluid. As such, the tube-wave velocity is approximately 97% that of the fluid velocity (1460-1480 m/s). Similarly in steel cased boreholes the young's modulus of steel is 2 orders larger than the compressibility of water and the tube-wave speed is less than 1% that of the fluid velocity.

Observed V_{to} within this research has been 1460 – 1520 m/s usually ~1480 m/s for uncased clean wells.

4.6 Tube-wave baffling experiments

Standard techniques to suppress the Rayleigh generated tube-wave include distancing the shot from the borehole (WVSP and OVSP only), reducing the fluid level in the borehole, trenching between the shot point and the borehole, or similarly placing the shot point on the opposing side of the drilling mud pits. Reducing this wave is important as it typically has the largest amplitude, has a long wave train, is broadband and reflects off impedance boundaries in the borehole. However, in terrestrial and particularly hard rock VSP this is rarely achieved until very large offsets.

Unconventionally a few experiments have been conducted along with several patents in the attempts to baffle the Rayleigh generated tube-wave (Pham et al., 1993; Milligan, et al., 1997; Daley et al., 2003). Milligan et al 1997 successfully used closed cell foam baffles between 0.5 m spaced hydrophone elements, in his shallow unconsolidated sedimentary experiment. However, this approach is flawed as the cells collapse under pressure and the baffles are only useful to a depth of 50 m (Milligan, et al., 1997). Daley and Pham both reflected the Rayleigh generated tube-waves by acoustic impedance mismatching. Daley inserted an inflatable bladder above the sensors and Pham inserted a syntactic solid foam composed of 17.6% (by

weight) hollow glass micro bubbles. These experiments were based on the principle of the baffle providing an acoustic impedance contrast to reflect or absorb the energy of the Rayleigh tube-wave.

Inflatable bladders are logistically difficult to implement, they require high pressure compressors at the surface and an air hose to be deployed in the borehole. This is impractical for small diameter boreholes used in mineral exploration and an added cost to the survey. Syntactic foam is rigid and increases the weight on the cable. For a baffle design to be successful and adopted by the mineral community it needs to be light weight, flexible, inexpensive and easily deployable. As such, I trialled a similar experiment to that of Milligan in a hard rock borehole, but with open cell acoustic foam. Open cells should not collapse under confining pressure. Foam baffles of 1 m length were placed in between receivers 24-23, 20-19, 16-15, 12-11, 8-7, 4-3 and above receiver 1. Comparison shots were taken before and after baffling at two different depth intervals. The results are shown below in Figure 4-8. The top depth interval is 40 to 270 m and the lower section is 270 to 400 m.
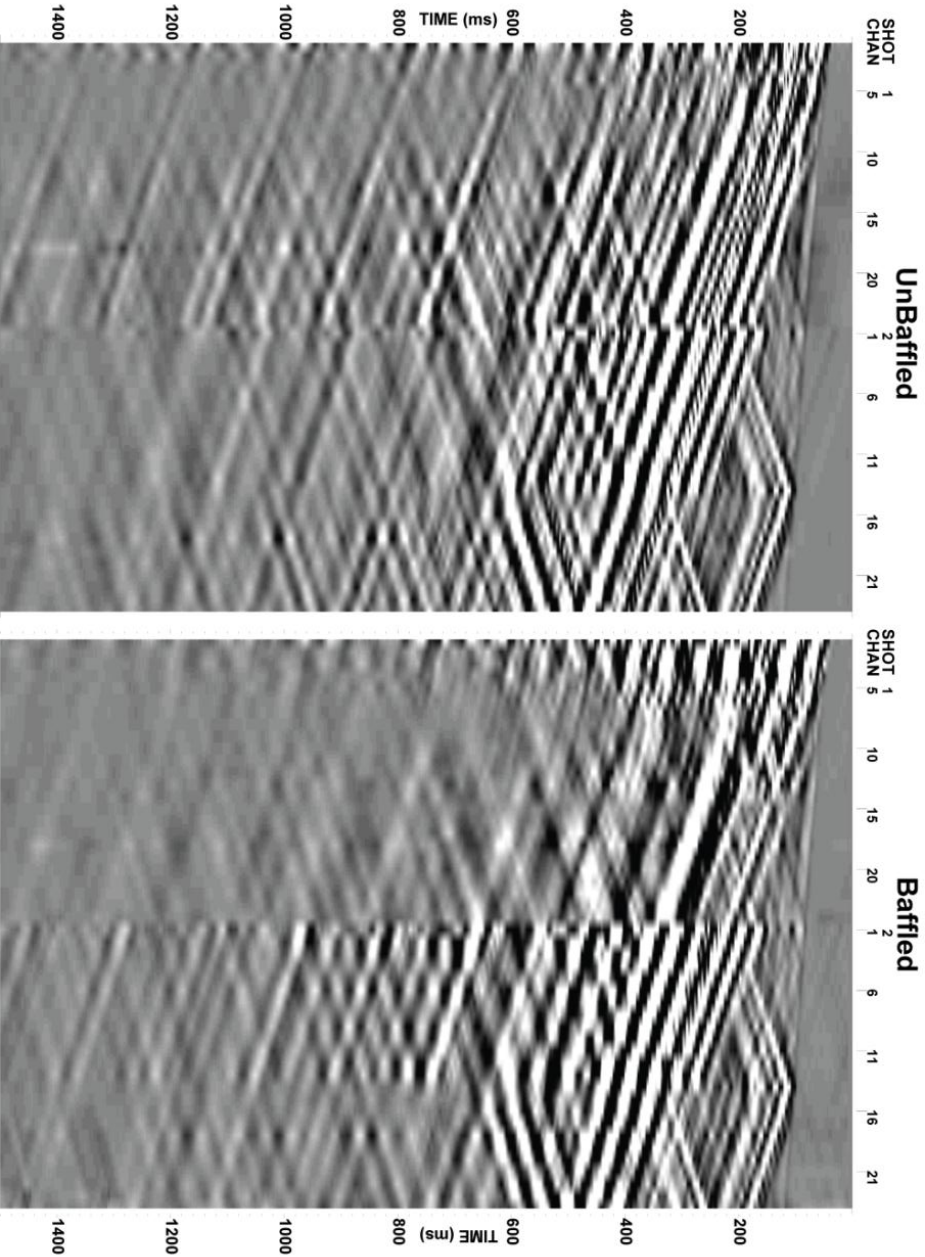
Figure 4-8. Hard rock hydrophone VSP tube-wave baffling experiment using open cell foam. Panel A) left is un baffled and panel B) baffled data. 1 m open cell acoustic foam was placed in between every 4th hydrophone element pair (24-23, 20-19, 16-15, 12-11, 8-7, 4-3 and above 1). There is no apparent suppression of tube-waves. Depth is from 40 to 400m, stations every 10 m baffles every 40 m.

The experiment was unsuccessful in the suppression of tube-waves and inconclusive if any improvement was evident. The only two observations which could be made are, the baffles helped suppress cable-waves and at greater depths the down-going tube-waves above the string needs to be baffled correctly, or else, an imbalance in tube-wave amplitudes would occur between string moves i.e. if the top section of the borehole is surveyed with baffles in place and then the string moved down 230 m (for a 24 channel 10 m spaced string), there exists 230 m of free water above the string in which tube-waves can manifest. These need to be dealt with fully in order to merge the data together.

Failure of the experiment was assumed due to insufficient acoustic dampening properties of the foam, insufficient baffling (length, radius and spatial density) and the possibility of tube-wave healing occurring between baffles. A second test was attempted this time with only the top 4 hydrophone elements baffled either side by 1 m baffles. The diameter of the baffles was adjusted so the borehole was filled. This test was disastrous with the baffles bunching in the hole and acting as a piston. No data were collected.

It was observed that tube-waves dissipate quickly within screened sections of water wells. This is assumed due to the combination of the interfacial wave being dispersed (diffracted) by the screen lattice and dissipation of energy into the compliant gravel annulus. Consequently the axial component of the tube-wave is reduced. The thought of creating an energy dissipating/absorbing baffle that used scattering interference was entertained. Subsequent designs included baffling with two main designs;

     1) Slotted PVC cylinder filled with gravels (never tested).

     2) Corrugated hosing which interferes with axial particle displacement.

The idea for the corrugated baffle design came about one day as I was watching my washing machine discharging its contents on the dry Perth sandy soil. I observed the flow from the 10 m extension hose was slower than that when discharging directly into the sink. Thus, the corrugated nature of the hose disrupts laminar flow and slows water propagation.

To test the corrugated baffle idea a 2 m x 40 mm diameter PVC test rig was created as shown in Figure 4-9. Tube-waves were successfully generated with the

experimental setup and a very slow tube-wave velocity of 370 m/s was measured with an in-house hydrophone. This velocity is in agreement with Equation 4.2 and Henriet et al. (1983) for 40 mm PN9 PVC casing. Baffles 60 mm long were cut then from 28 mm diameter corrugated water hose and placed above and below the hydrophone. The results of the corrugated baffle test are shown in Figure 4-10. Panel A) shows the un-baffled baseline data and panel B) shows successful suppression of the Rayleigh generated tube-wave and the induced tube-wave generated at the air water interface. Air-wave noise was present in the data as the borehole casing was coupled to the air.
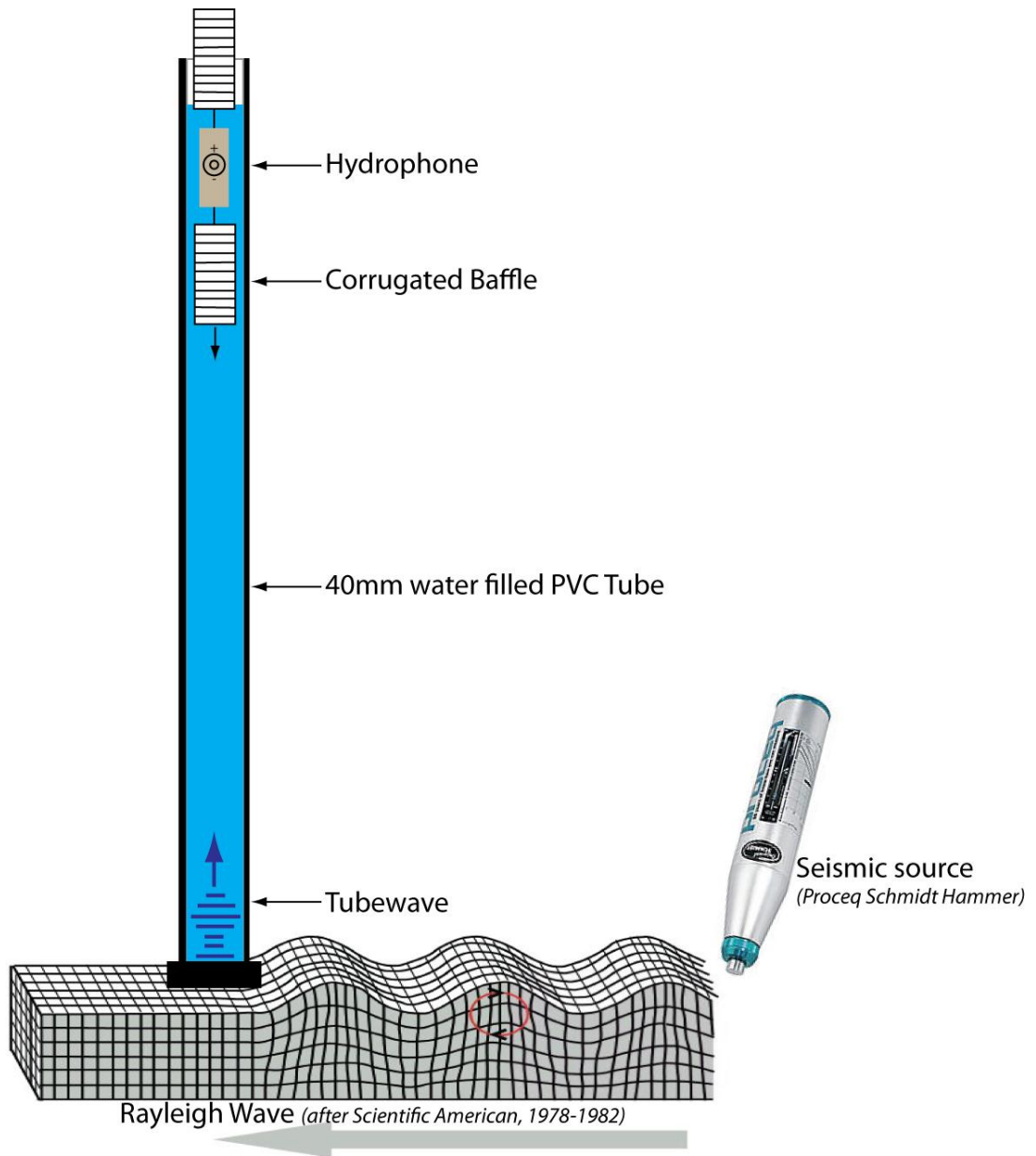
Figure 4-9. Schematic of tube-wave test rig constructed at Curtin University.
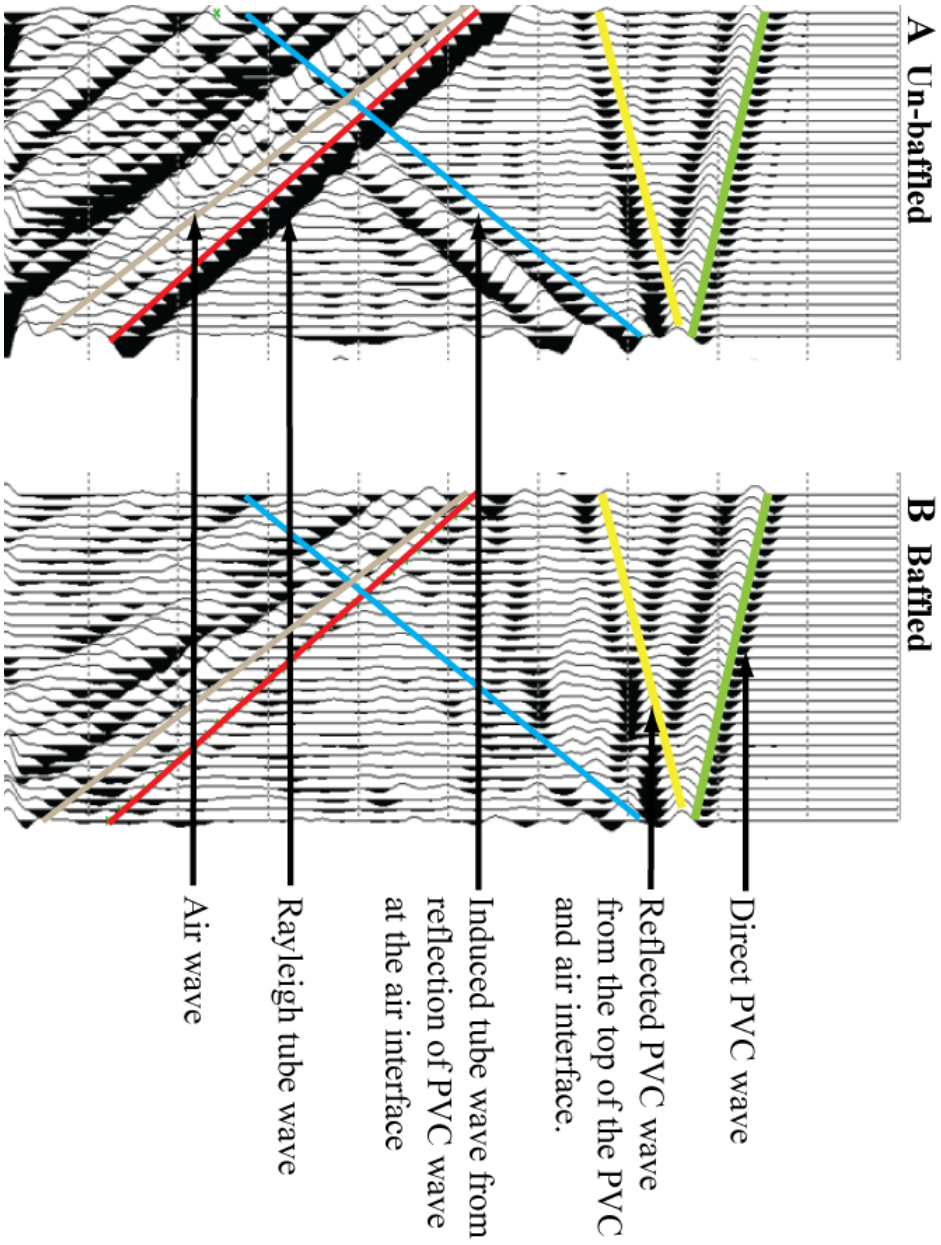
Figure 4-10. Baffling experiment with a tube-wave test rig constructed at Curtin University. Panel A) shows un-baffled data and panel B) successful suppression of the primary and reflected tube-waves. The red line in the right panel indicates peak amplitude times for the un-baffled primary tube-wave.

Air wave

Rayleigh tube wave

Induced tube wave from reflection of PVC wave at the air interface

Reflected PVC wave from the top of the PVC and air interface.

Direct PVC wave

The test rig results justified a field trial in a real borehole setting. Two diameters of corrugated pipe were purchased for testing, 50 and 100 mm, in a PQ (123 mm diameter) borehole. Agricultural drainage pipe was fit for the purpose due to its semi rigid yet flexible corrugated design and ability to drain water readily. The test borehole, BH1, is located on BHP's Marthas Vineyard lease in Kambalda, Western Australia. BH1 is the primary research borehole of the following chapters. Geology and information pertaining to BH1 can be found in Chapter 6.

To eliminate un-predictable induced tube-waves that are generated at fracture zones the baffles need to be installed in-between the hydrophone elements. It was decided to baffle half of the hydrophone string (12 channels = 120 m of baffles) for the trials. To minimise risk and potential loses down-hole the smaller diameter 50 mm corrugated pipe was selected. To secure the baffles to the hydrophone string and reduce the likelihood of snagging in the borehole, conical sections with slotted discs for retro fitting were machined from solid plastic as shown in Figure 4-11. The baffles were installed in-between the bottom 12 channels in the field using battery drills and hand tools and shown in Figure 4-12.
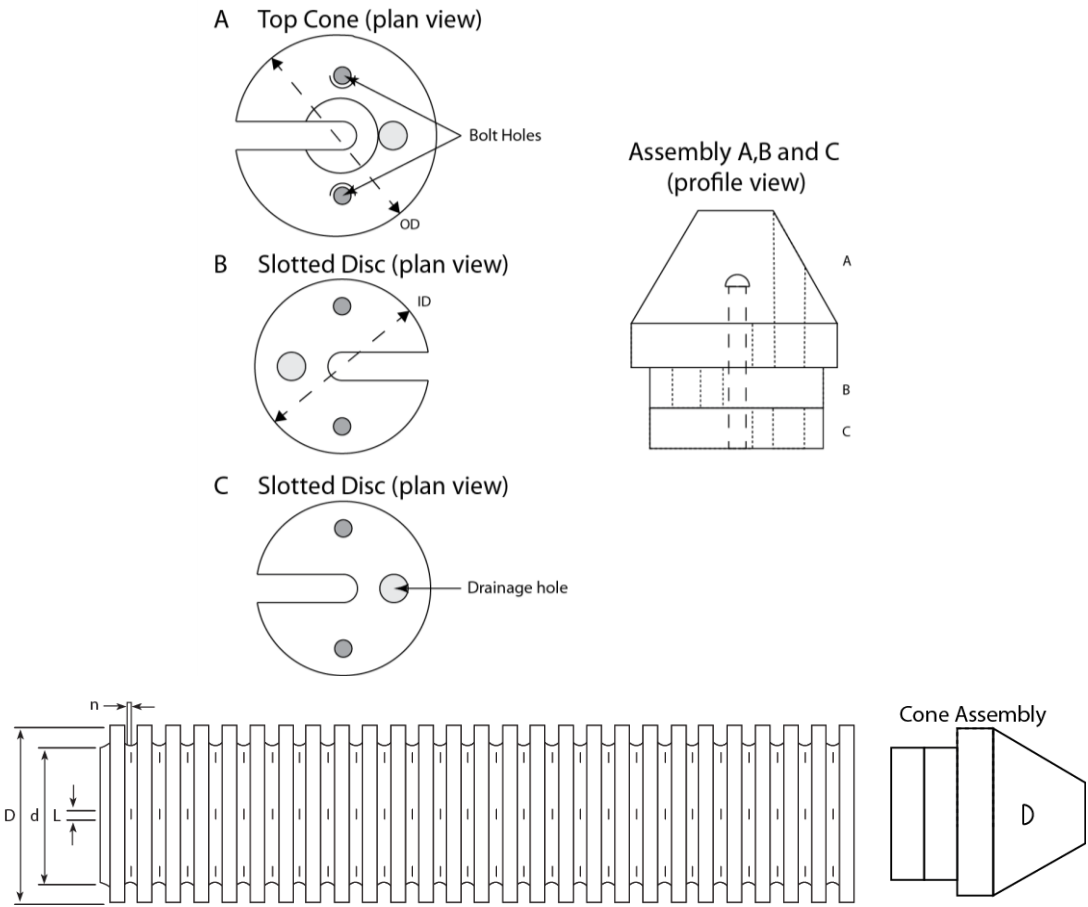
Borehole size (mm)	Baffle outside diameter D (mm)	Baffle inside diameter d (mm)	Baffle to borehole cross-section area ratio	SLOT SIZE n x L (mm)	WEIGHT (Kg/m)
BQ – 60	50	44	0.16	1.25 x 4	0.175
NQ – 76	65	55	0.21	1.25 x 5	0.23
HQ – 96	80	68	0.19	1.25 x 5	0.35
PQ – 123	100	86	0.17	1.25 x 7.4	0.475

Figure 4-11. Schematic of the corrugated baffle cone and slotted disc assembly and table of baffle sizes for BQ to PQ sized boreholes.

Figure 4-12. 50 mm corrugated baffles installed on the lower 12 channels of the hydrophone string.

The 100 mm Ag pipe was deemed too risky to send to depth because of a known borehole transition at the base of the borehole collar which extended to a depth of 33 m. The use of this baffle was restricted such that the top of the baffle remained within the borehole collar.

The experiment was conducted in four steps as illustrated in Figure 4-13. Firstly a baseline data set was acquired with no baffling in the borehole, then a 20 m section of 100 mm Ag pipe was tested followed by a continuous 50 mm baffle installed over 120 m of the hydrophone string. Finally a combination of the two baffles together was tested. Deployment of the baffles is shown in Figure 4-14. The water table depth was estimated in the field at 25 m.
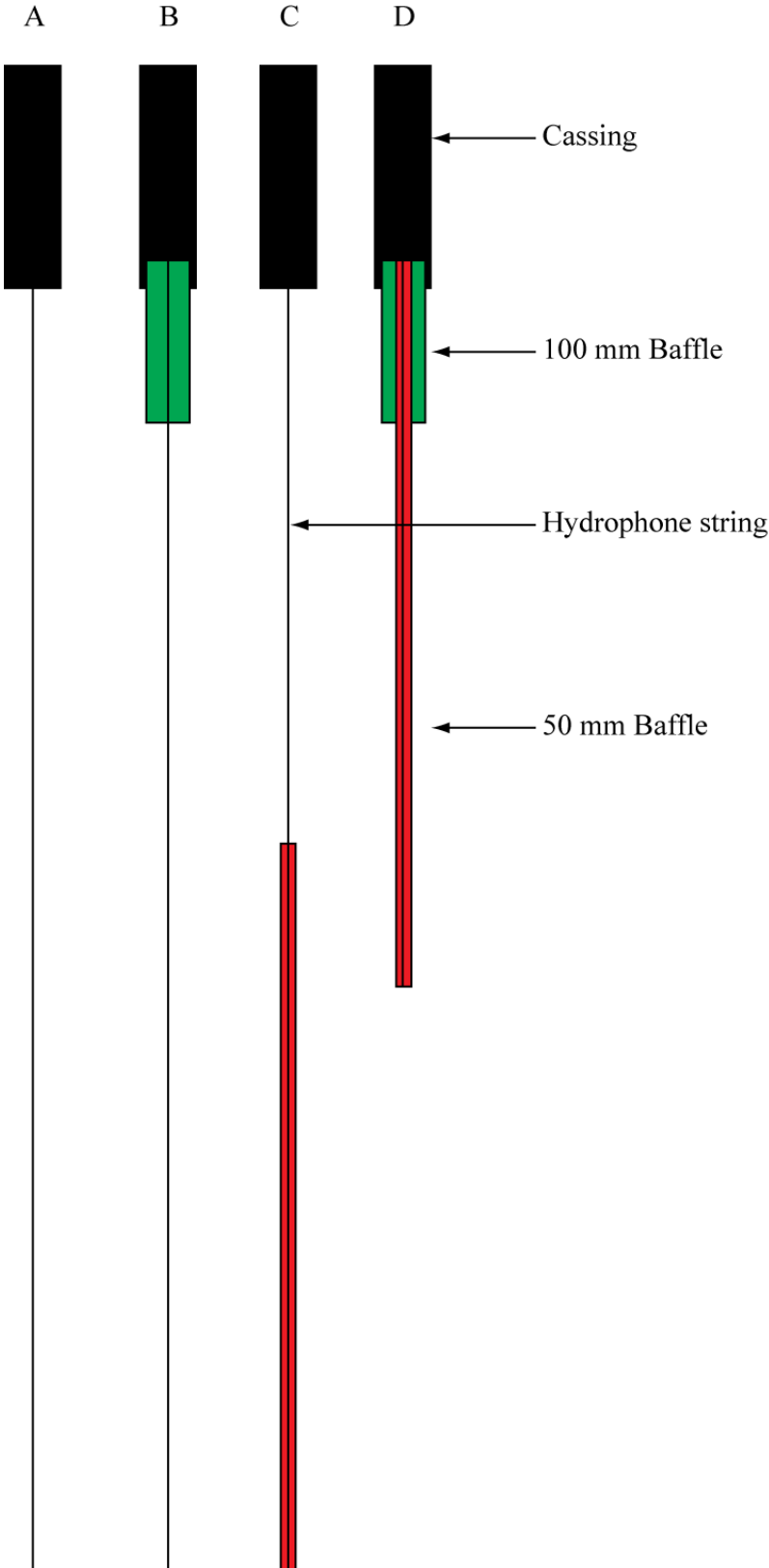
Figure 4-13. Schematic of tube-wave baffle experimentation set up with A) no baffles (baseline), B) 100 mm baffle installed between 30 to 50 m, C) 50 mm baffle installed on channels 13-24 with channel 1 deployed at 20 m, and D) a combination of 100 and 50 mm baffles deployed to a depth of 30 m.

Figure 4-14. Top frame - Installation of 100 mm Ag pipe baffle. Bottom left frame – 100 mm baffle suspended at the top of collar while 50 mm baffle is being threaded through the 100 mm baffle. Bottom right frame – 50 mm baffle (with hydrophone in foreground) being deployed over the sheave wheel.

4.6.1 Corrugated baffle field results

Data were collected with a 10 m spaced 24 channel hydrophone string. Unfortunately after testing, 3 channels were found to be intermittently inactive. The data were collected with 5 m infill stations. As such, 2 dead channels normally

appear together in the profiles. Field results are shown in Figures 4-15 and 4-16 and are discussed below.

Baseline data (Figure 4-15a).

The baseline data show a weak primary down-going (P_d) direct wave, multiple down-going tube-wave (T_d) events (casing, Rayleigh and Rayleigh multiple tube-waves). There is also a cable-wave response which saturates the upper 10 to 15 channels (130 to 180 m). Fracture induced tube-waves occur at 180 m. These are weaker than the primary tube-waves.

50 mm baffles 130 to 250 m (channels 13-24, Figure 4-15b)

The inclusion of the 50 mm baffle has increased SNR, background noise is reduced and the induced tube-waves are now more apparent. Cable-wave noise is more pronounced and has had a shift to higher frequency due to the extra weight of the baffles tensioning the cable. This data is aliased and appears to have up- and down-going cable waves. Tube-waves do not appear to have been suppressed.

To isolate the hydrophone cable from the sheave wheel and any associated noises such as wind and tripod movement, the cable was clamped off at the collar and suspended on a damper (Section 4-4). However, cable-waves were transmitted onto the cable via surface waves vibrating the borehole collar. Additional foam was then used to isolate the damper from the collar and new baseline data collected (Figure 4-16a).

50 mm baffles with increased isolation from collar (Figure 4-15c)

Addition of the extra foam to isolate the sandwich board from the collar suppressed the high frequency cable-wave and this no longer appears aliased. However, it was not sufficient to suppress the primary down going cable-wave. The overall result of increased cable isolation has been to attenuate cable related waves which in turn will help wavefield separation during processing.
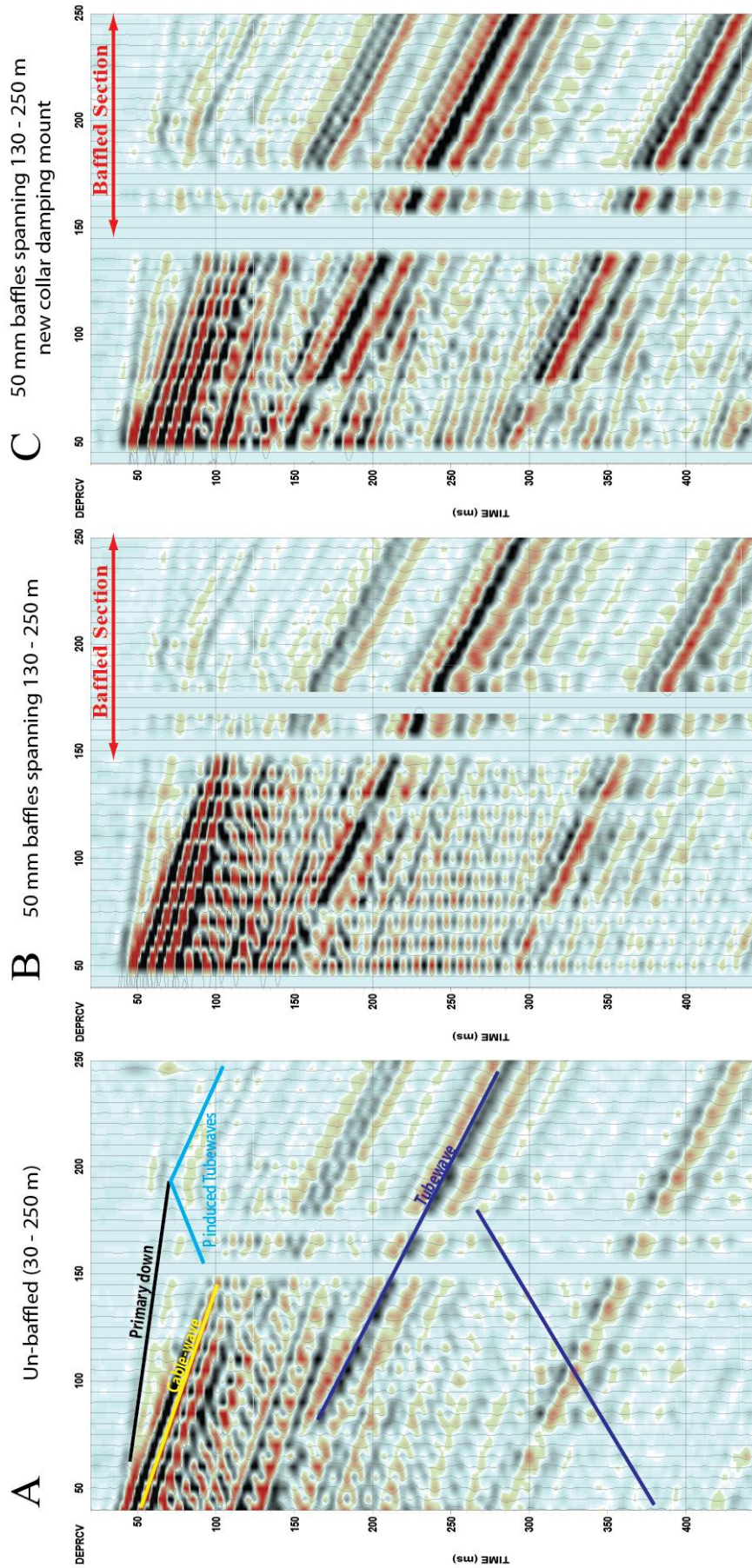
Figure 4-15. 50 mm corrugated baffle results: A) Base line data 30 to 250 m 24 channel hydrophone with no baffles. **B)** Data after the addition of baffles from 140 to 250 m. The data is cleaner and amplitudes more balanced, however tube-waves have not been suppressed, the cable-wave is more prominent and higher in frequency. **C)** Additional dampening of the hydrophone string from the collar applied. This has reduced but not eliminated the effects of cable-waves.
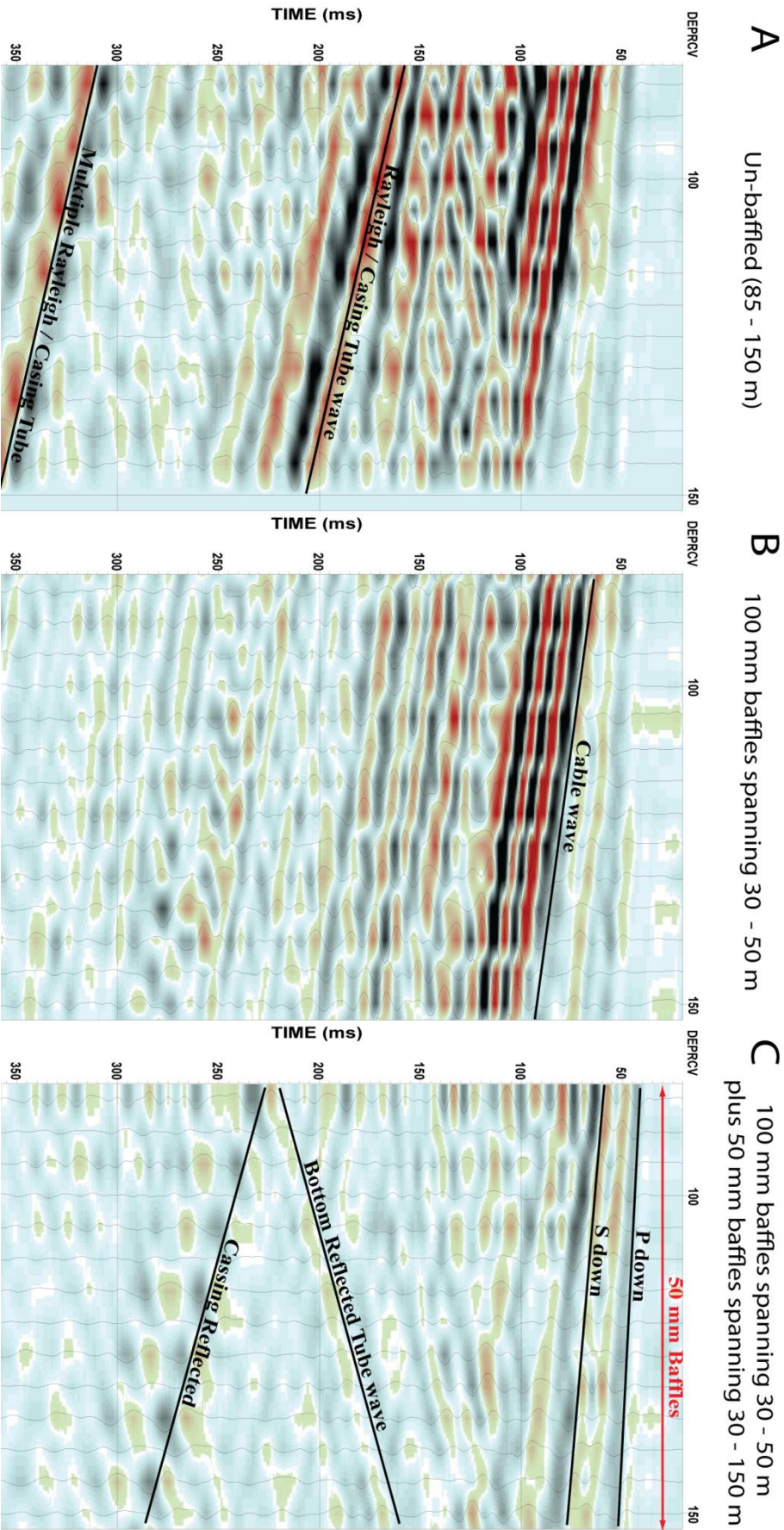
Figure 4-16. 100 mm corrugated baffle results: A) Baseline data after secondary cable-wave dampening. B) Suppression of the Rayleigh tube-wave after installation of the 100 mm top baffle. C) Suppression of cable and tube-waves after combination of 100 and 50 mm corrugated baffles (100 mm baffle from 30 to 50 m)

This section clearly shows suppression of the Rayleigh tube-wave and its multiples. Cable-wave data is still very dominant despite the increased isolation at the collar, and this masks any up going reflected wavefields. There is evidence of up-going tube-waves at late times.

100 mm baffles at 30 to 50 m and 50 mm baffles at 30 to 150 m with increased isolation from collar (Figure 4-16c)

This section shows a further improvement with the suppression of the cable-wave. There is still some cable-wave present but at amplitudes comparable to that of the P- and S-waves. Some up-going energy is now evident in the early times where P and S reflections would naturally occur given sufficient impedance contrasts of geological contacts.

Well defined up- and down-going tube-waves are present at later times. The up-going tube-wave has been generated by the down-going body wave traversing the bottom of the borehole. This tube-wave has not interacted with the 100 mm baffle as it comes from the bottom. The proceeding down-going tube-wave has been reflected from the bottom of the 100 mm baffle. Both these up and down going tube-waves have interacted with the 50 mm baffle. These are of comparable amplitudes to that of the other wavefields present.

4.6.2 Discussion

It was assumed that a corrugated baffle is going to be most effective when the surface area of the baffle is working on the same volume of water inside and outside the baffle such that;

$$A_{in} = A_{out}$$

$$r = \frac{R}{\sqrt{2}}$$

Where;   R – borehole radius, r –mean radius of the Baffle

As such it was expected that the 50 mm baffle would be less effective than the 100 mm baffle in the PQ borehole.   However, it was anticipated that the 50 mm

continuous baffle may have an effect in attenuating the tube wave due to the length of water column it works on. The association of distance that the baffle creates disruption and tube-wave suppression has not been established.

If the baffle inside and outside diameters are calculated with respect to the cross-sectional area of the PQ borehole, the 100 mm baffle fills 15% of the water column and has a periodicity of 80 corrugations / m. This is significant compared to the 50 mm baffle which occupies 3.2% cross-sectional area of the PQ borehole and has a periodicity of 170 corrugations / m. Thus there is a relationship between tube-wave suppression and the amount of cross-sectional area the baffle occupies.

Considering the tube-wave is an interfacial wave, if the baffle is in near contact with the borehole it will have the greatest suppression effect and restrict fluid particle motion within the borehole. The 100 mm baffle was successful in this and has a baffle to borehole circumference ratio of 81% compared to 41% for the 50 mm baffle.

4.7 Viscosifiers

Hardage (2000) reported higher fluid densities improve hydrophone coupling and Gal'perin (1983) reported that tube-waves dissipate more readily in higher viscosity drilling mud than in fresh water, as particle motion within a borehole is dependent on the density and the bulk modulus of the borehole fluid. However, no comprehensive studies on the effects of drilling fluid densities and viscosities with respect to VSP measurements have been reported. The effects of different viscosity borehole fluids were observed during hydrophone VSP surveys conducted in borehole BH2, Kambalda in 2010 (location can be found in Chapter 6).

Data were collected with a 24 channel hydrophone string and 800 kg weight drop hammer source. The hydrophone string was isolated from the drill rig and suspended on a foam damper at the collar. Two mobilisations were required to survey the borehole as there was a blockage at 550 m and the drill rig needed to be remobilised to clean the borehole. Cleaning and flushing of the borehole used a lower viscosity

drilling fluid. The earlier, higher viscosity drilling fluid had been used to help hold the borehole up. The resulting two data hydrophone ZVSP data sets collected over the upper section are shown in Figure 4.17. There is a distinct difference in SNR between the two surveys with an average first break amplitude increase of 7 dB in the "viscous mud" data. The higher viscosity drilling fluid has improved the "apparent coupling" of the hydrophone to the formation. It is also encouraging to note that very high quality converted shear waves were recorded during the high viscosity survey.
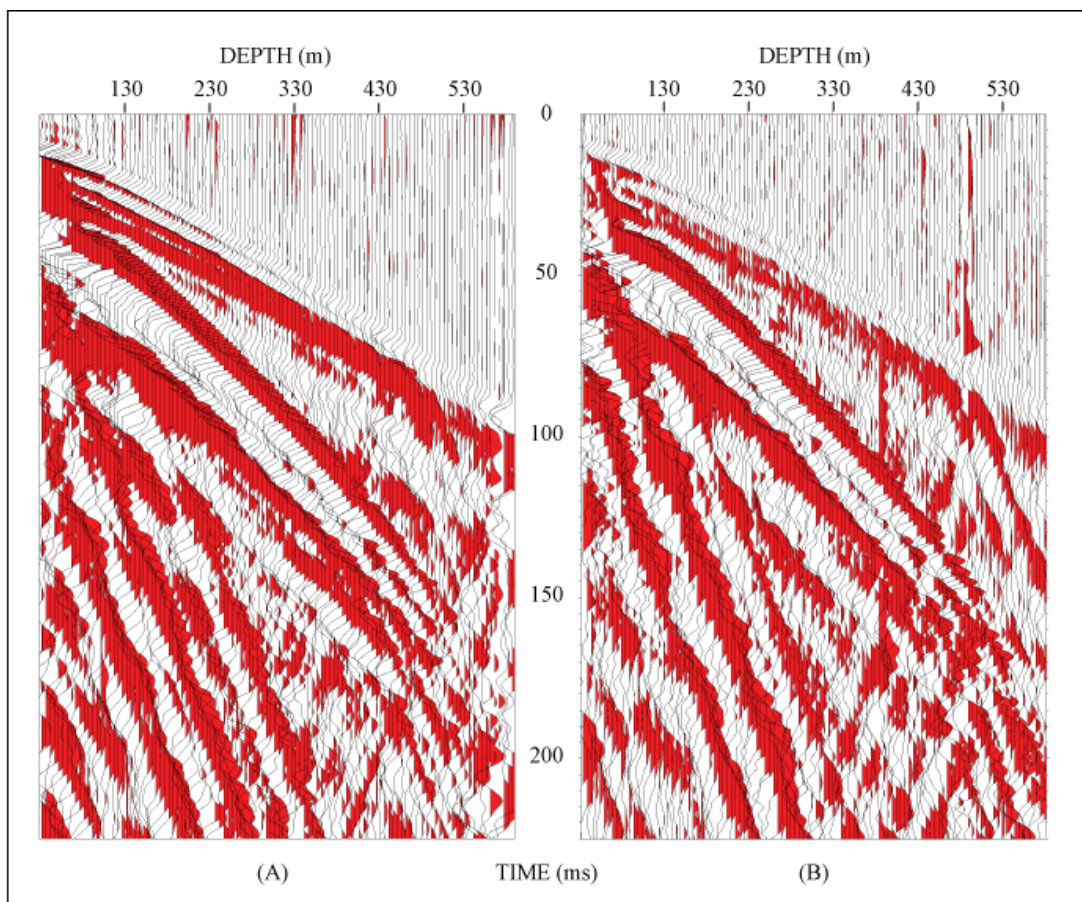
Figure 4-17. Shot gathers from the same portion (35 to 535 m) of BH2 before and after flushing the hole with different drilling systems. In panel A) a high viscosity drilling fluid was used to hold up the borehole. Panel B) was collected after flushing the hole with a lower viscosity drilling fluid.

The drilling fluid system used was as follows;

- Soda Ash 0.25-0.5 kg / 1000 ltrs (treat calcium hardness and pH)
- PAC-L 4-6 kg / 1000 ltrs (Fluid loss control agent)
- PAC-R 0.5-2.0 kg / 1000 ltrs (Viscosifier)
- FILTREX 25 ltrs / 1000 ltrs (Filtration control/inhibitor agent)

Flushing of the hole used the same system less the addition of FILTREX. All drilling products are from the Australian Mud Company. Technical data sheets can be found at their website (AMC, 2011).

FILTREX is a high molecular weight polymer emulsion that is added to water based drilling fluid to reduce the rate with which drilling fluid pressure invades the borehole wall during drilling. FILTREX does not yield any viscosity nor increase the specific gravity (SG) of the overall mud system used (Van Niekerk, 2011). Thus the only factor which could have contributed to the difference in hydrophone coupling between surveys is the quantity of PAC-R viscosifier used. AMC PAC-R is a polyanionic cellulosic polymer of high molecular weight and is an extremely effective viscosifier in fresh or salty water. After talking with the drillers, it was established that a higher concentration of PAC-R was used during drilling to help stabilize the borehole due to the presence of shear zones.

It is not possible to know the viscosity of the drilling fluids used during drilling or flushing the borehole without having been present to take mud samples. However, AMC kindly ran viscosity tests of PAC-R at different concentrations using a fluid SG comparable to that of a known borehole at Flying Fox nickel mine, within the Yilgarn, some 230 km south west of BH2. The results are provided below in Table 4.1.

Table 4-1. Viscosity of AMC PAC-R at different concentration levels (Van Niekerk, 2011).

PAC-R Viscosity at	1 kg per 1000 L	2 kg per 1000 L	3 kg per 1000 L	4 kg per 1000 L	5 kg per 1000 L
600 rpm (cPs)	6.5	15.5	27.0	41	61
300 rpm (cPs)	4.0	10.0	17.5	28	44
SG at 25 C	1.064	1.064	1.064	1.064	1.064

4.8 Tube-wave aliasing

The single most important process in VSP imaging is the effective separation of transmitted and reflected wavefields. Wavefield separation includes removal of all unwanted waves such as tube-waves. Successful wavefield separation requires correct spatial sampling during acquisition. Tube-wave frequencies overlap seismic frequencies and are the slowest wavefield experienced in hard rock VSP. If survey design is based on expected P and S velocities and receiver station spacing of 5 to 10 m the tube-wave will be aliased in hard rock data.

Aliasing of wavefields with respect to the spatial sampling interval is calculated from the following equation (Hinds, et al., 1996),

$$DSI = \frac{V_{min}}{2f_{max}}$$

Equation 4-3

where DSI - down-hole sample interval

V_{min} - V_t tube-wave velocity

f_{max} - highest tube-wave frequency

Plotting the sample interval with respect to frequency and using a tube-wave velocity of pure water 1500 m/s in Equation 4-3, shows that at 10, 5 and 3 m station spacing's, tube-waves will alias at approximately 75, 150 and 250 Hz respectively. This is shown in Figure 4.18 for tube-wave velocities of 1500, 1200 and 900 m/s for comparison.
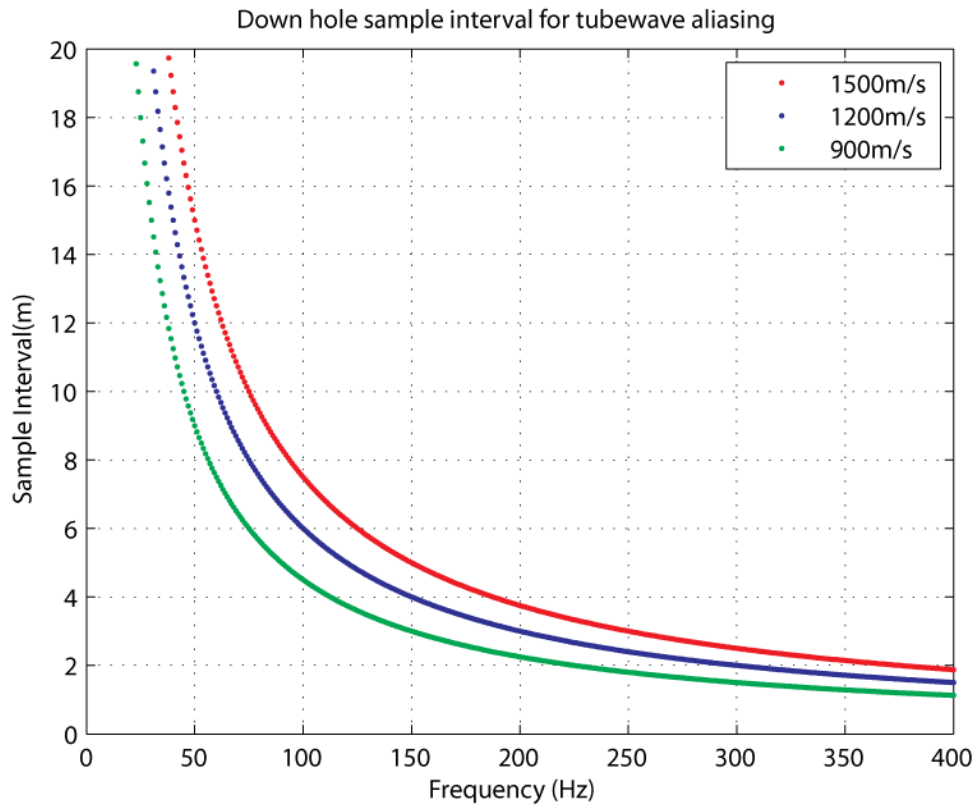
Figure 4-18. Theoretical downhole sampling interval at which tube-waves alias spatially with respect to frequency. Tube-wave velocities of 1500 m/s (approximate hard rock maximum), 1200 m/s and 900 m/s are shown.

To verify tube-wave frequencies exist in our data at our seismic frequencies we collected data in BH2 from 345 to 585 m (total 240 stations) at 1 m stations. The test was conducted under "viscous mud" conditions (section 4.7). The frequency – wavenumber (*f-k*) spectrum with the data disseminated down to 3, 5 and 10 m station spacing is shown as Figure 4.19. The *f-k* plot confirms tube-wave exist across all seismic frequencies and are aliased at 70 and 140 Hz in the 10 and 5 m data sets respectively, in agreement with Equation 4-3.
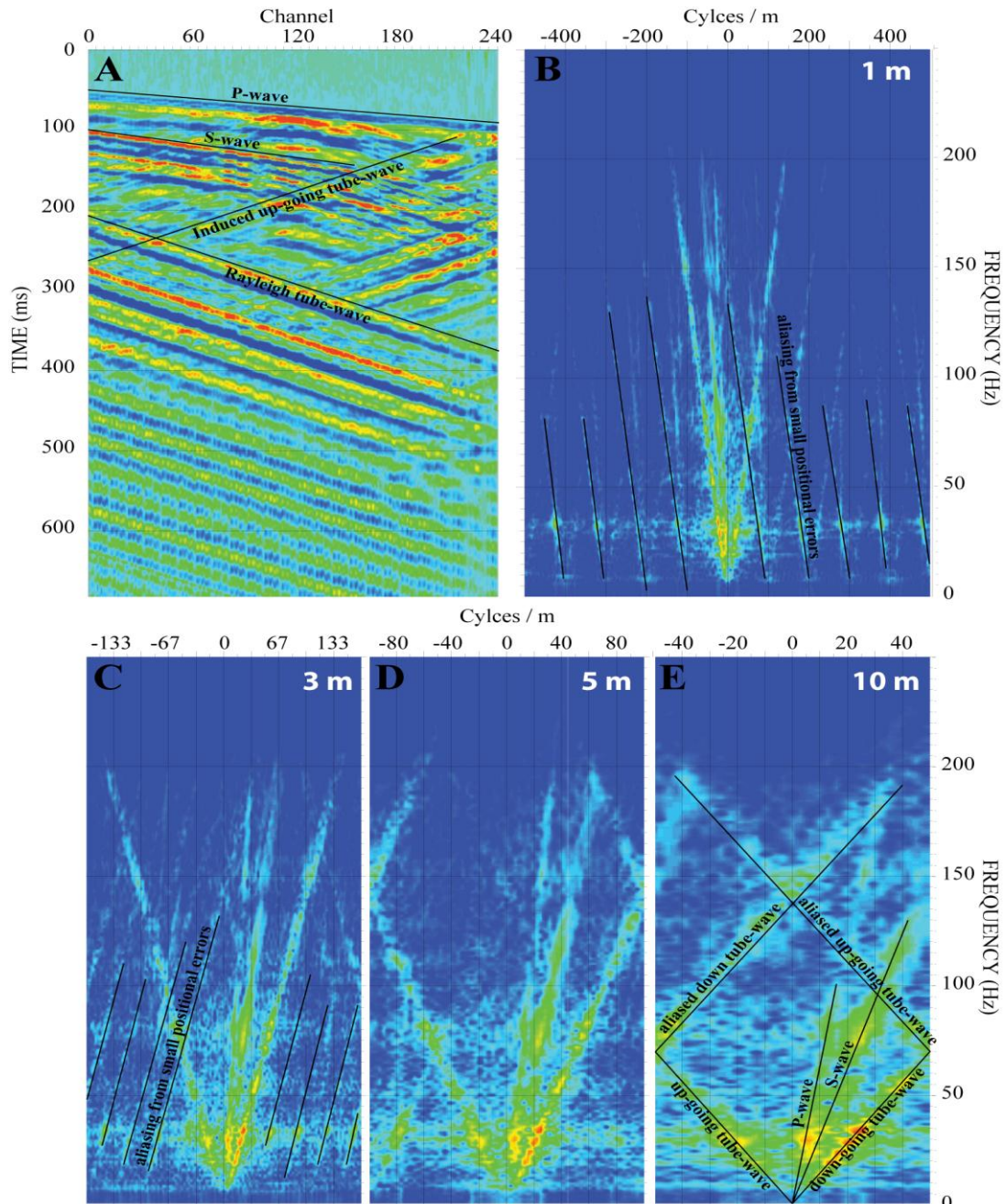
Figure 4-19. *f-k* **analysis of tube-wave spatial aliasing. The input data (panel A) was collected with a 24 channel 10 m spaced hydrophone string moved at 1 m station increments to obtain a 240 channel receiver gather for the borehole interval 335 m – 585 m. An 800 kg weight drop hammer was used as the source 75 m from the borehole. Panels B, C and D are the** *f-k* **spectrum of the input down sampled to 3, 5 and 10 m receiver station spacing.**

Figure 4.19 shows tube-wave energy is the most coherent event in the *f-k* spectrum. This is seen as a strong linear event in the -ve wavenumber quadrant and an equal and opposite event mirrored in the +ve quadrant. Down-going P- and S-wave events

are also visible in the +ve quadrant. Wrap-around of the tube-wave in the frequency domain occurs in the 5 and 10 m data at 140 and 70 Hz respectively. The wavenumber at which the aliased data wrapped is the Nyquist wavenumber (k_N) and is defined as half the spatial sampling distance (Sheriff, 2002);

$$k_N = \left(\frac{1}{2}\right)\frac{1}{DSI}$$

Equation 4-4

It can be noted here that aliasing in the wavenumber domain occurs in the 1, 3 and 5 m disseminated data. This is highlighted in panels B and C as events parallel to the tube-wave. This phenomena occurs due to positioning inconsistencies when infill sampling.

4.9 Conclusions

Hydrophones offer an inexpensive opportunity to conduct borehole seismology surveys where borehole diameters are limited. The ideal survey situation for borehole hydrophone seismology is;

1. Stable open hole that has been mudded with a high viscosity drilling fluid,
2. The recording cable is isolated from the sheave wheel,
3. Spatial sampling is sufficient to properly register tube-waves.
4. Tube-wave baffles are utilised.

As hydrophones are passively coupled to the formation through the borehole fluid the primary source of ambient noise is via the hydrophone cable. Isolating the hydrophone string from the sheave wheel and rig mast or tripod and suspending the cable from the collar with a damping device eliminates this significantly, improving SNR.

Higher viscosity fluids improve SNR by reducing the ambient noise and improving the "apparent coupling" of the hydrophone to the formation. Also with appropriate use of drilling fluids and borehole preparation, induced tube-waves from fracturing and washout zones can be partially negated. The full effects of different drilling

fluids is not known and is worthy of further investigation. The term "apparent coupling" has been used here as fluid viscosity affects particle motion of all wavefields in all directions. However, the axial component of the tube-wave is affected more than the radial component, as the radius of the borehole is much smaller than the axial extent. Thus, the fluid is doing more work 'suppressing' particle motion in the axial direction. In addition the radial distance that the viscous fluid does work on is equal for all wavefields that transmit radially from the borehole wall to the hydrophone.

Tube-waves are the dominant source of coherent noise in hard rock environments and they propagate up and down the hole for many oscillations. Corrugated baffle concepts tested show extremely encouraging results to completely suppress tube-waves during acquisition. The corrugation of the pipe disrupts laminar flow and tube-wave propagation. The most effective suppression of unwanted wavefields was observed for a co-centric baffle arrangement where a 50 mm baffle was placed inside the 100 mm baffle. This arrangement suppressed the Rayleigh tube-wave and eliminated high amplitude cable-waves simultaneously. Inter-hydrophone baffles are required to negate fracture induced tube-waves. Further tests are required to ascertain the optimum baffle diameter for different borehole diameters. Tests should include different corrugation dimensions (inner and outer diameters) and periodicity.

With the correct spatial sampling and high SNR it is possible to remove tube-waves with application of multichannel filters and deconvolution. However, to eliminate processing artefacts from amplitude imbalances, hydrophone strings should be specifically designed to correctly spatial sample the tube-wave without requiring infill stations.

5 Comparison of Hydrophone and 3C Geophone VSP

5.1 Introduction

In order to substantiate hydrophone VSP imaging it is necessary to evaluate the techniques ability to discriminate and separate out different wavefields. To achieve this, hydrophone VSP data need to be evaluated against an industry standardised technique such as 3C geophone VSP. Consequently I acquired hydrophone and 3C geophone VSP's consecutively in borehole BH1. This borehole is located within a 28 km^2 3D seismic survey in Kambalda, Western Australia. Geology of the Kambalda area and borehole logs of BH1 are given in Chapter 6 where the VSP results are used for time to depth calibration of the 3D seismic cube, and the up-going wavefield profiles, VSP-CDP and migrated images are analysed in relation to the origin of reflections and the results are used to characterise seismically the lithology.

Both data sets were acquired using equivalent acquisition geometry of 5 m station spacing from 100 to 1000 m depth. A near offset shot point of 28 m and an 800 kg weight drop hammer source was used. The 3C data were collected with two 5 m spaced AMC-VSP-3-48M shuttles supplied and operated by ASTO Geophysical Pty Ltd. A reference geophone was placed near the borehole collar to correct trigger timing variances. The hydrophone data were collected using a 24 channel string manufactured by V-Cable and a 24 channel DAQ-Link III seismograph. A reference geophone was not possible with the hydrophone configuration.

Borehole BH1 is deviated between 5 to 11 degrees, with an approximate 85 degree dip (from horizontal) at the collar to the South. The geometry of the survey is graphically displayed below in Figure 5-1. As BH1 is not vertical and borehole tools inherently precess (rotate) within the hole, the 3C data required rotational corrections to maximise the P- and S-wave energies to the vertical and horizontal planes. Comparisons have been made between data sets, after 3C rotational corrections, after removal of tube-wave energy from the hydrophone data and after the removal of down-going wavefields. These results are discussed in turn in the following sections.
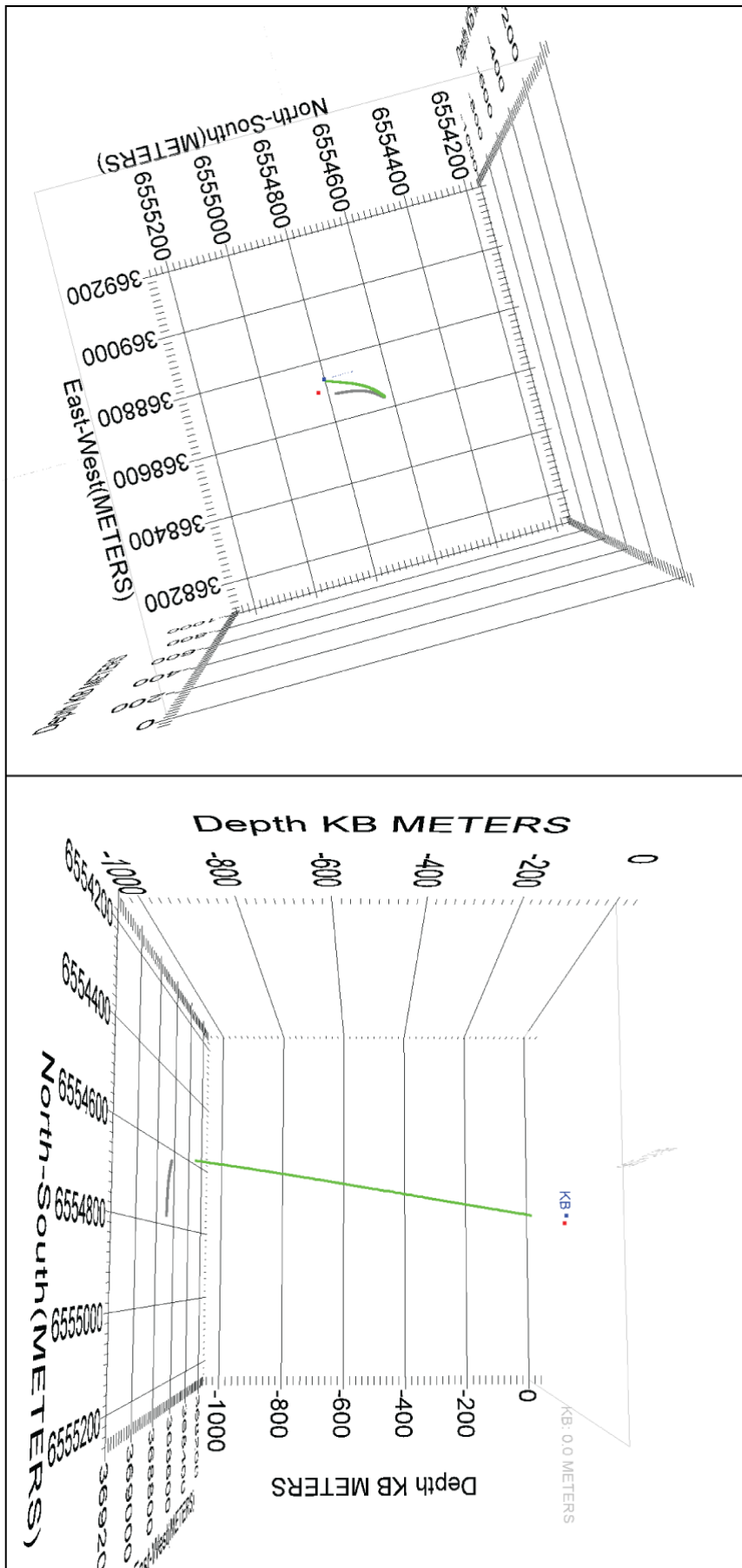
Figure 5-1. Geometry of BH1. ZVSP source is indicated by the red square, green line represents 5 m geophone stations and the grey shadow line is the borehole deviation in the horizontal direction.

5.2 3C data and component rotation

The orthogonal orientation of 3C geophone components, the acquisition geometry of ZVSP and the disparity of P- and S-wavefield particle motion means that 3C geophone tools record mostly P- on the vertical and S-wavefields on the horizontal components. The magnitude of the recorded P- and S-waves is dependent on the degree of deviation of the geophone axis from the source receiver plane. To correct the 3C geophone X, Y and Z data, rotation corrections must be applied to maximise P- and S-waves onto the P, R and T orientations respectively (Figure 2-11).

The 3C data were of good quality with the P component having strong coherent first arrivals. Nonetheless, the data were pre-conditioned to smooth the first breaks prior to first break picking and determination of the rotation angles. Pre-conditioning used a rectangular *f-k* reject polygon shown in Figure 5-2 which was bounded by 0 to 200 Hz and -60 to 60 cycles/km to remove any high frequency noise. Transformation and filtering in the *f-k* domain is discussed in Sections 5.5 and 5.6.5.

Hodogram analysis was performed on the horizontal X and Y components to rotate to the R and T directions. Some traces required manual rotation when the first breaks were noisy and when the rotation angle was 180 degrees out of phase. The rotation angles were then saved and applied to the raw data.

The rotation results applied to the raw data are shown below in Figure 5-3. Rotation was successful in minimising P-wave energy in the T component, however, the R component shows weak P-wave first arrivals. Strong down-going S-wave and converted P- to S-wave is visible in the R and T data at 4 depth levels. The depths at which these P-S conversions occur roughly divide the profile into 5 sections where different slopes (velocities) and signal characteristics can be defined. The T panel shows strong down going S-wave at different frequency and phase to that seen in the R panel as well as reflected S-wave. Also evident in the T panel is converted P- to S-wave, reflected S-wave and possible P to S-wave reflections.

A second Hodogram analysis was performed on the R and Z components to correct for borehole dip. This maximizes the P component and minimizes the P-wave energy in the R component. The dip corrected P and R data are shown in Figure 5-4.
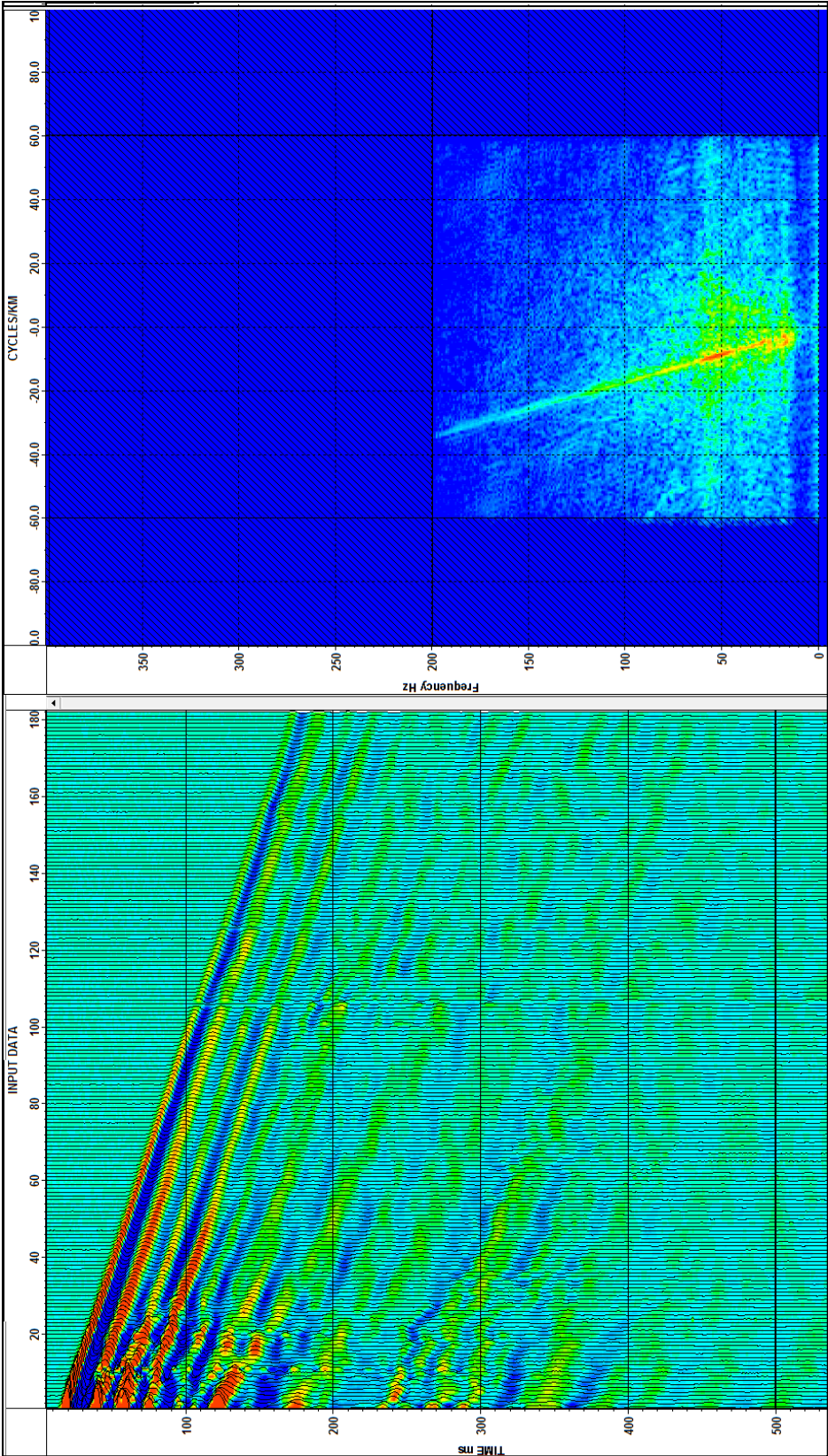
Figure 5-2. FK spectrum of the P component and filter boundaries used to create a reject polygon to precondition the raw data prior to Hodogram analysis.
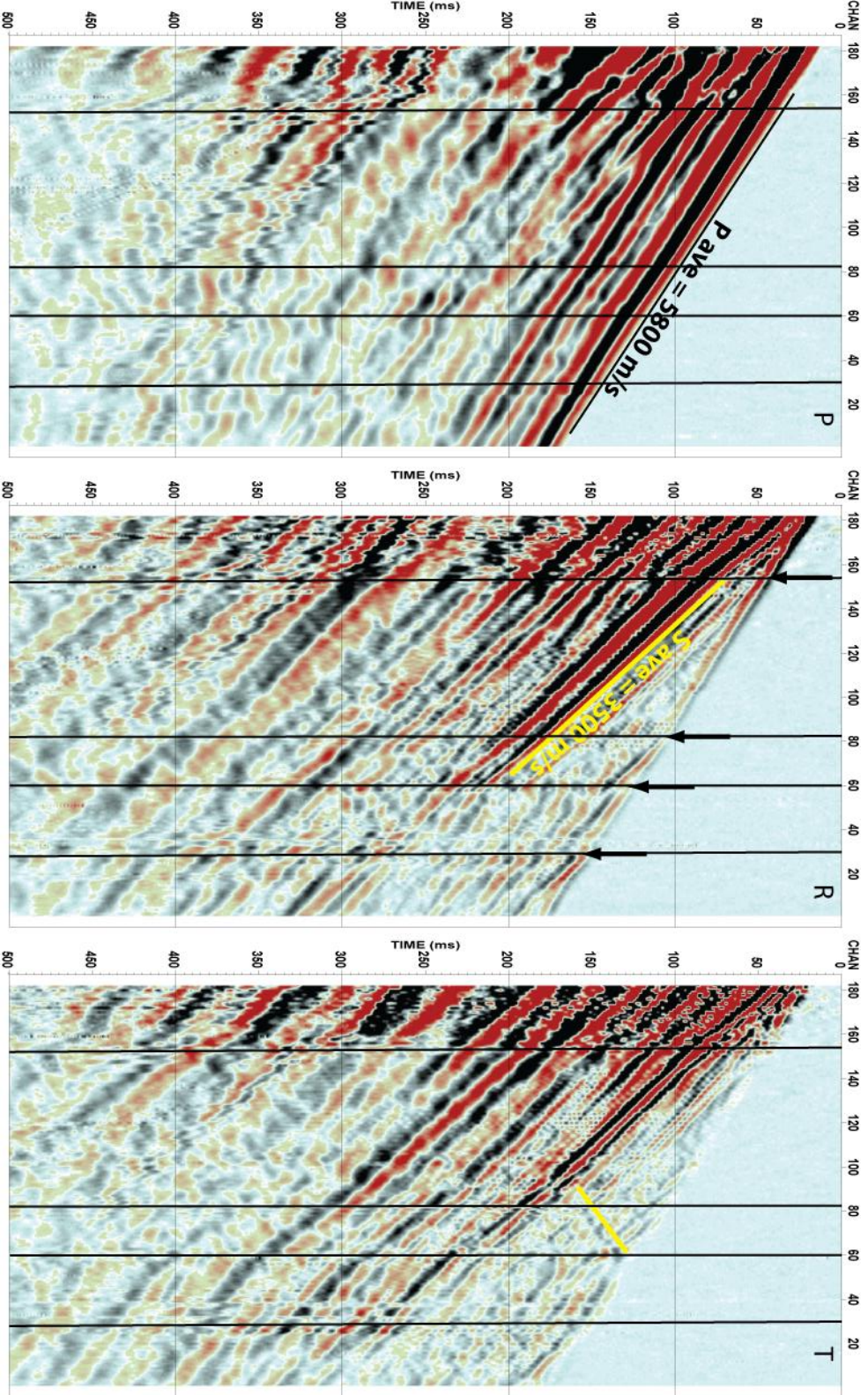
Figure 5-3. Raw 3C data after component rotation by hodogram analysis. From left to right P, R, and T. Also shown are average P and S-wave velocities and locations of converted S-waves (black arrows)
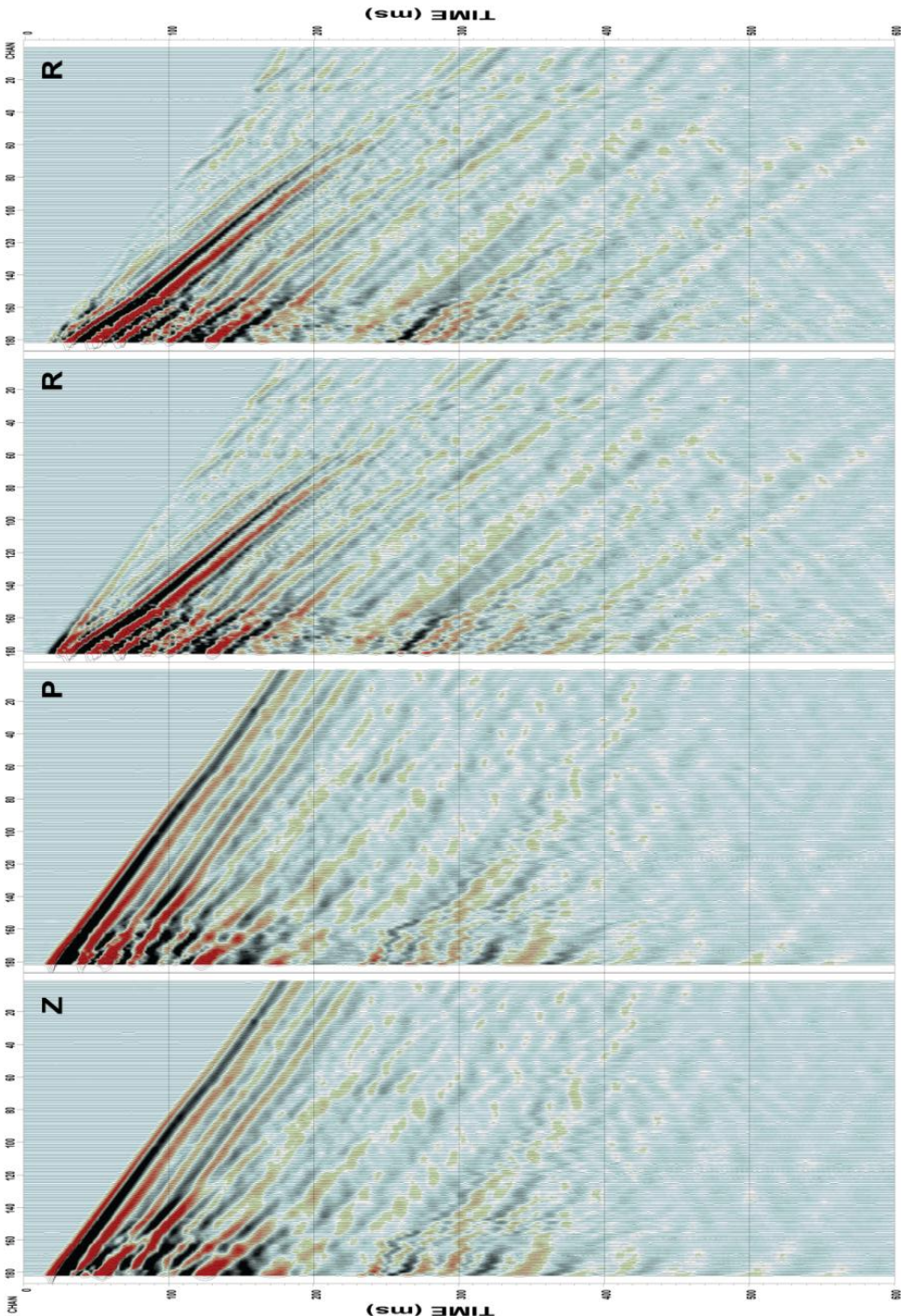
Figure 5-4. Rotation of P and R to account for borehole dip. Left two panels are the P before and after dip correction respectively. Similarly the right two panels are the dip corrected Radial data.

5.3 Raw hydrophone data

The raw hydrophone data (W) are shown below as Figure 5-5. The data were difficult to acquire as the borehole was in close proximity (approximately 100 m) to the Goldfields Highway which connects Kambalda and Kalgoorlie mining districts. As such, heavy traffic causing surface waves were experienced and this introduced background Rayleigh tube-wave noise into the data. First breaks show variable quality down the hole with induced tube-wave interference causing amplitude variations. Data quality degrades below 500 m where there is an increase in the occurrence of fracture induced tube-waves. These are comparatively low amplitude tube-waves to the Rayleigh tube-wave but are still destructive to the first breaks and later arrivals. Geology is partially to blame for the loss of amplitude and data quality. This is discussed further in Chapter 6. Due to the sensitivity of hydrophones to ambient noises, stacking was not done in the field. Instead multiple shots were taken and edited before stacking and further processing.

First breaks are discernible to the bottom of the profile despite poor data quality. Also evident are multiple down-going P-wave $(P_d)^2$ and S-wave (S_d) wavefields. The first arrivals have an average velocity of 5800 m/s and the S_d an average of 3500 m/s resulting in a V_P/V_S ratio of 1.66.

The W data is striped in appearance due to shot to shot inconsistencies between receiver group moves. The data were collected in 8 string moves; 95 to 325 m, 100 m to 330 m, 325 to 555 m, 330 to 560 m, 555 to 785 m, 560 to 790 m, 785 to 1015 m and 790 to 1020 m.

At later times the Rayleigh tube-wave appears aliased. This in fact is due to arrival time shifts in the Rayleigh tube-wave and can be seen in the enlargement of Figure 5-6. This is likely caused by fluctuations in the water level when more volume of string is deployed as all other tube-waves which originate from stationary points in the borehole are in phase with each other.

---

[2] The lower case subscripts d and u are used to denote down- and up-going waves respectively and are always used in conjunction with a sentence case capital prefix to denote what type of wavefield e.g. P_d = down-going P-wave and C_u = up-going cable-wave.
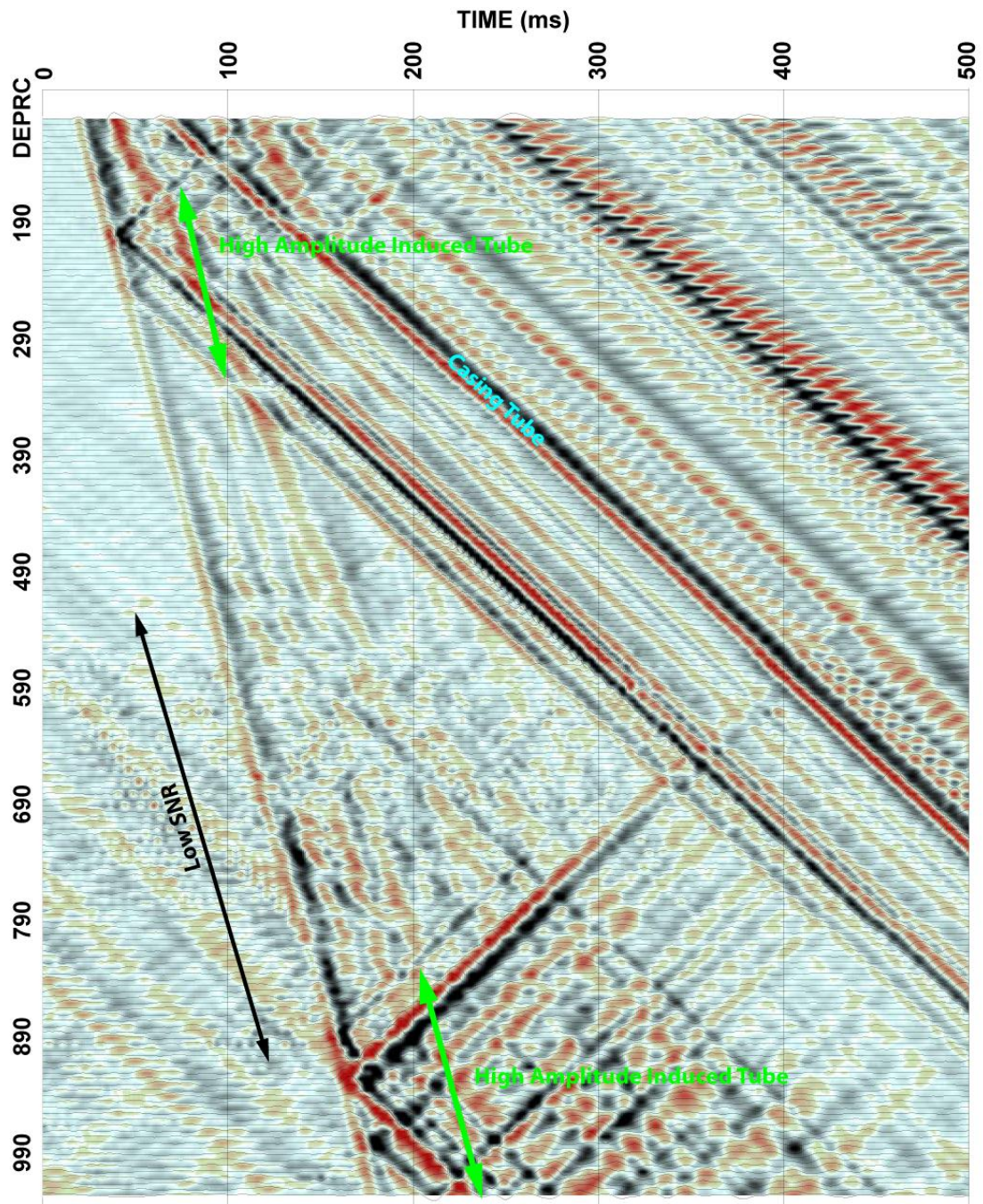
Figure 5-5. Raw hydrophone ZVSP data collected in borehole BH1. Data were collected using a 24 channel string with 10 m spaced elements. Multiple string moves were required to acquire data at 5 m stations between 100 to 1000 m (95 to 1020 m actual)
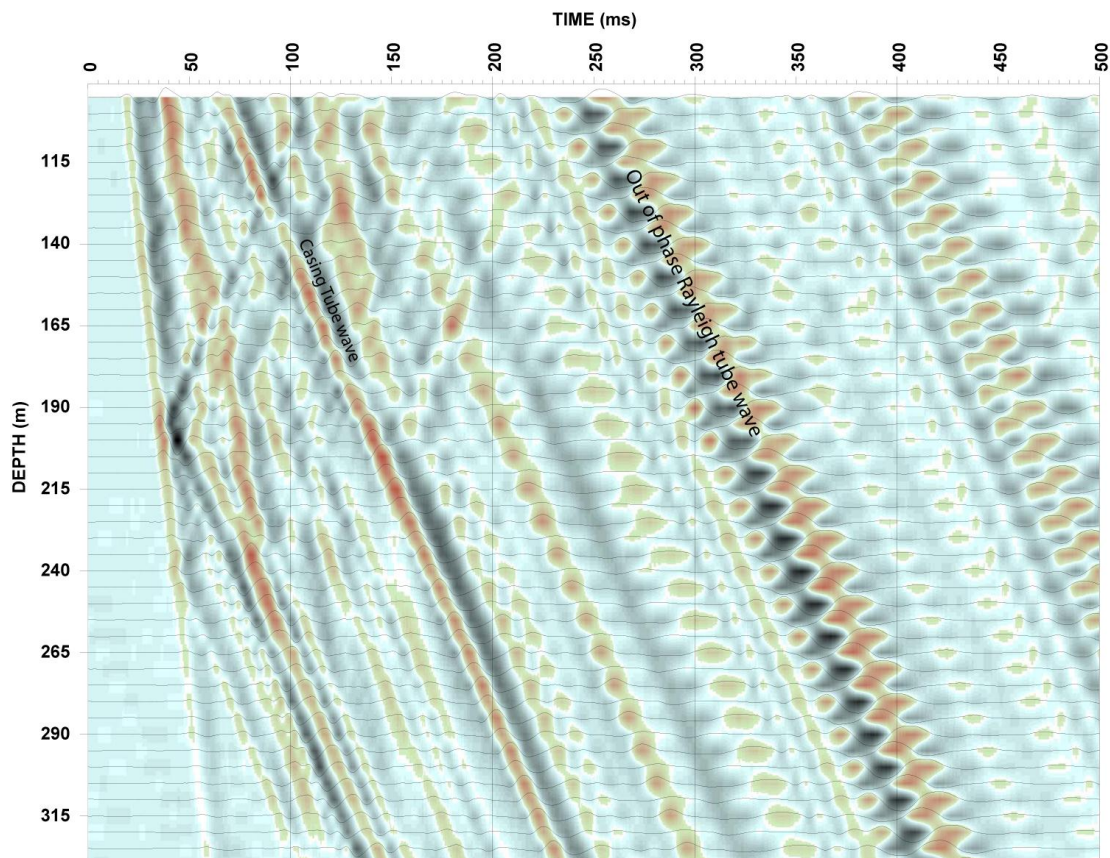
Figure 5-6. Enlarged section of Figure 5-5 highlighting out of phase Rayleigh tube-waves caused by water fluctuations in the borehole from hydrophone string moves.

5.4 Frequency content of VSP data

The average amplitude – frequency spectrums of the W, P, R and T data are shown below in Figure 5-7. As the same source and acquisition geometry was used for both data sets the total frequency content is similar in all components with a usable frequency range up to approximately 100 Hz. The W spectrum is noisy compared to the geophone components which have lower frequency content, while the horizontal R and T components are less responsive to signals in the 40 to 75 Hz range. The frequency range appears to be between 10-200 Hz. All spectra have a local 20 Hz peak.

134
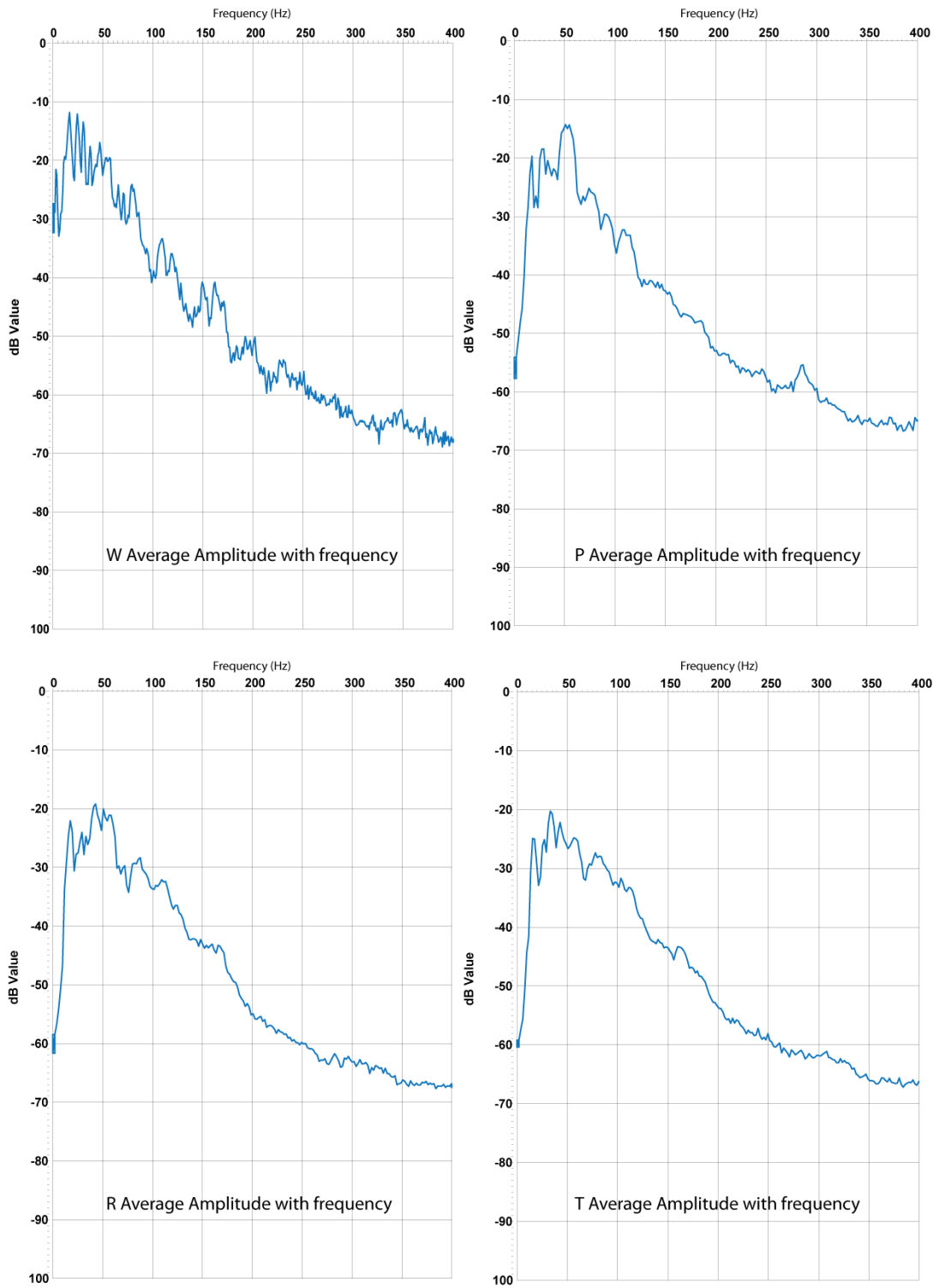
Figure 5-7. Average Frequency spectrum of W, P, R and T components.

5.5 Spatial aliasing analysis

The Fourier transform converts a time function (e.g. waveform, seismic trace) to the frequency domain and a spatial function to its wavenumber domain via the duality of $f = 1/T$ and duality of $k = 1/\lambda$ respectively (Sheriff, 2002), where f = frequency (Hz), T = period of the waveform (s), k = wavenumber (cycles/m) and λ = wavelength (m). For a 2D Fourier transform, from the distance time domain to the wavenumber frequency domain, a 1D transform is applied twice, first in the time direction then in the spatial direction as follows;

   i.   Input Data $P(x,t)$

   ii.   Apply 1D Fourier Transform in the time direction;
$$\int P(x,t)e^{(-i\omega t)}dt = P(x,\omega)$$

  iii. Apply 1D Fourier Transform in the spatial direction ;
$$\int P(\omega,x)e^{(ik_x x)}dx = P(k_x,\omega)$$

Inspection of the W, P, R and T f-k spectrums in Figures 5-8a and 5-8b identifies all the wavefields present in the data. Overlaid on the spectrums are solid and dashed colour coded lines identifying the P and S wavefields, tube-wave (T) and cable-wave (C) noise and the wavefields which have been aliased. Down-going P-wave is clearly visible in the W, P and R down-going quadrants (left side of f-k plot) and has good energy up to 150 and 250 Hz in the W and P data respectively. In the opposite up-going quadrant P- and S-waves are not coherent, however, the P data does have a triangular region of energy up to 55 Hz where P- and S-waves are expected.
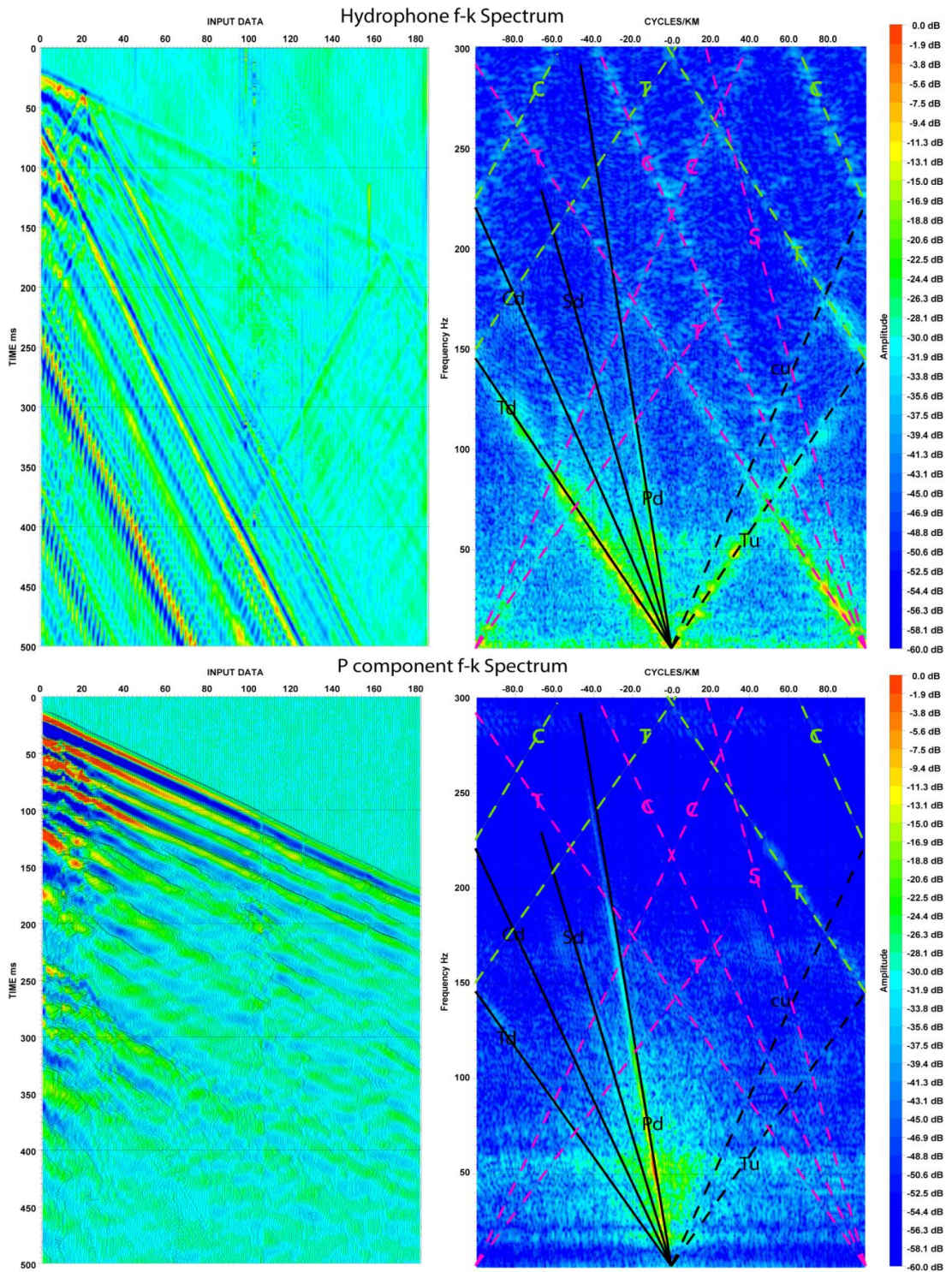
Figure 5-8A. Input and *f-k* spectrums of the Hydrophone (top) and 3C P component (bottom) data.
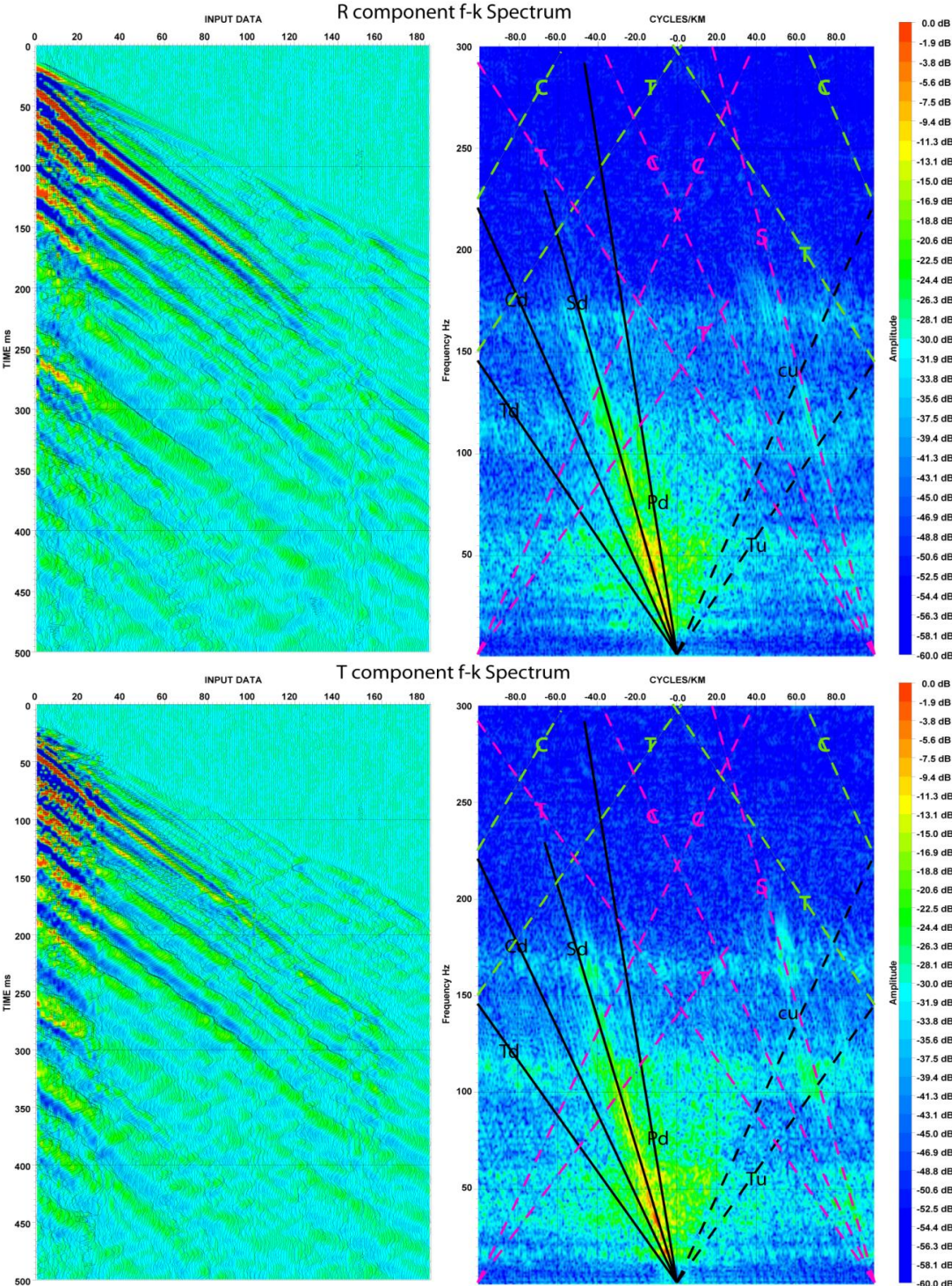
Figure 5-8B. Input and *f-k* spectrums of the 3C R component (top) and 3C T component (bottom) data.

As hydrophones are suspended within the fluid column, tube-waves (T_d and T_u) prevail in the W data, whereas geophones are clamped to the borehole wall, restricting the disturbance of tube-waves. As such low amplitude T_d is present in the P data as this component is aligned with the borehole axis, the primary axis of tube-wave particle displacement. For the same reason cable-waves (C_d and C_u) are present in the W data but it is not apparent in the P data.

The most dominant wavefields in each spectrum have been aliased. The hydrophone T_d, T_u, C_d and C_u wavefields suffer from aliasing in the frequency and wavenumber domains. Aliasing in the frequency domain (Section 4-7) occurs at 150 and 225 Hz for the tube- and cable-waves and the data wraps at this point. Aliasing in the wavenumber domain occurs at 100 cycles/km (the Nyquist wavenumber (k_N) for 5 m receiver stations). Aliasing in the wavenumber domain is caused by small inaccuracies in positioning of the receivers. In the hydrophone data this is strong at $\pm$ k_N due to the 24 receivers being rigidly connected thus having the same positioning error and reinforcing the positioning effect. Similarly in the R and T data, the strong S_d is aliased in the k domain, however, this has a more smeared appearance as there are many more variations in positioning error with moving the geophone shuttles.

5.6 Tube-wave processing

Two approaches have been tested to remove tube-waves from the hydrophone data; 2D median filtering and wavelet subtraction. Each method has its limitations and no one method can be considered the best approach for all data situations. For either of these methods to work favourably the data needs to be pre-conditioned.

In addition to these methods *f-k* filtering has been used to remove coherent noise (which may include tube-wave).

5.6.1 Data pre-conditioning

Commonly VSP data is sorted to create a supper gather of all receivers prior to processing. This is a necessary step when dealing with 3C data collected by a single

or small number of shuttles, as wavefield separation processing techniques require multiple neighbouring traces. A minimum of 6 traces can yield satisfactory wavefield separation using a 3 trace median filter (Kuzmiski, 2010).

In the case of the 10 m hydrophone array, where data has been in-filled with 5 m stations, if the SNR is low, random noise fluctuations exist between shot gathers and time shifts are present in Raleigh tube-wave arrivals between shot gathers, creating a super gather will create misalignments and amplitude imbalances in the super gather which will cause artefacts during processing. This is discussed further in section 5-6-7. It has been found that it is better to pre-condition the individual field records, balance trace amplitudes and perform wavefield separation on field records prior to stacking and creating a super gather.

Preconditioning of the individual field records is shown in Figure 5-9 and involved the following processing:

- Running average removal (mean value 100 samples)
- Automatic gain control (1400 ms AGC window)
- Predictive deconvolution (1400 ms window)
- Orsmby band-pass filter (5-15-155-220 Hz)

Preconditioning removed low frequency noise such as that seen in trace 24; removed reverberation and sharpened tube-wave events (deconvolution) and balanced amplitudes against the background noise giving the appearance of increased signal.
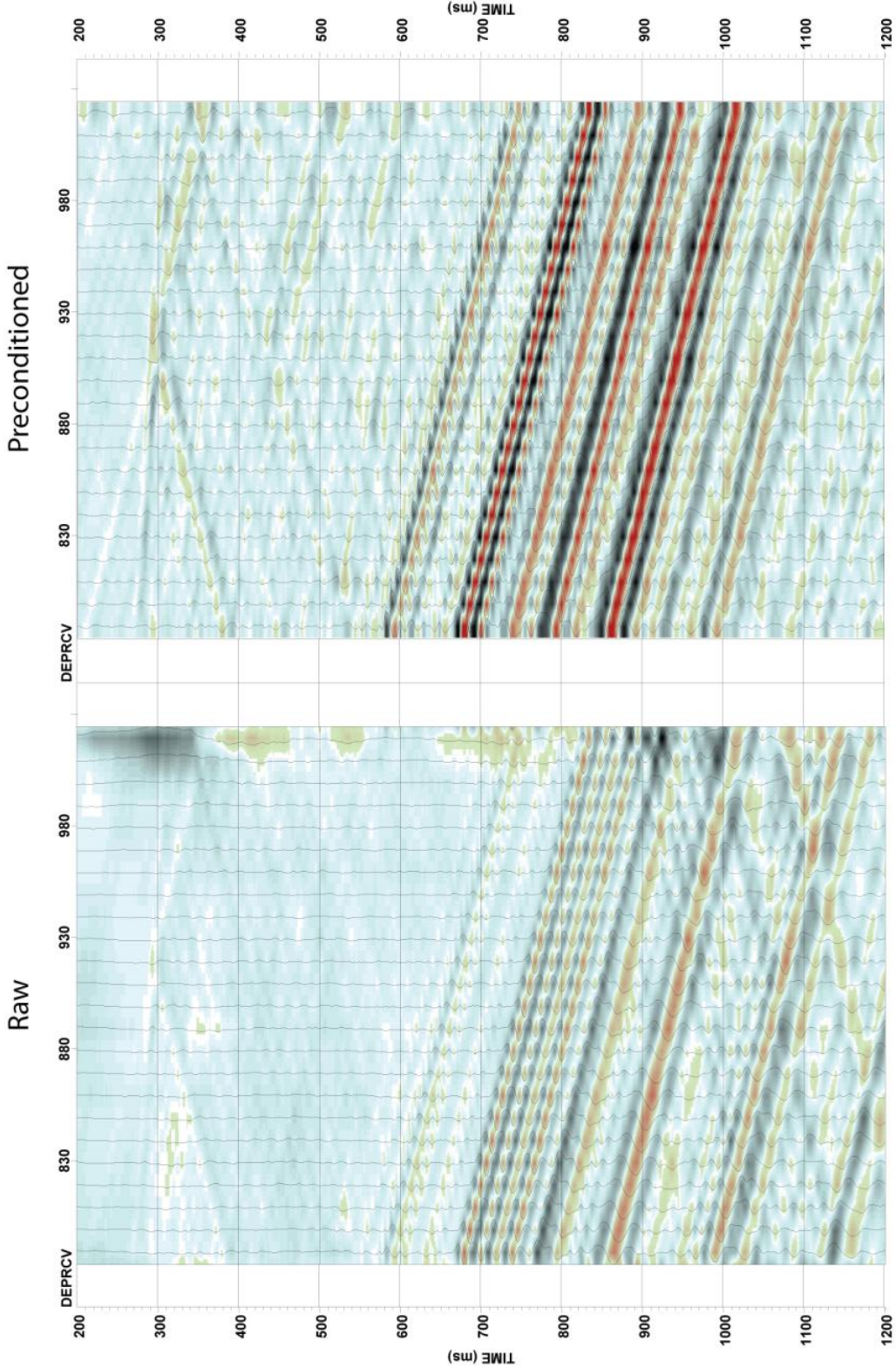
Figure 5-9. FFID6 from string position 790 m Raw data before and after pre-conditioning.

5.6.2 2D median filtering

A median filter is defined as a nonlinear filter where the output is the median value within a running window (Sheriff, 2002). A 2D median filter (or 2D mean or 2D RMS filter) is where the running window is defined across multiple neighbouring traces and the filter sorts samples at equal times across the trace window, then generates a new trace of the same length. In VSP wavefield separation by 2D median filtering, the horizon which is to be filtered or separated is flattened to a datum (c.f. section 2.4, conversion from FRT to +TT or -TT), such that, the peak amplitude of the event is at a common time across all traces. Events aligned along the horizon are then enhanced by the filter, along with all other coincidentally flattened horizons with the same move-out (e.g. multiples and reverberations). The enhanced horizon can then be subtracted from the original data, removing that particular wavefield from the data. An example of this procedure for tube-wave removal is graphically shown in Figure 5-10 where a 7 trace filter has been applied to a single 24 channel hydrophone field record FFID06.

2D filters operate on the central trace of the spatial window. As such, there are edge effects at the beginning and end of each filtered record where the operator is lacking information from one side of the window and null traces are added. This can be seen in the above example as higher amplitude events in the first and last two traces of the filtered record where tube-wave still exists.
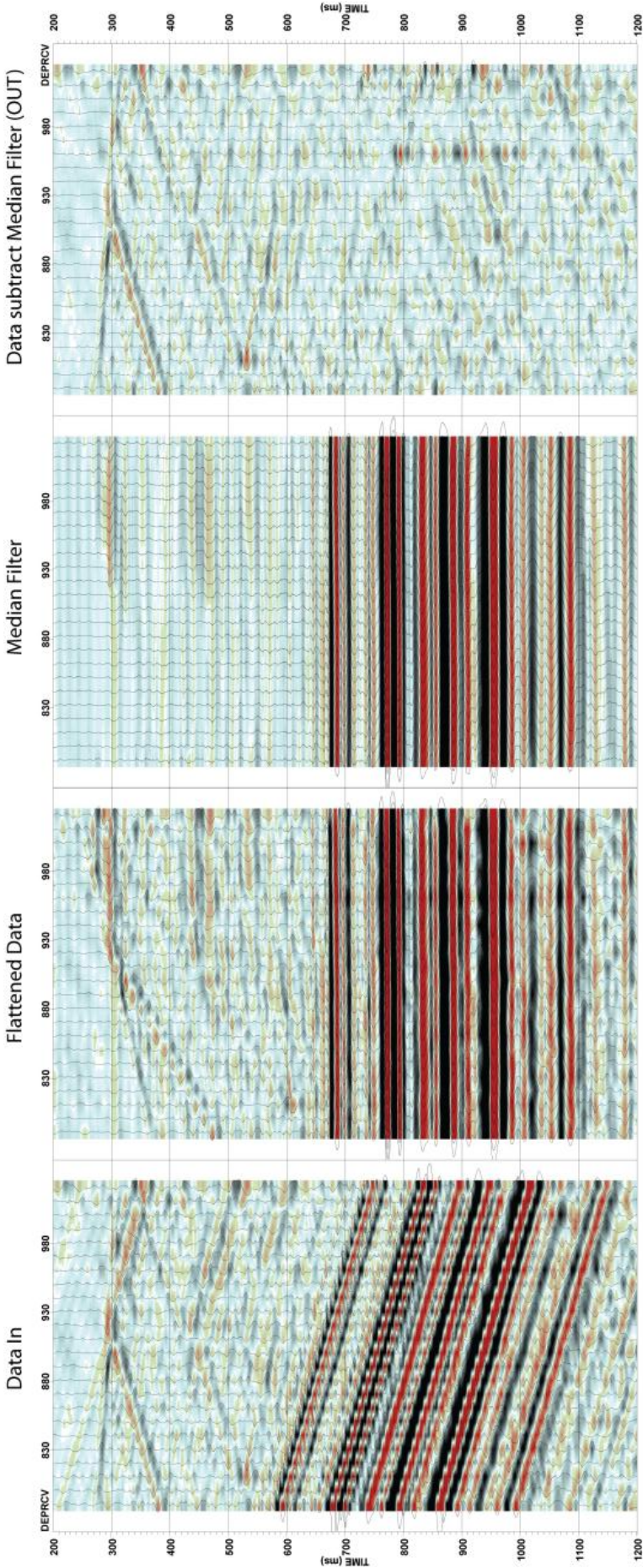
Figure 5-10. Tube-wave removal using a 7 trace 2D median filter on a 24 channel shot record (FFID06) from BH1. From left to right the input data, data flattened to 700 ms from tube-wave picks, median filter output (enhancement), median filter output removed from the flattened data and then un-flattened back to FRT.

5.6.3 Model based wavelet extraction

A model wavelet extrapolation technique Wave-by-Wave (WBW) based on Blias (2007) optimisation approach was trialled to remove tube-wave noise from the hydrophone data. This method examines the data within a defined time window over a defined number traces which is guided along a picked horizon. It then creates a model wavelet and subtracts it from the data trace by trace. The routine determines the wave-shape function for each wavefield (r), amplitude (a) and time (τ) functions from the initial conditions (picked horizons) and solves the Eigen-value problem to determine time shifts which are used to flatten the data and determine the amplitudes. The advantage of this method is that the operator is applied to one trace at a time reducing the amount of trace to trace smearing typical of 2D median or FK filters and it is adaptive i.e. it is allowed to change spatially and temporally. To successfully implement the routine to hydrophone tube-wave removal, unconventional parameters need to be used. The spatial window was restricted to 6 traces (but can be as little as 3) as tube-wave energy is very continuous, this ensures that any wavelet variation due to other wavefields is not captured in the wavelet modelling. The window length was 600 ms, which captured the entire Rayleigh and Casing tube-wave-trains. The window was guided along move-out picked on the upper strongest tube-wave (casing tube-wave) and given a -550 ms starting offset. The offset is required to capture tube-waves above the picked horizon. Note that in our data example we have more than 200 ms before the FB. This pre-trigger is due to a 130 ms free-fall time between when the optical trigger triggering and the weight drop striking the force spreading plate. This lengthy pre-trigger allows us to shift the WBW filters starting offset above the FB to capture tube-waves above our picked horizon. In the absence of this pre-trigger a bulk time shift can be applied, however, it has proven to be advantageous for processing to record ambient tube-waves during the pre-trigger time.
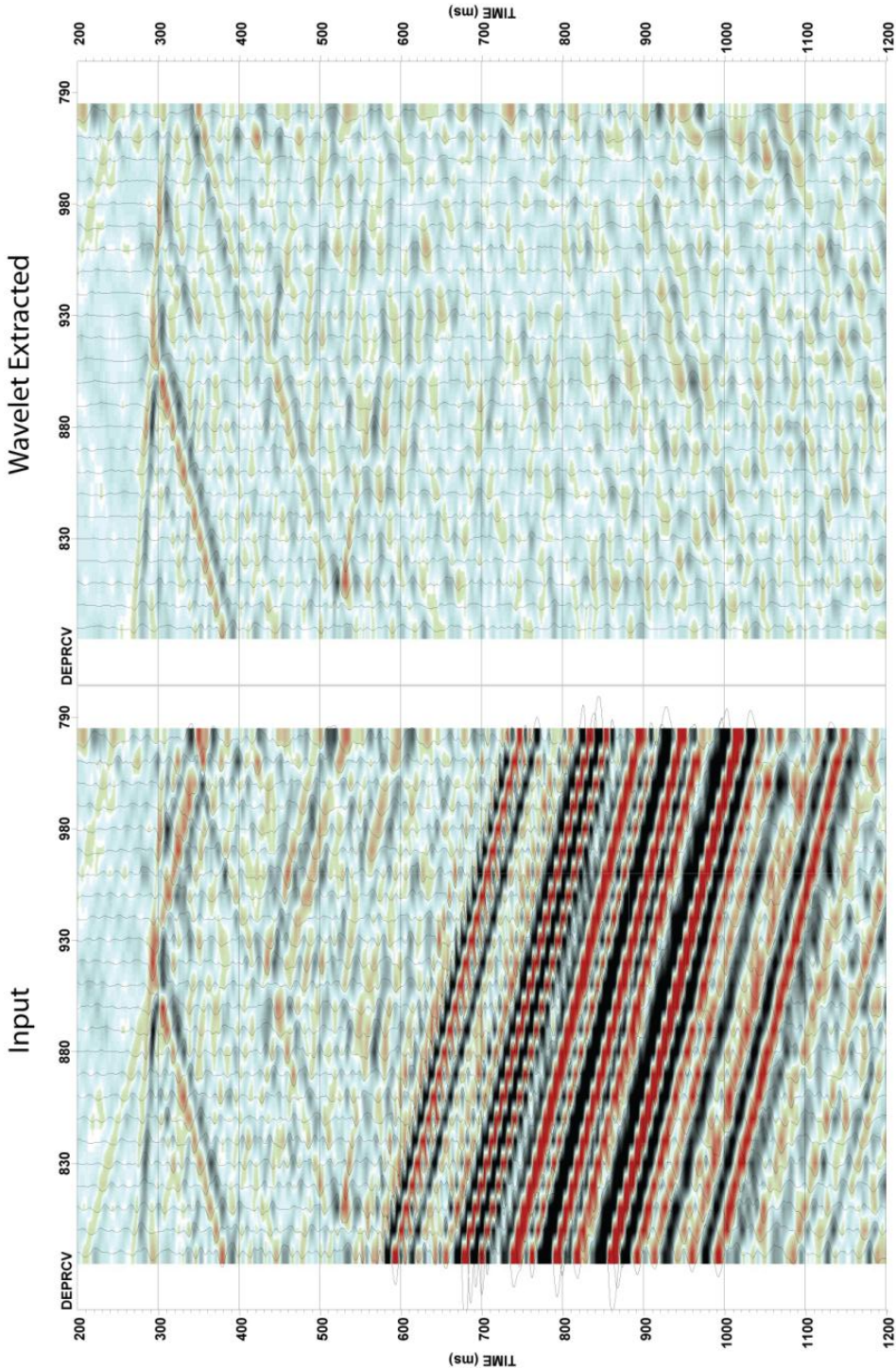
Figure 5-11. Down-going tube-wave separation by the wavelet extraction method of Blias (2007). The wavelet modelling used a 3 trace spatial window and 600 ms temporal window guided by move-out picked along the upper strongest tube-wave.

5.6.4 Comparison of 2D median filter and wavelet modelling subtraction for tube-wave removal

The two examples of tube-wave removal techniques examined above have been performed on field record FFID06 and a comparison of the two is shown below in Figure 5-12. At first inspection, the two methods have done a comparable job at removing the down-going tube-wave. In addition, the WBW technique has removed the high amplitude anomaly seen on the trace at 960 m and over all, the remaining wavefields have a more continuous appearance. The median filtered data has edge effects (section 5-6-2).

A down-going tube-wave event occurs above the first arrival in the WBW data, this is because the window and offset from the picked horizon did not capture this event. As this event is above the FB's it was muted from the data at a later processing stage. Both methods have effectively removed the T_d to reveal S_d. This is identifiable by its velocity; it is slower than P_d and faster than T_d and subsequently arrives after the FB and above the line where the casing T_d arrives. Both methods have also unmasked T_u which is obscuring the S_d events.

FFID06 was chosen semi-randomly to use as an example, it was the first shot record which required no editing out of bad traces. Both the WBW routine and 2D median approaches have variable results across all field records. All field records needed to be inspected and edited for noisy traces. Often multiple neighbouring traces were removed, where discrete noise events created high amplitude events across many channels. The WBW approach has an advantage in this situation as it requires as little as 3 traces to be effective.
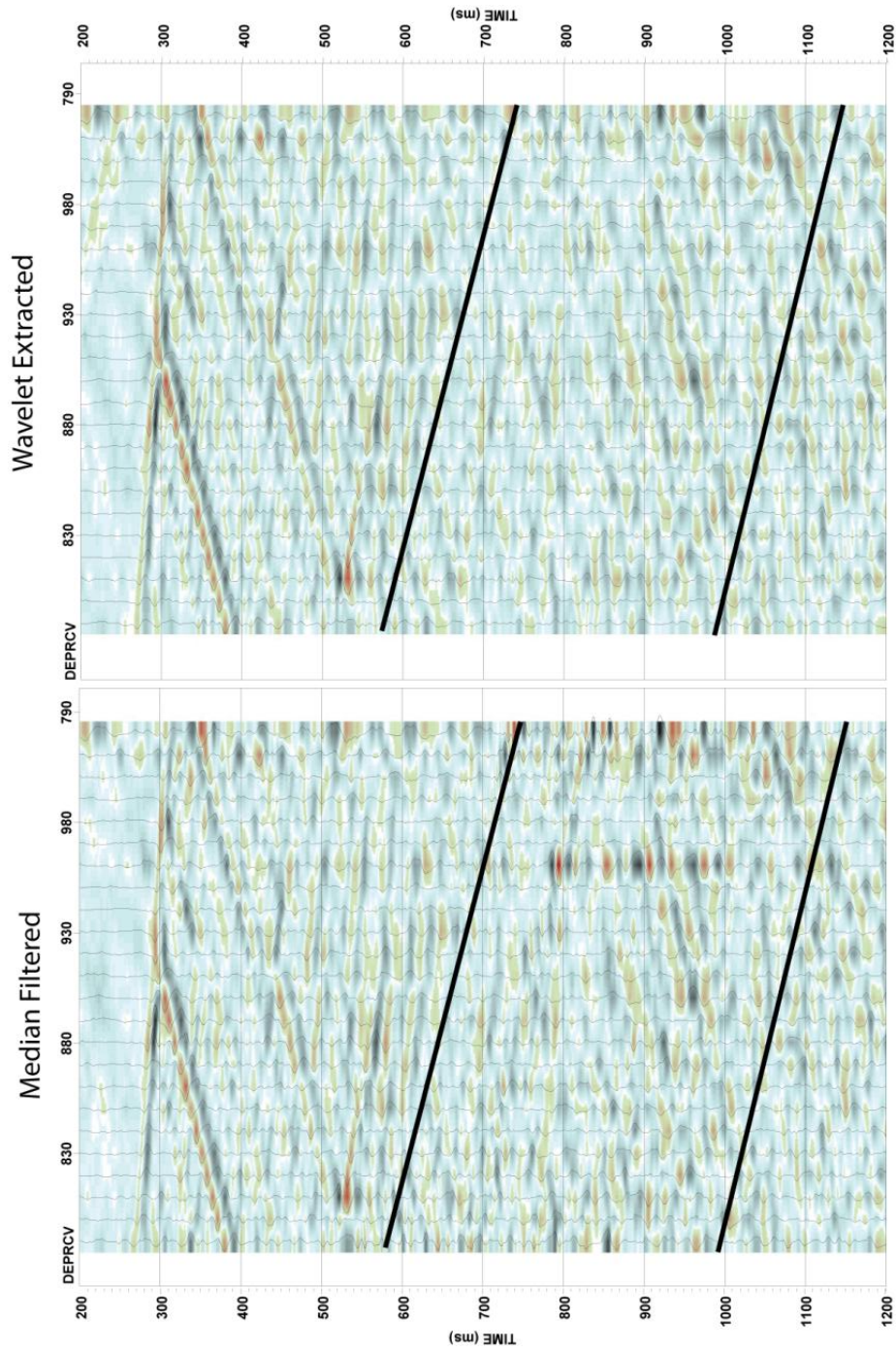
Figure 5-12. Comparison of tube-wave extraction by 2D median filtering and the wavelet extraction method. The left panel used a 7 trace 2D median filter to remove down-going tube-waves (Figure 5-10). The right panel used the model wavelet extraction method of Blias (2007) (Figure 5-11). Black lines indicate the high amplitude casing tube-waves have been removed.

5.6.5 **Wavefield separation by *f-k* filtering**

Another useful tool in wavefield separation, where events are linear, is the Fourier transform and filtering in the k-ω domain. To filter in the *f-k* domain we;

i. Start with a time series gather (FFID, common shot etc) and apply a 2D Fourier transform (Section 5-5).

ii. Define a reject zone in the *f-k* domain where we set the amplitude and phase spectrums to zero

iii. Apply the 2D *f-k* filter (ii) by multiplying its amplitude spectrum with the original input data set

iv. Apply the inverse Fourier Transform to the filtered data to return it to the time domain.

This is graphically displayed below in Figure 5-13 applied to FFID06. Due to the high amplitude of T_d relative to our seismic signal of interest and aliasing, *f-k* filtering in the FFID domain is poor due to aliasing and there is still evidence of T_d. This can be improved reducing the trace separation, by combing the shot gathers and filtering in the common shot domain. This will remove aliasing at our frequencies of interest; however, filtering will only be effective on good quality data where trace to trace amplitudes are balanced and discrete noises absent.
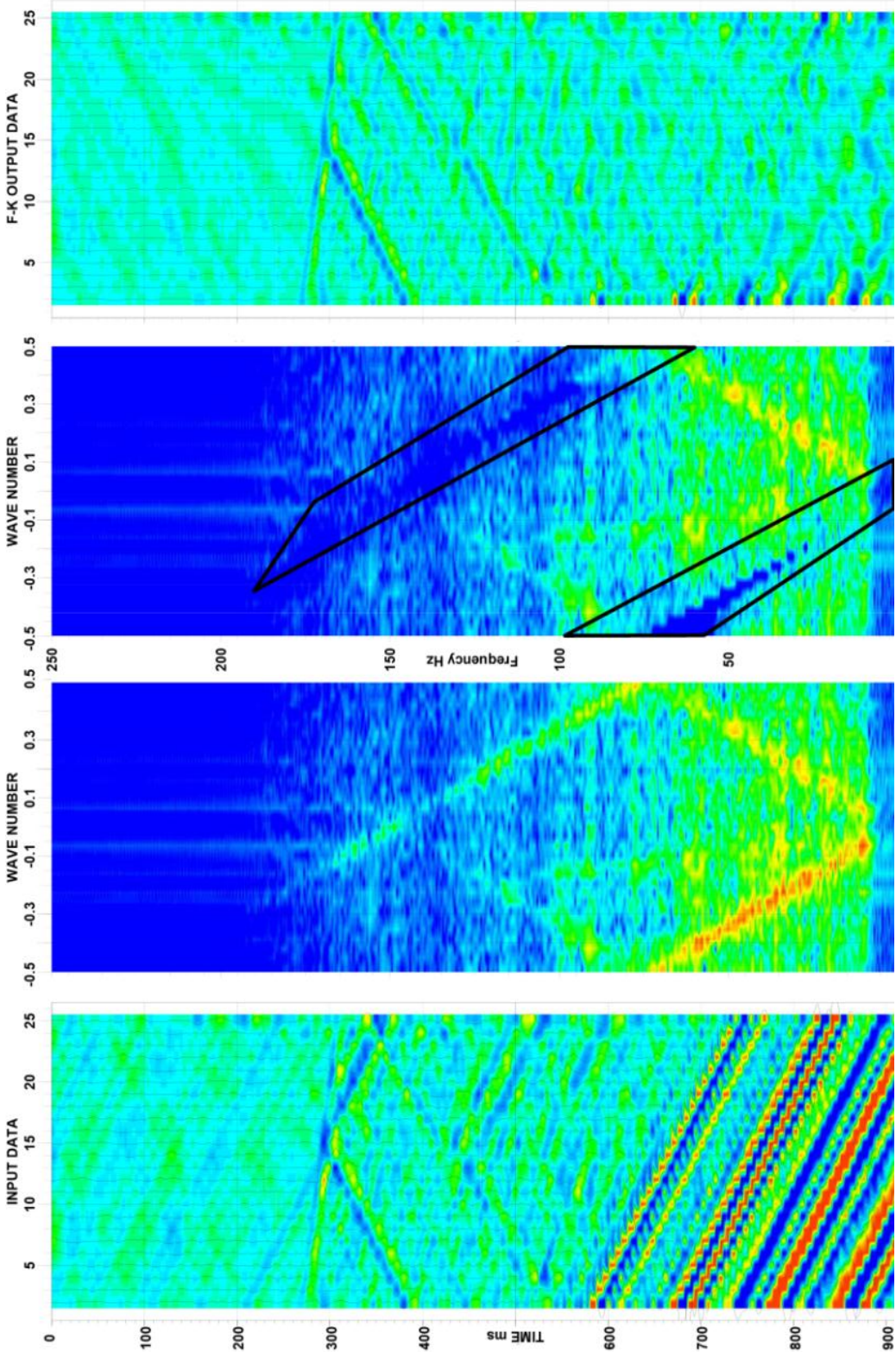
Figure 5-13. Down-going tube-wave removal by f-k filter applied to FFID06.

149

5.6.6 Filtering in the k domain

To minimise effects of spatial aliasing which can occur from small variations in station positioning (Sheriff, 2002), wavenumber filtering was applied to the 3C and hydrophone data. To determine the limits of the wavenumber filter the slowest wave and highest frequencies of interest need to be established similarly to dealing with tube-wave aliasing in section 4-7. As the wavenumber is the reciprocal of wavelength and propagation is directional (up and down) our equation for determining the maximum wavenumber of interest becomes the inverse of Equation 4-3 namely;

$$K_{\lim} = \pm \frac{2 f_{\max}}{V_{\min}}$$

Equation (5.1)

For our data the maximum frequency of interest is about 150 Hz, and the slowest wave is again our tube-wave although this should be virtually non-existent in well clamped 3C data. Thus our wavenumber filter should include all wave numbers between $\pm$ 0.2. Being conservative and wanting to exclude as little data as possible a $\pm$ 0.5 wavenumber filter was used.
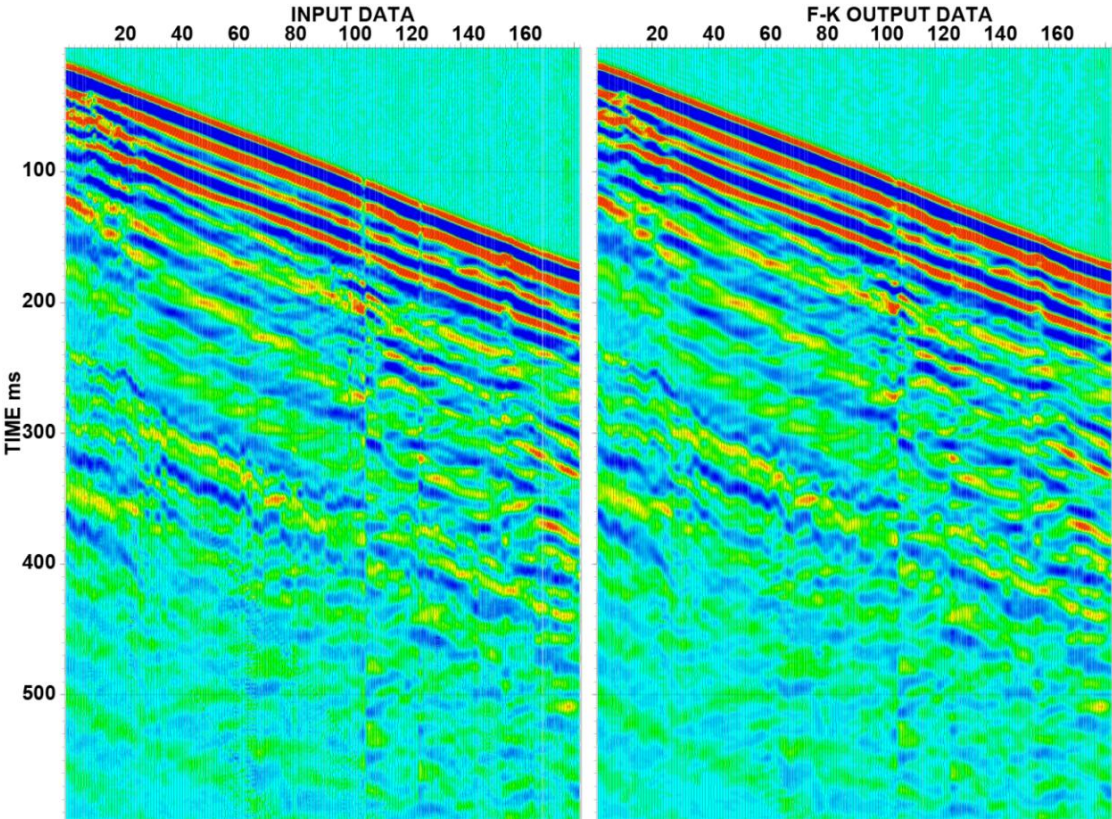
Figure 5-14. Wavenumber -0.5 to 0.5 filter applied to the 3C P data

150

5.6.7 Amplitude imbalances

The hydrophone data were acquired at 5 m receiver stations using a 10 m x 24 channel hydrophone array. Thus 5 m infill moves were required. This means the data can be processed in two ways: 1) with all the traces gathered to form a common shot gather of 184 traces (8 x 24 = 192, − 8 overlap stations) or 2) as individual field records (FFID) and then gathered to form a processed common shot gather. Both methods have potential problems when using 2D filters. Median filtering of common shot gathers requires all the traces in the gather to be balanced. Unbalanced traces from variations in alternating trace SNR will cause amplitude variations across the profile which will cause smearing by the median filter, introducing erroneous horizons. Trace equalisation by large window AGC or by normalising trace amplitudes from a scaling window about the direct arrivals can alleviate some amplitude imbalances if the wavefields are similar. However if the SNR variations include changing ground conditions between shots, discrete noises such as debris falling in the hole and noisy traces then isolated high amplitude noise events may be smeared across several traces.

On the other hand, gathering of processed FFID records to a common shot gather may enhance the edge effects of median filters where the individual profiles overlap to create the larger super gather. In the case of high amplitude noise such as tube-waves this leaves a high amplitude artefact which is detrimental in further processing.

5.7 Comparison of de-tubed W and 3C data

The best method for tube-wave removal for this data set was WBW and the full processing flow for the final "de tubed" hydrophone data (W_{dt}) can be found in Appendix IVa.

In order to qualitatively compare the tube-wave filtered hydrophone data which contains the P- and S- pressure fields, with the particle velocity vector fields of the 3C data, the geophone components were stacked together (vector fields were squared, summed and the square root taken). The stacked 3C data and tube-wave filtered data (W_{dt}) are shown below in Figure 5-15. The W_{dt} data is of inferior quality

and has lower fidelity in comparison to that of the 3C. True amplitudes have not been preserved in the data processing due to AGC functions used during wavefield separation and there are discontinuous sections where tube-wave removal has not been able to recover the masked signal. The hydrophone data is less continuous than the 3C data, which in part may be attributed to the lack of a trigger reference geophone and differences in source impulses, but the variation is mostly due to the removal of the tube-waves. Despite the lesser quality of W_{dt} there are obvious similarities with the P data, some of which have been highlighted in Figure 5-15. The W_{dt} data shows clear down-going P- and S-wave (P_d, S_d), there is some up-going energy present and variances in P_d velocity can be observed in the intervals previously defined by P-S conversion in Figure 5-3.
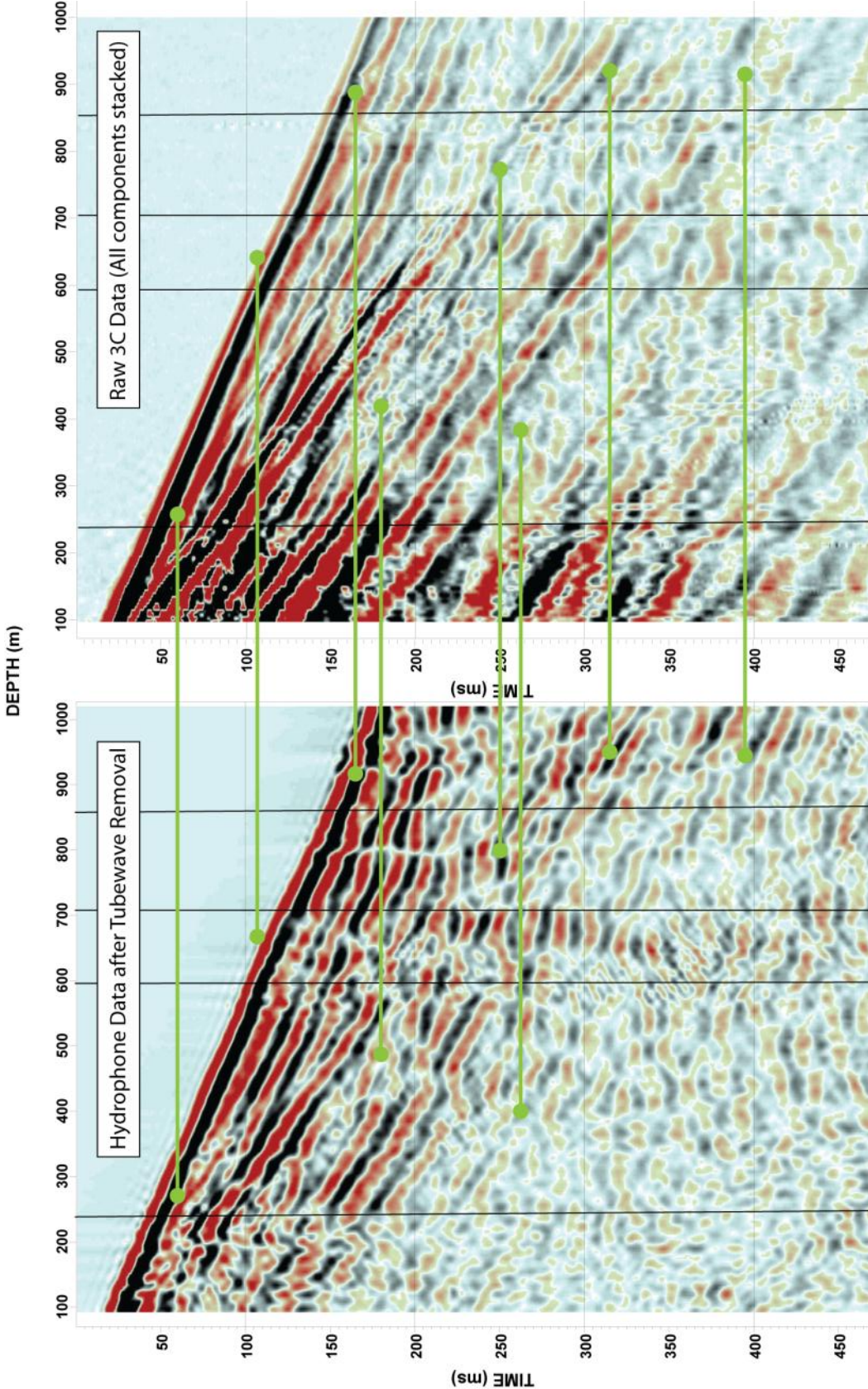
Figure 5-15. Combined 3C wavefield comparisons with hydrophone data after tube-wave removal.

5.8 P_u Wavefield separation

The W_{dt} and P data were then processed to remove down-going wavefields. The same data processing flow was used to remove the down-going wavefields in both profiles, specifically (1) a 2D median filter with a spatial window of 13 traces (2) a *f-k* fan filter removing all down-going velocities between 3000 to 6500 m/s, with a top mute killing all noise above the first break picks and (3) up-going signal enhancement with a 7 trace median filter followed by a *f-k* box filter with limits ± 40 cycles/km and 0 to 250 Hz. The results of each step as applied to the geophone data has been displayed below in Figure 5-16. The processing flow for the 3C and hydrophone down-going removal can be found in Appendix IVb.

As there is S_d-wave apparent in the W_{dt} data an additional processing step was required to remove this from the hydrophone profile. Estimation of the V_P/V_S ratio and trace header math was applied to FB times to flatten the S_d. Several V_P/V_S ratios were trialled. A final V_P/V_S ratio of 1.72 was used to flatten the S_d and a median filter applied.
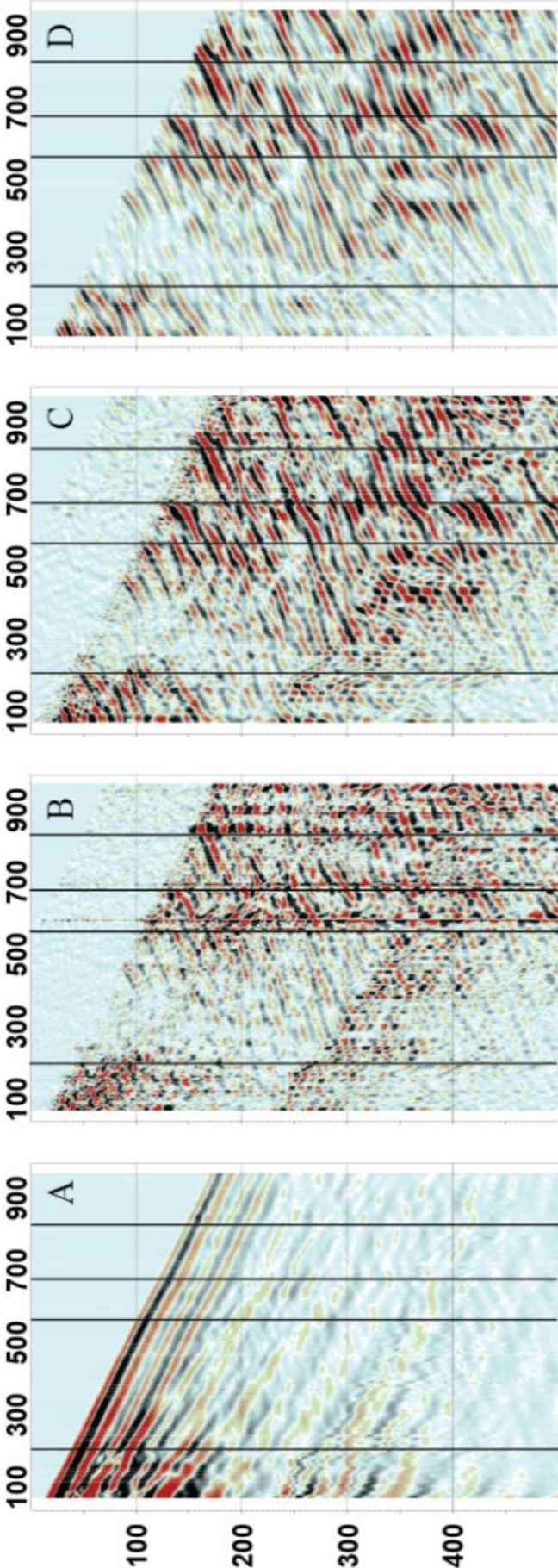
Figure 5-16. Processing steps for removing down going wavefields from the 3C data. A) raw data B) 11 Trace median filter C) f-k fan filter removing all down-going wavefields from 3500 to 6500 m/s and a top mute D) Up-going signal enhancement with a 7 trace median filter and an f-k box filter with limits 0 to 250 Hz and ± 20 cycles/km.

5.9 Comparison of P_U profiles.

After down-going wavefield removal the resulting up-going hydrophone and 3C ZVSP profiles (W_U and P_U respectively)[3] are shown in Figure 6-24. The two profiles have very similar features that have been highlighted by horizontal joiners. The sections in the hydrophone data which were compromised by tube-wave removal have recovered the up-going P-wave with surprising continuity. There is some dissimilarity in amplitudes at later times between the two processed profiles. This is due to the application of AGC during tube-wave removal and gives the W_U profile a more continuous appearance than the P_U, however, the P_U data is of slightly higher frequency and has fewer undulations. It could also be caused by the complexity of the wavefield in hard rock environments. Both methods have resolved good reflectors originating at depths of 235, 485, 590, 690 and 900 m (or 50, 80, 110, 130, and 160 ms). The upper most reflection at 50 ms is better defined in the 3C data. Identification and correlation to geological horizons and impedance contrasts is made in the follow chapter, however, an acoustic impedance plot has been overlaid to help make comparisons here.

---

[3] The upper case subscripts denote up (U) or down (D) wavefield separated profiles and are always used in conjunction with a sentence case capital prefix to denote what type of wavefield e.g. P_U = up-going P-wavefields and W_U = up-going hydrophone wavefields.
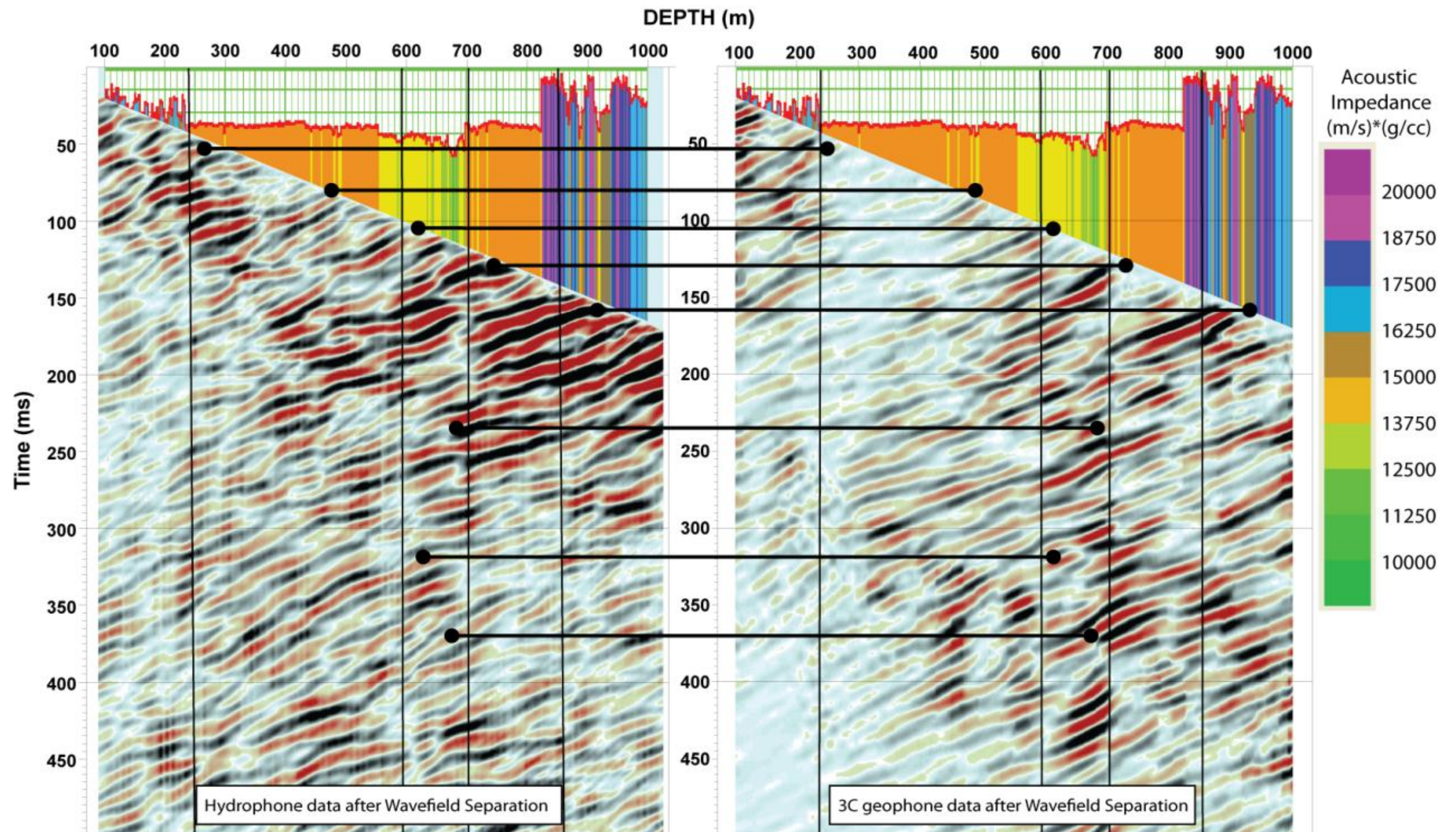
Figure 5-17. Comparison of wavefield separated 3C geophone and Hydrophone VSP data.

5.10 Summary

It has been shown that borehole hydrophones are able to resolve reflected seismic body waves comparable to that of borehole geophones. This is not easily achieved and care at the acquisition and processing stages needs to be taken. The high amplitude of the tube-waves and additional wavefield separation required in removing these from hydrophone data (c.f. 3C wavefield processing) does affect the overall result with some fidelity and coherency being lost in the final P_U profiles.

Model based wavelet extraction has been successful in removing strong coherent tube-wave noise without artefacts from the hydrophone data. The advantage of the method is that it can be applied to only a few traces, the filter operator is only applied to one trace at a time, eliminating trace to trace smearing and it is adaptive i.e. it is allowed to change spatially and temporally. To successfully implement this routine to hydrophone data it is necessary to use unconventional parameters.

It is promising to note that S-wave arrivals are present in the hydrophone profiles. However, the inability to distinguish directionality of polarised wavefields (S_V and S_H waves) and the mixing of all wavefields including tube-waves is a distinct disadvantage for identifying and separating different wavefields in hydrophone data. Great care needs to be taken to separate all wavefields, however, as the signal propagates in the source receiver plane, hydrophone data can be processed effectively by treating it as one would treat 3 component P and R data.

6 Characterisation of Hard Rocks

I present here the first hard rock hydrophone VSP imaging surveys conducted in Australia. Two imaging data sets are presented each addressing different acquisition strategies and characterisation goals. The first experiment was conducted on BHP Billiton exploration lease in the Agnew-Wiluna region of Western Australia. The VSP trials consisted of a zero-offset profile (ZVSP) with full borehole aperture and a walk away profile (WVSP). The VSP images produced, exhibit much higher resolution than surface seismic data.

The second hydrophone VSP imaging experiment was conducted in North Kambalda at BHP's Marthas Vineyard mining lease. Here, offset VSP CDP mapping and migration have been used to help constrain the 3D surface seismic velocity model of the area.

These case histories demonstrate that the application of reflection seismic for mineral exploration is likely to be much more effective when accompanied with borehole seismic methods.

6.1 Agnew-Wiluna Experiment

Hydrophone VSP trials were conducted in August 2009 south of BHP Nickel West Leinster Nickel Operations (LNO). The primary research aims of the experiments were to test the applicability of borehole reflection seismology in a complex hard rock environment and evaluate the 10 m x 24 channel hydrophone array for this purpose. Specific aims to the Agnew-Wiluna site were to determine if the basalt – ultramafic interface of economic importance in the area can be imaged and characterised by surface and borehole seismic methods. This test will also determine the potential of seismic techniques as an exploration method in the Agnew-Wiluna Belt.

6.1.1 Geology and geophysics of Agnew – Wiluna

The Agnew Greenstone Belt is a segment of the more extensive Norseman-Wiluna Greenstone Belt within the Yilgarn Craton. The Agnew Greenstone belt contains over 100 km of continuous strike length komatiitic rocks which host nickel-sulphide and other minerals. The area has been divided into an eastern and western succession (Platt et al., 1978). The west succession comprises of thick tholeiitic basalt, pillowed in places, with abundant sulphidic interflow sediments, spinifex textured komatiite and minor intercalated felsic sediments. To the east, the succession is dominated by felsic volcaniclastic sediments and lavas (rhyodacitic to dacitic) with intermittent komatiites and black sulphidic graphitic shale. All of the mineralisation is within the komatiites of this eastern felsic-sediment package dated at around 2700 Ma in age (Marston et al., 1981).

The Agnew deposit occurs within the overturned east limb (average dip about 80° to the west) of a secondary deformation (D_2) anticline. Open folds, plunging approximately 20° to the north are the prominent structural features in the area. These structures hold a strong penetrative bedding-parallel foliation and are probably related to the regional D_2 anticline (Barnes et al., 1988). An early deformation (D_1) produced isoclinal folds and a regional penetrative foliation. These structures were probably gently dipping when formed. D_2 produced large-scale NNW-trending upright folds, a regional foliation, and a vertical N-trending ductile fault on the west side of the belt. D_2 structures indicate a combination of ENE-WSW shortening, and right-lateral shear along the ductile fault. Both D_1 and D_2 were accompanied by metamorphism under upper greenschist to lower amphibolite facies conditions. The ore bodies are found within a regionally extensive ultramafic unit near the eastern margin of the greenstone belt. The greenstones are isoclinally folded along north-north westerly axes, and strike faulting is very prominent (Nickel et al., 1977).
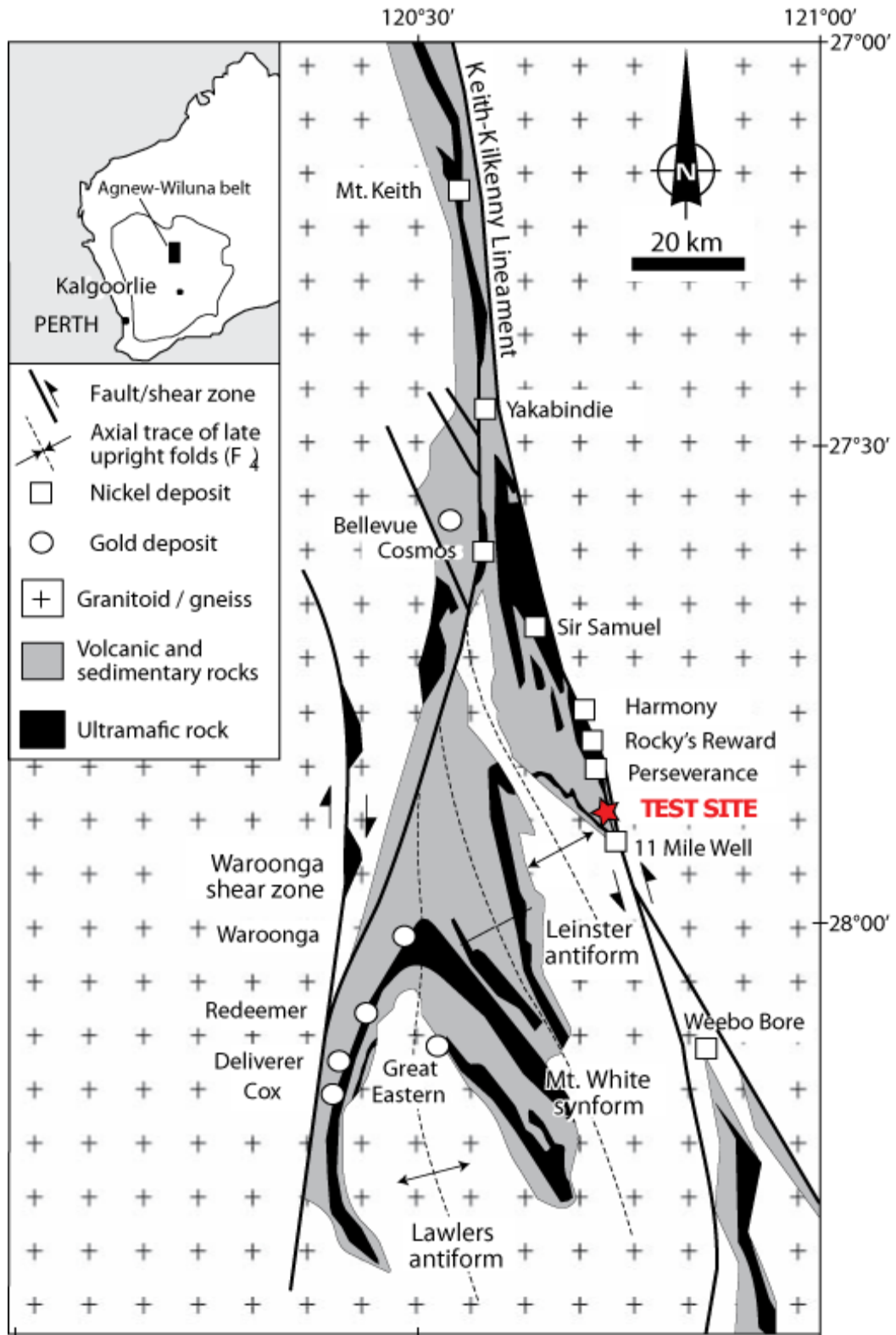
Figure 6-1. Simplified geologic map of the Agnew-Wiluna Greenstone Belt, showing location of the test site, active nickel mines (squares) and gold mines (circles). Modified from Duuring et al. (2012).

Mapping of mineralisation at the mine scale has relied heavily on drilling, gravity, magnetic and more recently EM and DHEM methods. Magnetic methods have clearly defined the division of the eastern and western successions of the Agnew greenstone belt in the survey area and highlight the presence of ultramafic units in the western flank. The 2nd vertical derivative magnetic map of the area is shown in Figure 6-2 alongside the surficial geology and location of the survey area (local grid coordinates).

Figure 6-2. Surficial geology left and 2nd vertical derivative magnetic profile of the Agnew field area. Dominant NNW structures are clearly defined by the magnetic data and the existence of folded UM units in the western flank of the area (supplied by BHP Billiton, Nickel West).

The hydrophone VSP experiments were conducted in borehole BH52. The simplified geology log of BH52 is displayed in Figure 6-3 along with the hypothetical structural model and field geometry of the VSP survey. In summary, the geology of BH52 shows a 46 m thick regolith layer overlying mafic basalt (M) of the western succession, a weak sediment layer intersects the hole at 100 m and a thick felsic package at 200 m. Mafic basalt predominates to a depth of 525 m with komatiitic ultramafic units (UM) intersecting the hole at 300, 440 and 455 m. Below this the borehole is dominated by the felsic intermediate (FI) volcaniclastic of the eastern

succession, which, is intersected by packages of UM at 555 and 695 m. Pegmatite is intersected in the hole at the base of FI units at 232, 380 and 690 m. Two dominant foliations are reported in structural geology logs 35 to 45$^{\text{o}}$ and 60 to 70$^{\text{o}}$.

6.1.2 Data Acquisition

The VSP surveys were conducted in an HQ (96 mm diameter) open hole dipping 68$^{\text{o}}$ to the east. A steel collar terminated at a depth of 140 m. This cased off the regolith (47 m) and weak upper MB layers. Surface geophones were deployed west of the collar and a short 2D seismic profile was collected concurrently. It was preferred to have the surface phones in both the easterly and westerly directions to collect refraction information over the borehole. However, due to the close proximity of the publically gazetted road this was not possible. The surveys conducted are described below and illustrated in Figure 6-3;

2D Surface reflection survey; 60 surface geophones were laid at 10 m station intervals, orthogonal to strike away from the borehole collar. A total of 54 shots were collected shooting away from the collar. Shots were at 10 m spacing with a 5 m skid and 2 m offset to the south i.e. shots were taken between the geophones and parallel to the receiver line. This resulted in a CMP fold[4] of 30.

The hydrophone string was deployed between 140 and 370 m depth during shooting of the 2D surface seismic to monitor tube-wave excitation variations with source offset. A minimum of 4 stacks was taken at each source location.

ZVSP: Shot offset was 45 m west (down dip) from the collar[5]. The 24 channel hydrophone string was deployed to four positions to obtain an overall receiver

---

[4] Fold is defined as the number of shots common to a mid point and is equal to the number of active receivers (N) divided by 2 x the shot station increment (n). Fold = N/2n Kearey, P., and M. Brooks, 1991, Introduction to geophysical exploration 2nd Edition: Publisher: Blackwell Scientific London Edinburgh.

[5] Assessment of the hydrophone data collected during the surface reflection survey determined that tube-wave contamination was apparent at all offsets. As a result it was decided there was no benefit in having a large offset to negate the Rayleigh tube-wave for the ZVSP. The source was kept in-line with the collar at an offset of 45 m in the down dip direction (west). This resulted in the Rayleigh tube-wave arriving at 130 ms in the profile. A down-dip offset was preferred over an up-dip offset as shooting over the borehole was considered dangerous with the chance of potentially exciting borehole collapse or dislodgements in the hole.

aperture of 455 m at 5 m separation between 160 to 615 m. These were; 160 to 390 m, 165 to 395, 380 to 610 m and 385 to 615 m.

Six stacks were taken for each hydrophone move and post stacked after bad shot editing. Typically the first stack was rejected as the impact zone was unsettled.

WVSP: Surface shots were taken at 10 m intervals ±500 m WSW-ENE of the collar (Figure 6-2). A minimum of 4 stacks were recorded at each shot location and post stacked after bad shot editing. The hydrophone string was deployed between 160 to 390 m above the UM contacts of interest.
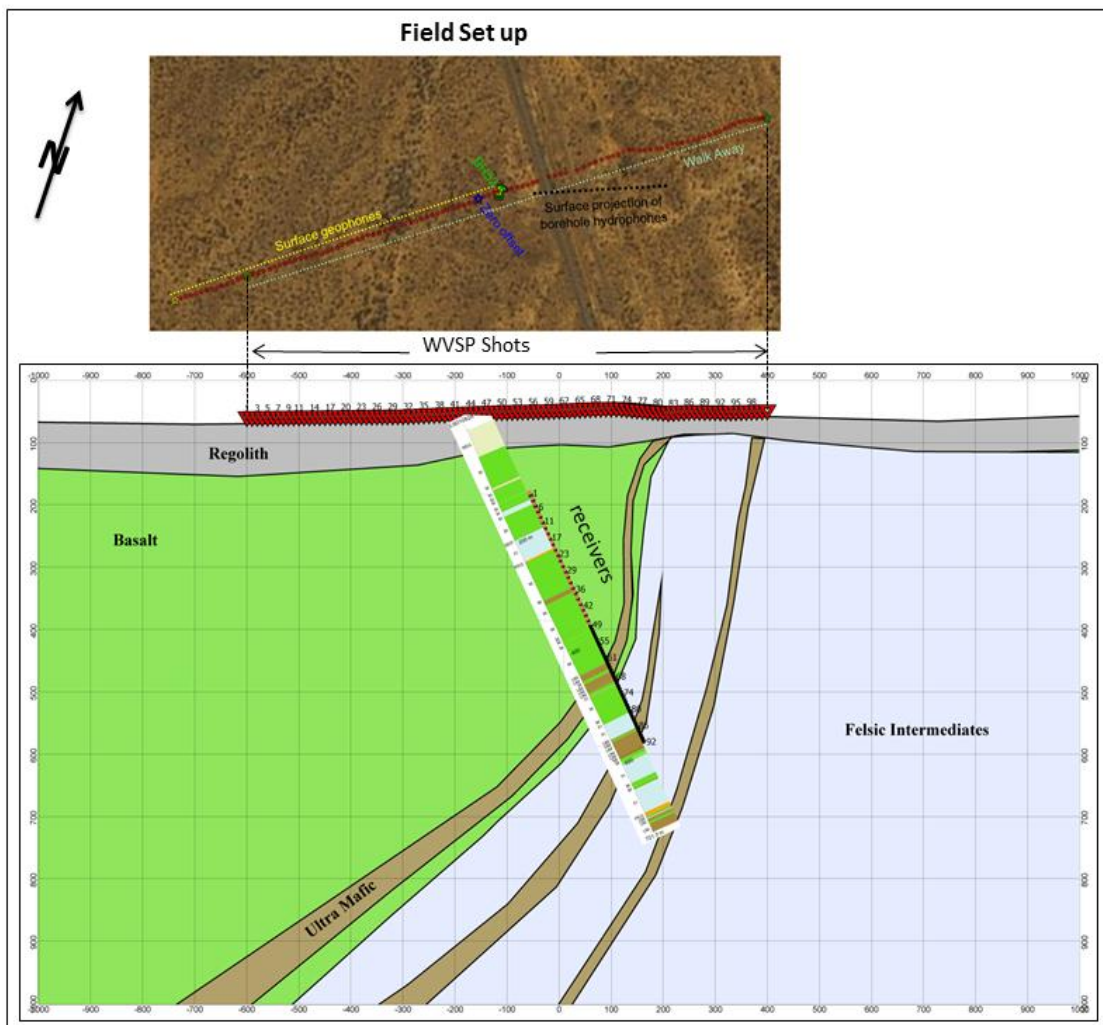
Figure 6-3. Schematic of the Agnew-Wiluna survey, structural concept, geologic units, borehole attitude and survey setup. Overlaid in the bottom panel is BH52 geology core log.

The following equipment was used for the experiments;

- V-Cable 24 channel borehole hydrophone string, elements spaced at 10 m separation, deployable to a maximum depth of 950 m.

- Seistronix EX6 distributed seismic system

- 60 x 10 Hz surface geophones

- 800 kg weight drop hammer hydraulically driven and mounted on a CAT287c ("Bobcat") mobile surface plant.

- GISCO radio-link and "in-house" Optical Trigger with a 130 ms pre trigger.

- Thales ZMax RTK GPS.

6.1.3 2D refraction

Refraction analysis of the 2D surface data was carried out on every 10th shot record. The first break arrival times from these records are shown in Figure 6-4. Refraction analysis used the generalised reciprocal method (Palmer, 1980) implemented into RadExPro Easy Refraction module. A simple two layer case was derived with an upper layer approximately 80 m thick and average velocity of 1850 m/s. Mapping of the layer was restricted to only 60 m in the centre of the profile due to the limited surface offsets and the depth of the layer. This has been overlaid onto the 2D surface reflection profile of Figure 6-5.
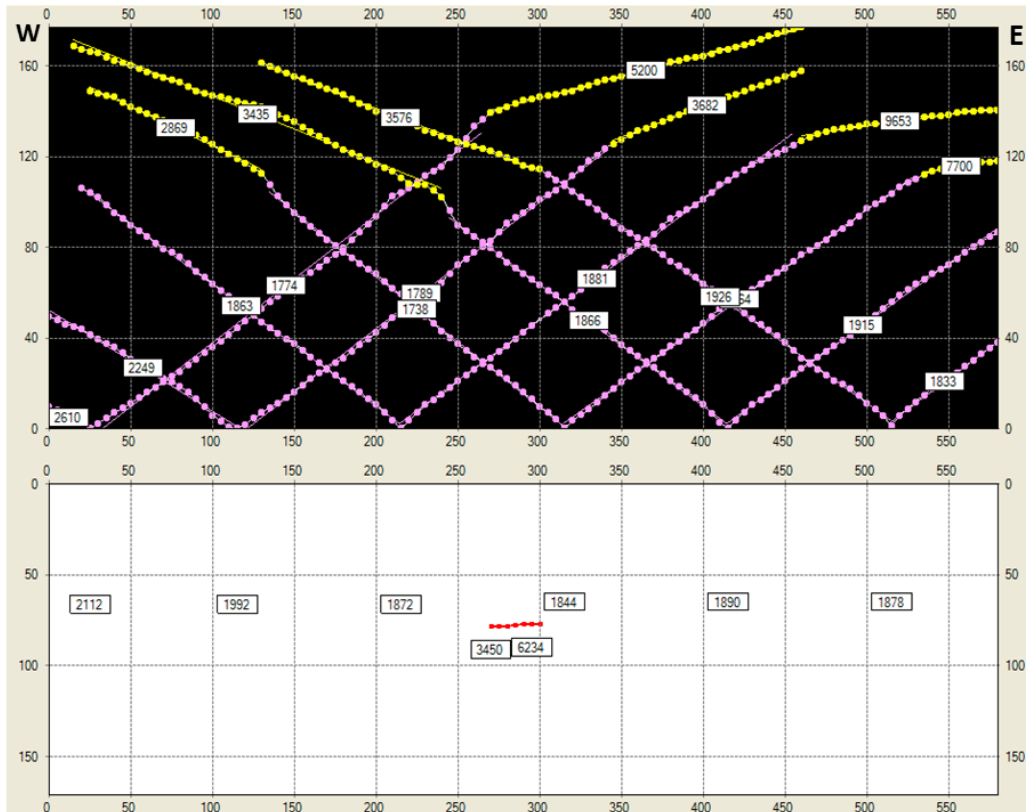
Figure 6-4. Refraction analysis data from Figure 5-4. Top panel shows the first break refraction profiles and velocities for a two layer case. Bottom panel is the resulting geological model with an upper layer of approximately 80 m thick and velocity of 1850 m/s gently dipping to the west.

6.1.4 2D surface seismic section

Very little processing was performed to create the 2D depth section of Figure 6-5 and there is good energy down to 1000 m. The final depth image resulted from; basic editing, filtering, surface and residual statics, spiking deconvolution, constant velocity analysis and depth migration. Refraction statics were not attempted as the offsets were not sufficiently large enough to gain refraction information along the complete profile. The final velocity model used for depth migration was determined from ZVSP results (Section 6-1-7).
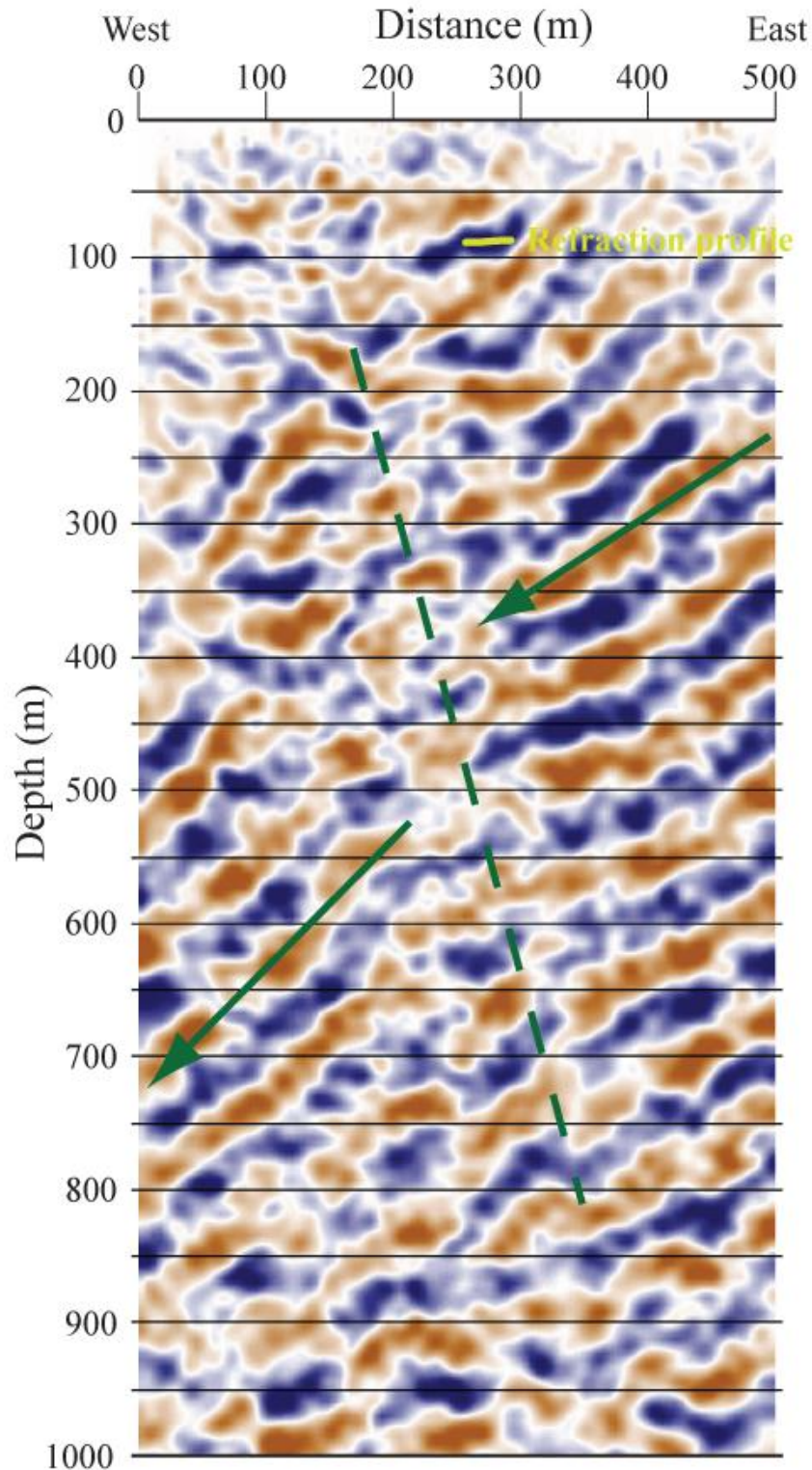
Figure 6-5. Final 2D surface seismic depth migrated section. Reflectors dip to the left of the section and there is a disruption in the middle of the section where dip changes. Refraction analysis profile has been superimposed onto the image. Image is approximately 1:1.

The final processed section is of unexpectedly high resolution considering the relatively short length of the profile and short shot offsets. The section shows clear westward dipping reflectors. In the middle of the section there is a marked change in reflection dip from approximately 30 to 50 degrees. However mapping of the steep westward deep reflections is not geometrically possible with the surface geometry used, therefore these steep reflectors must originate from out-of-plane structures. The location of the change in dip is consistent with signal changes observed in field records between shots at 100 to 130 m and 300 to 330 m, which were thought to originate from faulting.

6.1.5 Tube-wave anomalies

Raw ZVSP data shows 4 types of tube-waves and include induced tube-waves at 232.5, 348, 514 and 588 m. These induced tube-waves are labelled A to D in Figure 6-6 and have been correlated with borehole geology and core photos in Figure 6-7. These originate from; A) pegmatite intrusive, B) minor brittle fracture – fault, C) fault – fracture and D - a mafic intrusive. It can be noted here that at close inspection many of the other smaller amplitude induced tube-waves can be correlated to geology particularly at alternating M – UM and FI – UM zones. This is particularly evident below 520 m where multiple induced tube-wave events coincide with alternating FI and UM zones.

Amplitude of direct primary arrivals in the ZVSP data is between 1 to 5 dB compared to that of the tube-wave amplitudes of 10 to 25 dB. High amplitude induced tube-waves are particularly problematic when picking FB's as their excitation at the borehole wall coincide instantaneously with the direct arriving body waves and change the character of the FB through superposition of the two wavefields.
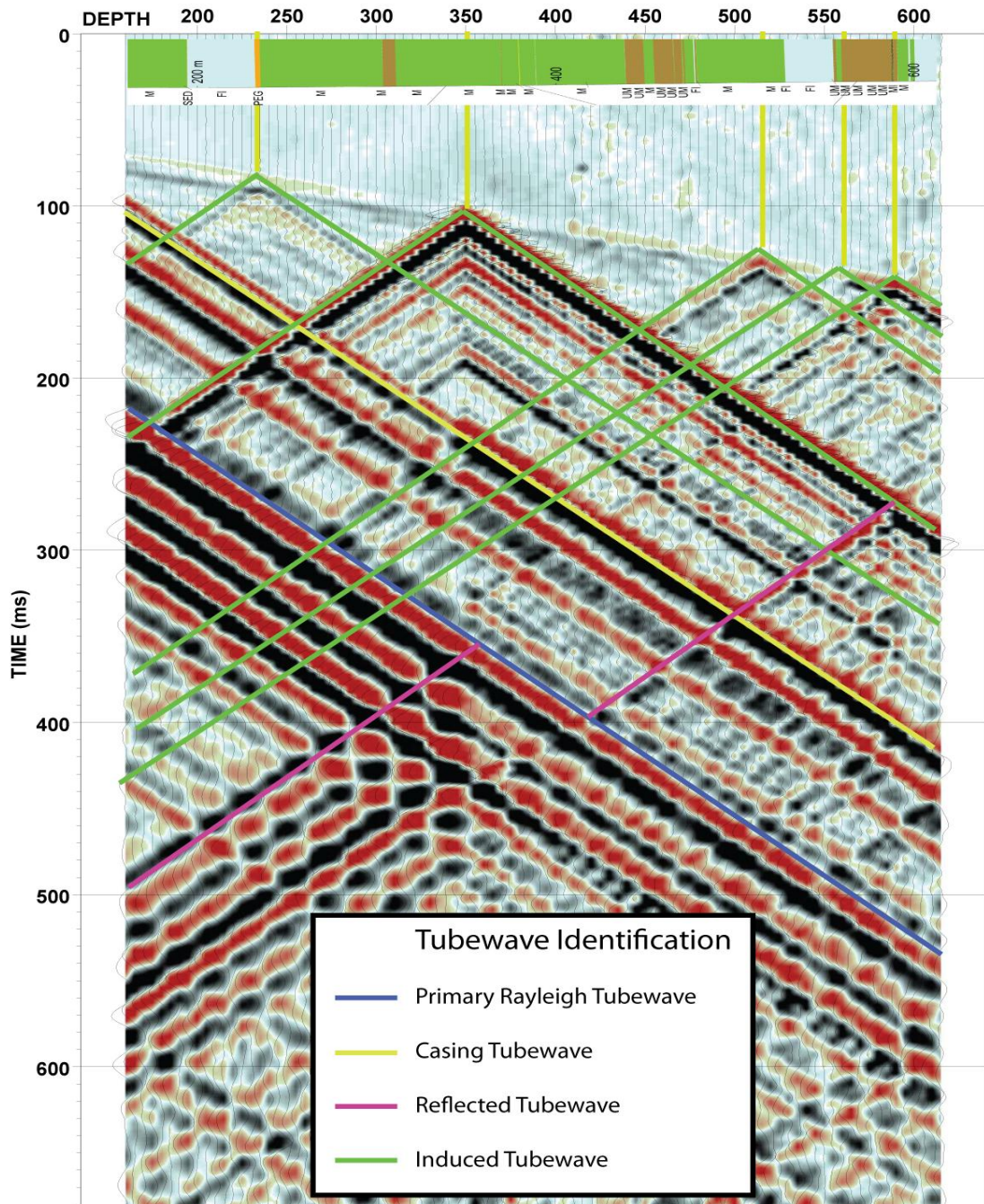
Figure 6-6. Raw hydrophone ZVSP data in BH52. Excessive tube-wave is observed. Casing tube-wave, Rayleigh tube-wave and major borehole impedance change induced tube-waves at 230, 350, 520 and 590 m. There is a major acoustic impedance change in the hole at 350 m which reflects the Rayleigh tube-wave and excites a very high amplitude tube-wave.
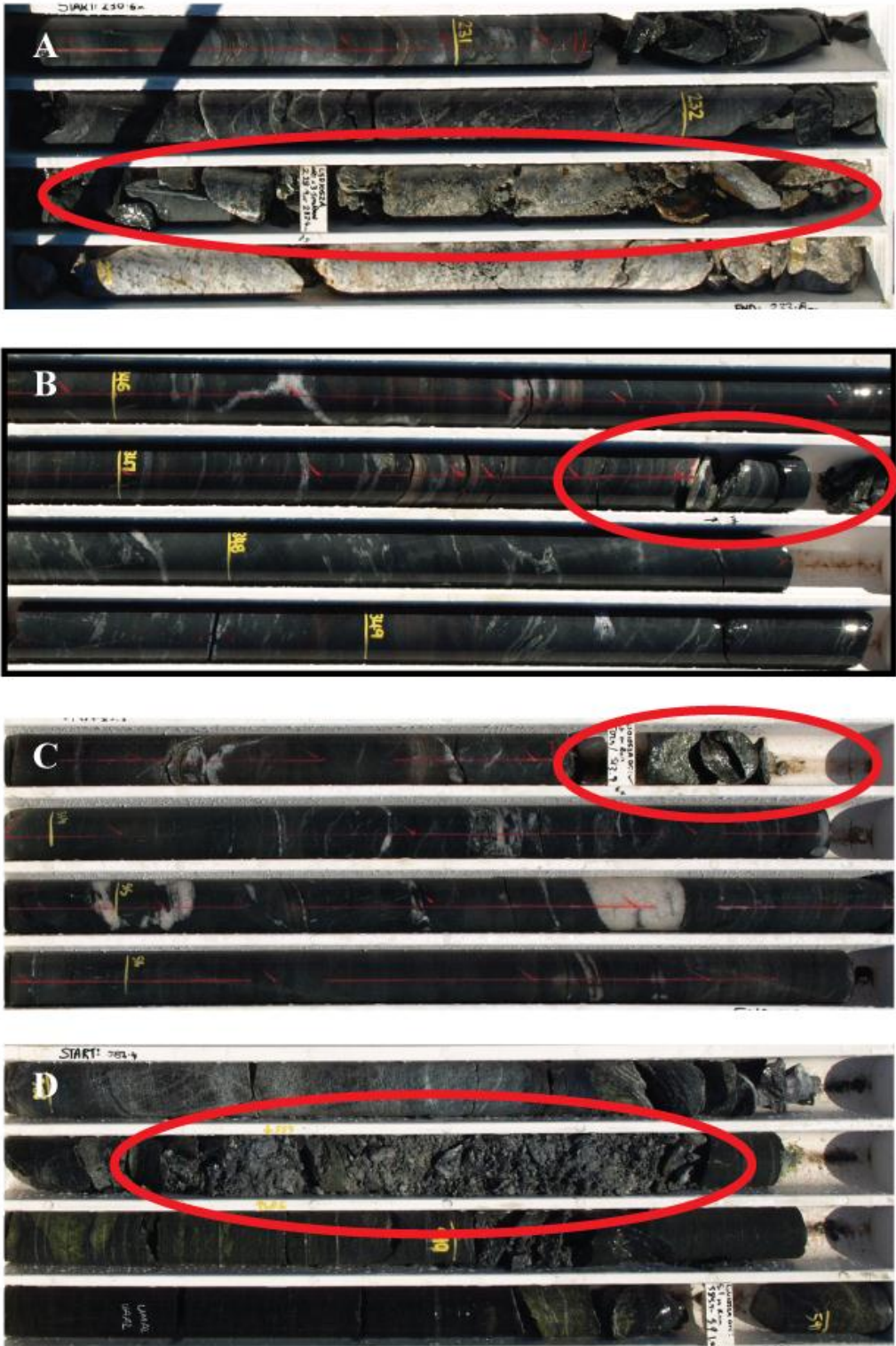
Figure 6-7. Causes of major induced tube-waves at A) 232 m, B) 347 m, C) 514 m and D) 588 m.

6.1.6 Reflected Tube-wave Stack

To investigate further the relationship between induced tube-waves and geology, I generated a corridor stack in depth which consists of only up-going tube-wave energy. This I have termed a reflected tube-wave Stack (RTWS). The general procedure used for generating a RTWS is as follows;

a. From the ZVSP common shot profile determine tube-wave velocity (V_T) and pick direct travel times (FB). Precondition the data with filters, deconvolution etc if necessary.

b. Flatten T_d using trace header math with Time = (Station Depth / V_T).

c. Median filter removal of T_d and un-flatten back to FRT.

d. Use standard flattening, Median filtering to remove P_d, S_d, P_u and S_u and return back to FRT. Only T_u wavefields now remain.

e. Clean data with *f-k* and or band-pass filter.

f. Create a 50 ms (or similar) window below the FB and apply a bottom mute to remove tube-wave multiples. A top mute can also be applied above the FB.

g. Flatten the remaining T_u wavefields and stack to create a single "ideal reflected tube wave trace", then reproduce this trace multiple times (3 to 5) to produce a RTWS in time.

   NOTE this is now in two-way tube-wave travel time. The depth at which the tube-waves were induced is preserved by the first trace (channel = depth) at which they appear in the record.

h. Convert to depth using a constant V_t model

The RTWS for BH52 is shown below as Figure 6-8. High amplitude tube responses can be correlated to structural features which disrupt the borehole wall and the weaker responses related to geological contacts. These have been verified with inspection of core photographs.

Figure 6-8. Reflected tube-wave stack overlying the graphical geology log of BH52. Large tube-wave responses can be correlated to structures such as faults and fractures which disrupt the borehole wall and the small responses are a result of acoustic impedance changes from geology changes.

6.1.7 Velocity profile

Direct arrival times were picked on the raw data after removal of bad field records and stacking to a common shot gather[6]. First breaks were noisy despite stacking and do not have a continuous character due to induced tube-wave contamination. Timing inconsistencies due to small positioning errors with the 5 m in-fill stations are also present. Manual static shift attempts were made to negate these but inconsistencies in shot amplitudes, despite stacking, made this difficult to account for. As such, FB's were picked on 10 m spaced data for a more accurate velocity model. Due to the noisy first breaks, the 10 m interval velocities are erratic, with P-wave interval velocities extremes of 2500 to 18,500 m/s.

A 1-dimensional velocity model using selective arrivals did not resolve layers spanning less than 3 x 10 m receivers (20 m). Integrating geology into the process by plotting the geology log in the interpretation window was also used to constrain the velocity model. Two such models are presented below in Figure 6-9 and Table 6-1. In model 2, we can see an erroneous large interval velocity at 500 m depth, from picking on 10 m spaced traces. Both models have a low velocity layer of 2800 m /s to 140 m and can be generalised as having 4 velocity zones between; 140 – 220 m, 220 – 380 m, 380 – 470 m and below 470 m.

---

[6] A common shot gather is when all the receivers from all receiver group moves are displayed for a common shot point such as a zero-offset to form a ZVSP profile as opposed to a common shot record which is a stack of the field records shot at a common shot point and common receiver group location.
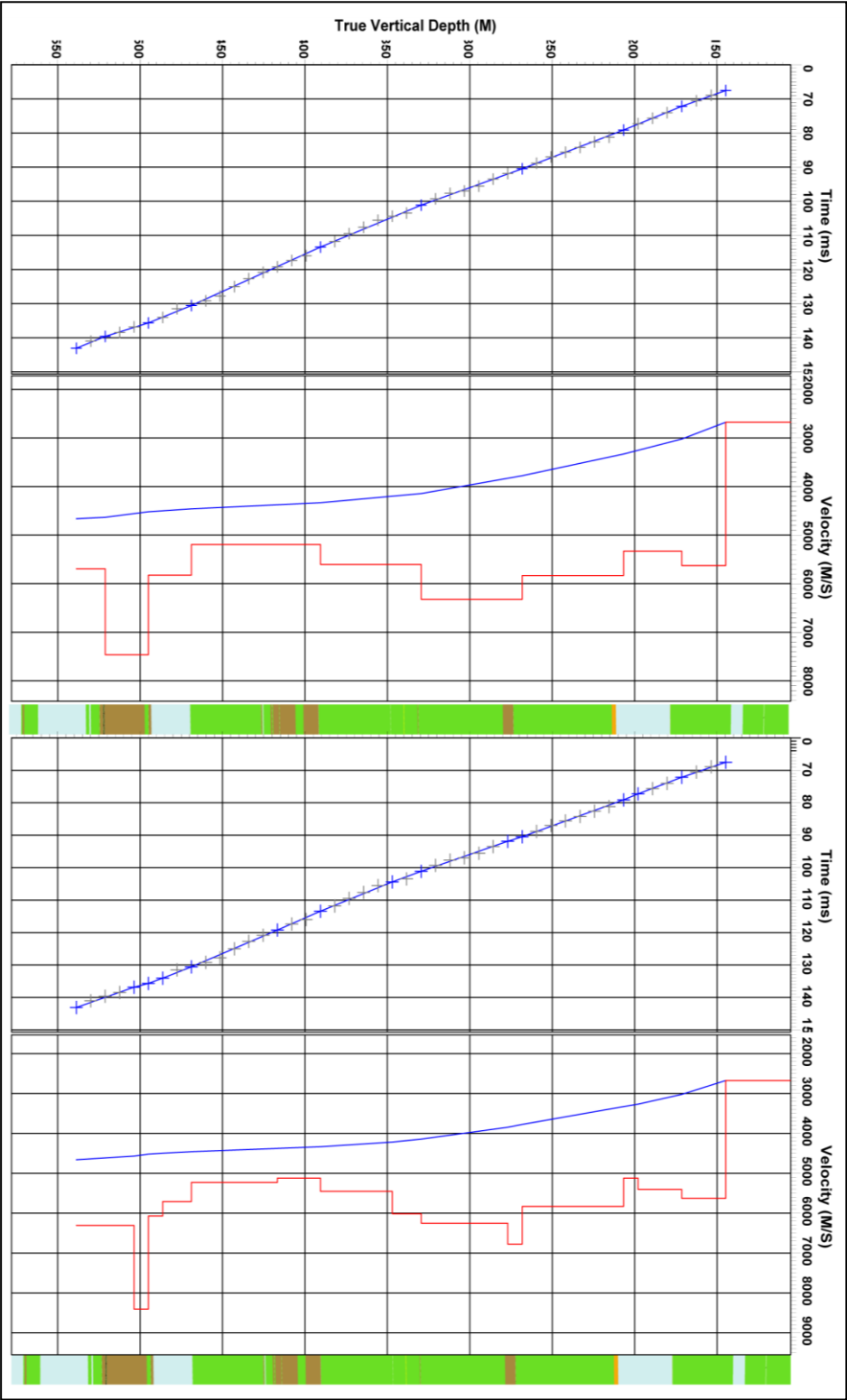
Figure 6-9. Two ZVSP velocity profile schemes for BH52 picked using 10 m spaced hydrophone data and borehole geology as a guide for intervals. Left scale is true vertical depth (TVD), whereas the geology log was measured in borehole depth and has been stretched to fit. The data is also tabulated below in Table 5.1.

Table 6-1. BH52 layer velocities for models 1 and 2 (Figure 6-9).

Measured Depth		True Vertical Depth	First Break Pick	FB Pick Corrected (Datum)	Velocity Interval	Velocity Average	Velocity RMS
A	160	144.7	67.52	54.09	2675	2675	2675
	190	171.4	72.16	58.84	5628	2913	3022
	230	206.7	79.11	65.46	5331	3158	3329
	300	268.2	90.47	76	5832	3529	3777
	370	329.5	101.14	85.7	6323	3845	4144
	440	390.6	113.42	96.6	5604	4043	4334
	530	468.9	130.58	111.68	5193	4199	4459
	560	495	135.68	116.16	5825	4261	4520
	590	521.2	139.62	119.67	7464	4355	4633
	610	538.7	143.1	122.74	5693	4389	4662
B	160	144.7	67.52	54.09	2675	2675	2675
	190	171.4	72.16	58.84	5628	2913	3022
	220	197.9	77.26	63.74	5404	3105	3268
	230	206.7	79.11	65.46	5121	3158	3330
	300	268.2	90.47	76	5832	3529	3777
	310	277	91.86	77.3	6777	3583	3847
	370	329.5	101.14	85.7	6252	3845	4145
	390	347	104.38	88.61	6017	3916	4219
	440	390.6	113.42	96.6	5454	4043	4335
	470	416.7	119.22	101.7	5121	4097	4378
	530	468.9	130.58	111.68	5229	4199	4460
	550	486.3	134.06	114.73	5710	4239	4498
	560	495	135.68	116.16	6071	4261	4521
	570	503.7	136.84	117.2	8405	4298	4570
	610	538.7	143.1	122.74	6307	4389	4662

6.1.8 Wavefield separation

Two processing attempts were made on this data set. The first attempt used a standard processing approach where the data were collated into a common shot gather and processed as a single ZVSP profile using median filters. This approach had adverse effects with smearing of high amplitude noise leaving artefacts from tube-waves. These artefacts can be traced through panels b) to e) of Figure 6-10. The second processing attempt, performed tube-wave wavefield separation on common shot records then, processed the remaining wavefields as a common shot profile. This avoided the previous described amplitude anomalies at the cost of extra

processing time, however, it did not eliminate all tube-wave processing artefacts. Raw shot gathers, receiver gathers, wavefield separated gathers and VSP CDP profiles of the second processing run can be found in Appendix V.

In general the wavefield separation of tube-waves required three steps; 1) Flattening of the down-going tube-waves and subtraction by a 2D median filter, followed by, 2) an identical 2D median filter applied to flattened up-going tube-waves. Prior to each median filter automatic gain was applied to enhance and balance primary and reflected waves against the tube-waves. Automatic gain was removed after each filter operator and a gentle band-pass filter applied prior to the next step of processing. Down-going body waves were then removed and finally 3) an *f-k* filter was applied to remaining wavefields to remove remnant tube-waves and down-going events.

A similar median filter approach was used to remove the down-going primaries leaving the up-going primary reflected waves. A top mute was applied to the data which were then converted to two-way travel time, a mild 3 trace mix and optimised band-pass filter were applied to enhance reflections. The resulting ZVSP wavefield separated gather is shown as Figure 6-11. This figure shows good correlation with the reflectors intersecting the borehole log at geology changes.
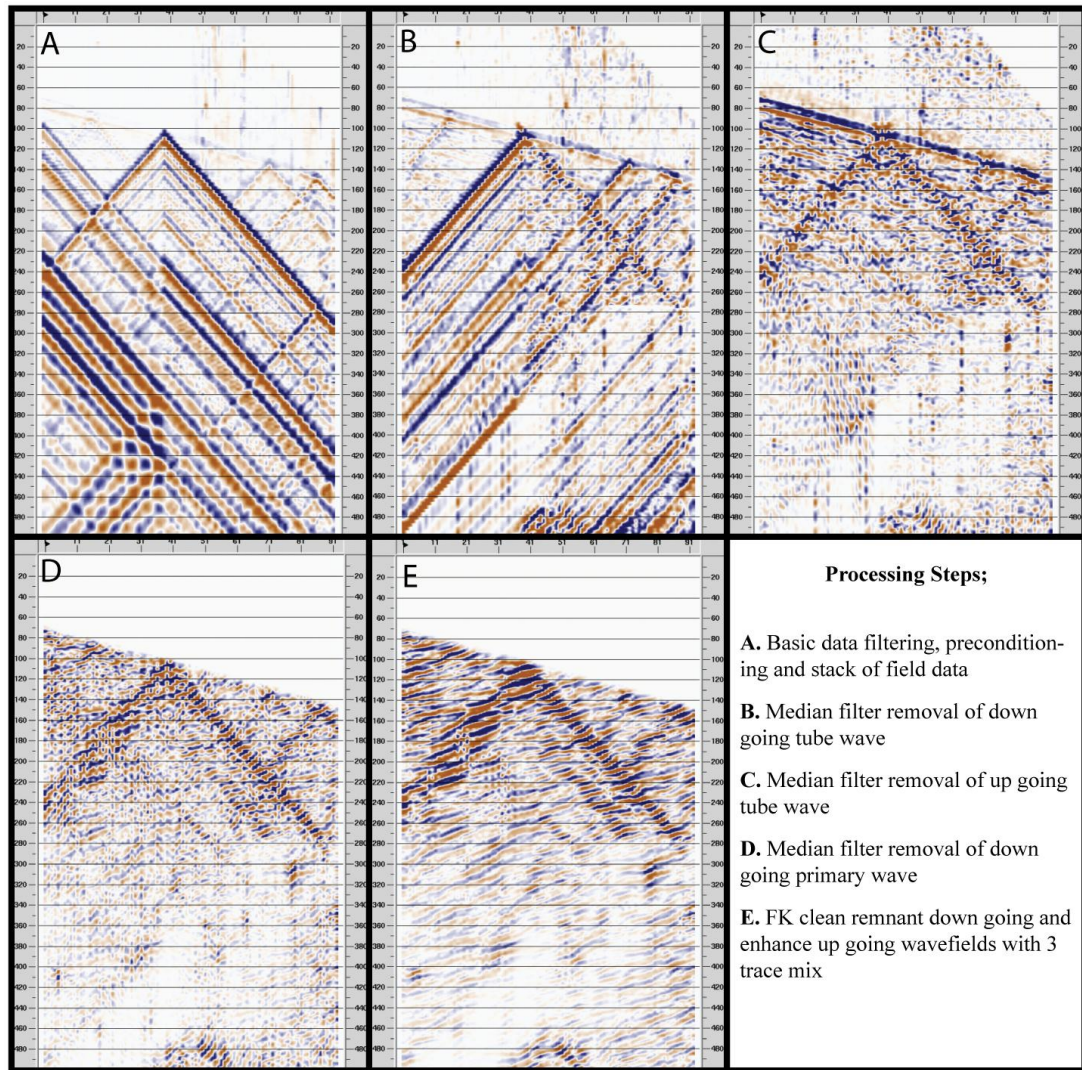
Figure 6-10. Wavefield separation processing steps applied to common shot gather ZVSP profile. Strong amplitude tube-wave and inconsistent balancing of traces between the 5 and 10 m infill stations has caused amplitude artefacts.

6.1.9 ZVSP

The final wavefield separated data used the above median filtering scheme but was applied in the FFID domain. The resulting TWT up-going profile, corridor profile and corridor stack are presented below in Figure (6-11). The graphical geology log has been superimposed behind the profiles. This is not consistent with a quantitative analysis approach as the VSP is in time and the geology in depth. For qualitative purposes we can assume an average velocity of 5870 m/s from the top receiver at 160

m (140 ms TWT) to the bottom receiver at 615 m (295 ms TWT) and stretch the geology log to fit between these known points. Amplitudes have been enhanced in the corridor display and shows 4 good continuous reflectors and several less coherent events. The high amplitude anomaly encircled by ellipse A (Figure 6-11) is a tube-wave artifact which originated by the fault which crosses the borehole at 200 ms. The conversion to TWT enhances the error in FB picks and manifests as disrupted and wavy reflectors as seen in ellipse B (Figure 6-11).
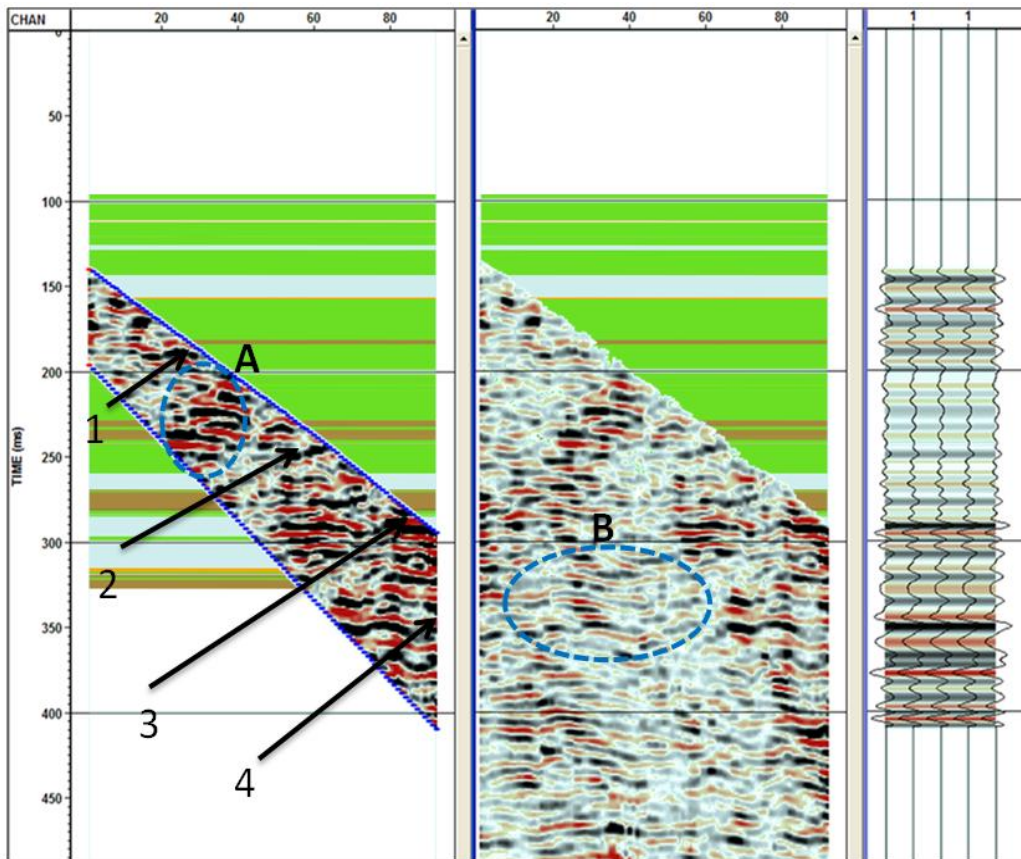
Figure 6-11. Zero-offset hydrophone VSP data for BH52, Agnew-Wiluna. The central panel is the enhanced TWT wavefield separated up-going profile.

Stacking of the corridor profile has reduced the high amplitude tube-wave anomaly as these are dispersed across varying times (ellipse A), as opposed to the P-wave reflections which occur at the same TWT and constructively stack. The corridor stack can roughly be divided into an upper reflective section above 200 ms, a lower amplitude section between 200 to 285 ms containing multiple reflectors, and a section below the strong reflection at 290 ms which is of lower frequency but

contains higher amplitudes. This lower section could be divided into two subdivisions above and below the reflection at 360 ms.

6.1.10   WVSP

The hydrophone string was positioned between 160 to 390 m for the WVSP. This has an in-hole receiver aperture of 230 m compared to 455 m in the ZVSP. However, laterally the extent of the WVSP was ± 500 m at 10 m shot stations. As such the WVSP tests more ground away from the borehole and reflectors will be illuminated from many angles to create a more accurate image of the structure.

The wavefield separation methodology designed for the ZVSP was adapted to the WVSP. Similar reflectors observed in the ZVSP were observed in the near offset WVSP gathers and these reflectors could be traced to far offsets. Amplitudes were similar to the ZVSP at near offsets, however, the SNR of primary to induced tube-wave amplitude did improve with the larger offsets. It is possible the variation of tube-wave amplitude with offset is due to the angle of incidence of the incident body-waves (Castagna, 1993), as well as body-wave amplitude radiation losses (signal strength) with offset.

6.1.11   Migrated Data

Kirchhoff VSP depth migration was applied to the up-going wavefield profiles to produce depth migrated images. A 1-D average velocity model was calculated from the ZVSP FB times and depths and is shown in the right side of Figure 6-12. This model was used for initial depth migration of the VSP gathers and time-to-depth conversion. The corresponding ZVSP and WVSP depth migrated sections are shown below in Figures 6-13 and 6-14. Mutes have been applied during the migration to restrict the image to only areas where it is possible to image given the geometry of the receivers and source. This creates an image cone around the borehole.

Prior to migration of the ZVSP, a surgical mute was applied to remove tube-wave artefacts. The resulting migrated ZVSP image (Figure 6-13) shows reflectors dipping

between 45 to 30 degrees to the west. A discontinuation through the section can be seen cutting through the borehole at 420 m vertical depth. The discontinuity propagates through the section vertically as a neutral (white) band. Frequency content is high with average wavelengths of 20 m, thus layers as thin as 5 to 10 m should be detectable. Imaging laterally beyond the extent of the borehole has not been achieved.
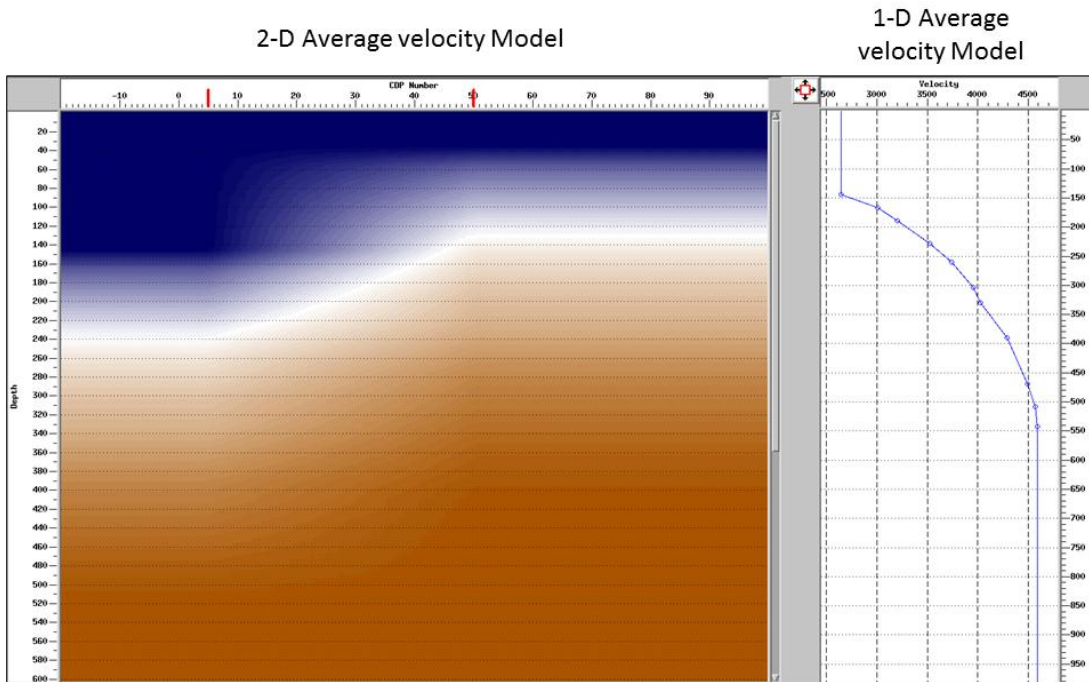
Figure 6-12. 1-D and 2-D Average velocity model used for pre-stack VSP depth migration of the Agnew-Wiluna hydrophone VSP profiles.

The frequency content between the ZVSP and the WVSP are similar, as well as the position of reflectors, however, the continuity and dip angles are steeper closer and above the hole in the WVSP, when compared to the ZVSP image. The migrated ZVSP image shows all reflectors as being orthogonal to the borehole track.

It was thought the wavefield separated WVSP up-dip shot records were contaminated with refracted arrivals, so several migration panels, with reduced up-dip shots were produced. These are shown as Figure 6-14.
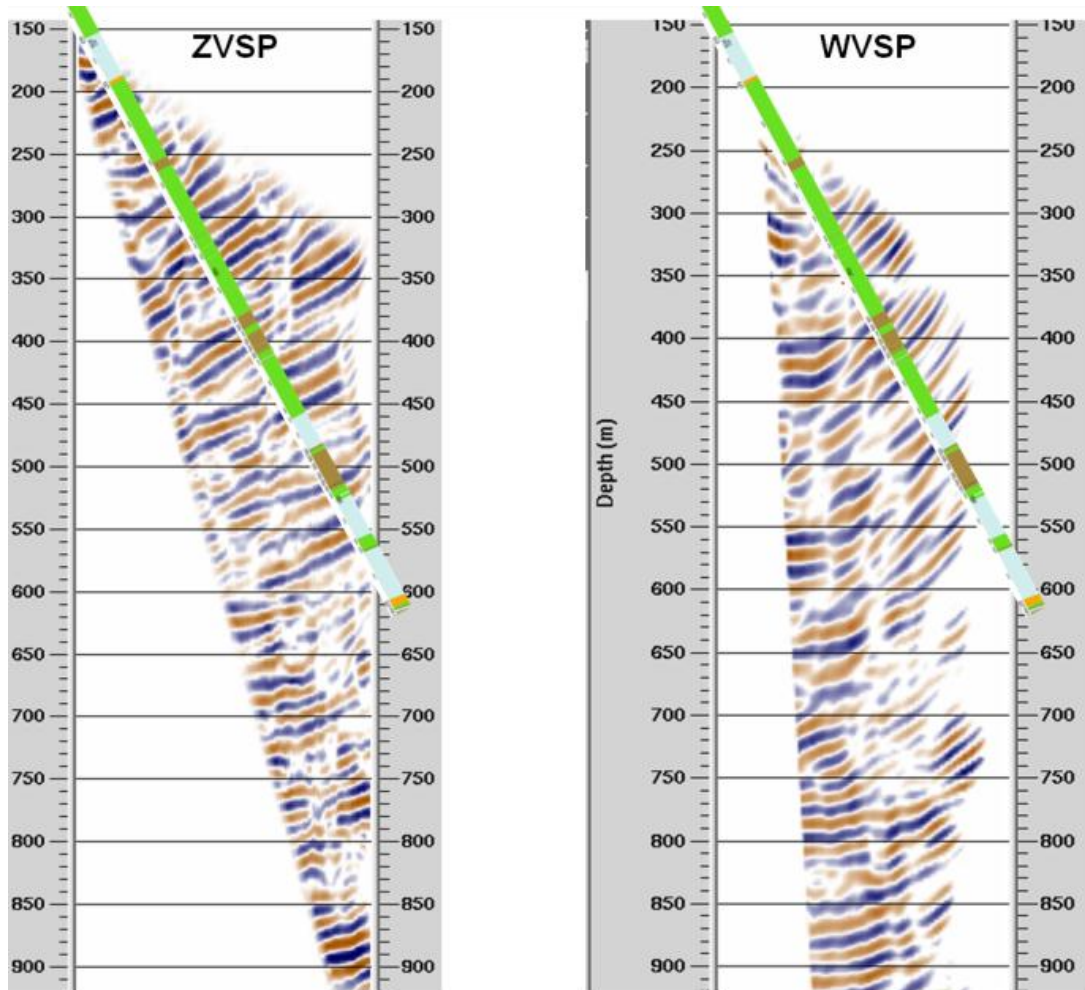
Figure 6-13. Migrated ZVSP (left) and WVSP (right) images overlaid with borehole geology. Images are approximately 1:1. Hydrophone coverage is between 145 to 550 m at 5 m stations for the ZVSP and 145 to 130 m at 10 m stations for the WVSP. The WVSP consists of offsets ± 500 m (from collar) at 10 m stations in the up and down dip directions.

The reduced up-dip migration panels are all very similar below 550 m. In general, continuity of reflectors increases as offset decreases, all panels have steeper dips in the up-dip portion of the sections than the ZVSP image. It is difficult to assess which panel is the most accurate but one could eliminate the + 500 m image.
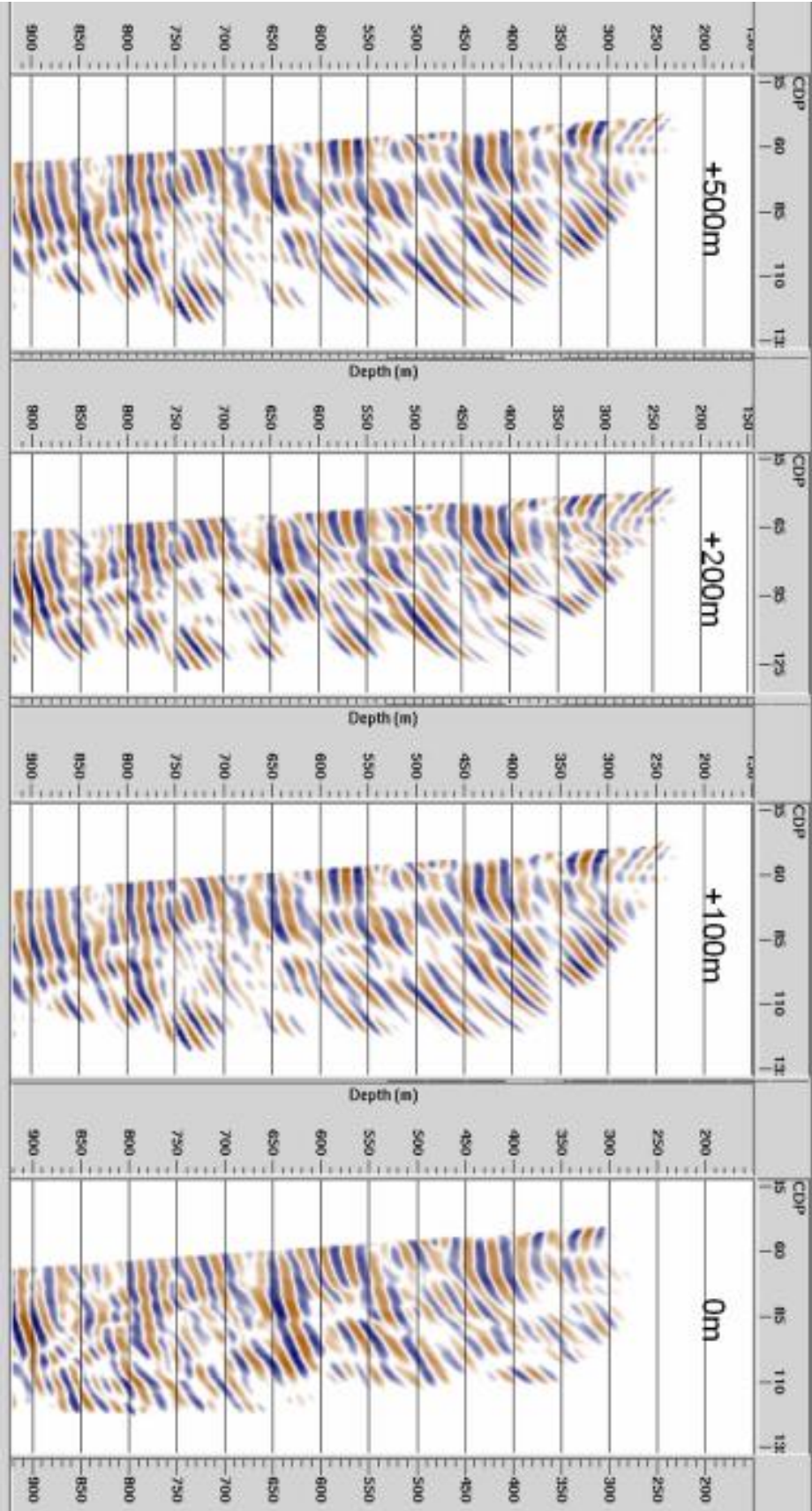
Figure 6-14. WVSP migration panels with limited up-dip offsets. From left to right the panels have up-dip offsets included to a maximum of +500, +200, +100 and 0 m. Down-dip offsets include from 0 to -500 m. Images are approximately 1:1.

Knowing that the general structure in the area is dipping to the west and the regolith cover is shallower at the borehole (46 m) than what was determined in the 2D surface seismic refraction analysis (80 m), the 1-D average velocity model was extended to a dipping 2-D model. This was done by increasing the overburden depth to 80 m down-dip at 250 m. The 2-D average velocity model is shown in Figure 6-12. This model was then used to produce WVSP depth migrated images of Figure 6-15. Here the contributions of the up-dip shots have been limited in several panels. Field nomenclature has been used to describe the limit of offsets used, i.e. the 1000 shot series are all the shot points in the up-dip direction (line 1), 2000 shots are all the shot points in the down-dip direction (line 2), 1000-1300 refers to the first 300 m of shot points along line 1.

A common artefact observed in VSP migration images is the apparent flip – flopping of reflections about the borehole axis. This is due to the limited angular coverage of surface source positions and the non-uniqueness of where reflectors can originate. Also apparent in the upper section of the borehole, are near field amplitude effects which have not been addressed by the Kirchhoff algorithm. Both these artefacts in general, illuminate the upper part of the borehole path with higher amplitudes and reflections dipping in the opposite direction than expected. This is particularly strong in our case where we have included shots from the up-dip direction.

To understand the origin of the reflections with relation to the geometry of the WVSP survey, I modelled seismic travel-times at the limits of the survey. The models and straight ray travel time analysis curves are shown in Figures 6-16a to 6-16e. It can be seen that, in a steeply dipping case, with a 75 degree reflector, a maximum down-dip offset of 500 m and an up-dip offset of 300 m, all reflection events originate from the up-dip side of the borehole (Figures 6-16a to 6-16c). Also determined through modelling was the maximum reflector dip angle, at which, reflections will be imaged beneath the borehole (Figure 6-16d and 6-16e). This occurs at approximately 37 degrees. Thus, it is unlikely that shallow dips (< 35 degrees) can exist in our migrated section above the borehole track and vice versa, steep dips (> 45 degrees) should not be presented below the borehole track. As such, we can eliminate migrated sections with these attributes as not representative of the geology.
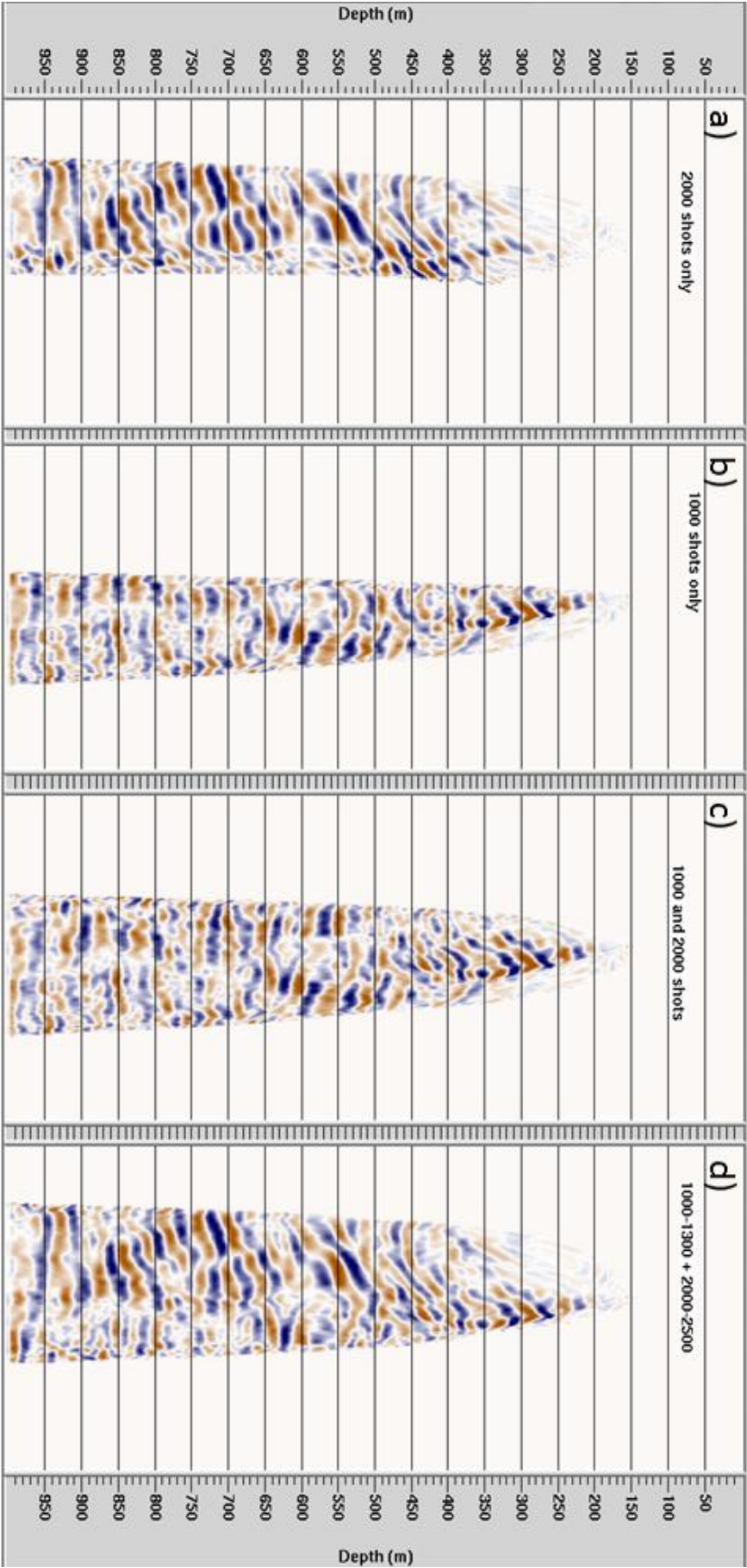
Figure 6-15. WVSP depth migrated images using the 2D velocity model and with limited shot point inputs. a) Down-dip shot points only b) up-dip shot points only c) all shot points and d) all down-dip and 0 to 300 m up-dip shot points included.

In essence, the Kirchhoff migration algorithm, takes a seismic element (amplitude, time and source receiver pair) from a trace and remaps the event to all neighbouring traces (different offsets) along an isochron surface (related to sample time and source receiver locations), in the same way an ellipse can be drawn on a grid with a string and two pins. This is done for all seismic elements and stacked to reinforce the true location of the reflection. This is why migrated sections "smile" at the edge where fold is low, and in the case of VSP migration images often appear smeared. In practice, the mapping only needs to be conducted over a section of the isochron away from the CDP. A tool in the migration imager's tool box, which helps restrict smiling, smearing and correctly position the seismic elements, is the ability to restrict and focus the migration aperture along the isochron. Thus, we can restrict the migration and imaging to certain dips. Multiple apertures were tested with the walk away data. These are shown in Figures 6-17a and 6-17b.

Reflection events common to most of the images occur at 450 and 565 m depth where, there are intersections of the massive mafic and ultramafic units at 450 m and alternating felsic and mafic packages at 565 m. There are many other reflections in the images that can be correlated to the borehole geology and these types of contacts.

a)

b)

c)
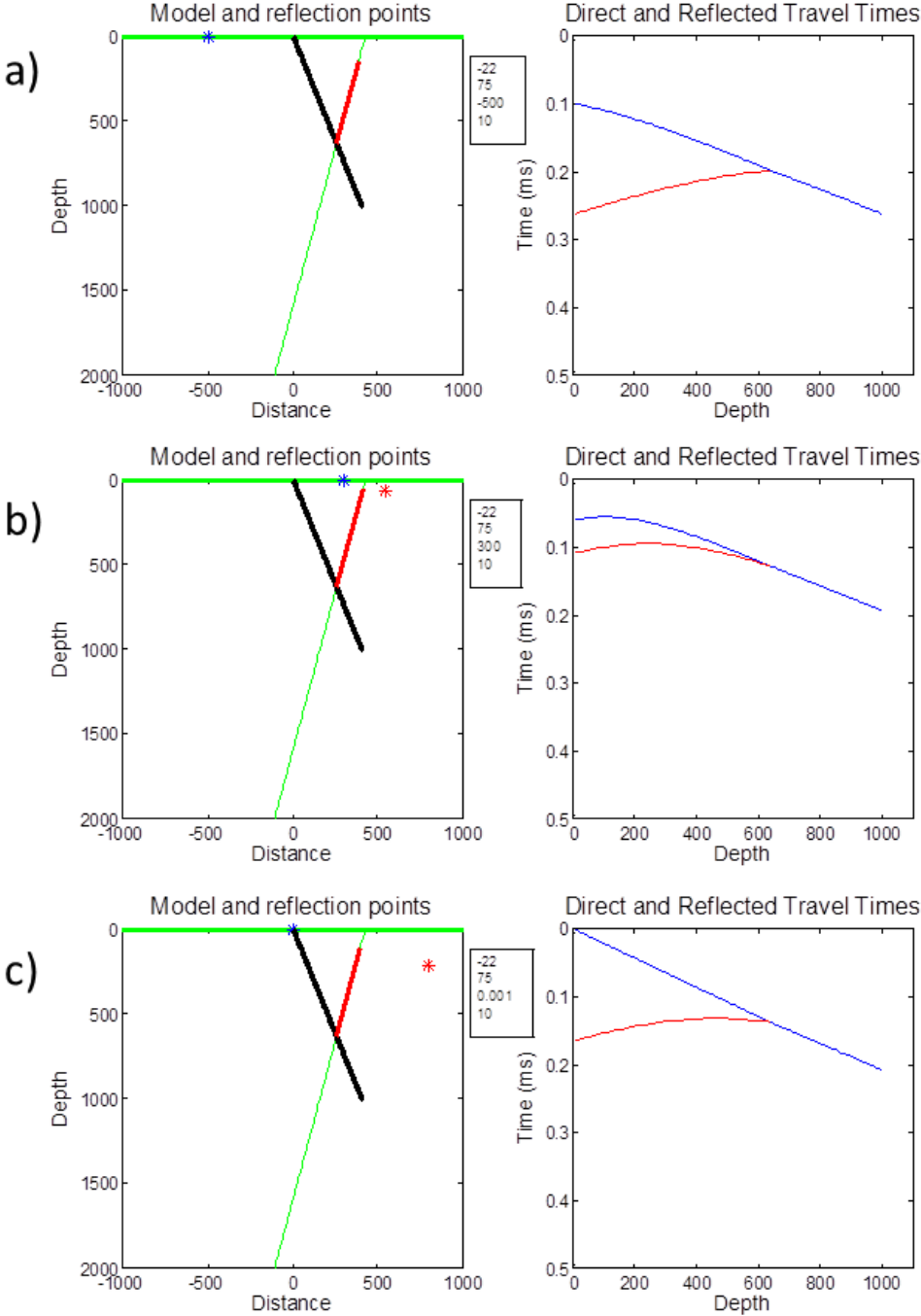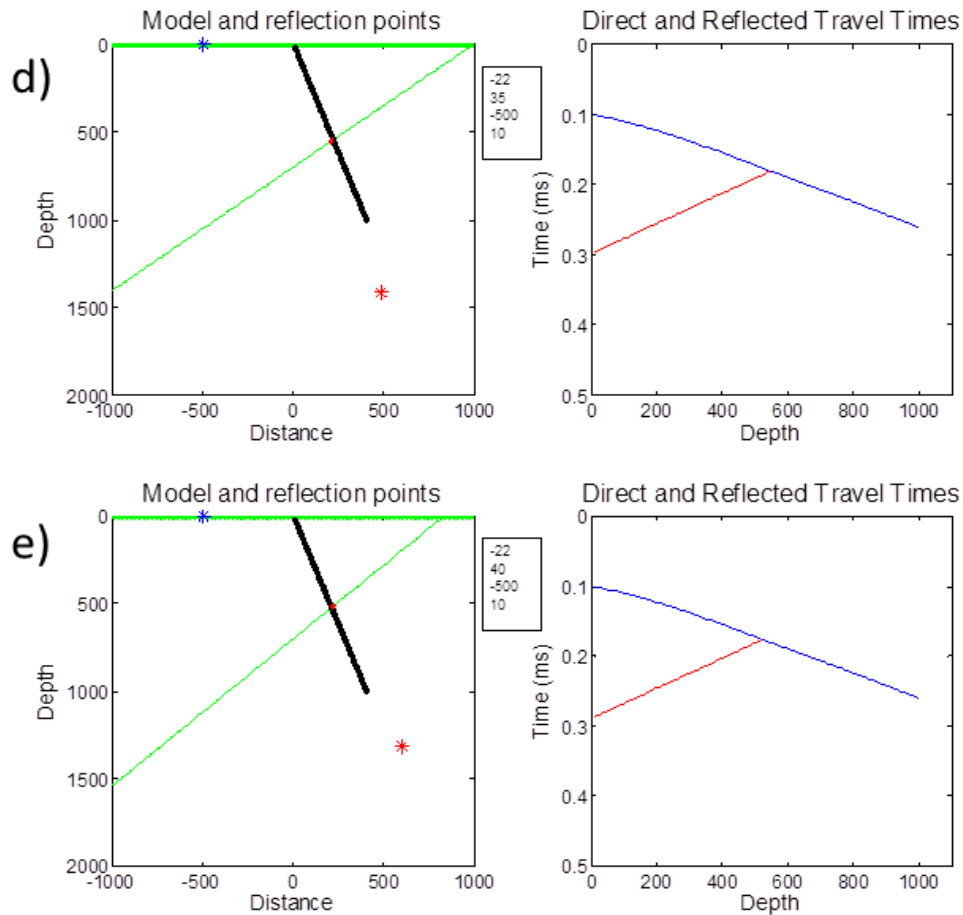
Figure 6-16. Straight ray travel time modelling of the direct and reflected arrivals for different shot locations and dips representative of the Leinster WVSP survey. Plots a), b) and c) are for a steep 75 degree reflector and -500, +300 and 0 m offsets respectively. Plots d) and e) use a shot point of -500 m and varying reflector dip of 35 and 40 degrees respectively. All models use a borehole dip of 68 degrees. Shot point – blue asterisk, Image point – red asterisk, borehole receivers – black, reflection points – red line; direct travel time blue and reflection travel time red.
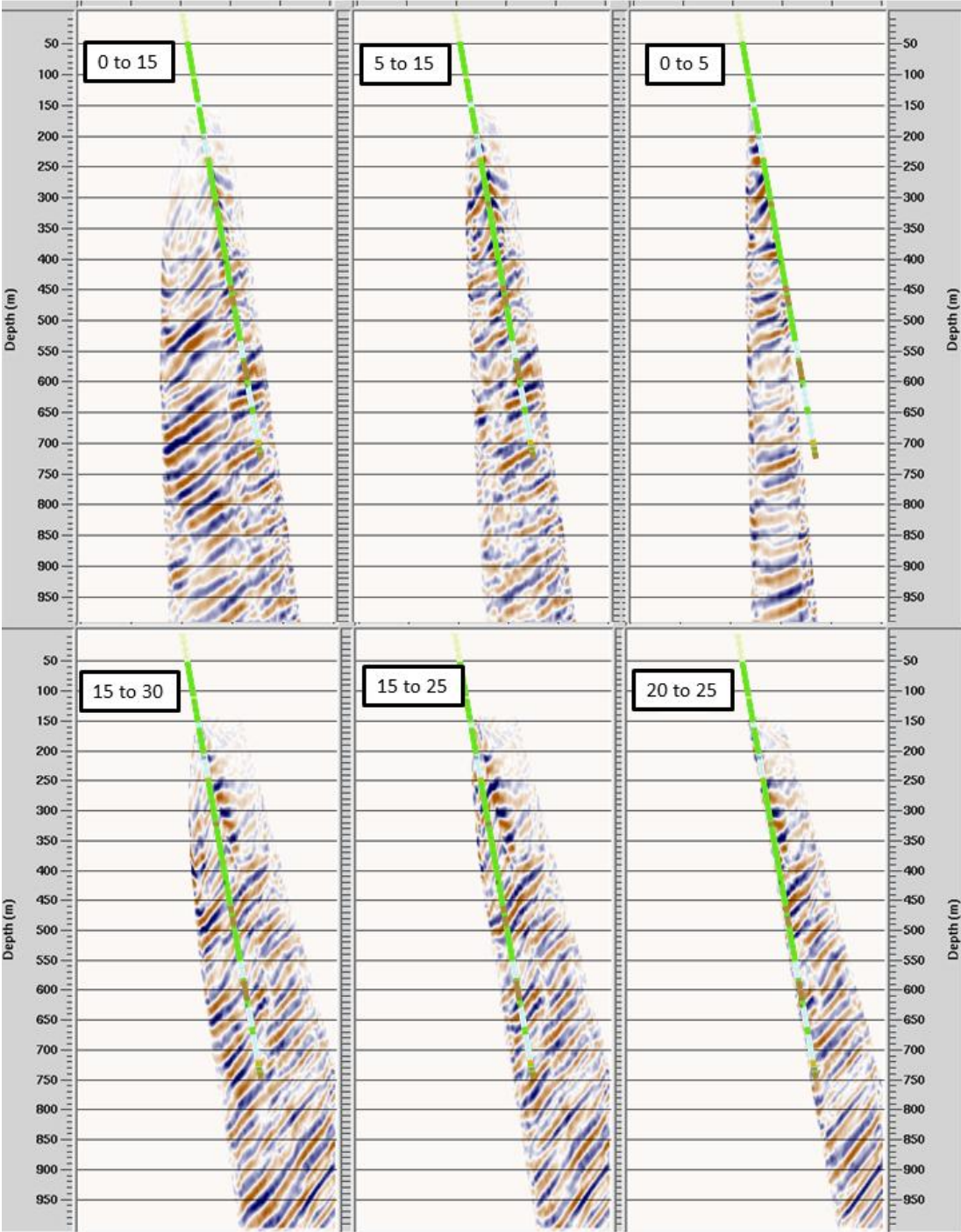
Figure 6-17a. WVSP depth migration aperture tests from 0 to 30 degrees.
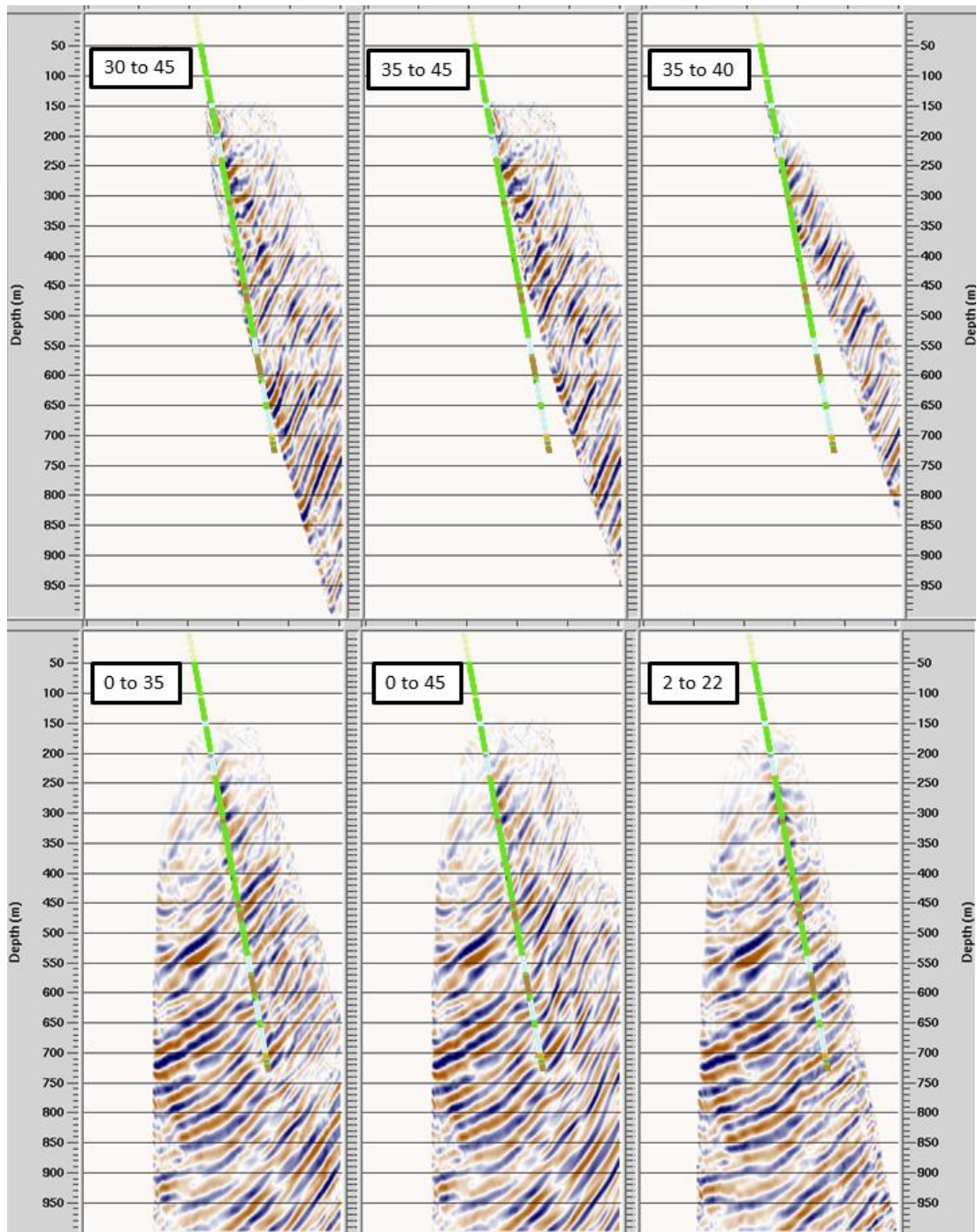
Figure 6-17b. WVSP depth migration aperture tests from 0 to 45 degrees.

6.1.12   Seismic Character of Agnew - Wiluna test site

There is a common pattern in the reflections observed in the various WVSP migration aperture images. Namely; a bright reflector which occurs at 450 m followed by a package of reflectors from 560 m to 750 m. Correlation of the geology log to the reflectors indicates reflections occur at the base of the felsic and at the base

of UM units. Without Petrophysical data (density, FWS or ultra-sonic PT) and poor interval velocities from the VSP it is difficult to confirm the origin of the reflectors. However, from the Nafe-Drake curve (Chapter 2) we know felsic units have a lower acoustic impedance than mafic units and from Salisbury et al (1996) we know a reflection coefficient between felsic and mafic units is approximately 0.06. There is also often a thin sediment package of assumed, lower density and slower velocity, at the base of the felsic units in the area (indicated by orange in the geology log) which will add to an impedance contrast. These facts together will explain the reflections originating at the intersection of felsic and mafic units observed at 565 m depth. The reflection from the base of UM into basalt (450 m) however is a little more difficult to explain as typically the velocity contrast between these units is low.

Laboratory experience of taking ultra-sonic measurements of ultramafic rocks from Kambalda, some 400 km to the south, is that, ultramafic rocks in the Yilgarn can have a slower P-wave velocity than their mafic counterparts, and their texture is often very different. The rocks of the Leinster mine area, 5 km to the north, have been subjected to peak metamorphic conditions of about 550°C and 3 kb pressures. The igneous precursors to the Agnew ultramafic rocks include spinifex-textured komatiites, olivine orthocumulates, olivine-sulphide cumulates (net-textured or matrix ore) and coarse-grained olivine accumulates. These have been almost entirely reconstituted mineralogically and texturally during metamorphism and have a penetrative deformation, although igneous textures are preserved in the olivine-sulphide cumulates and olivine accumulates Gole et al. (1987). Such alteration in texture and mineral alignments is likely to cause changes in seismic propagation and reflectance. This is an area of interest and discussion for hard rock seismologists and needs to be addressed with further petrophysical investigations.

Discussions with BHP structural geologists, note that there is a strong dominant foliation in the area which is dipping at about 30 degrees. However, structurally the lithology cross-cuts this foliation at a higher angle of approximately 65 degrees.

The reflector dip in the surface seismic (30 degrees) is in agreement with the shallow dips observed below the borehole in the WVSP images. However, within the WVSP there is a dispute with the dips above and below the borehole. The disagreement is

likely due to the complex structural and alteration effects in the area complicating the seismic response. It is possible that the lower frequency surface seismic and WVSP is responding to the pervasive foliation of the units and the higher frequencies observed in the WVSP, particularly above the borehole, is responding to structural features.

6.2 Marthas vineyard – Kambalda

Kambalda is a world class nickel and gold mining district with a pre-mined reserve of approximately 35 million metric tons containing 3 per cent nickel (Gresham, 1986; Stone and Masterman, 1998). It is located in the south-central part of the Norseman-Wiluna Greenstone belt of the Yilgarn Craton, Western Australia (Figure 6-18) and is considered a type-section for Archean komatiite associated nickel sulphide deposits. Regional scale tectonics control the architecture of Kambalda which is dominated by north-south faulting and folding (Beresford et al., 2002) which has formed the Kambalda Anticline. A fold structure within this forms the Kambalda dome and is shown in Figure 6-18. The Kambalda Dome plunges to the north, it is centred with a felsic intrusion (granite) and is truncated to the east by the Lefroy fault (Greenhalgh et al., 2000; Stone et al., 2005). Volcaniclastics and komatiites overlie the flanks of the dome and have undergone multiple suites of mafic (dolerite) and felsic (granite) intrusions as well as metamorphism between the upper greenschist to lower amphibole facies (Stone and Archibald, 2004). The generalised stratigraphic column of Kambalda is shown in Figure 6-19. Exploration targets nickel sulfides which accumulate at the base of the Kambalda Komatiites (Tripod Hill and Silver Lake members) which are in contact with the top of the Lunnon Basalt. Two geological cross-sections transecting the north and the south of the Kambalda Dome are shown in Figure 6-20. Cross-section B-B′ in the south illustrates the structure and lithology of the Kambalda Dome. Cross-section A-A′ in the north is more complex and shows significant reverse faulting and stacking of sequences.

In 2009 a large mine-scale exploration 3D seismic survey which covered 27.4 km^2 was conducted to the north of Kambalda. This survey is the largest Australian hard rock 3D surface seismic survey to date. Shown in Figure 6-21 is the location of the survey area, the extent of the 3D surface seismic receivers, the surficial regional geology, the collars of boreholes BH1 and BH2, and the location of cross-section A-A′ some 4 km south of BH1. The survey area is surrounded by active mining tenants, however, the site is considered in the green-fields exploration phase with only boreholes BH1 and BH2 having been drilled at the time of this research. Boreholes

BH1 and BH2 were diamond core drilled with PQ drill rods (123 mm diameter and uncommon for deep holes in the area) to target depths of 1061 m and 1204 m respectively. Hydrophone VSP surveys were conducted in both boreholes with the primary aim of depth calibrating the 3D surface seismic. Secondary to this, was to determine the origin of reflectors observed within the 3D seismic data. Initial borehole targeting was based on early inspection of the 3D seismic time volume.

BH2 did not intersect the Lunnon Basalt, but paralleled a shear and remained in granite for the majority of the hole (770 m). This was not considered representative of the regional geology profile and deemed unsuitable for time to depth calibration of the 3D seismic volume. BH1 also intersected 585 m of granite intrusion, however, it did terminate in a sequence of alternating basalts and granite.
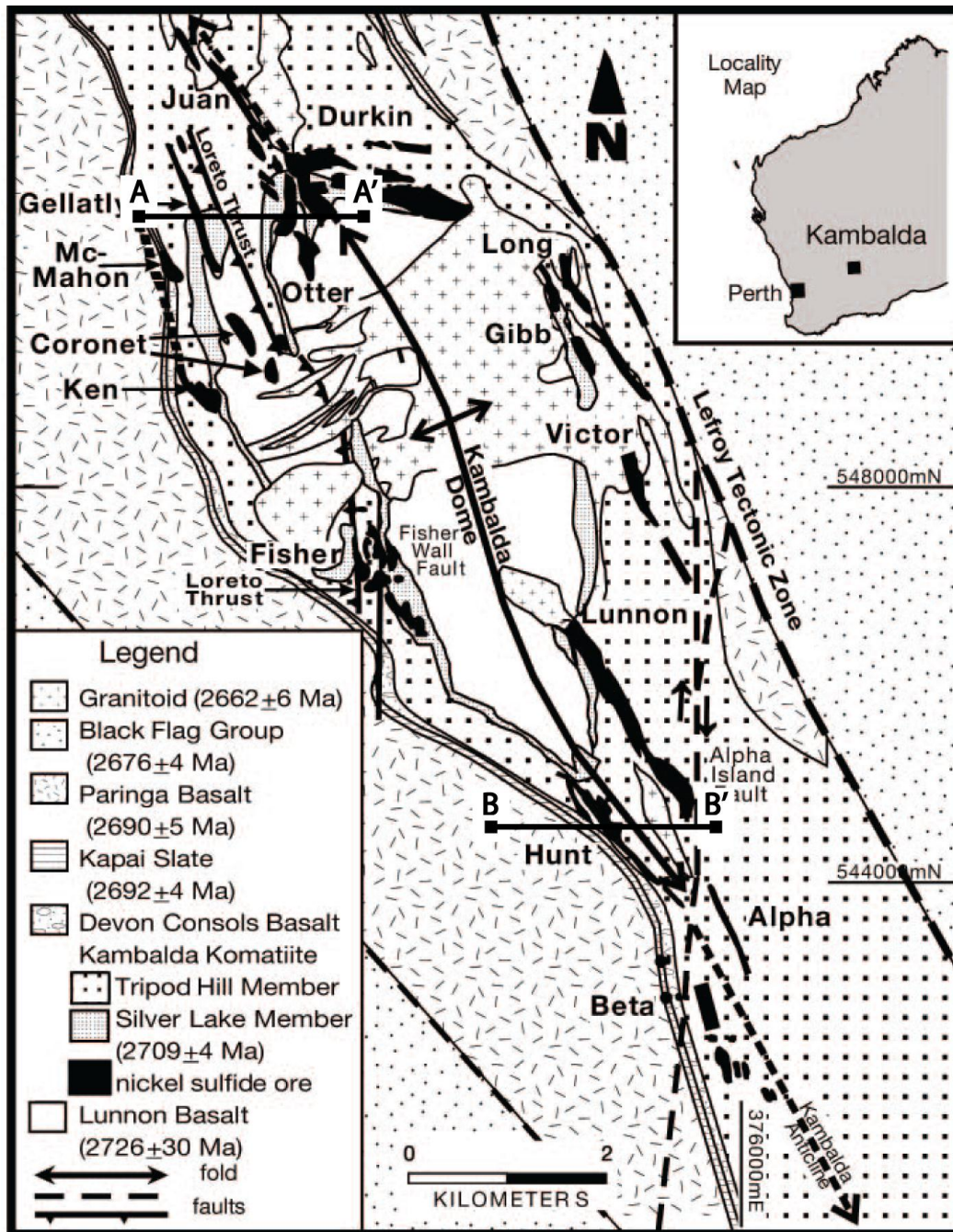
Figure 6-18. Regional structure and surficial geology of Kambalda. Tectonics controls the architecture and formation of the regional NNW-SSE double plunging anticline which forms the Kambalda Dome. Locations of cross-sections A-A' and B-B' of Figure 6-20 are shown. The Kambalda test site is approximately 2 km north of the most northern extent of this map (modified from Stone and Masterman, 1998).
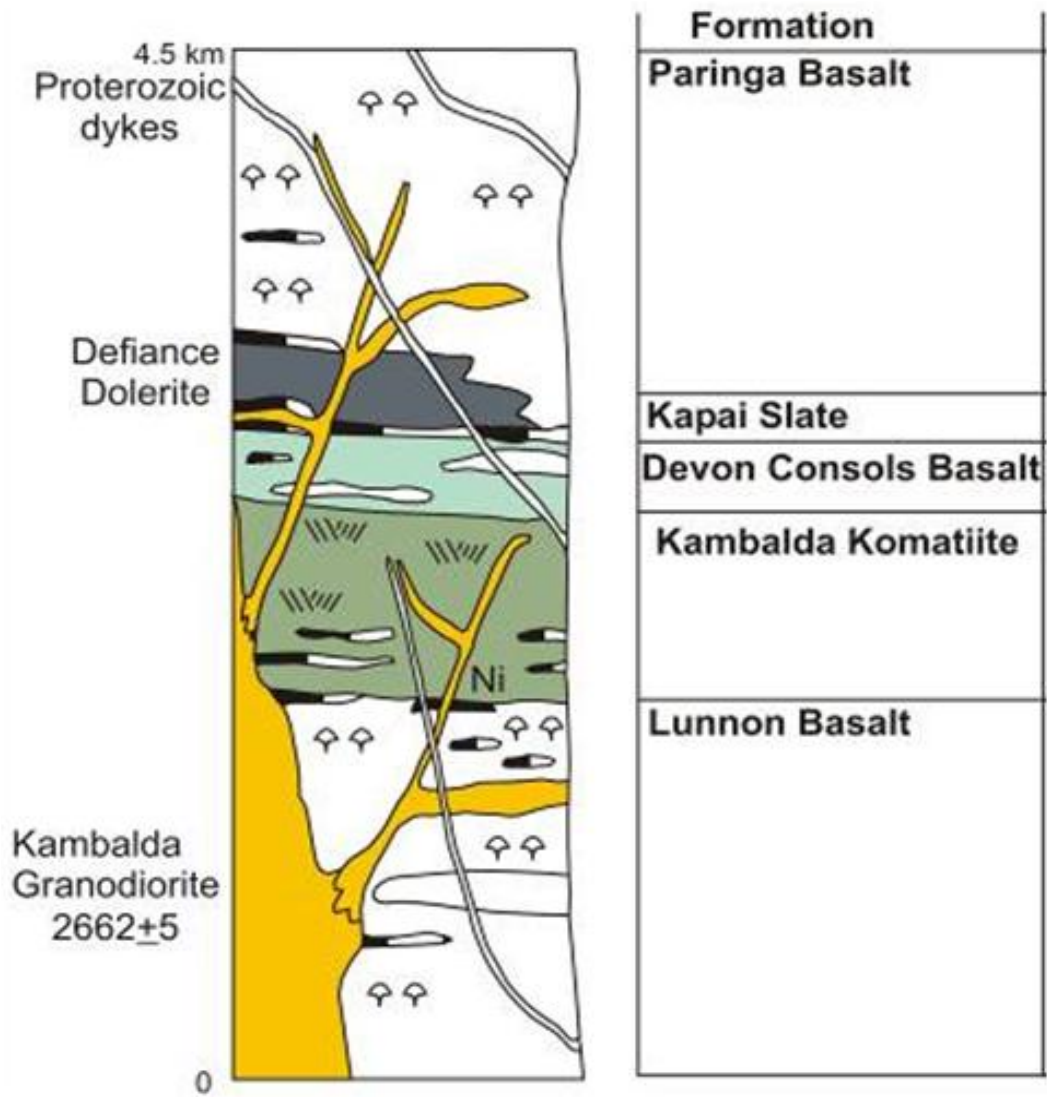
Figure 6-19. Stratigraphic column of the Kambalda Anticline.
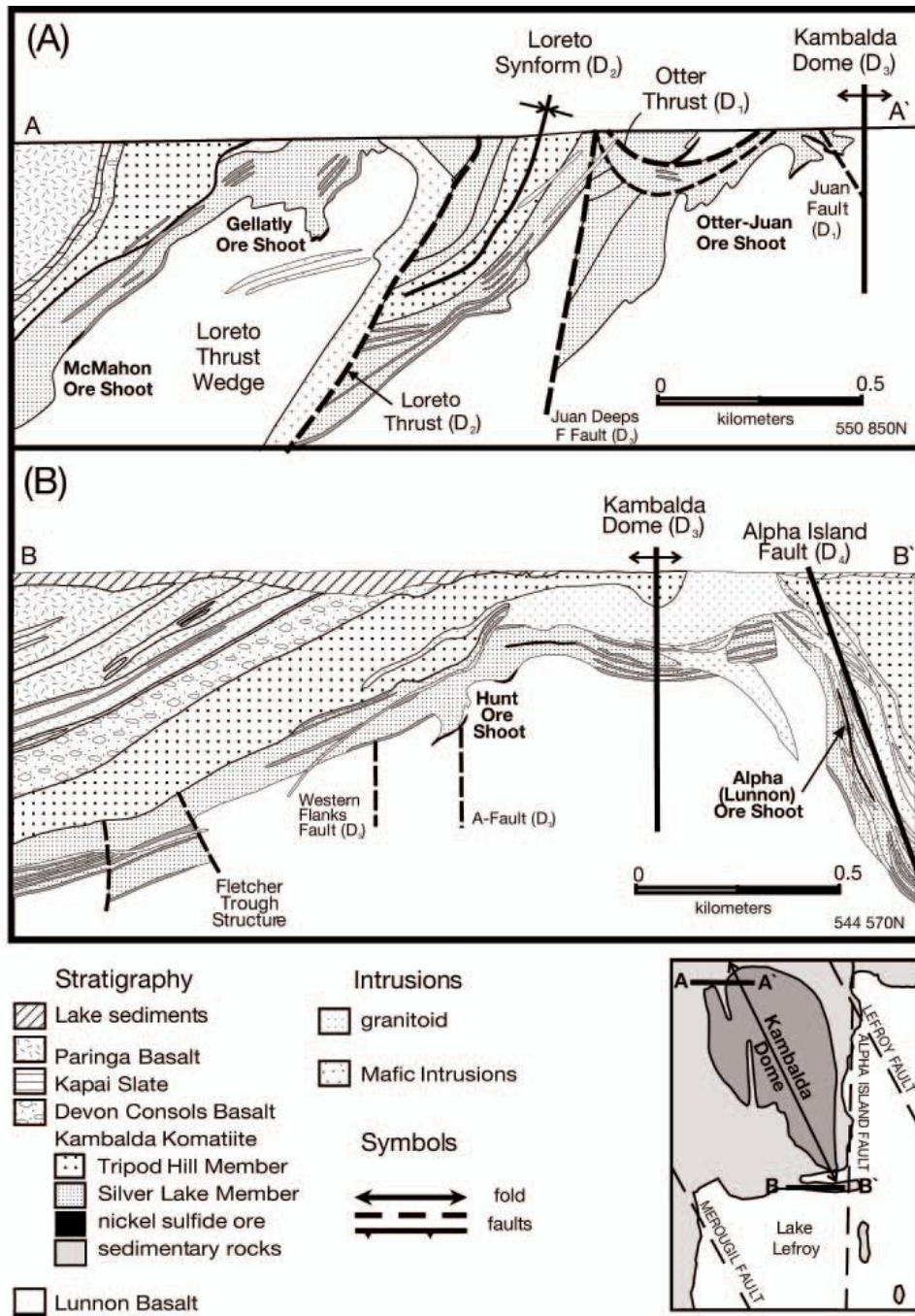
Figure 6-20. Cross sections of the Kambalda Dome (A) Cross section of the northwest flank of the dome across the McMahon, Gellatly and Otter-Juan ore shoots. West-dipping reverse faults have formed a series of wedges of the Lunnon Basalt footwall. (B). Cross section of the south part of the dome across the Hunt and East Alpha ore shoots on opposing flanks of the dome. The thickness of the ore shoots, sedimentary units, and felsic intrusions is exaggerated for clarity (from Gresham and Loftus-Hills, 1981; Archibald, 1985; and Banasik, 1996).
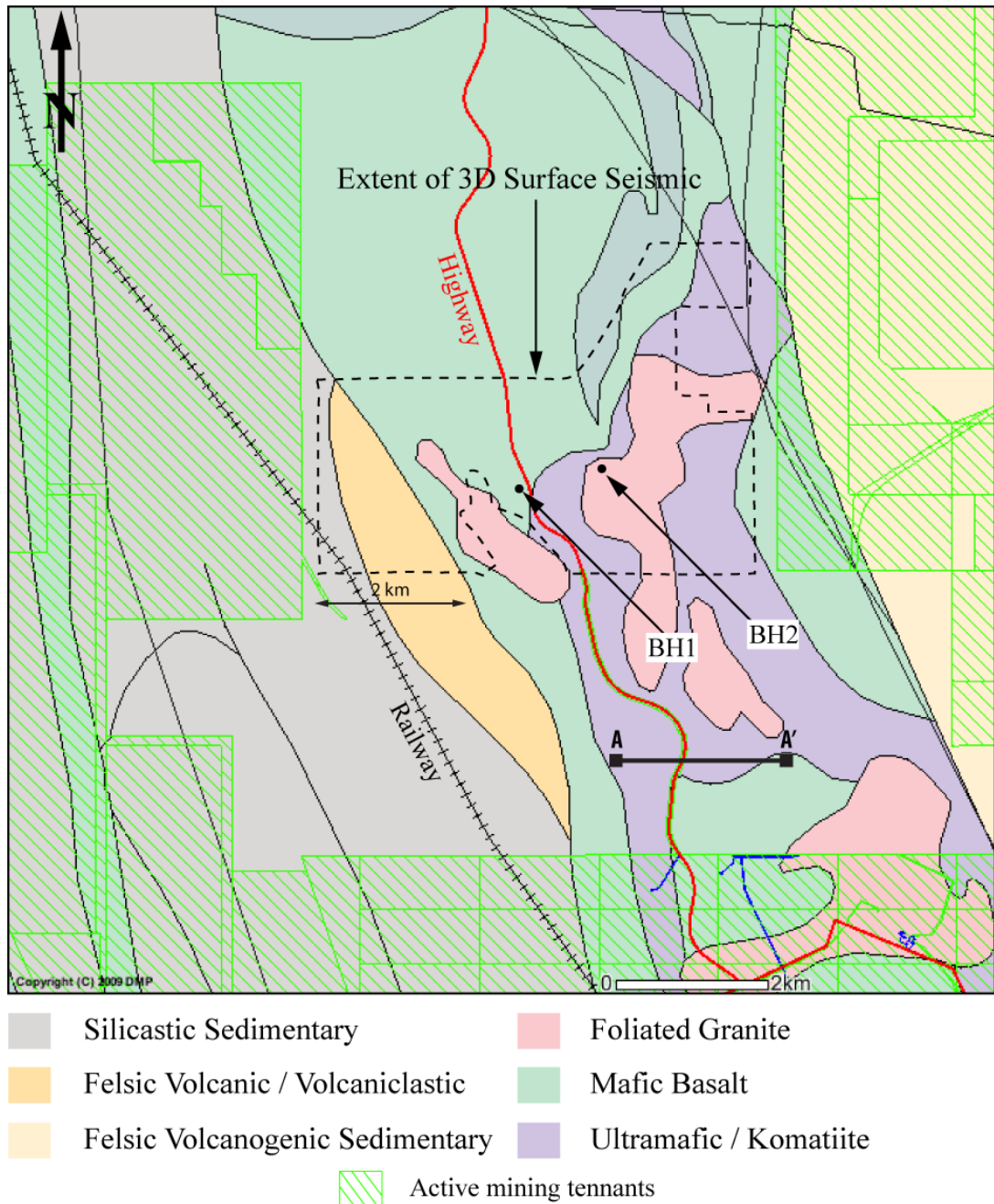
Figure 6-21. Regional geology and location of BH1 and BH2. Location map of BHP 3D seismic survey (open source department of mines and petroleum).

6.2.1 Petrophysics

Borehole BH1 was diamond core drilled with a PQ drill bit to a target depth of 1061 m. The borehole was logged with the following techniques: geologically, natural gamma, FWS, hydrophone VSP and 3C geophone VSP. Ultrasonic pulse-

199

transmission (PT) measurements were made on 47 core samples and BHP supplied specific gravity (SG which is equivalent to density) measurements on core samples at 1 m spacing in the basalt and ultra-mafic units. SG sampling, however, was not conducted on granite cores. FWS data were collected and processed by SURTRON Wireline Services. Inconsistency between the seismic velocity derived from the FWS and the VSP check-shot resulted in the FWS being reprocessed at Curtin University. Natural gamma was logged during the 3C geophone survey with a sensor combined into the tool. The PT tests were conducted at BHP Leinster during a site visit.

A generalised geology log is supplied below as Table 6-2 along with the average SG of the different rock units. Geology is graphically displayed alongside FWS, natural gamma, and a "blocky" density model in Figure 6-22. A blocky density log was created from SG measurements supplied by BHP and those taken on granite core samples during P-T testing. Gardners equation (Equation 6-1) was used to derive a density model from the FWS P-wave velocity. Gardner's equation is an empirical relationship that states density is proportional to the ¼ power of the P-wave velocity;

$$\rho = \alpha V_P{}^\beta$$

Equation 6-1

where α and β are constants dependant on geology. Typically α is 0.31 when VP is in m/s and β = ¼. These values generally work well in petroleum exploration. However in hard rock these require calibration to the geology. It was found that no single set of constants was able to accurately represent the geological contrasts seen in BH1. Multiple constants would be required to represent the main geological groups, felsic, mafic and ultramafic. As such the blocky density model developed from the SG core measurements was used to calculate an acoustic impedance (AI) log and reflectivity function.

Table 6-2. BH1 summary geology log and average SG of the rock units.

From	To	Rock Description	SG (kg/m³)
0.0	10.6	Lost Core	
10.6	18.0	Regolith	
18.0	23.6	Mafic Basalt - Devon's Consol	2.88
23.6	24.7	Intermediate Dolerite	2.68
24.7	28.0	Mafic Basalt - Devon's Consol	2.88
28.0	30.1	Intermediate Dolerite	2.68
30.1	123.8	Mafic Basalt - Devon's Consol	2.88
123.8	126.0	High MgO Mafic	2.95
126.0	147.3	Ultramafic	2.94
147.3	151.3	Granite	2.63
151.3	241.3	Ultramafic	2.94
241.3	828.3	Equigranular Granite (starts becoming more salt & pepper around ~800m)	2.63
828.3	887.9	Mafic Basalt	3.00
887.9	898.3	Equigranular Granite (more Salt & Pepper)	2.63
898.3	919.4	Mafic Basalt	3.00
919.4	940.1	Equigranular Granite (more Salt & Pepper)	2.63
940.1	971.4	Mafic Basalt	3.00
971.4	983.1	Equigranular Granite (more Salt & Pepper)	2.63
983.1	989.4	High MgO Mafic	2.95
989.4	996.9	Equigranular Granite (more Salt & Pepper)	2.63
996.9	997.5	Mafic Basalt	3.00
997.5	1007.3	Equigranular Granite (more Salt & Pepper)	2.63
1007.3	1011.7	High MgO Mafic	2.95
1011.7	1012.1	Equigranular Granite (more Salt & Pepper)	2.63
1012.1	1031.7	Mafic Basalt	3.00
1031.7	1035.6	Equigranular Granite (more Salt & Pepper)	2.63
1035.6	1040.2	Mafic Basalt	3.00
1040.2	1046.8	Equigranular Granite (more Salt & Pepper)	2.63
1046.8	1069.4	Mafic Basalt	3.00
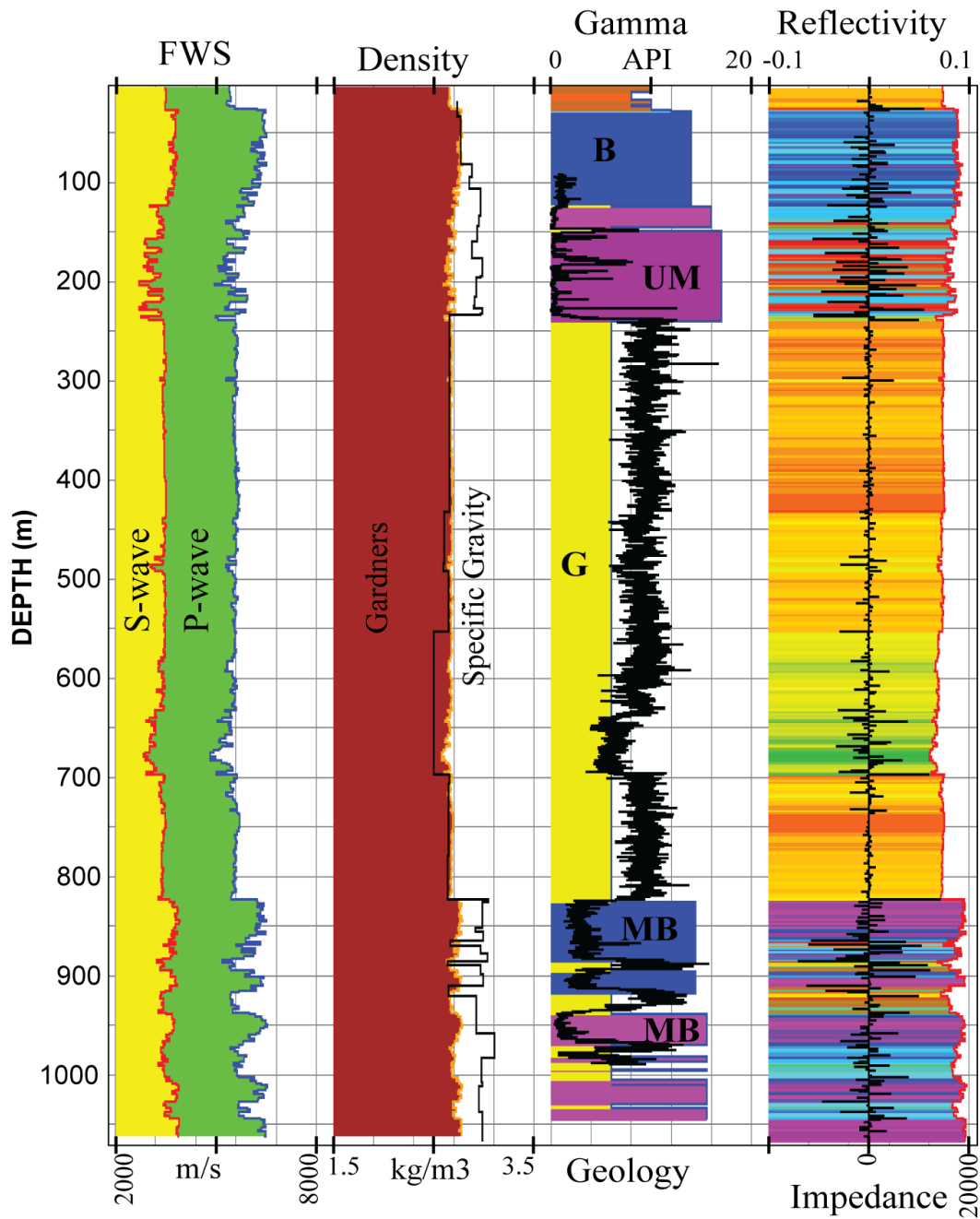
Figure 6-22. BH1 borehole logs. From left to right, track 1) Full-waveform sonic (FWS) P-wave and S-wave data, track 2) Density data derived from Gardner's relationship and measured from rock samples (Specific Gravity), track 3) Natural gamma and summarized geology where B-basalt, G-granit, UM-ultramafic and MB-mafic-basalt and track 4) acoustic impedance and reflectivity.

6.2.2 Pulse transmission tests

Verification of seismic velocities was conducted by ultra sonic PT tests conducted on 47 drill-core samples. Sample depths were chosen based on anomalies seen in the processed VSP data and from visual inspection of the core by walking the hole. The tests were conducted with a signal generator set at 1.0 MHz and shear wave transducers. The resulting waveforms were recorded and analysed on a 2 GHz digital oscilloscope and saved to csv files. The arrival times of the P- and S-waves were determined visually on screen by rotating the transducers. Shear-wave transducers are polarised, as such they need to be co-orientated to maximise the S-wave amplitudes. Rotating the transducers out of phase, minimising the s-wave amplitudes, is a handy trick in correctly identifying wavefields during analysis. In addition the length of each core, the samples' weight in air and the samples' weight in water were measured. These parameters allowed V_P, V_S, V_P/V_S ratio, SG and AI to be calculated. P-wave velocity ranges between approximately 4500 to 6800 m/s. S-wave velocity ranges between approximately 2700 to 4200 m/s and the average V_P/V_S ratio is 1.70. Cross-plots of the measured V_P, V_S versus specific gravity, and V_P/V_S have been created and are shown below in Figure 6-23. These plots show distinct grouping of densities with relative consistent spreads of V_P and V_S except in the density range of 2.9 to 3.0 kg/m3 which has a large distribution of both V_P and V_S.

Also shown in Figure 6-23 is the correlation between the FWS, SG and P-wave velocity core measurements of BH1. There is a good relationship between FWS and SG measurements in the granite and the lower basalt units. Both data sets follow the same density / velocity trend, however, the ultramafic units do not follow this trend and have an anomalously low velocity with respect to the deep mafic basalts of similar density. The PT velocities do not correlate well with the FWS for all samples. This is not completely unexpected as S-wave transducers were used to make measurements, which, result in high amplitude S-waves and low amplitude P-waves, it is a relatively small sample set compared to the 5 cm sample interval of the FWS, the FWS tool averages velocity over approximately 1 to 2 feet compared to 50 to 150 mm in PT tests. It is also likely that picking of the low amplitude P-wave has not been visible in some instances and the first arrival picked is actually an S-wave. That said, the basalt and ultra-mafic sample measurements fall within a reasonable range

of expected velocities and it is typically only the granite samples which have a poor correlation.

6.2.3 Reflectivity and up-going VSP profiles

The Kambalda VSP data were collected and processed as described in Chapter 5 as part of the hydrophone array validation. The resulting hydrophone and geophone P-wave up-going profiles (W_U and P_U respectively) are shown as Figure 6-24b and have very similar features that have been highlighted (by horizontal joiners). The sections in the hydrophone data which were compromised by tube-wave removal have recovered the up-going P-wave with good (if not surprising) continuity. There is some dissimilarity in amplitudes at later times between the two processed profiles. This is due to the application of AGC during tube-wave removal and lends the W_U profile a more continuous appearance than the P_U profile. The P_U data however, is of slightly higher frequency content and has fewer undulations. Both methods have resolved reflectors originating at depths of 235, 485, 590, 690 and 900 m (or 50, 80, 110, 130, and 160 ms). The upper most reflection at 50 ms is better defined in the P_U data and corresponds to the top of the granite (235 m) and a weak, but clear, reflector can be seen at the base of the massive granite intrusion. Many of the other strong reflections are from structural and alteration features within the granite (485, 590 and 690 m) and the reflection at 160 ms is caused by alternating basalt and granite between 890 and 925 m. All of these reflectors have been labelled alphabetically with depth from *a* to *f* in Figure 6-24. To aid correlation of the reflectors to geological horizons the acoustic impedance log has been plotted along the depth axis in Figure 6-24b. Also noticeable in the W_U and P_U profiles is the occurrence of multiples, particularly in the P_U data from the top of the granite and base of the alteration zone. These multiples are indicated by ellipses in Figure 6-24b.
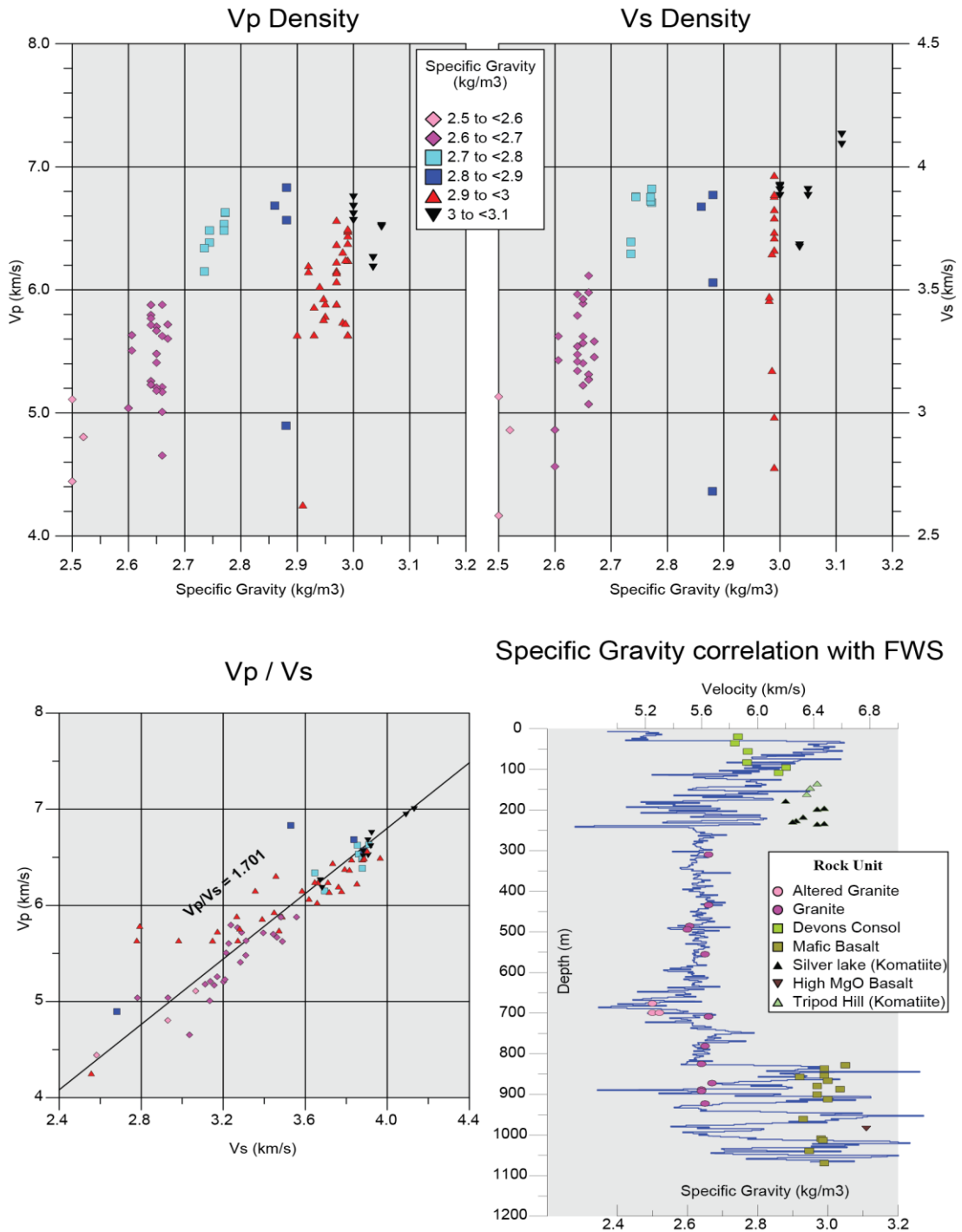
Figure 6-23. Pulse-transmission and specific gravity (SG) measurements of 47 drill-core samples taken from BH1. Cross-plots of V_P and V_S versus SG are displayed. SG has been colour coded by different SG ranges. Bottom left: V_P versus V_S has been plotted and has an average value of 1.70. Bottom right is a comparison of FWS P-wave and SG core measurements.

6.2.4 **VSP-CDP mapping**

As the VSP shot point was 28 m offset from the collar, and BH1 is deviated approximately 5-11 degrees, the receivers have an approximate maximum 190 m lateral aperture from the shot point. The lateral aperture of the receivers raises the possibility of seismic imaging from the borehole from such a near collar shot point. As such, VSP-Common Depth Point (VSP-CDP) mapping (Dillon and Thomson, 1984) and depth migration were performed on the up-going wavefield profiles. VSP-CDP mapping converts the profiles to two-way time (TWT) and places the traces into their true geographic position (assuming a vertically transverse isotropic horizontal layered earth). In Figure 6-25 the VSP-CDP mapping of the W_U and P_U data are shown. Also shown in Figure 6-25 are the; P- to S-wave conversion markers indicated in Figure 5-3 and the geology and FWS logs superimposed along the borehole path. The VSP-CDP mapping indicates our reflectors are dipping to the north, in agreement with the documented plunge direction of the Kambalda Anticline. The true seismic dip is not shown as the horizontal axis is exaggerated to see features within the profiles. As previously seen, CDP mapping of the P_U data has higher frequency content and a more continuous appearance than its W_U counterpart. However, the multiples previously seen in the P_U have also been transformed in the mapping process to the detriment of the P_U data and give the impression of a fault (Figure 6-25).
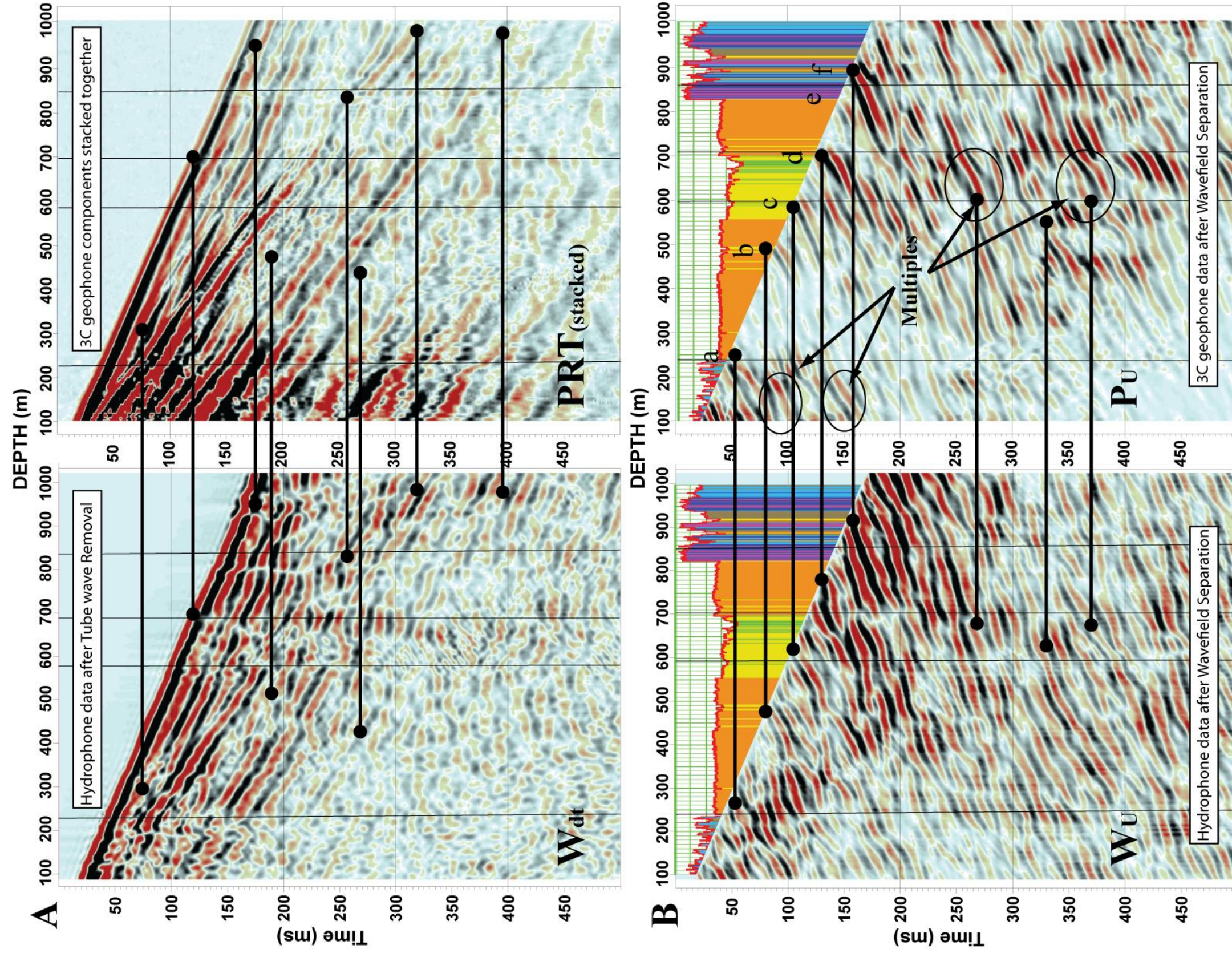
Figure 6-24. Comparison of up-going hydrophone and P component geophone VSP data. Identical wavefield separation processing flows (Section 5-6) were used on both the hydrophone and P component data. The acoustic impedance log has been superimposed along the depth axis for interpretation and horizontal markers to aid comparison of the profiles. Multiples are easily identified within the P_U profile.

207
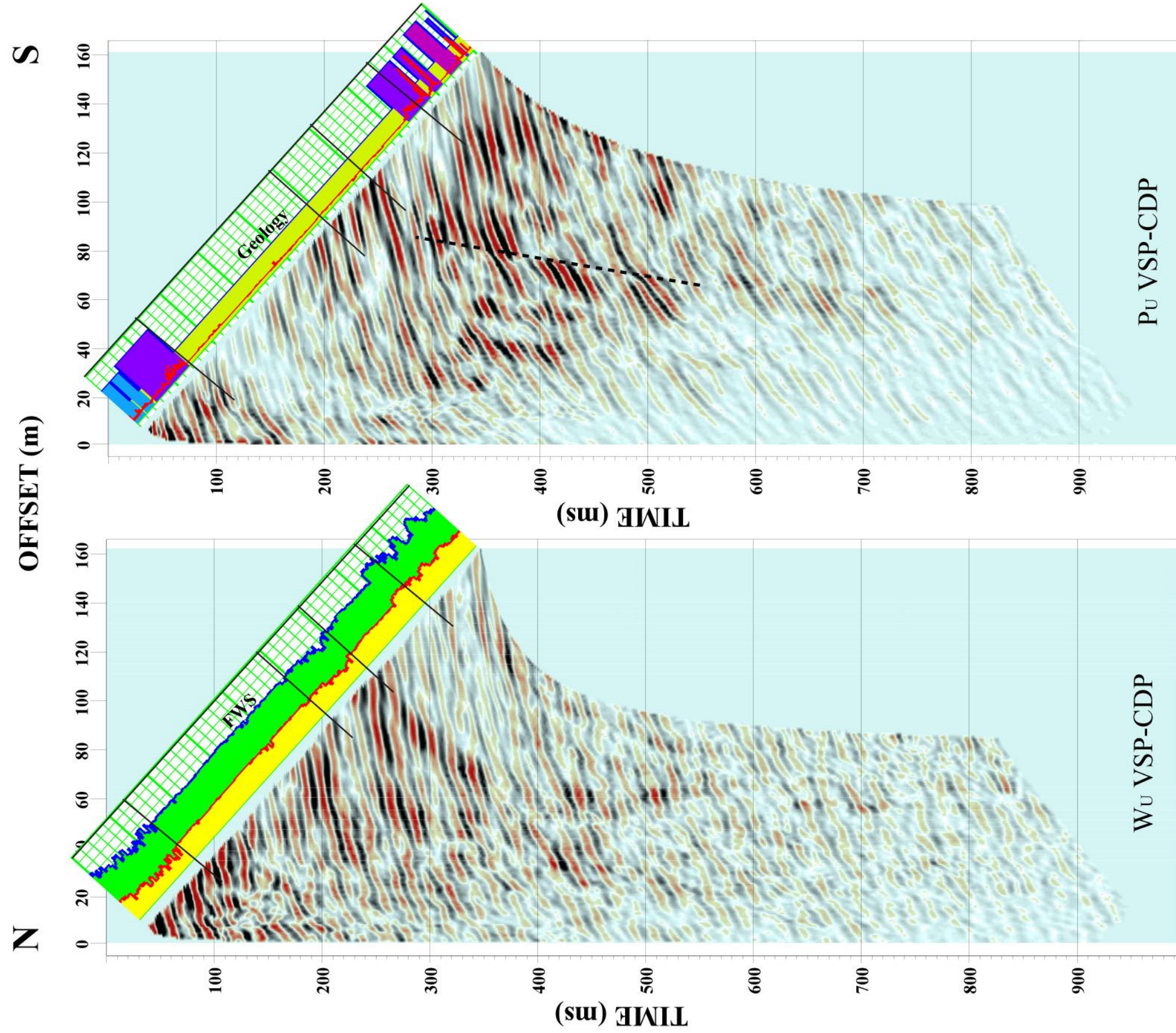
Figure 6-25. Comparison of up-going wavefield separated hydrophone and geophone data after VSP CDP mapping. The borehole is 28 m from the shot point, dips approximately 82º to the south with an orientation of 195º. The horizontal (offset) axis is greatly exaggerated. Reflectors in the profiles are clearly dipping to the north. Multiples identified in Figure 9b have been transformed onto the CDP image and give the illusion of a fault through the profile as indicated by the dashed line.

6.2.5 Seismic "well tie"

A seismic "well tie" is the process where a synthetic seismogram is matched to a real seismic trace and features from the well are correlated to the seismic data. The synthetic trace is produced through convolution of a wavelet with the reflectivity function derived from FWS and density logs. This "ideal trace" contains no multiples or processing artefacts and is compared with the actual seismic response observed from a trace extracted along the well path within the seismic cube.

I produced a synthetic seismic trace by convolving a 90^0 phase shifted 45 Hz wavelet with the reflectivity function shown in Figure 6-22. The reflectivity function is determined from density and velocity contrasts, which in turn determines the amplitude of the convolved synthetic seismic response. The blockiness of the density model has created anomalous seismic responses at density changes. However, these responses are low in amplitude compared with seismic responses dominated by velocity contrasts in the P-wave FWS data. The low response from density contrasts can be seen in Figure 6-26 at 550 m where velocity is relatively constant and density changes. Conversely, a large response due to velocity variations with density constant is displayed between 650 to 700 m.

Processing of the well tie involved;

- Loading of FWS data
- Creation of geology summary and density logs. Density log was derived from SG measurements and the geology summary log.
- Loading of 3D cube (final migrated version)
- Insertion of well track into cube
- Extraction of source signature from seismic cube surrounding borehole BH1
- Convolution of the reflectivity (continuous difference in depth of the impedance which is the product of velocity and density) with source wavelet and creation of synthetic seismogram along well path.
- Drift correction of FWS / synthetic seismogram using ZVSP average velocity table.
- Seismic well-tie: Correlation of synthetic seismogram with real seismic data (3D cube)

-    Match and identify reflections with geology.

A well-tie correlation of 65% was achieved between the synthetic seismogram (convolution of FWS and Density data sets) and the trace extracted from the 3D cube along the well path (Figure 6-26) The correlation value is strongly dependent upon good quality FWS and density data. The correlation achieved is considered high in hard rock seismic (Harrison and Urosevic, 2008).

6.2.6 Synthetic and corridor stacks

Corridor stacks were created from the W_U and P_U profiles converted to TWT using a very tight (25 to 50 ms) time window from the first breaks assuring that any multiples were muted from the profiles prior to stacking. The corridor stacks are shown in Figure 6-26 and have been compared with a trace extracted from the 3D seismic volume along the borehole path and a synthetic trace generated from borehole logs.

Visual inspection of the corridor stacks of Figure 6-26 show that the geophone stack is very similar to that of the hydrophone stack. Both corridor stacks correlate better with the trace extracted from the 3D volume than the synthetic trace. The poor correlation of the synthetic trace to the extracted trace can be attributed to poor quality FWS data and lack of a wire-line density log. Surprisingly the hydrophone stack has a better correlation at the base of the massive granite intrusion, however, the geophone has resolved the upper reflectors better. Superficially there is no clear advantage of the geophone over the hydrophone in the corridor stack. The 3D volume was depth migrated with check shot corrections determined from the hydrophone VSP. A 16 ms (80 m) shift was applied to account for refraction static corrections which used a 5000 m/s replacement velocity to correct for the slow velocity regolith layer. The six horizons identified in Figure 6-24b have correspondingly been labelled *a* to *f* in Figure 6-26.
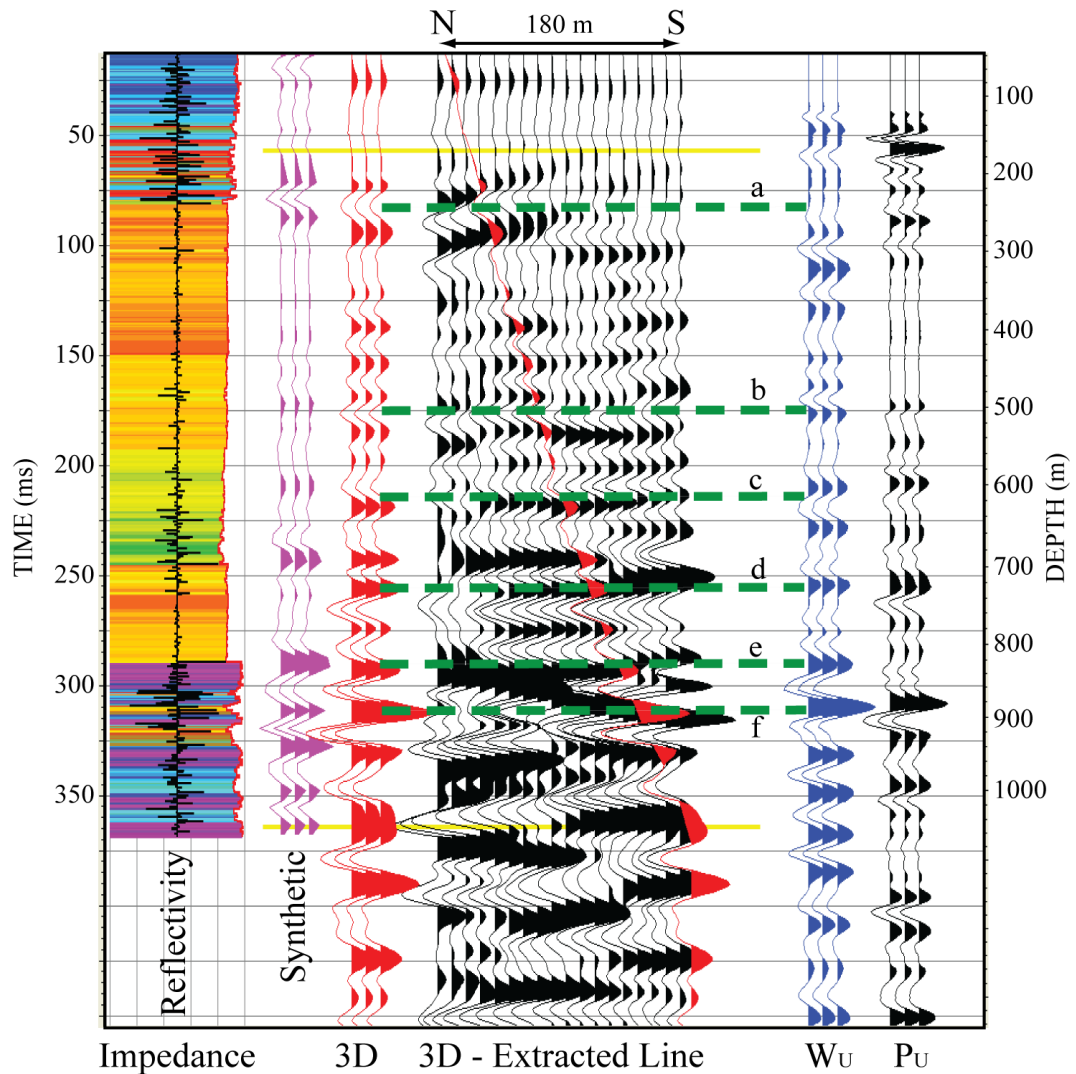
Figure 6-26. Comparison of hydrophone and 3C corridor stacks with geology after time to depth conversion. Time to depth conversion used a common velocity model derived from the 3C FB's and seismic divisions illustrated in previous figures.

6.2.7 Migrated ZVSP and 3D correlation

VSP pre-stack Kirchhoff depth migration (Dillon, 1988) was conducted on the W_U data. A 1-D velocity model ascertained from the hydrophone check shot data was used for the VSP depth migration and time to depth conversion of the 3D surface seismic data. The resulting VSP depth migrated has been spliced into the depth converted 3D surface seismic and is shown in Figure 6-28. Due to the limited lateral shot-receiver aperture, the VSP migration was restricted to a 5 degree imaging

aperture. This was to ensure correct mapping of horizons. As such, the depth migration has only imaged shallow dipping structures below the hole. There is a good correlation between the VSP image and 3D seismic with many of the horizons lining up and a strong reflector just below the hole being imaged. In Figure 6-28, formation tops and reflection events *a* to *f* have been marked along the borehole track. A basic interpretation has been made around these markers and faulting in the 3D seismic cube.
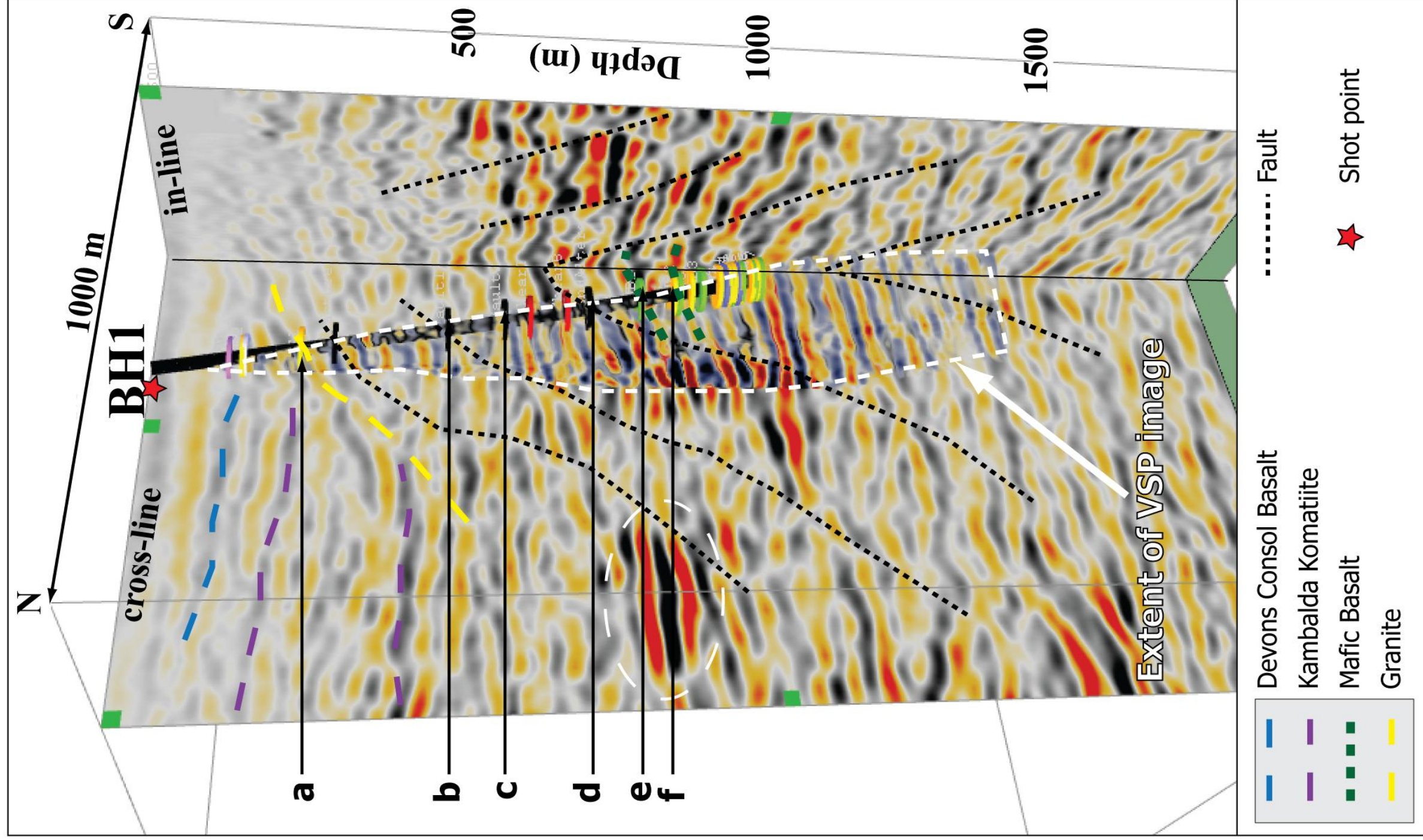
Figure 6-27. Migrated hydrophone VSP Image from BHP-DET Kambalda Borehole inserted (between dashed lines) into the Kambalda 3D seismic cube. The borehole path and VSP is approximately 15 degrees rotated from the cross-line. The 3D seismic cube and VSP were migrated using velocities derived from the VSP. There is good correlation with major horizons.

6.2.8 Seismic character of Marthas Vineyard

The acoustic impedance and reflectivity logs strongly suggest that the granite – mafic basalt interface at 830 m (event e) should create a strong reflector. However, this is not seen in the W_U and P_U profiles or the corridor stacks. It may be that unfavourable survey geometry and or the configuration of the interface, or possibly destructive interference from multiple interfaces have an effect here. Inspection of the full geology log shows that the section between 828 to 887 m, which is reported as a single mafic basalt unit in the geological summary, actually includes 9 felsic intrusive events. In a similar vein, the strong reflection directly below event e at 903 m (event f) may be due to constructive interference and tuning effects. The convolution of the reflectivity function and model wavelet to form the synthetic trace of Figure 6-26, does not account for such constructive or destructive interference effects. This would explain why the synthetic corridor stack has a poor correlation with the trace extracted from the 3D surface seismic, W_U and P_U corridor stacks. Zero-offset forward modelling and AVO analysis of the seismic response may be a better approach for correlation of borehole to seismic data.

There is a strong seismic reflection event to the north of BH1 which has been circled with a white dashed ellipse in Figure 6-27. This reflection event is of lower frequency and moderately flat lying. This is in contrast to the higher frequency reflection events seen around the borehole where many intrusive events are present. A lower frequency reflection may be caused by interference effects as discussed above. Furthermore the ultramafic komatiites of Kambalda have a spinifex texture which is a possible cause of preferential seismic transmission and attenuation. The flat lying appearance of this reflector is likely due to the reflector paralleling the axis of the Kambalda Anticline. Thus, this reflection could be a potential western flank UM - Lunnon Basalt target.

Structural analysis of the 3D cube away from the borehole surmises very steep WNW dipping reverse faults. The proximity of these faults to the borehole, the amount of granite intersected in the borehole and the large alteration zone within the granite intrusion, strongly suggests that the borehole has intersected an extension of the Loretto Thrust or similar structure.

It has now become apparent that further VSP surveys are needed to depth calibrate the 3D seismic cube in areas not effected by large scale faulting, shears and intrusions and to help resolve geological complexity of the area covered by the 3D surface survey. This will enable an improved exploration strategy and subsequent verification through drilling.

6.2.9 Attenuation and Q

Attenuation of a wave propagating in a media is caused by geometrical spreading, transmission losses, scattering and adsorption. Attenuation changes the amplitude and the shape of the wavelet. Spreading and transmission losses are due to the loss of energy with distance and crossing boundaries respectively. Scattering and adsorption are at the seismic scale and are dependent on the microstructure, fractures and elastic properties of the rock. Anelastic absorption is the transformation of seismic energy into heat. It can be described by the absorption coefficient α, the exponential decrease of amplitude with distance, or the seismic quality factor Q. Several definitions for the seismic quality factor Q exist and they can all be traced back to Knopoff and MacDonald (1958) expression, deduced for sinusoidal waves;

$$Q = 2\pi \frac{E_o}{\Delta E}$$

Equation 6-2

where E_o, is the maximum strain energy and ΔE is the energy dissipation per cycle. Q is related to adsorption by;

$$\frac{1}{Q} = \frac{\alpha V}{\pi f} = \frac{\alpha \lambda}{\pi}$$

Equation 6-3

where V, f and λ are velocity, frequency and wavelength respectively (Sheriff, 2002).

The seismic Q of rocks is of the order of 50 to 300 (Sheriff, 2002). The lower the Q value the larger the attenuation. Preferential attenuation of high frequencies increases the dominant signal period and degrades resolution. Knowledge of Q is desirable yet rarely measured.

VSP is the perfect in situ laboratory to investigate changes in amplitude and its causes at the seismic scale. Many methods to calculate Q from VSP data have been developed. The most fundamental is the amplitude decay method of McDonald (1958) and a reliable method in petroleum exploration is the spectral ratio method (Hauge, 1981). Other methods include, pulse broadening analysis (Ricker, 1953), pulse rise time analysis (Gladwin and Stacey, 1974), pulse power analysis (Stainsby and Worthington, 1985); spectral amplitude matching (Blias, 2012), the centroid frequency shift method (Quan and Harris, 1997), velocity dispersion based techniques (Sun et al., 2009), and wavefield inversion (Dietrich and Bouchon, 1985). Despite all these methods, current Q estimates from VSP can be unreliable and the attenuation mechanisms poorly understood, with only the spectral ratio and pulse rise time methods being widely accepted (Tonn, 1991). A review and comparison of the common methods can be found in Tonn (1991).

Data from the BH1 Kambalda 3C VSP (vertical component) was analysed using the amplitude decay method. This uses the interval velocity and ratio of amplitudes for two different distances $a(x_1)$ and $a(x_2)$ as follows;

$$\frac{1}{Q} = \frac{V}{\pi f \Delta x} \left[\ln \frac{a(x_1)}{a(x_2)} \right]$$ **Equation 6-4**

The amplitudes and corresponding Q^{-1} results are displayed in Figure 6-1 along with the VSP interval and FWS velocity plots. Comparison plots of the spectral ratio and centroid frequency methods are also given in Figure 6-29.
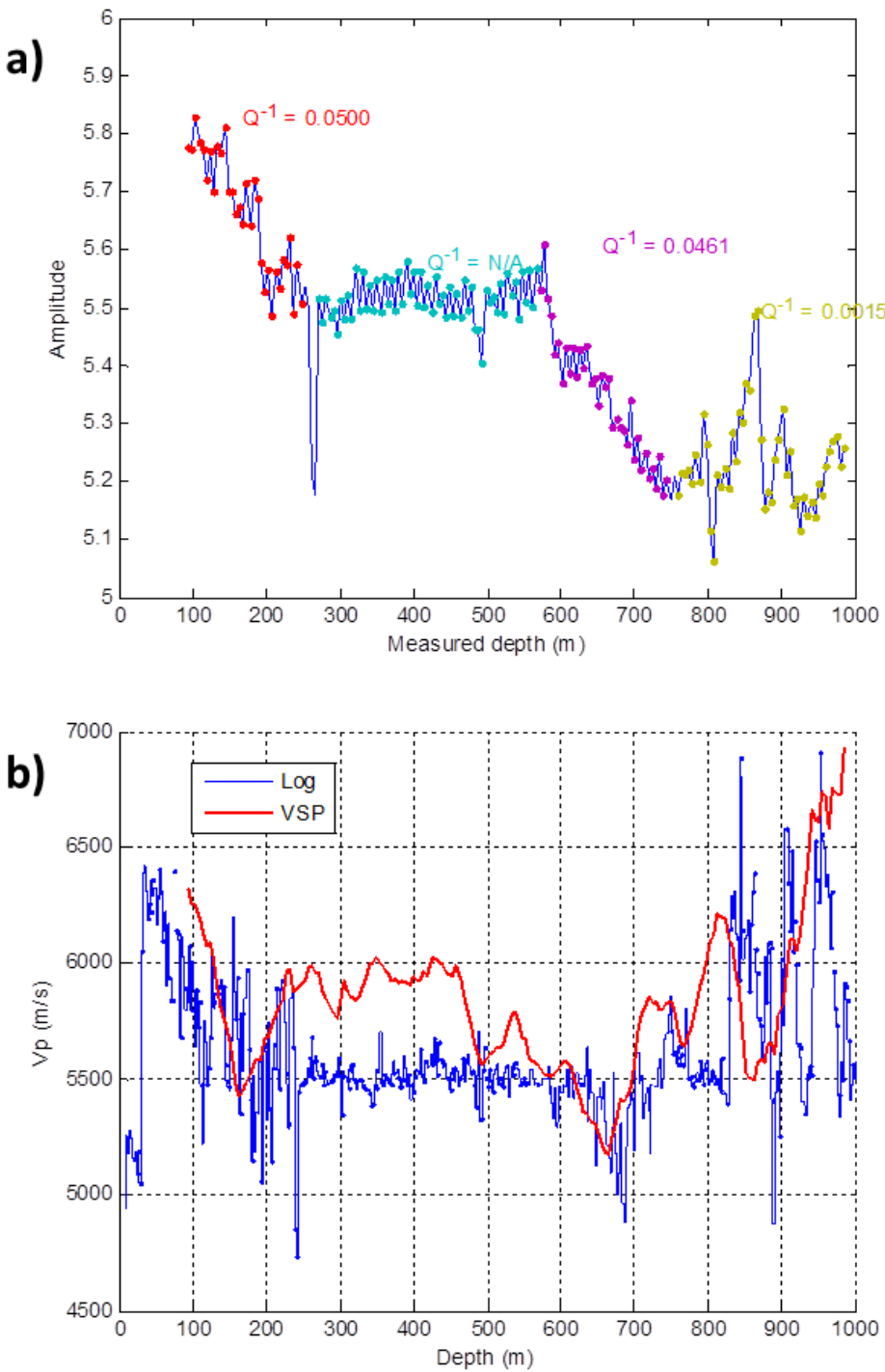
Figure 6-28. a) Inverse Q estimates using the amplitude decay method for BH1 3C geophone data. b) 3C geophone Interval velocities (VSP) and FWS (log) velocities for BH1. Courtesy of R Pevzner.
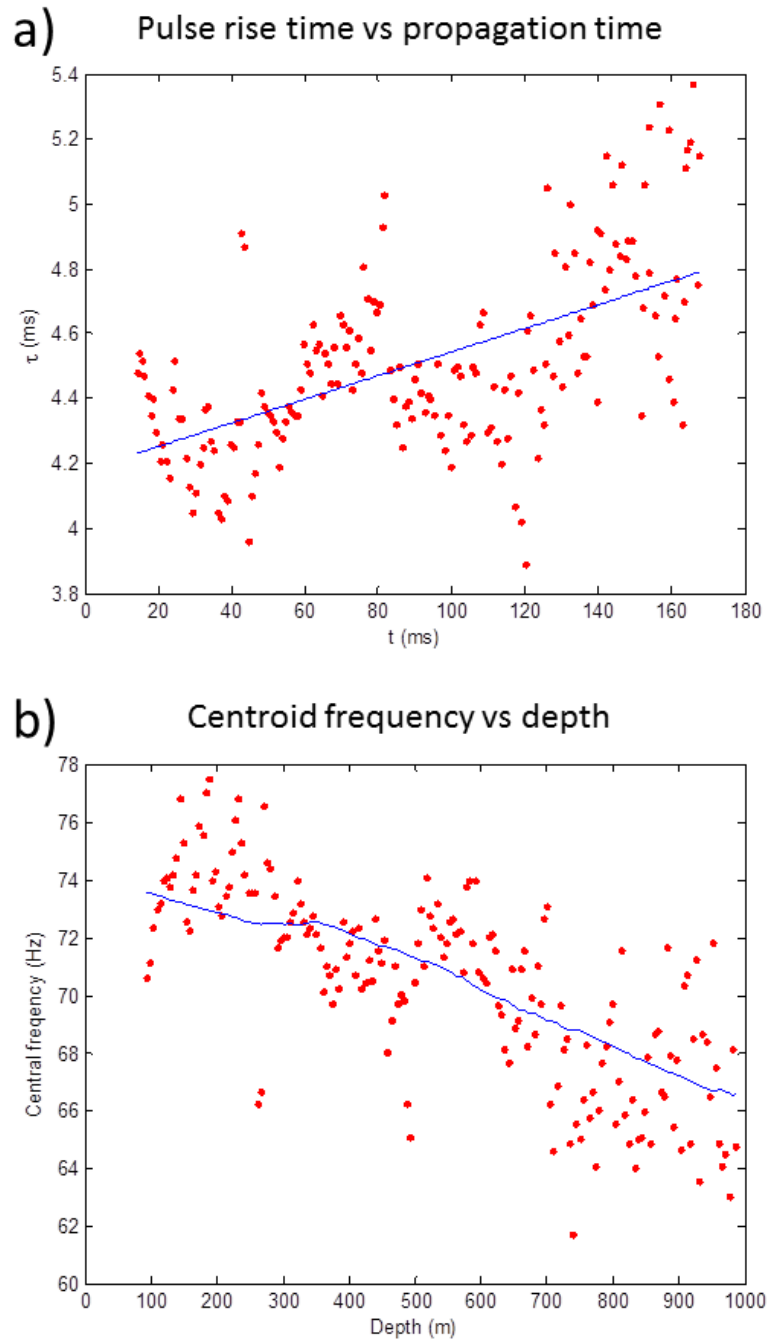
Figure 6-29. Pulse rise time a) and centroid frequency b) results of BHI Kambalda 3C VSP. Courtesy of R Pevzner.

The amplitudes of Figure 6-1a have been divided into 4 subgroups and the slope, or Q^{-1} value calculated. This results in Q values of 20, 21.7 and 666.7 respectively, disregarding the 2nd sector where the slope is 0.0. When the amplitude results are plotted alongside BH1 borehole logs from section 6.2.1, as shown in Figure 6-30, a correlation between the various lithological divisions can be made. The amplitude

plot clearly differentiates the altered granite (shear zone) from the competent granite. In contrast, there is a large amount of scattering in the pulse rise time and centroid frequency data shown in Figure 6-29. Both the pulse rise time and centroid frequency show an increase in Q, proportional to the ratio of rise time and frequency shifts with to depth respectively, however, this is very small in the pulse rise time data due to the high P-wave velocities.

Q analysis was not intended as a component of this research, however, it is important to note, that with high quality data, the quality factor can be determined in hard rocks and linked with lithology. This example shows that there is considerable contrast of Q in hard rocks and is another tool in the VSP tool box for characterising mineral deposits.
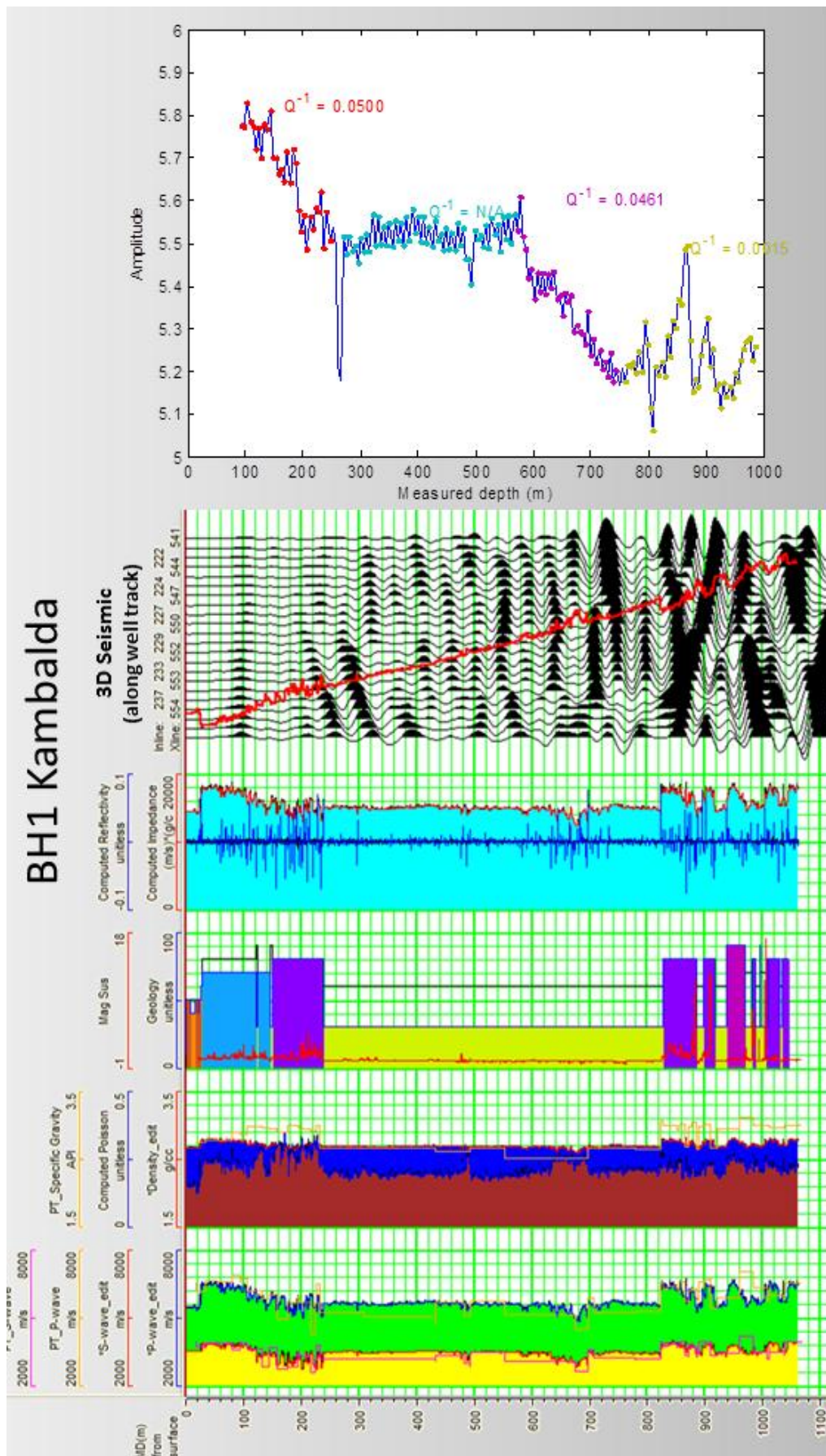
Figure 6-30. Comparison of borehole logs, 3D seismic and VSP amplitude for BH1 Kambalda.

223

6.3 Discussion

Petrophysical analysis shows it is easier to determine lithology directly from density and gamma logs (as commonly practiced in coal and sedimentary geology studies) and should be encouraged as standard practice particularly in mineral exploration which involves or plans to involve seismic surveys. Similarly FWS are integral to the correlation and understanding of seismic signals and need to be encouraged. The FWS at Marthas Vineyard was of a lower quality than usually acquired within a petroleum or environmental borehole. This is in part due to the irregularity of FWS logging being conducted in hard rock environments. The FWS technique is well understood in soft rocks but less so in hard rocks. Hence, tools need to be adjusted to borehole size and environment. It is likely the FWS conducted here should have been run at higher frequencies (>20 kHz) to produce stronger compressional events.

The synthetic trace produced from the convolution of FWS P-wave and density model suggests that seismic reflection responses are more sensitive to velocity changes rather than density. This is typical for hard rocks hosting minerals but not so for the mineralised parts where seismic response may be largely density driven.

FWS has been deterministic in identifying a large alteration zone within the Kambalda granite in an otherwise uninteresting geology log. Velocity variations due to the alteration such as that experienced in shear and fault zones (which will also experience large variations in density due to fluid and mineral exchanges) are likely candidates for strong seismic reflections. Variation between basic rock types such as felsic (granite) and mafic (basalts) rocks are also likely due to have good reflections due to the large velocity contrasts. However the velocity variation between similar rock types such as M and UM are not likely to have strong seismic responses. Seismic responses here maybe more pronounced in S-wave imaging or at differing incident angles due to the mineralogical and textural differences of these two rock types. Basalt generally is fine grain massive and the komatiite UM of the Kambalda region often has a spinifex (olivine crystals) texture.

It has now become apparent that VSP surveys can be beneficial for resolving structural complexities of higher order. Further VSP surveys are needed to help

resolve geological complexity of the area covered by the 3D surface survey. This will enable an improved exploration strategy and subsequent verification through drilling. The determination of granite intrusion signatures has aided the interpretation of the 3D surface seismic, allowing known seismic signatures to be traced away from the borehole and to be inferred elsewhere.

Much work is needed in determining the origin of reflection points and migration imaging in steep dipping complex environments. VSP migration imaging is as much an art as it is a science and an accurate earth image is not achievable without some priori knowledge and secondary geological and geophysical inputs.

7 Application of Vertical Seismic Profiling for characterisation of mineral deposits

Specific geometry of a VSP survey allows us to understand the characteristics of both transmitted and reflected wavefields. As such, VSP is an "in-field seismic laboratory", necessary for understanding the origin of seismic events. It further enables calibration of surface reflection images. Finally, the VSP survey can be designed to produce an image around the borehole, typically at much higher resolution than it is possible to achieve with the surface reflection method. The main drawback of the method relates to its high cost, particularly for the mining community. Hence the main objective of this research was to look into alternative ways of implementing VSP surveys that would be more effective and less expensive than currently offered by service providers. Within the realm of the available boreholes surveyed, these objectives have been met using a 24 channel hydrophone array. Thus, new research dimensions have been created, as well as new hope for the application of the VSP method in complex mineral exploration environment.

7.1 Summary

Before embarking on these investigations it was necessary to build a platform for it. For that purpose I have carried out several numerical tests that confirmed that VSP can be useful for understanding the generated wavefield and moreover, that it is possible to produce useful VSP seismic reflection images from angled boreholes in complex hard rock environments. The real benefit of the modelling exercises was to help design the optimum acquisition geometries, to understand wavefield processing challenges and understand complex patterns created from real deposits. Lessons learned from the modelling prior to field excursions were, migrated images suffer from a lack of aperture in the down-dip direction and require large down-dip offsets to compensate for this. This may be hard to accommodate in practice with very steeply dipping structures and limited source strengths. Up-dip and down-dip shots need to be carefully examined at each stage of processing to determine the limits at which reflection energy is no longer being added to the stack. In the up-dip direction

this is reached rapidly (approximately the lateral extent of the receivers in the up-dip direction). In the down-dip direction it is harder to create a "rule of thumb" and modelling of each individual geologic setting is advisable before acquisition. Careful evaluation of profiles with respect to polarity of direct wavefields and determination of refracted arrivals is also necessary to aid development of processing strategies and interpretation of resulting images. Forward modelling is important for testing different potential geological scenarios and matching modelled outcomes with the observed seismic signatures. This can be particularly useful in green-fields exploration where the geological architecture may not be well understood.

Results demonstrate that a borehole hydrophone array is capable of imaging structure in a complex environment. This is not easily achieved, care at the acquisition and processing stages needs to be taken. The general experience of hydrophones is that the data is noisy and "swamped" with tube-waves. The high sensitivity of the piezo-electric crystals to pressure variations at all frequencies, the lack of electrical damping from high frequency noises (>500 Hz) and passive coupling to the formation through the water column, leads to the susceptibility of the elements to sharp very low amplitude noises such as; cracking rocks, particles falling in the water column and ambient background noise due to mining activities and infrastructure. These influences can be reduced and SNR increased by utilising high viscosity drilling fluids (such as PAC-R) in VSP survey boreholes to reduce borehole breakout and improve the "apparent coupling" of the hydrophone to the formation by reducing the tube-wave to seismic signal ratio, as documented in Chapter 4. Increased SNR through the use of borehole fluid viscosifiers, combined with very closely spaced (e.g. 2 m) well calibrated (spatially) receivers will allow very high quality V_P and V_S data to be acquired in the future with hydrophones. This in turn will allow accurate measurement of interval velocities at a cost acceptable to mining practice. The VSP derived time to depth relationship is used to calibrate FWS logs while VSP reflectivity is used to correlate log-derived synthetic and surface reflection images. When combined with density measurements, VSP derived interval velocity profile can be used to compute a synthetic seismogram for calibration of seismic reflection images when FWS logs are not available.

To collect tube-wave data in a hard rock environment which is not aliased below 150 Hz, data should be collected at a maximum of 5 m. Preferably hydrophone data should be collected at 3 m or less station spacing to prevent aliasing of tube-waves (approximately 250 Hz) within the seismic bandwidth we are interested in. Hydrophone strings should be designed around these parameters to avoid using infilling with multiple small moves with larger spaced elements, thus avoiding potential aliasing in the wave-number domain and reducing the potential of trace to trace amplitude and noise imbalances. Provisions should also be made for a reference geophone when using an impact source.

A novel corrugated tube-wave baffle system which attenuates tube-waves through disrupting laminar flow, destructive interference and scattering has been presented. The baffle system can be implemented as an aftermarket device and deployed to any depth.

In summary the ideal borehole hydrophone VSP should be conducted under the following conditions;

1. 2 m spaced receiver elements (tube-wave properly sampled to 375 Hz)

2. Visco-elastic polymer filled borehole

3. Corrugated baffle system installed

4. Cable isolated to remove cable-wave

5. Reference geophone used to combat jitter in measurements

6. Data to be recorded as individual FFID records and inspected prior to stacking.

Non-standard wavefield separation has been successful in removing strong coherent tube-wave noise. The "wave-by-wave" model wavelet extraction method proved useful with hydrophone data where there are large variances in trace to trace noise. This routines success in wavefield separation with noisy data can be attributed to it requiring as few as 3 neighbouring traces and it is adaptable to spatial and temporal changes. However, no single method of tube-wave removal was determined to be the best for hydrophone data and each data set needs to be evaluated. Great care and

optimisation of parameters at each stage is required. It is necessary to: 1) pre-condition the data with deconvolution and band-pass filters to reduce noise and enhance signal, 2) edit and process all data as individual field records to avoid the artefact often associated with the application of 2D filtering.

7.2 Field demonstrations

The Agnew-Wiluna surveys demonstrated the imaging potential of ZVSP and WVSP. With only 24 channels in the borehole spanning 230 m and 50 x 10 m spaced surface shots in the down dip direction, an exceptionally good VSP-CDP stack was produced. The CDP stack is in strong agreement with the structural model of the area. This experiment also highlights the difficulty in obtaining an accurate image. The VSP-CDP transform used assumes a horizontally layered vertically isotropic earth. This is clearly inaccurate for this environment and a transform was applied to the data to rotate the CDP plane such that the borehole was in effect orthogonal to the rock interfaces. The transformed CDP stack then had a better representation of structural slopes. However, it is not possible to combine slanted traces with vertical traces in visualisation software for correlation to surface seismic data. VSP migration is required in such cases, or alternatively a separate code needs to be written to grid the slanted data and map it to vertical traces. Despite VSP giving a true velocity profile extrapolating this to 2 or 3 dimensions involves priori structural knowledge and leads to the classic seismic conundrum that; if an accurate velocity model is known, then you already know the structure that you are trying to image. As this is typically not the case, velocity modelling approaches such as layer stripping then need to be applied.

The Kambalda hydrophone ZVSP migration result has excellent correlation with the 3D seismic cube. The image obtained from the single near offset shot point, arises from the borehole being deviated and having some lateral aperture (approximately 160 m over the 610 m depth interval). The migration is restricted to imaging only shallow dipping events below the borehole due to the short offset. This example clearly demonstrates the usefulness of migration from deviated holes for "borehole ties".

It has also shown that the analysis of the transmitted wave field can be useful in identifying certain rock units. In brief, solid granites can be identified by low scattering while shears and altered zones are characterised by very high scattering. This suggests that proxy attributes can be computed from reflection data, such as instantaneous frequency scaled by the rate of change envelope, and be used to help the characterisation of rock units. In some cases sequence attributes (like peak frequency) may be possible to use, particularly over massive granite bodies. These attributes can be first verified on the up-going field (reflected) derived from VSP data and then used in 2D or 3D reflection volumes. Thus characteristics of both wavefields are of importance to exploration practice.

7.3 Conclusions

After conducting a number of borehole experiments in hard rock environments of the Yilgarn Craton the following conclusions can be made:

1) VSP imaging in a hard rock environment can yield valuable structural images at high resolution as a stand-alone tool, or, in combination with surface seismic and other petrophysical, geological and geophysical data sets.

2) VSP imaging can be achieved with a borehole hydrophone array so long as much care is taken at both the acquisition and processing phases. A dense hydrophone array is required to allow effective multichannel filtering of tube-waves.

3) Suppression of tube-waves in borehole hydrophone data at the acquisition stage can be achieved through the use of corrugated baffles. These baffles work by disrupting the prograde elliptical particle displacement close to the borehole wall. As such they need to be matched to the borehole diameter but are effective and deployable to any depth.

4) Visco-elastic polymers increase SNR in borehole hydrophone surveys by inhibiting tube-wave propagation.

5) Both transmitted and reflected VSP fields are of interest to exploration of mineral resources

6) Borehole seismic tests in the Kambalda and Agnew-Wiluna nickel districts validate the use of seismic methods for mineral exploration in these and similar mineral exploration environments.

Direct comparison of hydrophone VSP profiles with clamping geophone profiles in Kambalda, validated reflections in the hydrophone data after tube-wave wavefield separation. Tube-wave removal affected the overall result with some fidelity and coherency being lost in the P_u profiles, VSP-CDP stacks and migration images. Maintaining true amplitudes during tube-wave processing is difficult. Advancements in tube-wave suppression will alleviate much of these processing problems and exciting VSP images from hydrophone data is to be expected in the future.

The light weight, slim-line, passive coupling and high channel count of hydrophone arrays, combined with their low manufacturing cost, make hydrophone VSP extremely cost effective with low down-hole risk. It has been shown that a 24 channel hydrophone array can spatially sample a borehole at least 4 times faster than a two-shuttle clamping geophone array.

7.4 Further Work

A very strong foundation of how to use a hydrophone array in hard rock environments has been presented. This now opens the possibility of hydrophones being used for more than just velocity, check-shot or tomographic applications with reflection images now being achievable. Firstly however, further study should be conducted to fine tune the corrugated baffle array and the use of visco-elastic polymers. The 50 mm continuous baffle seemed ineffective in a large (by comparison) 123 mm borehole. It is assumed that the baffles are most effective when they are close to the borehole wall, however, the corrugation profile/depth and periodicity will affect the performance. Bench tests can easily be performed in a laboratory environment with a water tank, transducers and different baffle configurations to determine these before commissioning a full scale set of baffles for

different sized boreholes. In addition to the baffling a high density hydrophone string is necessary to allow effective filtering of any remaining tube-waves. This recommendation has been followed by Curtin researchers and 2 m spaced element hydrophone system has been ordered. Further testing of the corrugated baffles design is to be conducted with baffles matched to an HQ borehole.

The use of drilling fluid viscosifiers has shown to improve SNR of borehole hydrophone data by decreasing the amplitudes of tube-waves within the fluid column. It is assumed the added viscosity restricts the particle motion of the tube-waves. This is expected to occur in both the axial and radial directions and needs to be verified. This may also reduce amplitudes of the radial propagating body-waves. The PAC-R viscosifier does not change the density of the borehole fluid and as such does not affect the propagation velocity (Equation 4-2) of the tube-waves. Again water tank experiments can be set up to quantify the effects of PAC-R and other drilling additives. This should be conducted with input from drillers, drilling mud manufactures and wire-line geophysicists. Part of the DET CRC program is to develop new down-hole remote sensing technology that is impregnated in carbon-fibre drill rods. Down-hole techniques such as borehole radar and gamma probes are sensitive to conductive fluids and density respectively. As such a fluid which can aid borehole hydrophone use without effecting (or even better, aiding) other remote sensors will be beneficial to VSP use and the DET CRC program.

Since hydrophone strings are inexpensive, a large number of elements can easily be designed and utilised for borehole seismic studies. This gives rise to recording more 3D VSP during 3D reflections seismic work. The string(s) can be left in the boreholes to listen passively to the sources used for the surface reflection survey. The potential benefit of such measurements is significant. It is likely that very high resolution images can be constructed surrounding the boreholes, which would significantly increase precision of targeting and help drilling programs.

7.4.1 Tube-waves and potential uses

Tube-waves are sensitive to changes in the shear modulus of the formation, the bulk modulus and density of the borehole fluid (Equations 4-1 and 4-2). Accordingly tube-waves should reflect at lithologically constrained impedance contrasts within the borehole environment. The reflected tube-wave analysis of the Agnew-Wiluna borehole below 520 m (Figure 6-8) strongly supports this and suggests that hydrophone tube-wave analysis could be utilised as a lithological in-hole mapping tool. Already there are reports of tube-wave reflection logs in sonic logging (Burns and Cheng, 1986) and reflected tube-wave plots in VSP for fracture analysis as fracture induced tube-waves have high amplitudes. The pressure sensitivity of the hydrophone array is ideal for detecting lower amplitude geologically induced tube-waves, however, as lithological induced tube-waves are the weakest tube-wave, many of the stronger tube-waves need to be eliminated. I have shown that it is possible to remove the strong Rayleigh and casing tube-waves with a correctly borehole matched corrugated baffle at the top of the hole, like wise we can use a similar bottom baffle to remove the bottom reflected tube-wave. However, it is not possible to suppress the high amplitude induced tube-waves which occur from changes in borehole condition, fractures and faults with corrugated baffles without removing the wanted stratigraphical induced tube-waves. As such, this data would need to be collected separately to a body-wave reflection VSP where the use of inter hydrophone baffles and full tube-wave suppression is preferred.

In a similar vein as the aforementioned RTWS analysis there is information about the borehole to be obtained from hydrophone FB amplitude analysis. As tube-waves are induced by body waves interacting at the borehole wall all FB in a hydrophone survey are affected. This has been observed in the high variability of FB amplitudes in the Agnew-Wiluna and Kambalda data sets. Within these data sets we see higher FB amplitudes where tube-waves have been induced from fractures and other changes in the borehole environment. An analysis between hydrophone and 3C FB amplitudes in conjunction with RTWS and Q analysis may yield information about formations and fractures intersected by the borehole.

The fabric and metamorphic composition of ultramafic rocks such as spinifex texture and alignment of olivine crystals found in the komatiite's of the Yilgarn Craton, may be anisotropic to propagation of body waves, this could be one of the reasons that UM rocks found in the Yilgarn Craton are often slower in P-wave velocity than Mafic (Basalt) in the area which is contradictory to what the Nafe-Drake curve predicts. This phenomenon is likely the cause of the hypothesised geologic induced tube-waves seen in the Agnew - Wiluna case study below 590 m. Thus, studying RTWS and FB amplitudes in hydrophone data could aid the delineation of basalt / UM contacts of mineral importance in the Yilgarn Craton.

References

Adam, E., B. Milkereit, B. Roberts, and D. Schmitt, 2000, VSP survey at a VMS deposit, Matagami, Quebec: SEG Technical Program Expanded Abstracts, **19**, 1126-1129.

Aki, K., and P. G. Richards, 1980, Quantitative Seismology: Theory and Methods: W H Freeman and Co.

Alfuhaid, F., 2009, Vertical seismic profiling for recovery of near well hydrostratigraphy, Perth basin, Western Australia: BScHons, Curtin University of Technology.

Almalki, M., B. Harris, and J. C. Dupuis, 2011, Simultaneous vertical seismic Profiling in two wells and the virtual source method; Perth Basin Western Australia.: Presented at the 73rd EAGE Conference & Exhibition incorporating SPE EUROPEC 2011

AMC, 2011, Australian Mud Company; Product data sheets A-Z. : Imdex Ltd

Anderson, N., and S. Cardimona, 2002, Forward seismic modeling: the key to understanding reflection seismic and Ground Penetrating Radar (GPR) techniques.: Presented at the The 2nd Annual Conference on the Application of Geophysical and NDT Methodologies to Transportation Facilities and Infrastructure.

Balch, A. H., M. W. Lee, J. J. Miller, and R. T. Ryder, 1982, The use of vertical seismic profiles in seismic investigations of the earth: Geophysics, **47**, 906-918.

Bancroft, J. C., 2007, A Practical Understanding of Pre-and Poststack Migrations: Prestack: Soc of Exploration Geophysicists.

Barnes, S. J., M. J. Gole, and R. E. T. Hill, 1988, The Agnew nickel deposit, Western Australia; Part I, Structure and stratigraphy: Economic Geology, **83**, 524-536.

Barton, D. C., 1929, The seismic method of mapping geologic structure: American Institute of Mining and Metallurgical Engineers.

Bellefleur, G., L. Matthews, B. Roberts, B. McMonnies, M. Salisbury, G. Perron, D. Snyder, and J. McGaughey, 2004, Downhole seismic imaging of the Victor Kimberlite, James Bay Lowlands, Canada: a feasibility study: SEG Technical Program Expanded Abstracts, **23**, 1229-1232.

Beresford, S., R. Cas, Y. Lahaye, and M. Jane, 2002, Facies architecture of an Archean komatiite-hosted Ni-sulphide ore deposit, Victor, Kambalda, Western Australia: implications for komatiite lava emplacement: Journal of volcanology and geothermal research, **118**, 57-75.

Berryhill, J. R., 1977, Diffraction response for nonzero separation of source and receiver: Geophysics, **42**, 1158-1176.

Biot, M. A., 1952, Propagation of Elastic Waves in a Cylindrical Bore Containing a Fluid: Journal of Applied Physics, **23**, 997-1005.

Birch, F., 1961, The velocity of compressional waves in rocks to 10 kilobars, part 2: Journal of Geophysical Research, **66**, 2199-2224.

Blias, E., 2012, Optimization Approach to Q-Factor Estimation From VSP Data: WIPO Patent No. 2012058257.

Bording, R. P., and L. R. Lines, 1997, Seismic modeling and imaging with the complete wave equation: Soc of Exploration Geophysicists.

References

Bortfeld, R., 1961, Approximations to the Reflection and Transmission Coefficients of Plane Longitudinal and Transverse waves. : Geophysical Prospecting, **9**, 485-502.

Brown, R. J., R. R. Stewart, and D. C. Lawton, 2002, A proposed polarity standard for multicomponent seismic data: Geophysics, **67**, 1028-1037.

Brown, S., D. Groves, and P. Newton, 2002, Geological setting and mineralization model for the Cleo gold deposit, Eastern Goldfields Province, Western Australia: Mineralium Deposita, **37**, 704-721.

Burns, D. R., and C. H. Cheng, 1986, Determination of In-Situ Permeability from Tube Wave Velocity and Attenuation: Presented at the 27th Society of Petrophysicists and Well Lolg Analysts Annual Logging Symposium.

Calvert, A. J., and Y. Li, 1999, Seismic reflection imaging over a massive sulfide deposit at the Matagami mining camp, Quebec: Geophysics, **64**, 24-32.

Campbell, A., A. Fryer, and S. Wakeman, 2005, Vertical seismic profiles--more than just a corridor stack: The Leading Edge, **24**, 694-697.

Cao, S., and S. Greenhalgh, 1995, High-resolution seismic tomographic delineation of ore deposits: Exploration Geophysics, **26**, 315-318.

Carcione, J. M., G. C. Herman, and A. P. E. ten Kroode, 2002, Seismic modeling: Geophysics, **67**, 1304-1325.

Castagna, J. P., 1993, AVO analysis - Tutorial and Review, Offset-dependent reflectivity: theory and practice of AVO analysis: Society of Exploration Geophysicists.

Cheng, C. H., and M. N. Töksoz, 1982, Generation, propagation and analysis of tube waves in a borehole.: Presented at the SPWLA 23 Annual Logging Symposium. , Society of Petrophysicists & Well Log Analysts.

Chopra, S., and B. Hardage, 2010, Introduction to this special section: Borehole geophysics: The Leading Edge, **29**, 678-679.

Claerbout, J. F., 1970, Coarse grid calculations of waves in inhomogeneous media with application to delineation of complicated seismic structure: Geophysics, **35**, 407-418.

Claerbout, J. F., 1971, Toward a unified theory of reflector mapping: Geophysics, **36**, 467-481.

Cosma, C., and P. Heikkinen, 1996, Seismic investigations for the final disposal of spent nuclear fuel in Finland: Journal of Applied Geophysics, **35**, 151-157.

D'Addario, G. W., 1986, Australia Geology: Bureau of Mineral Resources, Geology and Geophysics.

Daley, T. M., R. Gritto, E. L. Majer, and P. West, 2003, Tube-wave suppression in single-well seismic acquisition: Geophysics, **68**, 863-869.

Day-Lewis, F. D., K. Singha, and A. M. Binley, 2005, Applying petrophysical models to radar travel time and electrical resistivity tomograms: Resolution-dependent limitations: Journal of Geophysical Research, **110**, 1 - 17.

Debicki, E. J., 1996, MITEC's Exploration Technology Division: Helping reverse the trend of declining mineral reserves in Canada: CIM bulletin, **89**, 53.

Dietrich, M., and M. Bouchon, 1985, Measurements of attenuation from vertical seismic profiles by iterative modeling: Geophysics, **50**, 931-949.

Dillon, P. B., 1988, Vertical seismic profile migration using the Kirchhoff integral: Geophysics, **53**, 786-799.

Dillon, P. B., 1988, Vertical seismic profiling migration using the Kirchhoff integral: Geophysics, **53**, 786-799.

Dillon, P. B., and R. C. Thomson, 1984, Offset Source VSP surveys and their Image Reconstruction, : Geophysical Prospecting, **32**, 790-811.

Dix, C. H., 1939, Interpretation of Well-Shot Data: Geophysics, **4**, 24-32.

Dix, C. H., 1945, The interpretation of well shot data II: Geophysics, **10**, 160-170.

Dobrin, M. B., and C. H. Savit, 1960, Introduction to geophysical prospecting: McGraw-Hill

Drummond, B., B. Goleby, and C. Swager, 2000, Crustal signature of Late Archaean tectonic episodes in the Yilgarn craton, Western Australia: evidence from deep seismic sounding: Tectonophysics, **329**, 193-221.

Duncan, A., B. Amann, K. O'Keeffe, P. Williams, T. Tully, A. Wellington, and G. Turner, 1998, Examples from a new EM and electrical methods receiver system: Exploration Geophysics, **29**, 347-354.

Duuring, P., W. Bleeker, and S. W. Beresford, 2012, Structural Modification of the Komatiite-Associated Harmony Nickel Sulfide Deposit, Leinster, Western Australia: Economic Geology, **102**, 277-297.

Eaton, D. W., B. Milkereit, and M. Salisbury, 2003, Seismic methods for deep mineral exploration: Mature technologies adapted to new targets: The Leading Edge, **22**, 580-585.

Elders, J., and A. Wellington, 1998, An application of reverse coupling to increase signal strength beneath conductive sediments-Miitel Mine, Kambalda, W.A: Exploration Geophysics, **29**, 355-360.

Eupene, G. S., P. H. Fee, and R. G. Colvillle, 1975, Ranger One uranium deposits: Australasian Institute of Mines and Metallurgy.

Fagin, S. W., 1998, Model-based depth imaging: Soc of Exploration Geophysicists.

Fessenden, R., 1917, Method and apparatus for locating ore bodies; U.S. Patent No. 1,240,328.

Freire, S. L. M., and T. J. Ulrych, 1988, Application of singular value decomposition to vertical seismic profiling: Geophysics, **53**, 778-785.

Gaiser, J. E., J. P. DiSiena, and K. J. McCoole, 1983, Deviated borehole VSP: Offset reflection point mapping: SEG Technical Program Expanded Abstracts, **2**, 530-533.

Gal'perin, E. I., 1974, Vertical Seismic Profiling: Society of Exploration Geophysicists.

Ganley, D. C., and E. R. Kanasewich, 1980, Measurement of Absorption and Dispersion From Check Shot Surveys: Journal of Geophysical Research, **85**, 28.

Gardner, G. H. F., 1985, Migration of seismic data: Society of Exploration Geophysicists.

Gladwin, M. T., and F. Stacey, 1974, Anelastic degradation of acoustic pulses in rock: Physics of the Earth and Planetary Interiors, **8**, 332-336.

Gole, M. J., S. J. Barnes, and R. E. T. Hill, 1987, The role of fluids in the metamorphism of komatiites, Agnew nickel deposit, Western Australia: Contributions to Mineralogy and Petrology, **96**, 151-162.

Green, A. G., and J. A. Mair, 1983, Subhorizontal fractures in a granitic pluton: Their detection and implications for radioactive waste disposal: Geophysics, **48**, 1428-1449.

Greenhalgh, S. A., and S. Bierbaum, 2000, Underground seismic reflection experiment in a gold mine: Exploration Geophysics, **31**, 321-327.

Greenhalgh, S. A., I. M. Mason, and C. Sinadinovski, 2000, In-mine seismic delineation of mineralization and rock structure: Geophysics, **65**, 1908-1919.

References

Gresham, J. J., 1986, Depositional environments of volcanic-peridotite-associated nickel sulfide deposits with special reference to the Kambalda dome: Geology and metallogeny of copper deposits: Berlin, Springer Verlag, 63-90.

Gulati, J. S., 1998, Borehole seismic surveying: 3C - 3D VSP and land vertical cable analysis: MSc, University of Calgary.

Gulati, J. S., R. R. Stewart, and B. H. Hoffe, 2001, Vertical hydrophone cable acquisition and imaging on land: Geophysics, **66**, 1190-1194.

Hallenburg, J. K., 1984, Geophysical logging for mineral and engineering applications: Penwell Corp.

Hardage, B. A., 1981, An examination of tube wave noise in vertical seismic profiling data: Geophysics, **46**, 892-903.

Hardage, B. A., 2000, Vertical Seismic Profiling: Principles: Pergamon.

Haren, E., and P. K. Williams, 2000, Mine geology practices at the sunrise open pit: Presented at the 4th international Mining Geology Conference.

Harrison, C., 2009, Feasibility of Rock Characterization for Mineral Exploration Using Seismic Data: PhD, Curtin Unversity.

Harrison, C., and M. Urosevic, 2008, Towards direct detection of gold bearing rock formations from seismic data: St. Ives gold Camp, Western Australia: SEG Technical Program Expanded Abstracts, **27**, 1860-1864.

Hauge, P. S., 1981, Measurements of attenuation from vertical seismic profiles: Geophysics, **46**, 1548-1558.

Hein, K. A. A., 2002, Geology of the Ranger Uranium Mine, Northern Territory, Australia: structural constraints on the timing of uranium emplacement: Ore Geology Reviews, **20**, 83-108.

Henriet, J. P., J. Schittekat, and P. Heldens, 1983, Borehole seismic profiling and tube wave applications in a dam site investigation Geophysical Prospecting, **31**, 72-86.

Hinds, R. C., N. L. Anderson, and R. Kuzmiski, 1996, VSP interpretive processing: Theory and practice: Soc Exploration Geophysicists.

Huygens, C., 1690, Traitè de la Lumiere.

Jolly, R. N., 1953, Deep-hole geophone study in Garvin County, Oklahoma: Geophysics, **18**, 662-670.

Juhlin, C., 1995, Finite-difference elastic wave propagation in 2D heterogeneous transversely isotropic media1: Geophysical Prospecting, **43**, 843-858.

Juhlin, C., J. Lindgren, and B. Collini, 1991, Interpretation of seismic reflection and borehole data from Precambrian rocks in the Dala Sandstone area, central Sweden: First Break, **9**, 24-36.

Kan, T. K., M. L. Batzle, and J. E. Gaiser, 1983, Attenuation measured from VSP: evidence of frequency-dependent Q: SEG Technical Program Expanded Abstracts, **2**, 589-590.

Kearey, P., and M. Brooks, 1991, Introduction to geophysical exploration 2nd Edition: Publisher: Blackwell Scientific London Edinburgh.

Knopoff, L., and G. J. MacDonald, 1958, Attenuation of small amplitude stress waves in solids: Reviews of Modern Physics, **30**, 1178.

Krohn, C. E., S. N. Blakeslee, S. T. Chen, J. R. Myron, R. K. McClure, and J. T. Parks, 1995, A cost-effective reservoir imaging method using multiazimuth offset VSPs: The Leading Edge, **14**, 787-794.

Kuzmiski, R., 2010, SEG Continuing Education Course - Borehole geophysics: Theory and practice Presented at the Society of Exploration Geophysics - Annual General Meeting.

Levin, F. K., and R. D. Lynn, 1958, Deep-hole geophone studies: Geophysics, **23**, 639-664.

Marston, R. J., D. I. Groves, D. R. Hudson, and J. R. Ross, 1981, Nickel sulfide deposits in Western Australia; a review: Economic Geology, **76**, 1330-1363.

Marzetta, T. L., M. Orton, A. Krampe, L. K. Johnston, and P. C. Wuenschel, 1988, A hydrophone vertical seismic profiling experiment: Geophysics, **53**, 1437-1444.

McCollum, B., and W. W. LaRue, 1931, Utilization of existing wells in seismograph work: AAPG Bulletin, **15**, 1409-1417.

McKay, A. D., 2010, Australia's Identified Mineral Resources 2010: Geoscience Australia.

Milligan, P. A., J. W. Rector I, and R. W. Bainer, 1997, Hydrophone VSP imaging at a shallow site: Geophysics, **62**, 842-852.

Monash, C., G. Omnes, and H. C. Wu, 1984, Locating a fault through the offset VSP method in the bass island trend, Chautauqua County, New York: SEG Technical Program Expanded Abstracts, **3**, 836-839.

Moon, W., A. Carswell, R. Tang, and C. Dilliston, 1986, Radon transform wave field separation for vertical seismic profiling data: Geophysics, **51**, 940-947.

Muller, K. W., W. L. Soroka, B. N. P. Paulsson, S. Marmash, M. A. Baloushi, and O. A. Jeelani, 2010, 3D VSP technology now a standard high-resolution reservoir-imaging technique: Part 1, acquisition and processing: The Leading Edge, **29**, 686-697.

Myers, J. S., 1993, Precambrian Tectonic History of the West Australian Craton and Adjacent Orogens: Annual Review Of Earth And Planetary Sciences, **21**.

Myers, J. S., and A. H. Hickman, 1990, Pilbra and Yigarn Cratons - Regional geology mineralisation: Australian Institute of Mining and Metallurgy.

Nafe, J. E., and C. L. Drake, 1963, Physical properties of marine sediments, The sea: Interscience publishers, 3, 794-815.

Nickel, E. H., P. D. Allchurch, M. G. Mason, and J. R. Wilmshurst, 1977, Supergene alteration at the Perseverance nickel deposit, Agnew, Western Australia: Economic Geology, **72**, 184-203.

Norris, A. N., 1990, The speed of a tube wave: The Journal of the Acoustical Society of America, **87**, 414-417.

Osman, N., C. Simmat, J. Hargreaves, and I. Mason, 2003, Three-dimensional kinematic imaging of borehole radar data: Exploration Geophysics, **34**, 103-109.

Palmer, D., 1980, The Generalized Reciprocal Method of Seismic Refraction Interpretation: Soc Exploration Geophysicists.

Pham, L. D., C. E. Krohn, T. J. Murray, and S. T. Chen, 1993, A tube wave suppression device for cross-well applications: SEG Technical Program Expanded Abstracts, **12**, 17-20.

Platt, J. P., P. D. Allchurch, and R. W. R. Rutland, 1978, Archaean tectonics in the Agnew supracrustal belt, Western Australia: Precambrian Research, **7**, 3-30.

Porter, D. J., and K. G. McKay, 1981, The nickel sulfide mineralization and metamorphic setting of the Forrestania area, Western Australia: Economic Geology, **76**, 1524-1549.

Pretorius, C., A. Jamison, and C. Irons, 1989, Seismic exploration in the Witwatersrand basin, Republic of South Africa: Presented at the Proceedings of Exploration.

References

Prospect, 2011, Major Resource Projects Map - March 2011: Department of Mines and Petroleum.

Prospect, 2011, Significant Resource projects in Western Australia - March 2011: Department of Mines and Petroleum.

Quan, Y., and J. M. Harris, 1997, Seismic attenuation tomography using the frequency shift method: Geophysics, **62**, 895-905.

Rajeswaran, D., 2008, Hydrophone and geophone vertical seismic profiling for the subsurface characterisation of the Beenyup managed aquifer recharge site, Perth, Western Australia: BSc Hons, Curtin University of Technology.

Ricker, N., 1953, The form and laws of propagation of seismic wavelets: Geophysics, **18**, 10-40.

Robein, E., 2010, Seismic Imaging: A Review of the Techniques, Their Principles, Merits and Limitations: EAGE.

Salisbury, M. H., B. Milkereit, G. Ascough, R. Adair, L. Matthews, D. R. Schmitt, J. Mwenifumbo, D. W. Eaton, and J. Wu, 2000, Physical properties and seismic imaging of massive sulfides: Geophysics, **65**, 1882-1889.

Salisbury, M. H., B. Milkereit, and W. Bleeker, 1996, Seismic imaging of massive sulfide deposits; Part I, Rock properties: Economic Geology, **91**, 821-828.

Schmitt, D. R., J. Mwenifumbo, K. A. DPflug, and I. L. Meglis, 2003, Geophysical logging for elastic properties in hard rocks: A tutorial., *in* D. Eaton, B. Milkereit and M. H. Salisbury, eds., Hardrock Seismic Exploration: Society of Exploration Geophysicists.

Schneider, W. A., 1978, Integral formulation for migration in two and three dimensions: Geophysics, **43**, 49-76.

Sheriff, R. E., 2002, Encyclopaedic Dictionary of Applied Geophysics: Society of Exploration Geophysicists.

Shuey, R., 1985, A simplification of the Zoeppritz equations: Geophysics, **50**, 609-614.

Spencer, T. W., F. E. Davis, R.-C. Wu, and M. Zeitvogel, 1983, VSP measurement of seismic attenuation: SEG Technical Program Expanded Abstracts, **2**, 590-592.

Stainsby, S., and M. Worthington, 1985, Q estimation from vertical seismic profile data and anomalous variations in the central North Sea: Geophysics, **50**, 615-626.

Stolz, E. M. G., 2003, Direct detection of gold bearing structures at St Ives, WA: DHEM vs DHMMR: Exploration Geophysics, **34**, 131-136.

Stone, D. G., 1983, Predicting pore pressure and porosity from VSP data: SEG Technical Program Expanded Abstracts, **2**, 601-604.

Stone, W. E., and N. J. Archibald, 2004, Structural controls on nickel sulphide ore shoots in Archaean komatiite, Kambalda, WA: the volcanic trough controversy revisited: Journal of structural geology, **26**, 1173-1194.

Stone, W. E., S. W. Beresford, and N. J. Archibald, 2005, Structural setting and shape analysis of nickel sulfide shoots at the Kambalda Dome, Western Australia: implications for deformation and remobilization: Economic Geology, **100**, 1441-1455.

Stone, W. E., and E. E. Masterman, 1998, Kambalda nickel deposits, *in* D. A. Berkman. and D. H. Mackenzie., eds., Geology of Australian and Papua New Guinean mineral deposits Australasian Institute of Mining and Metallurgy Monograph 347-356.

Sun, L. F., B. Milkereit, and D. R. Schmitt, 2009, Measuring velocity dispersion and attenuation in the exploration seismic frequency band: Geophysics, **74**, WA113-WA122.

Suprajitno, M., and S. A. Greenhalgh, 1985, Separation of upgoing and downgoing waves in vertical seismic profiling by contour-slice filtering: Geophysics, **50**, 950-962.

Surhone, L. M., M. T. Tennoe, and S. F. Henssonow, 2010, Yilgarn Craton: Betascript Publishing.

Swager, C. P., 1997, Tectono-stratigraphy of late Archaean greenstone terranes in the southern Eastern Goldfields, Western Australia: Precambrian Research, **83**, 11-42.

Tang, X., 2003, Determining formation shear-wave transverse isotropy from borehole Stoneley-wave measurements: Geophysics, **68**, 118-126.

Telford, W. M., L. P. Geldart, and R. E. Sheriff, 1990, Applied geophysics: Cambridge Univ Press.

Tonn, R., 1991, The determination of the seismic quality factor from VSP data: A comparison of different computational methods 1. : Geophysical Prospecting, **39**, 1-27.

Truax, B., 2001, Handbook of Acoustic Ecology, (CD-ROM version): Computer Music Journal, **25**, 93-94.

Turner, G., I. M. Mason, J. E. Hargreaves, and A. Wellington, 2000, Borehole radar surveying for orebody delineation: Presented at the Eighth International Conference on Ground Penetrating Radar, SPIE-International Society for Optical Engine.

Urosevic, M., 2000, A study of seismic wave propagation as applied to seismic imaging in the Southern Sydney Basin: Ph D, Curtin University of Technology.

Urosevic, M., and B. Evans, 2007, Feasibility of seismic methods for imaging gold deposits in Western Australia. : Minerals and Energy Research Institute of Western Australia.

Urosevic, M., E. Stolz, and S. Massey, 2005, Seismic exploration for gold in a hard rock environment - Yilgarn Craton, Western Australia: Presented at the 67th Meeting, EAGE.

Van Niekerk, S., 2011, Personal Communication RE:PAC-R density and Viscosity

Van Sandt, D. R., and F. K. Levin, 1963, A study of cased and open holes for deep-hole seismic detection: Geophysics, **28**, 8-13.

Van Schaack, M. A., and J. C. Costa, 1996, XSP-CDP Mapping In Complex Media Without Raytracing: Presented at the Soc Exploration Geophysics Annual Meeting.

Virieux, J., 1986, P-SV wave propagation in heterogeneous media: velocity-stress finite-difference method: Geophysics, **51**, 889-901.

Western Areas, 2008, Mineral resources doubles at Spotted Quoll with bonanza 7.2% nickel grade: Western Areas NL.

White, J. E., 1953, Signals in a borehole due to plane waves in the solid: Journal of Acoustic Society of America, **25**, 905-915.

White, J. E., 1965, Seismic waves: Radiation, transmission and attenuation: McGraw-Hill.

White, J. E., 2000, Seismic Wave Propagation: Society of Exploration Geophysicists.

Widess, M. B., 1973, How thin is a thin bed: Geophysics, **38**, 1176-1180.

References

Wright, C., 1981, Seismic methods in mineral exploration. : Economic Geology, 863-870.

Wyatt, K., and S. Wyatt, 1981, The determination of subsurface structural information using the vertical seismic profile: Presented at the 51st Annual International Meeting.

Yilmaz, Ö., 2001, Seismic data analysis: Society of Exploration Geophysicists.

Zhou, B., and S. Greenhalgh, 1997, A synthetic study on Crosshole Resistivity Imiaging using different electrode arrays: Exploration Geophysics, **28**, 1 - 5.

Zoeppritz, K., and L. Geiger, 1919, Über Erdbebenwellen II. Laufzeitkurven: Nachrichten der Königlichen Gesellschaft der Wissenschaften zu Göttingen, Mathematisch-physikalische Klasse.

Appendices

List of appendix figures

Appendix I

M-file to produce VSP travel-time curves in a simple 2 layer case. The layer velocities, borehole, receiver, source and reflector geometry can be set to mimic deviated boreholes drilled into a any dipping layer from any deviated borehole. The code produces two graphical outputs: 1) A plot of the assigned borehole, geology, source, receivers, the source image point and illuminates the reflection surface corresponding to the assigned geometry; 2) A travel-time plot of the direct arrivals and reflection. An example has been provided below in Figure A1 using the following parameters;

>> Model Travel Times

Layer depth (m) = 555

Layer dip (+ive down-dip to the right) in degrees = 33

Velocity (m/s) v1 = 3333

Velocity (m/s) v2 = 5555

SOU X offset from collar (m) = -200

Borehole Deviation (from vertical in degrees) = 11

Depth of top Receiver (m) 55

Depth of bottom Receiver (m) 755
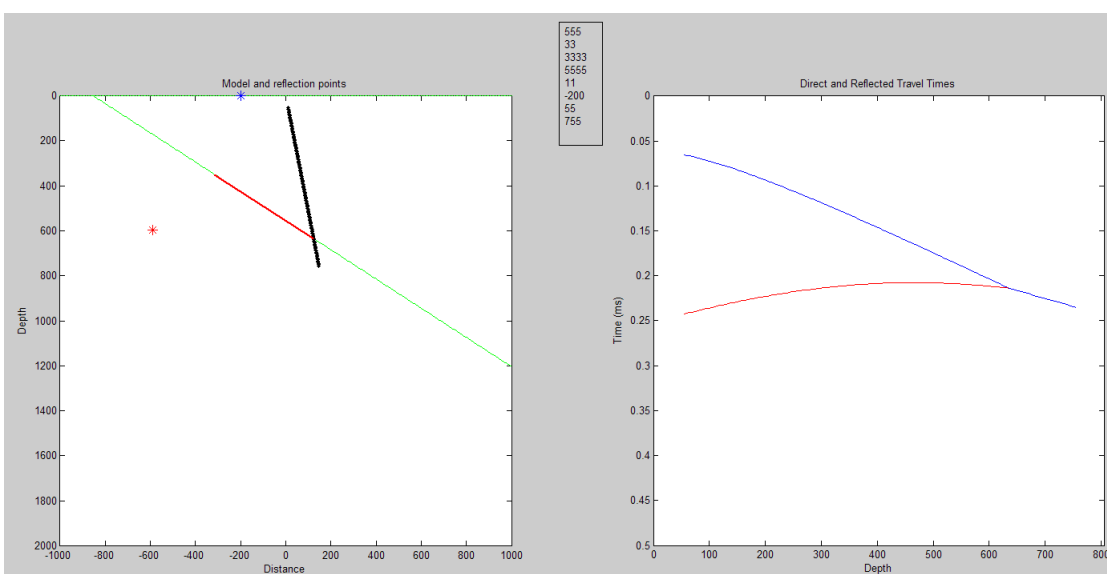
Figure A 1. Output from Model Travel-Time code.

246

Note; the above example is not a typical borehole and dipping layer geometry expected in mineral exploration. Typically the borehole would be drilled in the opposite orientation to intersect the borehole orthogonally. This example was used to illustrate the hyperbolic nature of direct and reflected travel times.

M-file code

```
%   plots travel time given a certain geometry and velocities
%%%%%%%%%%%%%%%%%%%%%%%%%%%%%%%%%%%%%%%%%%%%%%%%%%%%%%%%%%%%%%%%%

clear all
close all

%   model limits
x=[-1000:5:1000]; z=[0:5:2000];

%   second layer
% laydepth =555; dip=65; slope=-1;
laydepth=input('Layer depth ');
dip=input('dip in degrees = ');
slope=input('Slope down-dip to right = -1 or down-dip to the left = 1
');

% angles of second layer
alpha1=slope*(dip*pi)/180; alpha=(dip*pi)/180;

% Layer XY slope x intercept
x2=x; z2=laydepth-x2.*tan(alpha1);
plane=polyfit(x2,z2,1); A=plane(1); B=plane(2);

%   Velocities
% v1=3500; v2=5000;
v1 = input('Velocity v1 = ');
v2 = input('Velocity v2 = ');

%   Shot point
% soux=0;
soux=input('SOU X ');
souz=0;
if soux == 0
    soux=0.001;
else
    soux = soux;
end

%   borehole geometry
% bhztop=50; bhzbot=750; bhdip=0;
% beta=(bhdip*pi)/180;
bhdip=input('Borehole Dip (from vertical) ');beta=(bhdip*pi)/180;
bhztop=input('Depth of top Reciever  ');
```

247

```matlab
bhzbot=input('Depth of bottom Reciever  ');

chans =(bhzbot-bhztop)/5;
number_of_5m_channels = chans + 1
bhz=[bhztop:(bhzbot-bhztop)/chans:bhzbot];
beta1=((pi()/2)-beta)*180/pi();
delta=(180-dip-(90-bhdip));
theta=(180-(dip+2*delta));

bhx=[0-bhz.*tan(beta)];

if bhdip < 0
    bhxtop=min(bhx);
    bhxbot=max(bhx);
else
    bhxtop=max(bhx);
    bhxbot=min(bhx);
end

%%%%%%%%%%%%%%%%%%%%%%%%%%%%%%%%%%%%%%%%%%%%%%%%%%%%%%%%%%%%%%%%%%%%%%%%%%%%%
%%%

%   Geometry points from inputs

%   Point P
px=-B/A;
pz=souz;
%   length PS
% SOU-P
ps=sqrt((soux-px)^2);
%   length PQ
% Distance to Q
pq=2*ps*cos(alpha);
delx=pq*cos(alpha);
delz=pq*sin(alpha);
%   point Q from point P
qx=px -(delx*slope);
% point Q (image of P)
qz=pz +(delz);



%   Image point
Iz=qz;  Ix=qx+(ps*slope);    Im=[Ix Iz];
% Image Point



%   Image point intersection with PQ, ImageBHtop/Bhbot and direct ray

LA = [(Iz-bhzbot), -(Ix-bhxbot);(qz-pz), -(qx-px)];
% Lines PQ and BHbot image
bmin = [(Iz-bhzbot)*bhxbot-(Ix-bhxbot)*bhzbot;(qz-pz)*px-(qx-px)*pz];

LB = [(Iz-bhztop), -(Ix-bhxtop);(qz-pz), -(qx-px)];
% Lines PQ and BHtop image
bmax = [(Iz-bhztop)*bhxtop-(Ix-bhxtop)*bhztop;(qz-pz)*px-(qx-px)*pz];

LL = [(bhzbot-bhztop), -(bhxbot-bhxtop);(qz-pz), -(qx-px)];
% Lines PQ and BH
```

248

```matlab
blay = [(bhzbot-bhztop)*bhxtop-(bhxbot-bhxtop)*bhztop;(qz-pz)*px-(qx-
px)*pz];


%    Image points on PQ and BH intersection
PIntmin = inv(LA)*bmin;
PIntmax = inv(LB)*bmax;
PIntlay = inv(LL)*blay;


if bhzbot > PIntlay(2)
% image points on PQ to plot
    xint=[PIntmax(1),PIntlay(1)]; zint=[PIntmax(2),PIntlay(2)];
    chansup =  round(sqrt( (PIntlay(1)-bhxtop)^2 + (PIntlay(2)-
bhztop)^2 )/5)
    chansdown = chans-chansup+1
else
    xint=[PIntmin(1),PIntmax(1)]; zint=[PIntmin(2),PIntmax(2)];
    chansup =  chans +1
    chansdown = 0

end


%    Direct Ray
%%%%%%%%%%%%%%%%%%%%%%%%%%%%
dpath=sqrt( (bhx-soux).^2 + (bhz-souz).^2 );
% Length direct ray path

% Above
if zint(2) < max(bhz)
    bhxup = linspace(bhxtop,PIntlay(1),chansup);
    bhzd = linspace(bhztop,PIntlay(2),chansup);
    dray = sqrt( (bhxup-soux).^2 + (bhzd-souz).^2 );
else
    bhxup = linspace(bhxtop,bhxbot,chansup);
    bhzd = linspace(bhztop:bhzbot,chansup);
    dray = dpath;
    bhzdd=bhz;
end

% Below

bhxd = linspace(PIntlay(1),bhxbot,chansdown);
bhzdd = linspace(PIntlay(2),bhzbot,chansdown);
drayd = sqrt( (bhxd-soux).^2 + (bhzdd-souz).^2 );

TTd = dray./v1;
dint = sqrt( (PIntlay(1)-soux).^2 + (PIntlay(2)-souz).^2 );
TTint = dint/v1;
TTdd = TTint + (drayd-dint)./v2;


%   Reflection points
%%%%%%%%%%%%%%%%%%%%%%%%%%%%%
if PIntlay(2) > max(bhz)
    Refx = [bhxtop, bhxbot];
    Refz = [bhztop, bhzbot];
else
    Refx=[bhxtop, PIntlay(1)];
    Refz=[bhztop, PIntlay(2)];
```

```matlab
end

if Refx(1) == 0
    refx = zeros(1,chansup);
    refz=linspace(Refz(1),Refz(2),chansup);
else
    refx=linspace(Refx(1),Refx(2),chansup);
    refz=linspace(Refz(1),Refz(2),chansup);
end


%  Reflection Travel Times
TTr=sqrt( (refx-Ix).^2 + (refz-Iz).^2 )./v1;



%   ********  PLOTS   ***********************************

figure(1)
aaa=[bhdip dip soux bhztop];
annotation(figure(1),'textbox',...
    [0.47 0.63 0.1 0.1],'string',aaa,'FitBoxToText','on');


%   model and SOU REC geometry
subplot(1,2,1)
%   Surface
plot(x2,0,'g','LineWidth',2)
hold on
%   Source
plot(soux,souz,'b*','MarkerSize',10,'LineWidth',2)
%   layer 2
plot(x2,z2,'gr','LineWidth',2)
hold on
%   borehole
plot(bhx,bhz,'.k')
hold on
set(gca,'YDir','reverse','FontSize',12)
hold on
%   Image point
plot(Ix,Iz,'r*','MarkerSize',10,'LineWidth',2)
hold on
plot(xint,zint,'r','LineWidth',3)
%%%%%%%% geometry points for calculations %%%%%%%%%%%%%%%%%%%%%%%%%%%
% hold on
% %  Reflector intercepts
%
plot(PIntmin(1),PIntmin(2),'co',PIntmax(1),PIntmax(2),'bo',PIntlay(1),
PIntlay(2),'ro')
% %  BHmin/max points
% hold on
% plot(bhxbot,bhzbot,'mo',bhxtop, bhztop,'mo')
% hold on
% %  P point
% plot(px,pz,'b*')
% %  Q point
% plot(qx,qz,'r*')
% % hold on
% % plot(layinttop(1),layinttop(2),'x',layintbot(1),layintbot(2),'x')



axis([min(x) max(x) -0.0001 max(z)])
```

250

```matlab
axis square % axis equal
xlabel('Distance','FontSize',14)
ylabel('Depth','FontSize',14)
title('Model and reflection points','FontSize',16)

hold on

%   Travel Time curves
subplot(1,2,2)

%   direct Ray
if bhzbot > PIntlay(2)
    plot(bhzd,TTd,'b',bhzdd,TTdd,'b','LineWidth',2)
else
    plot(bhzd,TTd,'b','LineWidth',2)
end
set(gca,'YDir','reverse','FontSize',12)
hold on
%   Reflection
if bhzbot < PIntlay(2)
    plot(bhz,TTr,'r','LineWidth',2)
else
    plot(refz,TTr,'r','LineWidth',2)
end
xlabel('Depth','FontSize',14)
ylabel('Time (ms)','FontSize',14)
title('Direct and Reflected Travel Times','FontSize',16)
axis([0 bhzbot+100 0 0.5])
axis square
```

Appendix II

Pressure and particle velocity

Here we derive the relationships between pressure and particle velocity as measured in seismic methods by hydrophones and geophones respectively. We do this using Newton's II law $(F = m \cdot a = \frac{dv}{dt})$, III law (action = reaction) and Hook's law $(stress \sim \sum strain)$. Let us consider a cylindrical plate at depth z and incident uniform plane wave, where particles only move up or down as shown in Figure 1. The coefficients used in the derivations are as follows:

P – Pressure or stress	$P = P(z,t)$	F – Force;	$F = A \cdot P$
ψ – displacement;	$\psi = \psi(z,t)$	v – particle velocity,	$v = \frac{\partial \psi}{\partial t}$
M – Elastic constant	general		
ε – strain (dimensionless)	$\varepsilon = \frac{\Delta l}{L}$	or ε – strain	$\frac{\frac{\partial \psi}{\partial t}dz}{dt} = \frac{\partial \psi}{\partial z}$
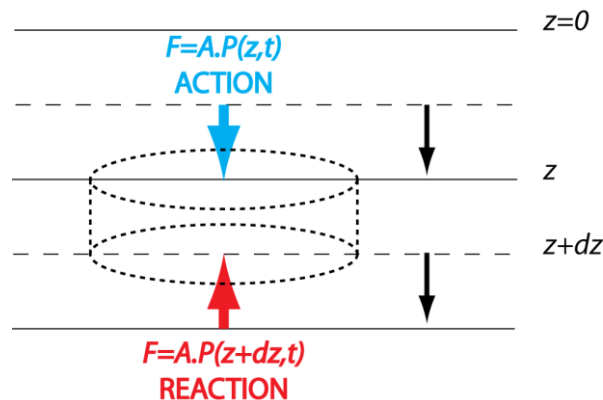
Figure A 2.Particle velocity and forces exerted on a small cylindrical plate from a plane wave in a uniform medium.

The total force in one direction is the difference between the two forces. i.e. the Net

$$\text{Force} = A[P(z,t) - P(z+dz,t)] \quad = \rho \cdot v \frac{dv}{dt} \quad = \rho(Adz) \cdot \frac{\partial v_{(z,t)}}{\partial t}$$

Since $\qquad \Delta z \to 0 \ \lim_{z>0} P_{(z,t)} \gg \dfrac{\partial v}{\partial t}$

Then $\qquad -\dfrac{\partial P_{(z,t)}}{\partial z} dz = \rho \dfrac{\partial v}{\partial t} dz$

And $\qquad \dfrac{\partial P_{(z.t)}}{\partial z} = -\rho \dfrac{\partial v_{(z,t)}}{\partial t}$

or $\qquad\qquad\qquad\qquad \dfrac{\partial v}{\partial t} = -\dfrac{1}{\rho}\dfrac{\partial P}{\partial z}$ $\qquad\qquad$ **Equation 2**

Strain (ϵ) is the fractional change in length divided by the original length and has no direction where $\Delta l \cong \dfrac{\partial \psi}{\partial z}\, dz$;

$$\epsilon = \frac{\Delta l}{L} = \frac{\left(\dfrac{\partial \psi}{\partial z}\cdot dz\right)}{dz} = \frac{\partial \psi}{\partial z}$$

Hook's Law relates stress and strain as a linear combination or simply stress $\sim$ strain.
$stress\ P_{(z,t)}$ and $strain\dfrac{\partial \psi}{\partial z}$

$$P_{(z,t)} = -M\frac{\partial \psi}{\partial z}$$

Differentiate with respect to $t\ \left(\dfrac{d}{dt}\right)$

$$\frac{\partial P}{\partial t} = -M\frac{\partial \psi}{\partial t \partial z} = -M\frac{\partial v}{\partial z} \qquad\qquad \textbf{Equation 3}$$

Comparing Equations 1 and 2; Geophones measure particle velocity (Equation 1) like Newton's Law and hydrophones measure pressure changes like Hook's Law.

Newton's II law $\qquad\qquad\qquad\qquad$ Hook's Law

$$a = \frac{1}{\rho}\frac{\partial P}{\partial z} \qquad\qquad \frac{\partial P}{\partial t} = M\frac{\partial}{\partial z}(v) = M\frac{\partial}{\partial z}\left(\frac{\partial\psi}{\partial t}\right)$$

$$\rho a = \frac{\partial P}{\partial z} \qquad\qquad = M\frac{\partial}{\partial t}\left(\frac{\partial\psi}{\partial z}\right)$$

$$\frac{ma}{dV} = \frac{dF}{dzdxdy} = \frac{dF}{dV} \qquad\qquad \frac{\partial P}{\partial t} = M\frac{\partial}{\partial t}\psi$$

$$ma \sim F \qquad\qquad P \sim M\psi$$

To eliminate pressure;

$$\frac{\partial}{\partial t}(Equation\ 1) \qquad\qquad \frac{\partial}{\partial z}(Equation 2)$$

$$\frac{\partial^2 v}{\partial t^2} = -\frac{1}{\rho}\frac{\partial^2 P}{\partial z\,\partial t} \qquad\qquad \frac{\partial^2 P}{\partial z\,\partial t} = -M\frac{\partial^2 v}{\partial z^2}$$

Substituting the right hand side into the left hand side and setting to zero

$$M\frac{\partial^2 v}{\partial z^2} - \rho\frac{\partial^2 v}{\partial t^2} = 0$$

$$\frac{\partial^2 v}{\partial t^2} = \frac{M}{\rho}\frac{\partial^2 v}{\partial z^2} \qquad\qquad \textbf{Equation 4}$$

Similarly eliminating particle velocity;

$$\frac{\partial}{\partial z}(Equation\ 1) \qquad\qquad \frac{\partial}{\partial t}(Equation 2)$$

$$\frac{\partial^2 v}{\partial z\,\delta t} = \frac{\partial}{-\partial z}\left(\frac{1}{\rho}\frac{\partial P}{\partial z}\right) \qquad\qquad \frac{\partial^2 v}{\partial z\,\partial t} = -\frac{\partial}{\partial t}\left(\frac{1}{M}\frac{\partial P}{\partial t}\right)$$

Substitute right hand side into left and set to zero

$$\frac{\partial^2 P}{\partial t^2} = \frac{M}{\rho} \frac{\partial^2 P}{\partial z^2}$$ **Equation 5**

Equations 3 and 4 now have an equivalent form, thus Equation 3 $\equiv$ Equation 4. Now let $c^2 = M/\psi$ where c is the velocity and M and ψ are held constant.

The solution is of the form $\quad U = f\left(t - \frac{z}{c}\right) + g\left(t + \frac{z}{c}\right)$ (d'Alembert's Equation). Thus;

$$\frac{\partial U}{\partial t} = f'\left(t - \frac{z}{c}\right) \cdot 1 \qquad\qquad \frac{\partial^2 U}{\partial t^2} = f''\left(t - \frac{z}{c}\right)$$

$$\frac{\partial U}{\partial z} = f'\left(t - \frac{z}{c}\right)\left(-\frac{1}{c}\right) \qquad\qquad \frac{\partial^2 U}{\partial z^2} = f''\left(t - \frac{z}{c}\right)\left(\frac{1}{c^2}\right)$$

or the full function

$$\frac{\partial U}{\partial t} = f' + g' \qquad\qquad \frac{\partial^2 U}{\partial t^2} = f'' + g''$$

$$\frac{\partial U}{\partial z} = \left(-\frac{1}{c}\right)(f' + g') \qquad\qquad \frac{\partial^2 U}{\partial z^2} = \frac{1}{c^2}(f'' + g'')$$

$$\Rightarrow \frac{\partial^2 U}{\partial t^2} = c^2 \frac{\partial^2 U}{\partial z^2} \Rightarrow c^2 = \frac{M}{\psi}$$

Remembering Equations 1 and 2 and since U is the solution, then;

$$\frac{\partial U}{\partial t} = -\frac{1}{\rho}\frac{\partial P}{\partial z} \qquad\qquad \text{and} \qquad\qquad \frac{\partial P}{\partial t} = -M\frac{\partial U}{\partial z}$$

Solve for P to obtain solution. Since P and v are of different dimensions we have

$$P = A \cdot f\left(t - \frac{z}{c}\right) + B \cdot g\left(t + \frac{z}{c}\right)$$

To determine the relationship between pressure and particle velocity we need to determine the coefficients A and B. From Equation 4; f and g or $f + g$ are solutions. To solve, we first take f then g. Thus;

for A
$$\frac{\partial U}{\partial t} = f' = -\frac{1}{\rho}\frac{\partial}{\partial z}(Af) = -\frac{1}{\rho}Af'\left(-\frac{1}{c}\right) \Rightarrow A = \rho c$$

$$-Mf'\left(-\frac{1}{c}\right) = \frac{\partial P}{\partial t} = Af' \Rightarrow A = \frac{M}{c} = \frac{c^2\rho}{c} = \rho c$$

for B
$$\frac{\partial P}{\partial t} = Bg' = -M\frac{\partial u}{\partial z} = -Mg'\left(+\frac{1}{c}\right) \Rightarrow B = -\frac{M}{c} = -\rho c$$

so $\qquad\qquad A = \rho c \qquad$ and $\qquad B = -\rho c$

Therefore; $\quad U = f\left(t - \frac{z}{c}\right) + g\left(t + \frac{z}{c}\right) \quad$ and $\quad P = \rho c f\left(t - \frac{z}{c}\right) - \rho c g\left(t + \frac{z}{c}\right)$

Where: $d = f\left(t - \frac{z}{c}\right)$ is for the down-going wavefield and $u = g\left(t + \frac{z}{c}\right)$ is for the up-going wavefield.

or $\qquad\qquad U = f + g$ **Equation 6**

Equation 7

$$\frac{P}{\rho c} = f - g$$

So the down-going wavefield $d = \frac{1}{2}\left(U + \frac{P}{\rho c}\right)$ and the up-going wavefield $u = \frac{1}{2}\left(U - \frac{P}{\rho c}\right)$.

Now P and U have the same units. So the difference between pressure and particle velocity is the sign. However, they are two independent variables $U = U_{(z,t)}$ and

$P = P_{(z,t)}$ where $M = K + \frac{4}{3}\eta$. Equation 5 is the general solution when M, ρ are held constant i.e. when $c = $ constant.

At a boundary, both the particle velocity and pressure are continuous, however, some energy is reflected back and some transmitted as shown below in Figure 2.
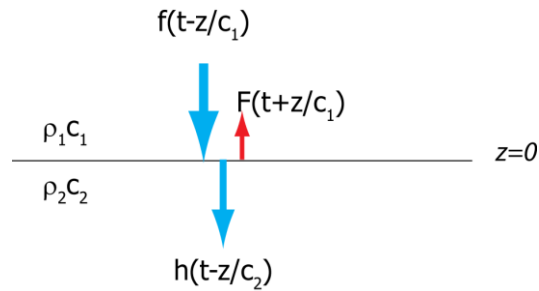
Figure A 3. Transmission and Reflection of energy at a boundary.

By the law of conservation of energy, for:

particle velocity $\qquad\qquad f\left(t - \dfrac{z}{c_1}\right) + F\left(t + \dfrac{z}{c_1}\right) = h\left(t - \dfrac{z}{c_2}\right)$ **Equation 8**

for pressure $\qquad\qquad \rho_1 c_1 f\left(t - \dfrac{z}{c_1}\right) - \rho_1 c_1 F\left(t + \dfrac{z}{c_1}\right)$ **Equation 9**

$$= \rho_2 c_2 h\left(t - \dfrac{z}{c_2}\right)$$

We can say that what goes up is a scaled version of the incident wavefield (what was going in at $z = 0$, $F(t) = Rf(t)$ or what goes down will be a scaled version of the input energy; $h(t) = Tf(t)$, where R and T are reflection and transmission coefficients respectively . Accordingly from Figure 2;

For particle velocity: $h(t) - Tf(t) = f(t)$

i.e.   (7) $Tf(t) - Rf(t) = f(t);$ $\qquad\quad T - R = 1 ; \quad T = 1 + R$

(8) $\rho_1 c_1 f(t) - R\rho_1 c_1 f(t) = T\rho_2 c_2 f(t);$ $\qquad \rho_1 c_1 - R\rho_1 c_1 = T\rho_2 c_2$

$$\rho_1 c_1 - R\rho_1 c_1 = (1 + R)\rho_2 c_2; \qquad \rho_1 c_1 - \rho_2 c_2 = R(\rho_2 c_2 + \rho_1 c_1)$$

$$R_u = \frac{(\rho_1 c_1 - \rho_2 c_2)}{\rho_1 c_1 + \rho_2 c_2} \qquad \text{and} \qquad T_u = \frac{2\rho_1 c_1}{\rho_1 c_1 + \rho_2 c_2}$$

For Pressure;

$$\rho_1 c_1 F(t) = R \cdot \rho_1 c_1 f(t) => F(t) = R \cdot f(t)$$

$$\rho_2 c_2 h(t) = T \cdot \rho_1 c_1 f(t) => h(t) = \frac{\rho_1 c_1}{\rho_2 c_2} T \cdot f(t)$$

Plug into (8);

$$\rho_1 c_1 f(t) - \rho_1 c_1 R \cdot f(t) = \rho_2 c_2 \cdot T \cdot \frac{\rho_1 c_1}{\rho_2 c_2} f(t);$$

$$1 - R = T \qquad \text{or} \qquad T + R = 1;$$

For pressure R is of opposite sign. When compared to particle velocity; $1 + (-R) = T$. Thus,

$$R_d = \frac{\rho_2 c_2 - \rho_1 c_1}{\rho_2 c_2 + \rho_1 c_1}, \qquad \text{or} \qquad T_d = T_u.$$

Particles in the air are free to move more than in water. The opposite is true with pressure. In water, it takes more pressure to move particles, so particle velocity and pressure are always opposite when the pressure required is large and the particle velocity is low.

Appendix III

The wave equation in acoustic modelling

The wave equation is defined as; an equation that relates the spatial and time dependence of a disturbance which can propagate as a wave (Sheriff, 2002). In the acoustic case, physical properties are described by distribution in space of two parameters; velocity of propagation of compressional waves $v_p(x_1, x_3)$ and density $\rho(x_1, x_3)$. The acoustic wave equation is described by the vector field of displacement velocities **u** and scalar fields of pressures p, which corresponds to the system of differential equations;

$$\textit{Equation 1:} \quad \frac{\delta u_1}{\delta t} = \frac{1}{\rho}\frac{\delta p}{\delta x_1}$$

$$\textit{Equation 2:} \quad \frac{\delta u_3}{\delta t} = \frac{1}{\rho}\frac{\delta p}{\delta x_3}$$

$$\textit{Equation 3:} \quad \frac{\delta p}{\delta t} = \rho v^2\left(\frac{\delta u_1}{\delta x_1} + \frac{\delta u_3}{\delta x_3}\right)$$

Differentiating equations (1) by x_1, (2) by x_3 and (3) by t we obtain;

$$\textit{Equation 4:} \quad \frac{\delta^2 u_1}{\delta t \delta x_1} = \frac{\delta\frac{1}{\rho}}{\delta x_1}\frac{\delta p}{\delta x_1} + \frac{1}{\rho}\frac{\delta^2 p}{\delta x_1^2}$$

$$\textit{Equation 5:} \quad \frac{\delta^2 u_3}{\delta t \delta x_3} = \frac{\delta\frac{1}{\rho}}{\delta x_3}\frac{\delta p}{\delta x_3} + \frac{1}{\rho}\frac{\delta^2 p}{\delta x_3^2}$$

$$\textit{Equation 6:} \quad \frac{\delta^2 p}{\delta t^2} = \rho v^2\left(\frac{\delta^2 u_1}{\delta t \delta x_1} + \frac{\delta^2 u_3}{\delta t \delta x_3}\right)$$

Substitution (4) and (5) into (6) we obtain the acoustic wave equation in pressure notation;

$$\frac{\delta^2 p}{\delta t^2} = \rho v^2 \left[\left(\frac{\delta \frac{1}{\rho}}{\delta x_1} \frac{\delta p}{\delta x_1} + \frac{1}{\rho} \frac{\delta^2 p}{\delta x_1^2} \right) + \left(\frac{\delta \frac{1}{\rho}}{\delta x_3} \frac{\delta p}{\delta x_3} + \frac{1}{\rho} \frac{\delta^2 p}{\delta x_3^2} \right) \right]$$

$$\textit{Equation 7:} \quad = v^2 \left(\frac{\delta^2 p}{\delta x_1} + \frac{\delta^2 p}{\delta x_3} \right) + \rho v^2 \left(\frac{\delta \frac{1}{\rho}}{\delta x_1} \frac{\delta p}{\delta x_1} + \frac{\delta \frac{1}{\rho}}{\delta x_3} \frac{\delta p}{\delta x_3} \right)$$

A Finite-difference method is then used to solve the differential equations at all points within the defined mesh/grid.

Elastic Isotropic Modelling

In elastic isotropic modelling the properties are described similarly to that of acoustic propagation of section 3.2 with the addition of shear wave velocity v_s to the model. The model thus has distribution in space of three parameters; v_p (x_1, x_3), v_s (x_1, x_3) and $\rho(x_1, x_3)$. From these variables Lames parameters λ and μ can be defined $\lambda = \rho(v_p^2 - 2v_s^2)$ and $\mu = \rho v_s^2$. Lames parameters correspond to elastic constraints $a_{12} = \lambda$ and $a_{55} = \mu$. Now the isotropic elastic approximation in time can be expressed as components of the displacement vector $\boldsymbol{u} = (u_1, u_3)$ and the stress tensor $\tau_{ij} = (i, j = 1, 3)$.

$$\textit{Equation 8.1:} \quad \frac{\partial \tau_{11}}{\partial t} = a_{11} \frac{\delta u_1}{\delta x_1} + a_{13} \frac{\delta u_3}{\delta x_3}$$

$$\textit{Equation 8.2:} \quad \frac{\delta \tau_{33}}{\delta t} = a_{13} \frac{\delta u_1}{\delta x_1} + a_{33} \frac{\delta u_3}{\delta x_3}$$

$$\textit{Equation 8.3:} \quad \frac{\delta \tau_{13}}{\delta t} = a_{55} \left(\frac{\delta u_1}{\delta x_1} + \frac{\delta u_3}{\delta x_3} \right)$$

$$\textit{Equation 8.4:} \quad \frac{\delta u_1}{\delta t} = \frac{1}{\rho} \left(\frac{\delta \tau_{11}}{\delta x_1} + \frac{\delta \tau_{13}}{\delta x_3} \right)$$

$$\textit{Equation 8.5:} \quad \frac{\delta u_3}{\delta t} = \frac{1}{\rho} \left(\frac{\delta \tau_{13}}{\delta x_1} + \frac{\delta \tau_{33}}{\delta x_3} \right)$$

Appendix IV

BH1 – Hydrophone tube-wave removal processing flow

#7: InputMult[INPUT DATA] - Input Multiple Data Sets 8 Inputs

   Input   1: [1] - 28-790-001-009 [216 Traces 0.0 - 1500.0 ms SR: 500.000 us]

   Input   2: [2] - 28-785-010-015 [144 Traces 0.0 - 1500.0 ms SR: 500.000 us]

   Input   3: [3] - 28-560-016-020 [120 Traces 0.0 - 1500.0 ms SR: 500.000 us]

   Input   4: [4] - 28-555-021-028 [192 Traces 0.0 - 1500.0 ms SR: 500.000 us]

   Input   5: [5] - 28-330-029-038 [240 Traces 0.0 - 1500.0 ms SR: 500.000 us]

   Input   6: [6] - 28-325-039-046 [192 Traces 0.0 - 1500.0 ms SR: 500.000 us]

   Input   7: [7] - 28-100-047-057 [264 Traces 0.0 - 1500.0 ms SR: 500.000 us]

   Input   8: [8] - 28-095-058-066 [216 Traces 0.0 - 1500.0 ms SR: 500.000 us]

  NO SORT ORDER

  Cache input data sets: Default Cache Size

  -- NO DATA SELECTIONS --

InputMult 1584 Traces Input

#8: Rave[MATH] - Running Average

  Rave Type: Mean Value #SamplesWindow: 100

SubInput   1:#7 - Input Multiple Data Sets   [INPUT DATA] - 2:#8 - Running Average [MATH]

#6: OrmsbyBP[FILTERING] - Ormsby Band-Pass 5.00/15.00-155.00/200.00 Hz

     Restore Mutes after Filtering

     Percent Zero Padding for FFT: 10.00 %

#5: TmpQuery[OUTPUT DATA] - Temporary Output File with QUERY

  Output Name: DeWow

  Create Sort Indexes

  PLOT Data Vertical 2

   Output Group# 6: 1: 28m ZVSP

TmpQuery - DeWow [TotalTraces: 1584]

Created Tue Mar 29 08:41:52 2011

#1: Input[INPUT DATA] - Input Data [11] - DeWow

  Seismic Input: [11] - DeWow

  NO SORT ORDER

  -- NO DATA SELECTIONS --

 [1584 Traces Input]

#2: AGC[SCALING] - Automatic Gain Control(AGC) L1/L2 Norm Equalization

  AGC Length: 1499.00 Scale: 1.000 Norm Eq: L1

#3: TmpQuery[OUTPUT DATA] - Temporary Output File with QUERY

  Output Name: 020 Bal

  Create Sort Indexes

  PLOT Data FULL Screen

  Output Group# 6: 1: 28m ZVSP

TmpQuery - 020 Bal [TotalTraces: 1584]

Created Tue Mar 29 08:57:12 2011

#4: Input[INPUT DATA] - Input Data [12] - 020 Bal

  Seismic Input: [12] - 020 Bal

  Sort Order[4]: FIELD_RECORD_NO

  -- NO DATA SELECTIONS --

 [1584 Traces Input]

#7: EditHed[HEADERS] - Header Edit

  MAP 1 ** DATA_FIRSTBREAK

    # IF DATA_FIRSTBREAK Equal To: -1.0000

     ADD [CONSTANT] 130.000

#5: VSPWaveSep[VSP] - VSP Wave by Wave Separation

  # Traces in One Spatial Window: 6

  Window to Determine Wave Parameters: 100.000000 [Up-Going Waves]

  Running Window: 20.000000 [Trace Weight Calc]

  Output Residual Wave Field

  4 Waves

1 : Tube Down-Going 300.00/0.90/*NO-Output - DownPriTube.tim

2 : Tube Down-Going 300.00/0.90/*NO-Output - DownChevTube.tim

3 : Tube Up-Going 300.00/0.90/*NO-Output - UpBottTube.tim

4 : Tube Up-Going 300.00/0.90/*NO-Output - UpChevTube.tim

#6: TmpQuery[OUTPUT DATA] - Temporary Output File with QUERY

   Output Name: WbW All

   Create Sort Indexes

   PLOT Data Vertical 2

TmpQuery - WbW All [TotalTraces: 1584]

Created Tue Mar 29 12:37:35 2011

BH1 – Wavefield separation processing flow

#7: InputMult[INPUT DATA] - Input Multiple Data Sets 4 Inputs

   Input   1: [8] - 790-785 05 WbW Stack [48 Traces 0.0 - 1500.0 ms SR: 500.000 us]

   Input   2: [16] - 560-555 05 Stack [48 Traces 0.0 - 1500.0 ms SR: 500.000 us]

   Input   3: [20] - 330-325 05 Stack [48 Traces 0.0 - 1500.0 ms SR: 500.000 us]

   Input   4: [24] - 100-095 05 Stack [48 Traces 0.0 - 1500.0 ms SR: 500.000 us]

   Sort Order[5]: DEPRCV

   Window Data: 0.000000 - 1130.000000

   -- NO DATA SELECTIONS --

InputMult 192 Traces Input

#9: MuteTrc[TRACE EDIT] - Muting - Interp, Offset[Trace] Dependent

   Mute File: F:\VISTA Projects\BHP 3C Hydro VSP\BHP 3C Hydro VSP-files\MiscFiles\28Top.mut

   Taper Mute Zones by 4 Samples

#10: EnsemStk[STACK] - Ensemble Header Stack

   Sort Key not Defined - Use Input Ensemble Sort Order

   Stack: 1 / (N + 1)

2 Headers Adjust on Stack

    SHOT_POINT_NO - First Value

    FIELD_RECORD_NO - First Value

#11: BWorth[FILTERING] - ButterWorth Filter

  Zero Phase Filter

  Low Cut: Stop- 5.00[Amp 5.000000] Pass- 15.00[Amp 95.000000]

  High Cut: Pass- 150.00[Amp 95.000000] Stop- 200.00[Amp 5.000000]

#12: BulkShft[STATICS] - Apply Bulk Time Shift

  Bulk-Shift: -130.0000 ms

#8: Output[OUTPUT DATA] - Output Data

   * Temporary Output File with QUERY

  Output Name: ZVSP deTube All

  Create Sort Indexes

  PLOT Data Vertical 2

Output - ZVSP deTube All [TotalTraces: 186]

Created Fri Sep 16 10:28:43 2011

#1: Input[INPUT DATA] - Input Data [29] - ZVSP deTube All NEW

  Seismic Input: [29] - ZVSP deTube All NEW

  NO SORT ORDER

  Window Data: 0.000000 - 1000.000000

  -- NO DATA SELECTIONS --

#3: EditHed[HEADERS] - Header Edit

  MAP 1 ** VWUSER_18

    # IF SHOT_POINT_NO Equal To: 95.0000

     ASSIGN [CONSTANT] 0.500

    # ELSEIF SHOT_POINT_NO Equal To: 325.0000

     ASSIGN [CONSTANT] 0.500

    # ELSEIF SHOT_POINT_NO Equal To: 330.0000

     ASSIGN [CONSTANT] 1.000

ELSEIF SHOT_POINT_NO Equal To: 560.0000
  ASSIGN [CONSTANT] 1.000
ELSEIF SHOT_POINT_NO Equal To: 555.0000
  ASSIGN [CONSTANT] 0.750
ELSEIF SHOT_POINT_NO Equal To: 785.0000
  ASSIGN [CONSTANT] 3.500
ELSEIF SHOT_POINT_NO Equal To: 790.0000
  ASSIGN [CONSTANT] 3.000

#2: Flatten[STATICS] - Flatten To Header Event
  Flatten Datum: 0.000 Header Item: VWUSER_18

#4: TmpQuery[OUTPUT DATA] - Temporary Output File with QUERY
  Output Name: Stat
  Create Sort Indexes
  PLOT Data Vertical 2
TmpQuery - Stat [TotalTraces: 186]
Created Fri Sep 16 10:41:17 2011

#1: Input[INPUT DATA] - Input Data [13] - Stat NEW
  Seismic Input: [13] - Stat NEW
  NO SORT ORDER
  -- NO DATA SELECTIONS --

#4: Flatten[STATICS] - Flatten To Header Event
  Flatten Datum: 100.000 Header Item: DATA_FIRSTBREAK

#6: Scale[SCALING] - Data Scaling
  Scale: 1.000 RMS Trim Median
  Gate Window: ENTIRE TRACE

#5: Flatten[STATICS] - Flatten To Header Event
  Flatten Datum: 100.000 Header Item: DATA_FIRSTBREAK [Reverse Flatten]

SubInput 1:#5 - Flatten To Header Event [STATICS] - 2:#9 - Apply F-K Designed Filter File [2D TRANSFORMS]

#11: OrmsbyBP[FILTERING] - Ormsby Band-Pass 5.00/15.00-155.00/220.00 Hz
       Domain Filter Application: Frequency
       Restore Mutes after Filtering
       Percent Zero Padding for FFT: 10.00 %

#12: TmpQuery[OUTPUT DATA] - Temporary Output File with QUERY
   Output Name: Stat scale Clean II
   Create Sort Indexes
   PLOT Data Vertical 1
    Output Group# 9: 5: ZVSP NEW separation
TmpQuery - Stat scale Clean II [TotalTraces: 186]
Created Thu Sep 22 09:05:23 2011

#1: Input[INPUT DATA] - Input Data [20] - Stat scale Clean II
   Seismic Input: [20] - Stat scale Clean II
   NO SORT ORDER
   -- NO DATA SELECTIONS --

#3: Flatten[STATICS] - Flatten To Header Event
   Flatten Datum: 100.000 Header Item: DATA_FIRSTBREAK

#4: AtmFilter[SIGNAL ENHANCEMENT] - Alpha trim mean filter
   ATM Filter Trcs: 13[3 Samples]Median Filter

#5: Flatten[STATICS] - Flatten To Header Event
   Flatten Datum: 100.000 Header Item: DATA_FIRSTBREAK [Reverse Flatten]

#6: OrmsbyBP[FILTERING] - Ormsby Band-Pass 5.00/15.00-155.00/200.00 Hz
       Domain Filter Application: Frequency
       Restore Mutes after Filtering
       Percent Zero Padding for FFT: 10.00 %

SubInput 1:Input Data [20] - Stat scale Clean II - 2:#6 - Ormsby Band-Pass [FILTERING]

#7: TmpQuery[OUTPUT DATA] - Temporary Output File with QUERY
   Output Name: P Down median II
   Create Sort Indexes
   PLOT Data Vertical 2
    Output Group# 9: 5: ZVSP NEW separation
TmpQuery - P Down median II [TotalTraces: 186]
Created Thu Sep 22 09:06:58 2011

#1: Input[INPUT DATA] - Input Data [22] - P Down median II
   Seismic Input: [22] - P Down median II
   NO SORT ORDER
   -- NO DATA SELECTIONS --

#4: FK_Filter[2D TRANSFORMS] - Apply F-K Designed Filter File
   F-K File: F:\Vista Files\BHP 3C Hydro VSP\BHP 3C Hydro VSP-files\MiscFiles\FansII.fkl
   Power: 1.00 TrcSmooth: 7 FreqSmooth: 5
   F-K Filter Operation: REJECT
   Apply removable Agc 300.00 ms

#5: MuteTrc[TRACE EDIT] - Muting - Interp, Offset[Trace] Dependent
   Mute File: F:\Vista Files\BHP 3C Hydro VSP\BHP 3C Hydro VSP-files\MiscFiles\ZVSP Top.mut
   Taper Mute Zones by 4 Samples

#2: AGC[SCALING] - Automatic Gain Control(AGC) L1/L2 Norm Equalization
   AGC Length: 1000.00 Scale: 1.000 Norm Eq: L1

#3: TmpQuery[OUTPUT DATA] - Temporary Output File with QUERY
   Output Name: 03 ZVSP Bal
   Create Sort Indexes

PLOT Data Vertical 2

 Output Group# 9: 5: ZVSP NEW separation

TmpQuery - 03 ZVSP Bal [TotalTraces: 186]

Created Thu Sep 22 09:20:08 2011

#1: Input[INPUT DATA] - Input Data [23] - 4 ZVSP Bal II

   Seismic Input: [23] - 4 ZVSP Bal II

   NO SORT ORDER

   Window Data: 0.000000 - 1000.000000

   -- NO DATA SELECTIONS --

#4: Flatten[STATICS] - Flatten To Header Event

   Flatten Datum: 0.000 Header Item: DATA_FIRSTBREAK [Reverse Flatten]

#6: AtmFilter[SIGNAL ENHANCEMENT] - Alpha trim mean filter

   ATM Filter Trcs: 7[1 Samples]Median Filter

#11: Flatten[STATICS] - Flatten To Header Event

   Flatten Datum: 0.000 Header Item: DATA_FIRSTBREAK

#13: MuteTrc[TRACE EDIT] - Muting - Interp, Offset[Trace] Dependent

   Mute By Header Values

   Apply Top Mute Header Item: DATA_FIRSTBREAK

   Taper Mute Zones by 4 Samples

#12: TmpQuery[OUTPUT DATA] - Temporary Output File with QUERY

   Output Name: 5 Enhanced

   Create Sort Indexes

   PLOT Data Vertical 2

    Output Group# 9: 5: ZVSP NEW separation

TmpQuery - 5 Enhanced [TotalTraces: 186]

Created Thu Sep 22 09:25:42 2011

Appendix V

Raw and processed data from Leinster hydrophone VSP 2009

Figures A4 and A5: Raw common receiver of channels a) 1 and 5, b) 9 and 13, c) 17 and 21

Figures A6 and A7: Raw stacked shot gathers at 100 m offset intervals a) Line 1 down-dip offsets 100, 200, 300 400 and 500 m. b) Line 2 up-dip offsets 100, 200, 300 400 and 500 m.

Figures A8 and A9: Down-going P wavefield separated shot gathers of Figures A6 and A7.

Figure A10: CDP gathers of wavefield separated data of Figures A8 and A9 with limited offset contributions a) all offsets, b) all down-dip, c) down-dip offsets from 200 to 500 m and d) up-dip offsets only.
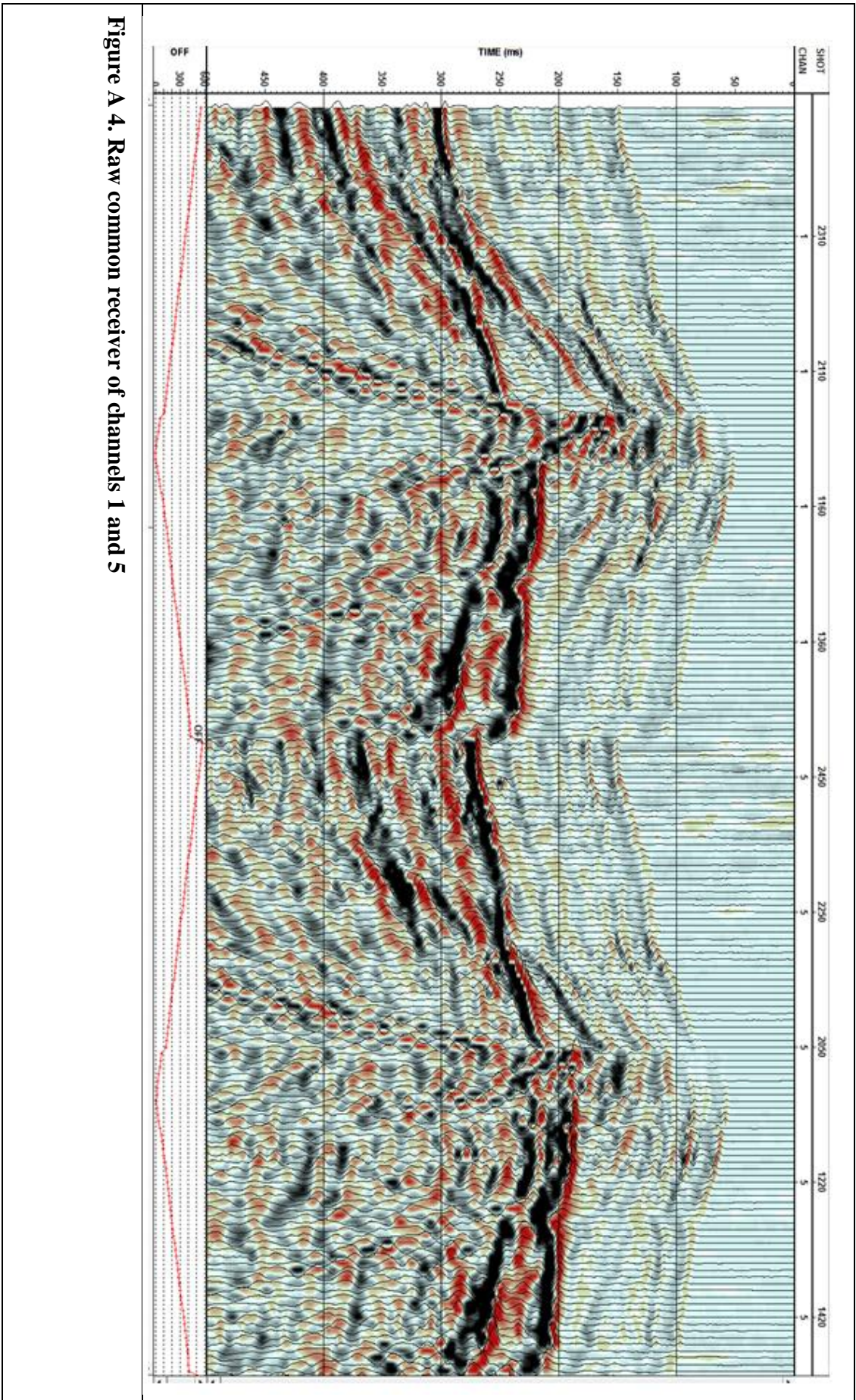
Figure A 4. Raw common receiver of channels 1 and 5
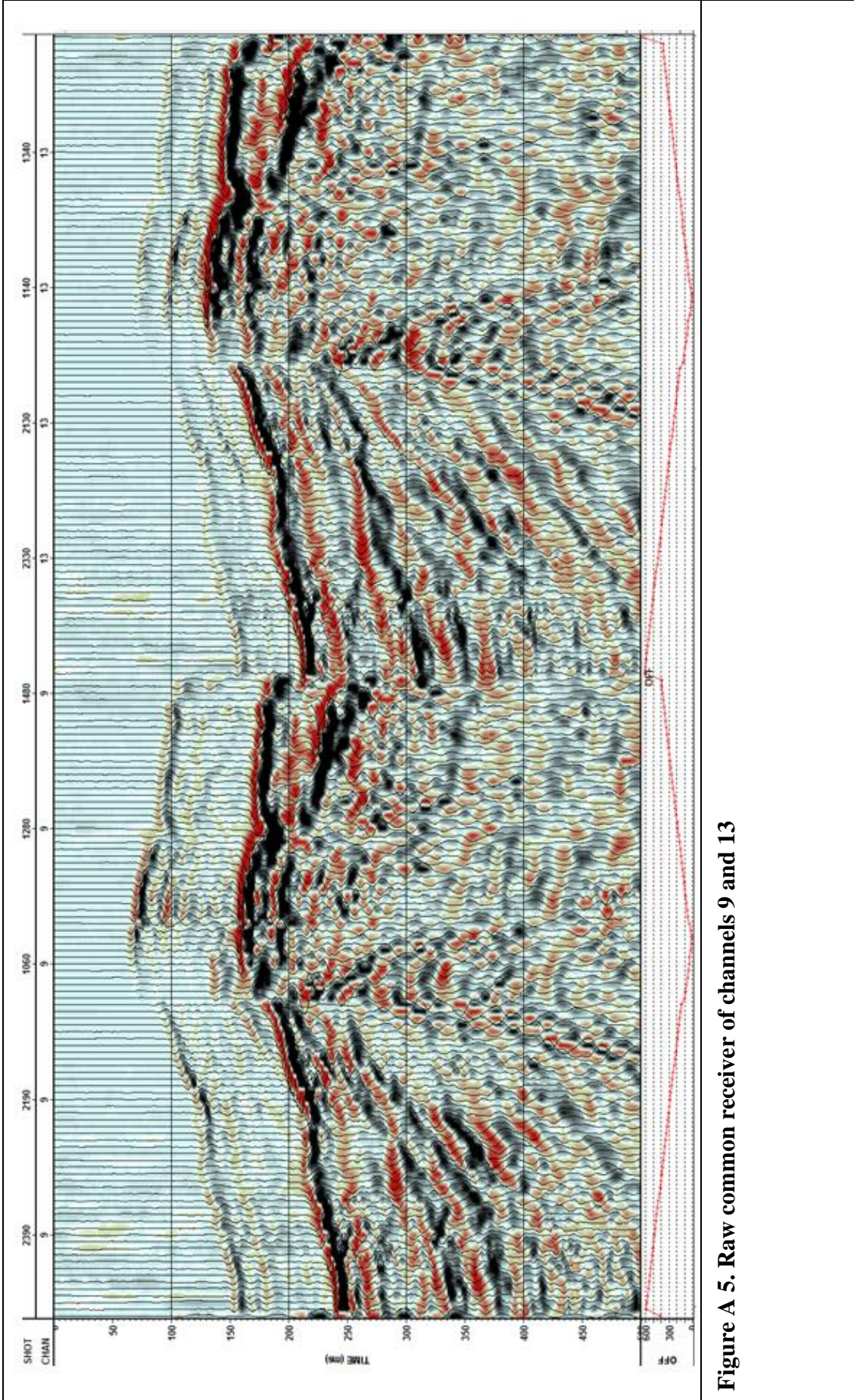
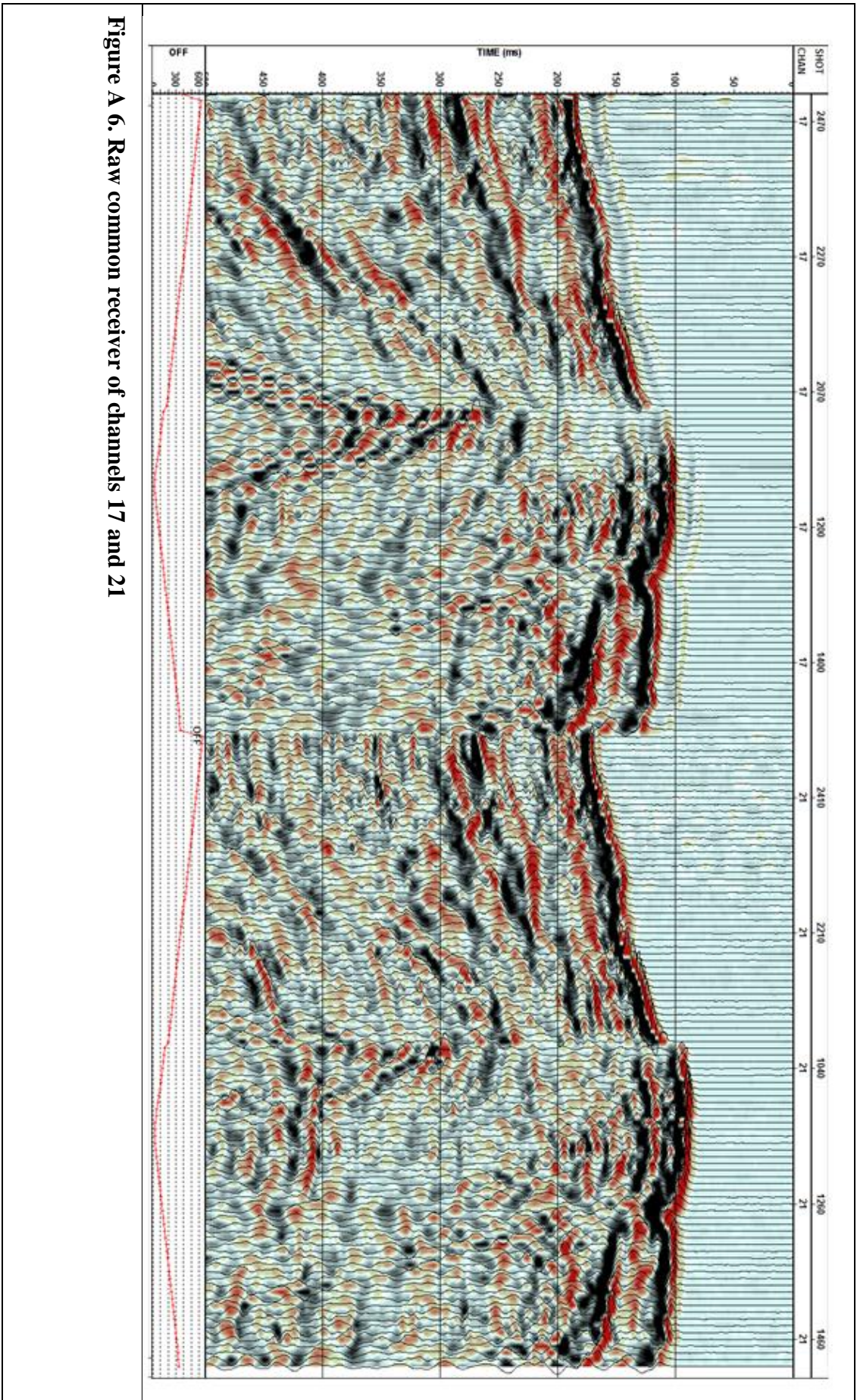**Figure A 5. Raw common receiver of channels 9 and 13**

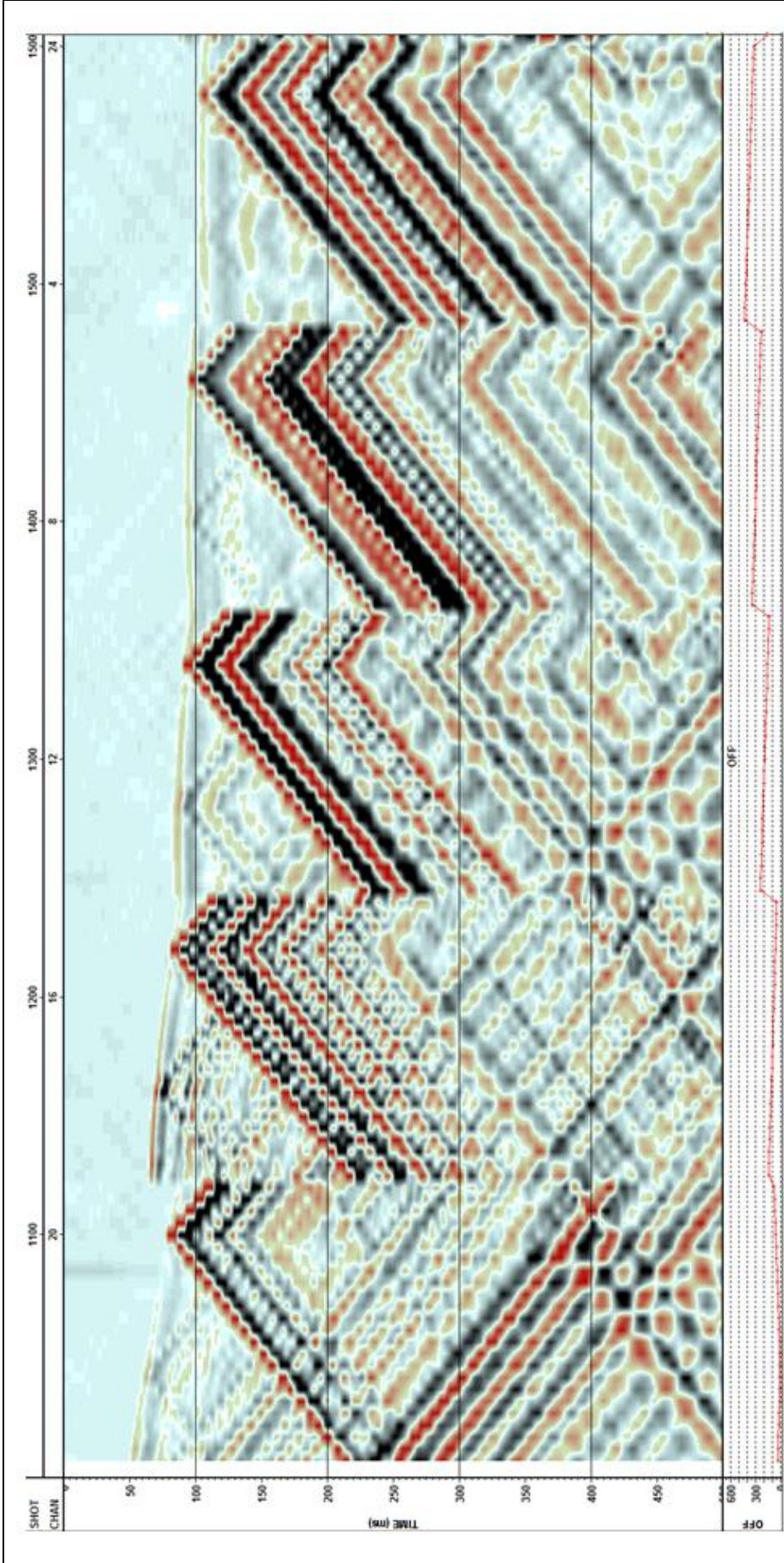**Figure A 6. Raw common receiver of channels 17 and 21**

Figure A 7. Raw stacked shot gathers for line 1 down-dip offset intervals 100, 200, 300 400 and 500 m.
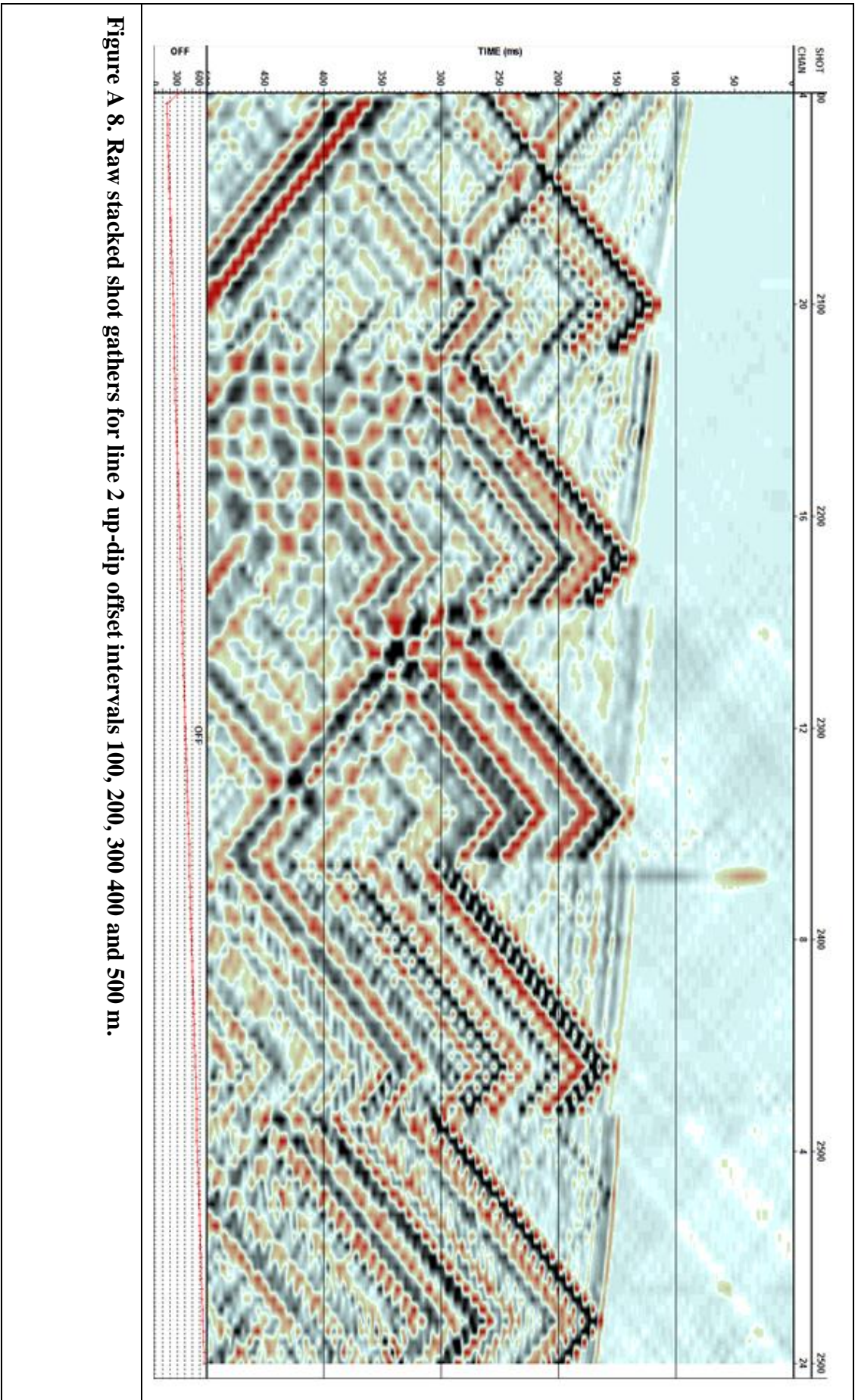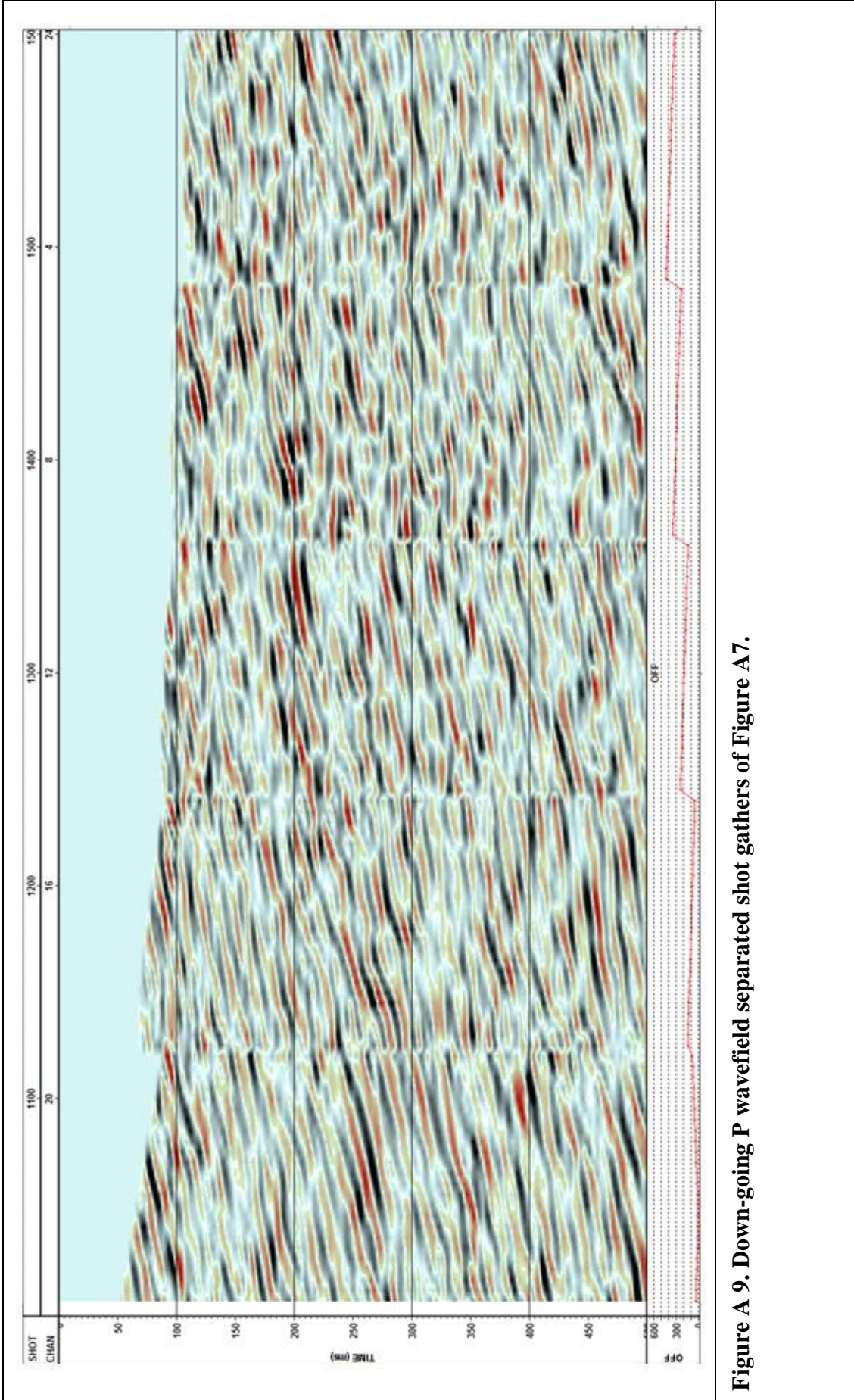
Figure A 8. Raw stacked shot gathers for line 2 up-dip offset intervals 100, 200, 300 400 and 500 m.

Figure A 9. Down-going P wavefield separated shot gathers of Figure A7.
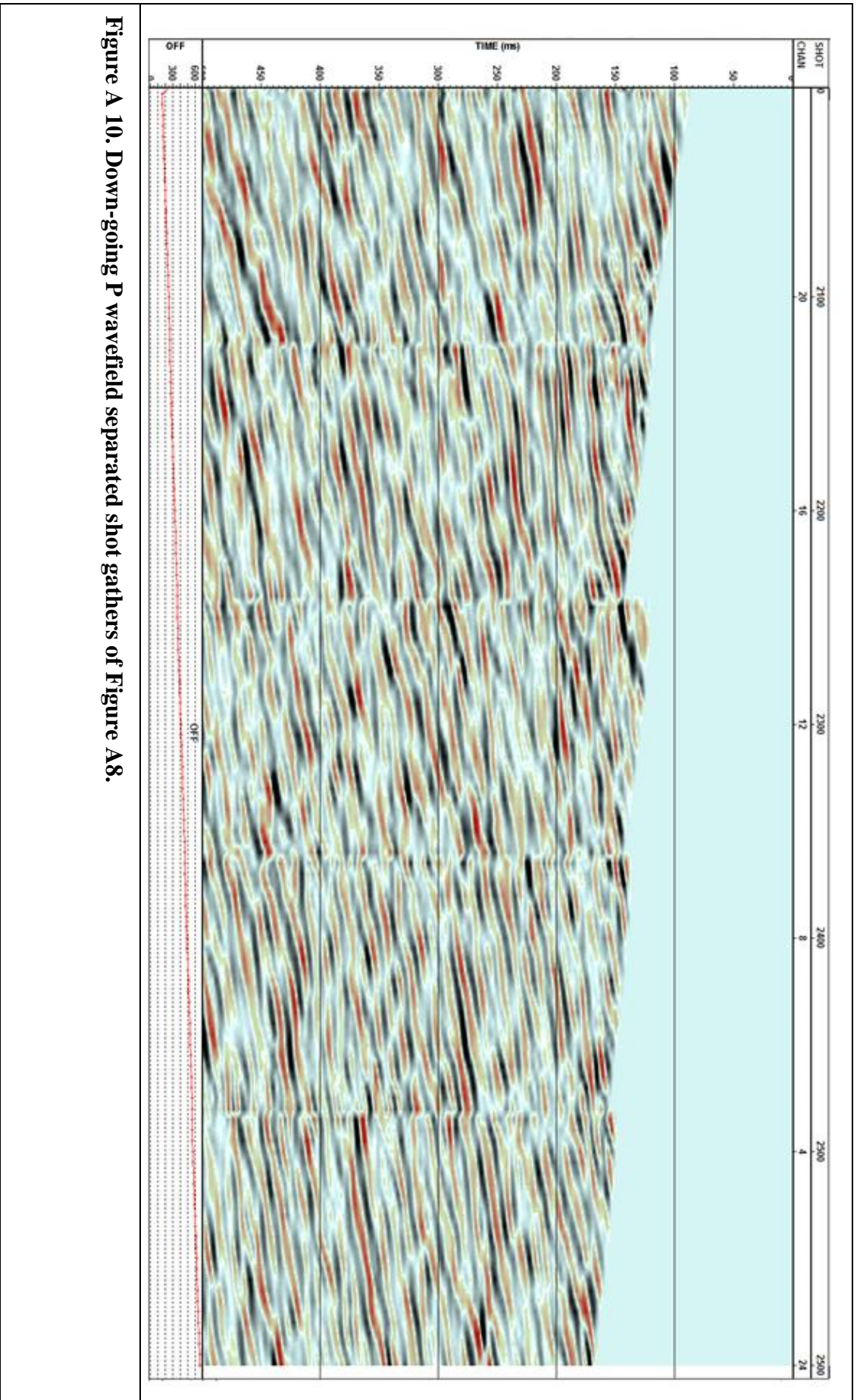
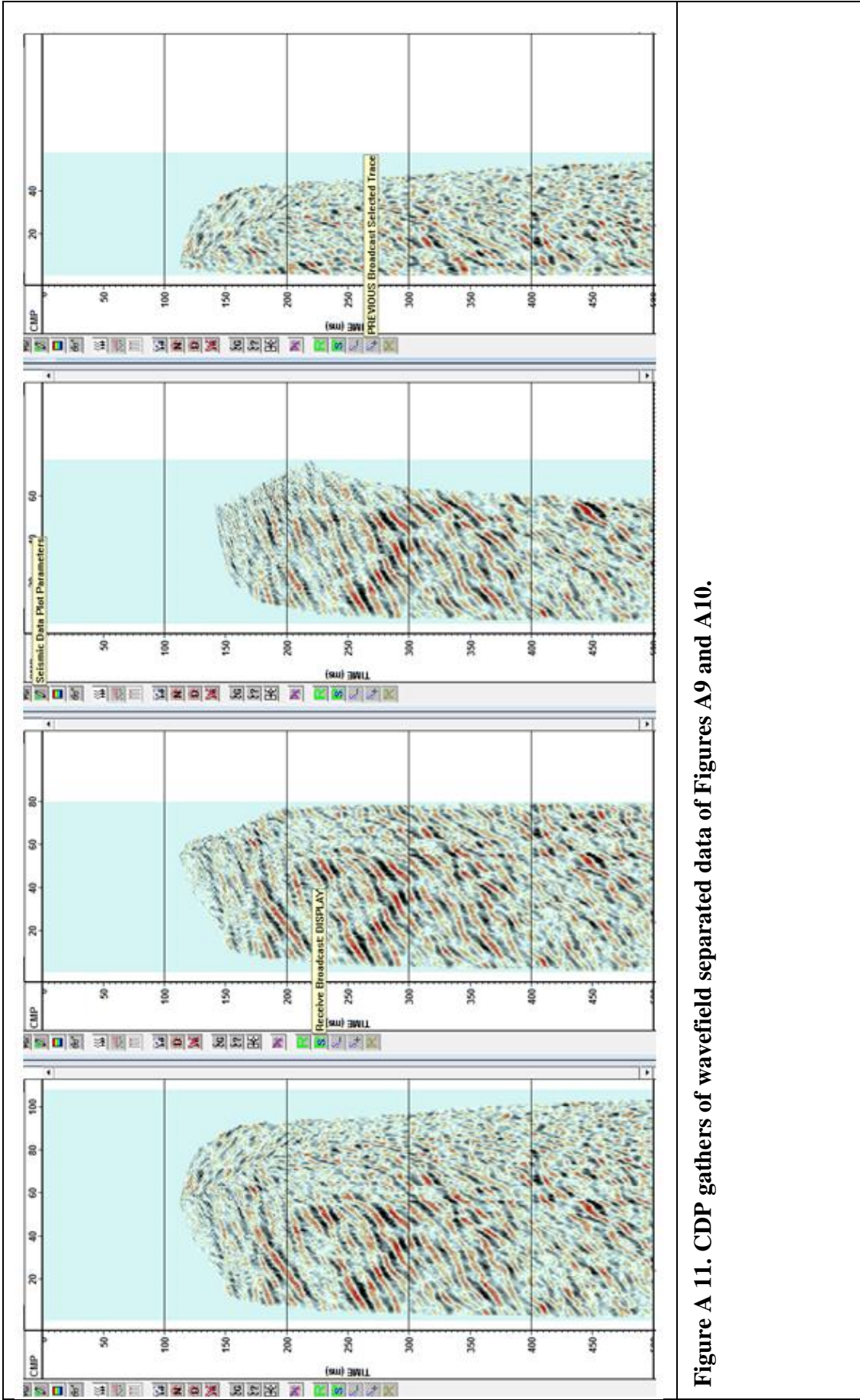**Figure A 10. Down-going P wavefield separated shot gathers of Figure A8.**

Figure A 11. CDP gathers of wavefield separated data of Figures A9 and A10.